The Dissertation Committee for Soraya Sofia Betancourt
certifies that this is the approved version of the following dissertation:

Some Aspects of Deep Formation Testing

Committee:

Larry W. Lake, Co-Supervisor

Elizabeth B. Dussan V., Co-Supervisor

Ekwere J. Peters

Carlos Torres-Verdin

Russell T. Johns

Some Aspects of Deep Formation Testing

by

Soraya Sofia Betancourt, B.S.; M.S.E.

DISSERTATION
Presented to the Faculty of the Graduate School of
The University of Texas at Austin
in Partial Fulfillment
of the Requirements
for the Degree of

DOCTOR OF PHILOSOPHY

THE UNIVERSITY OF TEXAS AT AUSTIN
May 2012

Some Aspects of Deep Formation Testing

Publication No. __________________

Soraya Sofia Betancourt, Ph.D.
The University of Texas at Austin, 2012

Supervisors: Larry W. Lake
Elizabeth B. Dussan V.

Abstract

Single-probe formation testers have been used since the 1950s to measure pore pressure and estimate mobility in fluid-bearing formations penetrated by a well. They are widely used in the oil and gas industry, with tens of measurements often made in every newly drilled well as part of the formation evaluation program. Each measurement consists of placing the tool in the wellbore in direct contact with the face of the formation, extracting a small amount of fluid (from 1 to 50 cm^3) from the rock and analyzing the fluid pressure response of the system.

Pressure interpretation is based on models that assume that temperature within the formation tester flowline remains constant during the tool operation. However, formation pressure measurement involves relatively fast volume and pressure changes within the flowline, which result in temperature changes. These temperature changes are modeled semi-analytically and their effect on pressure transients is analyzed. Temperature variations are accounted for by describing the pressure and temperature dependence of fluid

density in the continuity equation, and that temperature varies with both space and time. It is considered here that once a temperature change is imposed on the system, the primary mechanism of thermal transport to achieve equilibrium is conduction. Including temperature in the analysis requires taking into account flowline geometry, and well environmental conditions during the measurement– namely, wellbore temperature and type of drilling fluid in the wellbore, all of which are immaterial in the isothermal analysis.

Arguably, pressure behavior during formation tester measurements could be influenced by several factors. All previous studies related to formation testers assume perfect tool performance and provide explanations to pressure behaviors from the reservoir point of view (e.g., Stewart and Witmmann, 1979; Phelps et al., 1984; Proett and Chin, 1996, etc.). The approach followed here is diametrically opposite. The formation is considered 'perfect' from the point of view of pressure measurement, and physical phenomena (thermal transients) that may affect the measured pressure signal are studied. The focus is to understand fundamental aspects of the tool performance that can be studied analytically while minimizing, as much as possible, external parameters that add uncertainty.

This dissertation was motivated by inconsistencies observed between the pressure behavior in field measurements and existing (isothermal) theory. For instance, false buildups, buildup overshoots and long time required to reach pressure equilibration, have puzzled those involved in the interpretation of formation tester pressure transients for many years. These behaviors can be reproduced in pressure computations when accounting for temperature

variations. The focus of this dissertation is on modeling the tool capability to sense pressure transients associated with recompression of formation fluids several inches away from the wellbore, accounting for temperature variations during the measurement. This is relevant because it is desirable to characterize formation properties beyond the region affected by drilling mud filtrate invasion.

In practice, a discrepancy is often observed between formation mobility obtained from drawdown, which depends mostly on formation properties near the wellbore, and mobility obtained from the analysis of late-time buildup pressure, which in theory depends on formation properties farther from the wellbore (Moran and Finklea, 1962). This dissertation examines the influence of late-time tool storage effects caused by thermal equilibration of the flowline fluid on the pressure equilibration and buildup mobility interpretation. It was found that in some cases such late-time storage effects could exhibit a behavior that resembles that expected from spherical flow, that is, the flow regime characteristic of single-probe formation testers; and could therefore invalidate mobility determined by isothermal transient pressure analysis.

Formation tester flowline and probe design, test parameters (rate and volume), and environmental conditions during the measurement, mostly type of drilling fluid and wellbore temperature, are important variables in determining the magnitude of late-time storage effects, and hence the tool capability to detect a deep formation signal (spherical flow). Temperature variations affecting late-buildup pressure transients were observed to be more pronounced (listed in order of importance): as wellbore temperature increases; drilling

fluid is oil-based mud; flowline with large radius components (e.g. > 1 cm); large flowline volume; small probe radius (< 1 cm); and, large drawdown rate. Temperature effects on the late-buildup also tend to be more significant when mobility is in the 0.1 to 10 md/cp range, that is for those formations more likely, in theory, to exhibit spherical flow regime during buildup.

Table of Contents

Abstract **iv**

List of Tables **xi**

List of Figures **xii**

Chapter 1. Introduction **1**
- 1.1 Research Objectives 3
- 1.2 Specific Aspects of this Work 4
- 1.3 Overview of the Chapters 5

Chapter 2. Problem Statement **8**
- 2.1 Formation Testers 10
  - 2.1.1 Single-Probe Formation Tester Components and Basic Operation 16
  - 2.1.2 Pretest Sequence 17
  - 2.1.3 Environmental Conditions during the Pretest 18
- 2.2 Literature Review 20
- 2.3 Problem Description 29
- 2.4 Solution Approach 32

Chapter 3. Quantifying Pressure Transients Associated with the Formation during Pretests **34**
- 3.1 Introduction 34
- 3.2 Pressure Behavior during Drawdown and Buildup in a Pretest 36
- 3.3 Approach 49
- 3.4 Solution Method 53
- 3.5 Results 57
- 3.6 Discussion 64

Chapter 4. Analysis of Temperature Variations During the Pretest 77
4.1 Introduction 77
4.2 Theoretical Development 79
4.3 Problem Statement 87
    4.3.1 Scaling 89
    4.3.2 Dimensionless Groups 91
4.4 Solution Procedure 97
4.5 Results 97
4.6 Discussion 124

Chapter 5. Examples of Pressure Computations Accounting for Temperature Variations 129
5.1 Effect of Thermal Transients on Pretests that Maximize the Formation Signal 129
    5.1.1 Formation Mobility 0.01 md/cp 130
    5.1.2 Formation Mobility 0.1 md/cp 133
    5.1.3 Formation Mobility 1 md/cp 137
    5.1.4 Formation Mobility 10 md/cp 140
5.2 Some Comparisons of Computed and Measured Pressure Data 142
    5.2.1 Example 1 142
    5.2.2 Example 2 144
    5.2.3 Example 3 150
5.3 Discussion 152
5.4 Discussion of Other Factors that Could Influence the Pressure Behavior in the Tool 155

Chapter 6. Conclusions 163
6.1 Future Directions 170

Appendices 173

Appendix A. Thermodynamic Analysis of the Pretest 174

Appendix B. Analysis of the Temperature Variation in the Flowline during the Pretest 186
B.1 Conservation of Mass in the Flowline 186
B.2 Conservation of Energy in the Flowline 190
B.3 Problem Statement 193

Appendix C. Justification for Using the Mass Average Temperature in the Conservation of Mass Equation 201

Appendix D. Model Representation of a Formation Tester with Uniform Flowline Radius 205

D.1 Drawdown without Formation Inflow (Dry Drawdown) 206
D.2 Drawdown with Formation Inflow 209
D.3 Buildup 216
D.4 Alternative Solution of the Radial Temperature Distribution at the End of Drawdown 221

Appendix E. Multi-Radii Flowline with Constant Wall Temperature 227

E.1 Drawdown without Formation Inflow 229
E.2 Drawdown with Formation Inflow 230
E.3 Buildup with Formation Inflow 231
E.4 Buildup without Formation Inflow 232
E.5 Evaluation Procedure 232

Appendix F. Heat Transfer Accounting for the Surrounding Tool 238

F.1 Drawdown without Formation Inflow 239
F.2 Extension of the Solution to Multiple Flowline Components . . 241
F.3 Drawdown with Formation Inflow 242
F.4 Buildup 243
F.5 Extension of the Solution to Multiple Flowline Components . . 244
F.6 Validity of the QSS Formation Inflow Approximation 245
F.7 Spherical Flow with Flowline Storage (Variable Temperature) . 245

Appendix G. Laplace Transform Inversion Algorithm 249

Nomenclature 251

References 254

Vita 263

List of Tables

2.1 Typical range of operational parameters of single-probe formation testers. 17

3.1 Dimensions of the three tools used to evaluate the size of the formation signal. 57
3.2 Pretest that maximizes the formation signal for the *small probe radius* tool for given values of formation mobility. 57
3.3 Pretest that maximizes the formation signal for the *medium probe radius* tool for given values of formation mobility. 63
3.4 Pretest that maximizes the formation signal for the *large probe radius* tool for given values of formation mobility. 63

4.1 Typical tool parameters. 99
4.2 Parameters for the study of the variation of $1/\gamma$. 108
4.3 Flowline dimensions for the tool example. 118

5.1 Tool and wellbore parameters used for all the cases presented in Chapter 5. 130
5.2 Parameters for the 0.01 md/cp case with *large probe radius* tool. 132
5.3 Parameters for the 0.1 md/cp case - *large probe radius* tool . . 135
5.4 Parameters for the 0.1 md/cp case - *small probe radius* tool . 137
5.5 Parameters for the 1 md/cp case - *large probe radius* tool . . . 140
5.6 Parameters for the 1 md/cp case - *small probe radius* tool . . 140
5.7 Parameters for the 10 md/cp case - *large probe radius* tool . . 142
5.8 Parameters for the 10 md/cp case - *small probe radius* tool . . 142

List of Figures

2.1 The Wireline Formation Tester (1955) was the first commercial formation tester in the oil industry. Courtesy of Schlumberger. 12

2.2 Repeat Formation Tester (RFT) flowline 14

2.3 RFT probe assembly 15

2.4 Example of flowline pressure and volume measurements acquired with a formation tester. 19

3.1 Flowline pressure, P_{fl}, versus time. 39

3.2 Semi-logarithmic plot of buildup pressure data. 41

3.3 Log-log plot of buildup pressure data. 43

3.4 Pressure distribution in the reservoir during the spherical flow regime. 44

3.5 First example of different mobility values derived from a pretest. 46

3.6 Pressure vs. spherical time plot for determining mobility in the example shown in Figure 3.5 47

3.7 Second example of different mobility values derived from a pretest. 48

3.8 Spherical flow analysis for example shown in Figure 3.7 49

3.9 Third example of different mobility values derived from a pretest. 50

3.10 Spherical flow analysis for the example shown in Figure 3.9. . 51

3.11 Comparison of measured spherical and drawdown mobility values in one well. 51

3.12 Definition of ΔP_X, the maximum amplitude of spherical flow. 52

3.13 Maximum formation signal for the *small probe radius* tool ($k/\mu <$ 1 md/cp) 58

3.14 Maximum formation signal for the *small probe radius* tool ($k/\mu <$ 1 md/cp) 59

3.15 Maximum formation signal for the *small probe radius* tool ($k/\mu \geq$ 1 md/cp) 60

3.16 Maximum formation signal for the *medium probe radius* tool (0.001 – 100 md/cp). 61

3.17 Maximum formation signal for the *large probe radius* tool (0.001 md/cp $\leq k/\mu \leq$ 100 md/cp). 62

3.18 Buildup equilibration for the pretests that maximize the spherical flow signal with *small radius probe* tool. 65
3.19 Buildup equilibration for the pretests that maximize the spherical flow signal with *medium radius probe* tool. 65
3.20 Buildup equilibration for the pretests that maximize the spherical flow signal with *large radius probe* tool. 66
3.21 Pressure distribution in the reservoir at the onset of spherical flow for pretests that maximize the spherical flow signal (*small radius probe* tool). 70
3.22 Pressure distribution in the reservoir at the onset of spherical flow for pretests that maximize the spherical flow signal (*medium radius probe* tool). 71
3.23 Pressure distribution in the reservoir at the onset of spherical flow for pretests that maximize the spherical flow signal (*large radius probe* tool). 72
3.24 Pressure distribution in the reservoir for 0.1 md/cp formation, all tools. 73
3.25 Buildup pressure equilibration for 0.1 md/cp formation for (q,ΔV) that maximize the spherical flow signal for the three tools considered. 74
3.26 Buildup equilibration plots with tool noise. 75
3.27 Buildup equilibration plots with tool noise, *large* probe radius tool. 76

4.1 Example of false buildup during a pretest 78
4.2 Example of buildup overshoot during a pretest 79
4.3 Formation tester flowline. 81
4.4 Values of thermodynamic properties for computation of ΔP_{ddS}. 83
4.5 Values of thermodynamic properties for computation of $\Delta\Theta_{ddS}$. 84
4.6 Values of thermodynamic properties for computation of ΔP_{bu}. 86
4.7 Effect of reference pressure and temperature on dimensionless group Y 92
4.8 Effect of pressure and temperature on τ_{heat} (water). 94
4.9 Effect of pressure and temperature on τ_{heat} (oil). 94
4.10 Effect of pressure and temperature on $1/\gamma$. 95
4.11 Effect of parameter Y on P_D. 100
4.12 Effect of parameter Y on $\langle\Theta_D\rangle$. 101
4.13 Effect of parameter Y on buildup equilibration (0.1 md/cp). . 102
4.14 Effect of Y on buildup equilibration (1 md/cp). 103

4.15 Effect of Y on buildup equilibration (10 md/cp). 104
4.16 Effect of parameter $1/\gamma$ on the flowline pressure. 106
4.17 Effect of $1/\gamma$ on buildup pressure. 107
4.18 Effect of $1/\gamma$ on the average temperature. 109
4.19 Effect of $1/\gamma$ on the flowline temperature distribution. 110
4.20 Effect of parameter X on the pressure. 111
4.21 Effect of X on the buildup. 112
4.22 Effect of X on the average temperature. 112
4.23 Effect of overbalance on P_D. 114
4.24 Buildup pressure overshoot when $-P_D(0) > 0$. 115
4.25 Effect of overbalance on pressure equilibration. 115
4.26 Effect of overbalance on the average temperature. 116
4.27 Effect of overbalance on the temperature distribution. 117
4.28 Performance of a uniform radius tool vs. a multi-radii tool with pressure overbalance. 119
4.29 Performance of a uniform radius tool vs. a multi-radii tool without pressure overbalance. 120
4.30 Dry pretest. 123

5.1 Error in the buildup computation by assuming constant flowline volume, $k/\mu = 0.01$ md/cp. 131
5.2 Pressure equilibration with variable temperature for the pretest that maximizes the formation signal in 0.01 md/cp with *large probe radius* tool. 133
5.3 Error in the buildup computation by assuming constant flowline volume, $k/\mu = 0.1$ md/cp. 134
5.4 Temperature effects on pretests that maximize formation signal, $k/\mu = 0.1$ md/cp. 136
5.5 Error in the buildup computation by assuming constant flowline volume, $k/\mu = 1$ md/cp. 138
5.6 Temperature effects on pretests that maximize formation signal, $k/\mu = 1$ md/cp. 139
5.7 Temperature effects on pretests that maximize formation signal, $k/\mu = 10$ md/cp. 141
5.8 Example 1. Pressure log acquired with the *small probe radius* tool in oil-based mud, $\Theta = 366$ K (200 F). 143
5.9 Example 1. Buildup equilibration for first pretest. 144
5.10 Example 1. Buildup equilibration for second pretest. 145

5.11 Comparison of 24 spherical and drawdown mobility values measured with the *small probe radius* tool in one well. 146
5.12 Example of 'false spherical flow' in the derivative of a forward modeled pretest 148
5.13 Example 2. Pressure log acquired with the *small probe radius* tool in oil-based mud. 150
5.14 Example 2. Buildup equilibration. 151
5.15 Example 3. Pressure log acquired with the *small probe radius* tool in oil-based mud. 152
5.16 Example 3. Pressure log acquired with the *small probe radius* tool in oil-based mud. 153

A.1 Explanation of the equilibrium states of the system following a volume increase ΔV when the probe is set against an impermeable formation. 175
A.2 Adiabatic compressibility of water and hexadecane 180
A.3 Isothermal compressibility of water and hexadecane 181
A.4 Coefficient of thermal expansion of water and hexadecane . . . 182
A.5 Thermodynamic properties of water and n-hexadecane used for the computation of ΔP_{ddS}. 183
A.6 Thermodynamic properties of water and n-hexadecane used for the computation of $\Delta\Theta_{ddS}$. 184
A.7 Thermodynamic properties of water and n-hexadecane used for the computation of the pressure increase during a false buildup. 185

B.1 Definition of the coordinate system to model flow from the reservoir to the flowline. 189
B.2 Definition of the control volume and system of coordinates assumed in the conservation of energy equation for the heat conduction problem. 191

C.1 Ideal system divided by a frictionless piston. 201

D.1 Definition of the control volume used in the conservation of energy equation and coordinate system for the heat conduction problem. 206
D.2 Dimensionless average temperature for a drawdown without formation inflow 209
D.3 Dimensionless pressure for a drawdown without formation inflow 210
D.4 Dimensionless temperature profile at the end of a drawdown without formation inflow 211

E.1 Flowline model for the computation of Pressure and Temperature accounting for conduction and various flowline components of different radii. 228

F.1 Flowline model used for the calculation of P and Θ accounting for the presence of the tool 238

Chapter 1

Introduction

This research is related to the study of certain aspects of the performance of formation testers (Testers). Testers are used routinely in oil and gas wells to measure formation pore pressure, and to determine formation mobility (phase permeability-viscosity ratio). Typically, measurements are acquired in openhole wellbores during or after drilling as part of the formation-evaluation program. Testers are the only formation-evaluation tools that rely on the motion of formation fluids as measuring principle and, therefore, provide the most direct assessment of formation permeability.

The volume of reservoir investigated with these tools is considerably smaller than for a pressure transient well test. On the other hand, formation testers are used to make measurements at various locations along a wellbore, yielding a much higher resolution of the mobility in the borehole direction. Pressure data collected with a formation tester can, at the very least, quantify formation mobility with a shallow depth of investigation, that is, the mobility of the formation in direct contact with the tool. In addition, formation testers have the potential to estimate formation mobility in a reservoir region away from the wellbore (several wellbore radii away from the tool), this property is referred to as deep mobility. This deep mobility is of interest because no other tool or technique could provide flow properties in this region.

Testers have several configurations to measure formation pressure. The focus of this dissertation is on single-probe tools. More specifically, it is on the basic operation of a formation tester, referred to as the pretest. The pretest consists of withdrawing a small amount of fluid from the formation to create a pressure transient. Pretests are always performed whenever a tester is used as a precursor of longer-duration operations (interval tests, multiple probe tests, fluid sample acquisition, etc); however, pretests are often the only measurement acquired by a formation tester.

One area of concern with regard to formation tester pretests is that interpretation of pressure data to infer mobility in the reservoir region beyond the wellbore is not considered a reliable method. Part of the problem lies in the difficulty to identify a signal originating in the 'deep' formation during buildup (a formation signal). In addition, whenever this formation signal is identified, it has been frequently observed that inconsistencies arise between shallow and deep mobility. The mobility value corresponding to the shallow measurement should be, according to intuition, smaller than the deep mobility. The rationale is that the near wellbore region is expected to be more affected by formation damage during drilling. One possible explanation is that deep formation mobility is determined from the analysis of the rate of change of the pressure near the end of buildup, when it is close to equilibrium, and signal-to-noise ratio is low.

Since the introduction of formation testers in the 1950s, analysis of pretest transients assumes that temperature is constant during the measurement. Assessing the validity of the isothermal assumption is one of the objectives of this dissertation. Thermal transients are considered to be of interest based on observations of the tester behavior during *dry pretests*. During a dry pretest, the drawdown fails to establish hydraulic communication between the tool and the formation; therefore, no formation fluid enters the flowline. After a ‘dry’ drawdown, the pressure signal increases and may behave similar to a buildup. This pressure increase could be misinterpreted as the response of a permeable formation. To the best of the author’s knowledge, there have been no published explanations of the pressure behavior during a dry pretest. A hypothesis is that temperature decreases during drawdown and then must increase, causing pressure to increase accordingly. This hints to the possibility that temperature variation may also affect pressure measurements in permeable media.

Two publications were issued during the course of this research:

- “Inducing Spherical Flow Conditions with Formation Testers”, Betancourt, S.S., Dussan V., E.B., and Lake, L.W., Paper SPE 133523, presented at the Soc. of Petroleum Engineers Annual Technical Conference and Exhibition, September 2010.
- “Effects of Temperature Variations on Formation Tester Pretests”, Betancourt, S.S., Dussan V., E.B., and Lake, L.W., Paper SPE 146647, presented at the Soc. of Petroleum Engineers Annual Technical Conference and Exhibition, October 2011.

1.1 Research Objectives

The general objectives of this research are:

- Identify measurement parameters that maximize the pressure signal associated with formation compressibility (deep formation) to reduce uncertainty in mobility obtained from pressure transient analysis.
- Analyze the effects of temperature variations on pretest pressure transients.

1.2 Specific Aspects of this Work

Conventional analysis of pretests assumes isothermal conditions; in theory, formation pressure signal depends on several variables that fall into three categories: tool, formation, and test variables. Aside for corrections in pressure instrumentation, namely temperature compensation of pressure gauges, to the best of the author's knowledge, no effort has been made to understand the influence of the measuring instrument (the formation tester as a whole) on the investigated phenomena (the formation response). To address whether it is possible to detect an unambiguous formation response, the performance of existing tools is analyzed. Furthermore, it is desirable to identify pretest parameters that would maximize the 'deep' formation pressure signal.

The analysis of pretest pressure is refined by developing a model of the tool performance that accounts for environmental conditions during measurements. Analysis of temperature variations during pretests requires incorporating more variables into the problem: thermodynamic properties of the fluid in the flowline(typically oil base mud or water based mud), temperature, and pressure overbalance between static wellbore pressure and formation pressure.

An important aspect of this problem is that analysis of temperature variations requires recognizing that temperature varies locally within the flowline, which is the main formation tester component. A flowline consists chiefly of probe assembly, pretest mechanism and pressure gauge. Therefore, flowline design features must be considered. New variables are geometry and dimensions of flowline components, thickness of the tool material surrounding the flowline, and heat transport properties of the tool material and the flowline fluid. Solution complexity increases substantially compared to the isothermal case.

The solution approach in this research consisted of implementing an optimization scheme to identify pretest parameters that maximize the formation pressure signal. As a first approximation, this is done assuming that flowline fluid temperature remains constant. Next, a novel analysis of the effects of thermal variations on the tool performance is presented. This problem is solved by obtaining a semi-analytic solution for flowline storage that accounts for the thermodynamic behavior of the fluid and heat transfer between the flowline, the tool and the wellbore. The feasibility of detecting a formation signal is revisited with this improved flowline storage model.

The chief contribution of this work is that general insight has been gained on the relevant aspects of tool design and environmental conditions that may influence the behavior of the pressure signal during the pretest.

1.3 Overview of the Chapters

The roadmap of this dissertation is as follows. Chapter 2 provides a description of the design and operation of formation testers, and a review of the theory behind the interpretation of the pretest. This is followed by a more detailed description of the problem, the review of the literature, and a description of the solution approach.

Chapter 3 describes the optimization approach to maximize the formation signal during a pretest and results are presented for three tools. For this analysis it is assumed that flowline fluid temperature remains constant; therefore, the only relevant tool variables here are probe size and flowline volume.

The analysis of flowline storage accounting for temperature variations is in Chapter 4. A discussion of the thermodynamic behavior of the system (flowline and fluid) during the pretest provides both physical insight into the problem and some of the relevant scales for the mathematical model. Relevant equations are identified and the physical significance of the dimensionless groups that appear in this problem is discussed. Results are presented in dimensionless form and the pressure performance for several tool designs is analyzed.

Chapter 5 revisits the problem of assessing the feasibility of measuring a formation signal with the new flowline storage solution that takes into account the environmental conditions. The performance of specific tool designs, with pretest parameters that would maximize the formation signal, is evaluated to identify the environmental conditions that may interfere with the measurement. Finally, a summary of the results, conclusions, and recommendations are presented in Chapter 6.

Details on the mathematical derivations and proofs are presented in the appendices. Appendix A gives a more detailed thermodynamic analysis of the pretest than that presented in chapter 4. Plots of thermodynamics properties for water and hexadecane, that could be used to assess the magnitude of pressure and temperature changes for a given pretest, are also presented there. Appendix B, details the procedure followed to derive the boundary-value problems for the various cases studied here, namely, dry drawdown, normal drawdown, normal buildup, and false buildup. A proof for the justification of the use of mass-averaged temperature in the conservation of mass equation is presented in Appendix C.

Solutions in Appendices D, E and F are organized by their complexity, reflecting the way in which the problem was solved. The simplest model consists of a flowline with uniform radius (Appendix D) and constant temperature at the wall. This solution is extended to account for various flowline components with different radii (Appendix E). Finally, the presence of the surrounding tool, which has an effect on the time required for reaching thermal equilibrium, is taken into account in Appendix F.

All of the solutions presented have been tested. It is considered that the final product, that is, the multi-radii flowline with the surrounding tool, may be understood better by contrasting it with simpler solutions. Appendix F also discusses the validity of the quasi-steady state approximation of the formation influx in the mass conservation equation. The equations that must be solved to account for the formation compressibility (spherical flow) with flowline storage, including thermal variations in the flowline, are presented there. The Laplace Transform inversion algorithm used for the numerical computations is outlined in Appendix G.

Chapter 2

Problem Statement

Permeability is one of the most important properties used to characterize the production performance of hydrocarbon reservoir s (Muskat, 1949 and Bear, 1988). Measurements of permeability at different scales are useful to assess its spatial variation and its effect on fluid production.

Permeability measurements on rock samples are made routinely in the laboratory or in outcrops using permeameters and mini-permeameters (API, 1952; Muskat, 1949; Eigne and Weber, 1971; Jones, 1972, 1994; Hoggin et al., 1988; etc.). Even though the rock volume investigated is on the order of a few cubic centimeters, the advantage of this type of measurement is that it enables the assessment of spatial variation of permeability along the cored section of the reservoir. Permeability anisotropy at the scale of a core plug could be quantified with this technique by measuring sample permeability along different directions (Hoggin et al., 1998b).

Well tests are a widely used technique to assess the quality of a reservoir and a well (e.g. Earlougher, 1977; Mathews and Russell, 1967; Raghavan, 1993). The analysis of pressure and production history during tests yields, among others, reservoir permeability, pressure, volume, and damage (skin). The reservoir properties obtained from a well test correspond to a volume in the scale of the drainage area of the well. Well transient tests require that completion or drill stem hardware be present in the wellbore.

Formation testers perform small-scale pressure-transient tests on the formation near the wellbore while the well is being drilled or soon after. Since these tools are used typically in open-hole conditions, conveyed by wireline or the drilling string, they do not require additional production hardware. Pressure transients recorded during the operation of formation testers are used acquire measurements of the pore pressure of the reservoir at the sandface and to estimate the mobility (phase permeability-viscosity ratio). Formation testers have a high vertical resolution, as several measurements could be made along the wellbore.

The scale of the mobility estimated from the basic operation of a formation tester, the pretest, is similar to that of a laboratory permeameter (with the caveat that the flow geometry is different due to the presence of impermeable mudcake); this property is known as drawdown mobility. In some cases, a second mobility could be obtained from the analysis of flow regimes in the late-time portion of pressure buildup during the pretest. Buildup mobility is associated with a reservoir region farther from the wellbore (on the order of several borehole radii). The reservoir volume characterized by buildup mobility corresponds to a scale smaller than the drainage volume of the well. Formation testers may be used in other ways to investigate a larger reservoir volume (Schlumberger, 2006; Kuchuk et al., 2010); however, the test volume will still be smaller than the drainage volume of the well.

The focus of this research is the single-probe formation tester pretest because it is a fast and convenient way to acquire important reservoir information. Pretests are performed routinely, and several, typically tens of measurements, are made at different locations in a well. In addition, the single-probe formation tester, that is, the tool configuration used to perform pretests, is the simplest formation tester. This facilitates investigating the impact of pretest parameters, tool design, and environmental conditions, on the tool capability to measure a pressure signal originating from deep formation properties, that is, to determine buildup mobility.

A brief historical overview of the development of formation testers, some aspects of the design of present day formation testers, and the details of pretest operation are presented next. The purpose of this section is to introduce the terminology used throughout the dissertation. The literature review will concentrate on the theoretical development of current interpretation techniques and a discussion of the state of the art in the treatment of the environmental effects on formation tester measurements.

2.1 Formation Testers

Wireline Formation Testers were introduced in 1955 by Lebourg et al., (1956), as an alternative to drill stem testing (Kuchuk et al., 2010). Tool conveyance by logging cable and the ability to make measurements in an open hole were a technological breakthrough at the time; a picture of the first generation formation tester is shown in Figure 2.1. These first tools operated by positioning the tool at a desired depth in the well; pressing a seal pad against the borehole wall; then, firing an explosive charge into the formation to establish flow channels between the reservoir; and, filling a sample chamber with fluid from the formation. The sample chamber communicated with the formation by means of the internal tubing in the tester (the flowline); both sample chamber and flowline were at atmospheric conditions at the beginning of the test. The primary objective of these pioneering tools was to gather physical evidence of the production features of the formation. They collected one to five gallons of formation fluid and filtrate while simultaneously measuring (and transmitting to surface) the flowline pressure throughout the entire operation. Initially, the pressure measurement was used only to diagnose the status of the tool, but since the conception of the technique, there was a realization of the potential to determine the pore pressure and the permeability of the tested zone (Doll, 1952).

The next major technological breakthrough in the area of formation testing was the introduction of the Repeat Formation Tester (RFT) in 1975 by Schlumberger (Schultz et al., 1975, and Pelissier et al., 1979). The first-generation tools could only make measurements at one station in the well and had to be taken to the surface to be reconditioned if additional tests were required. The RFT allowed for several measurements to be done at various locations along the wellbore and introduced the concept of *pretest* to refer to the operation of withdrawing a small volume of fluid from the formation and recording the pressure signal until it reaches equilibrium with the pore pressure at the face of the formation, that is, the *sandface pressure*. The behavior of the pressure signal is analyzed to identify permeable regions in the formation and to ascertain the integrity of the packer seal before acquiring a fluid sample.

Since the introduction of the RFT tool, formation testers do not use

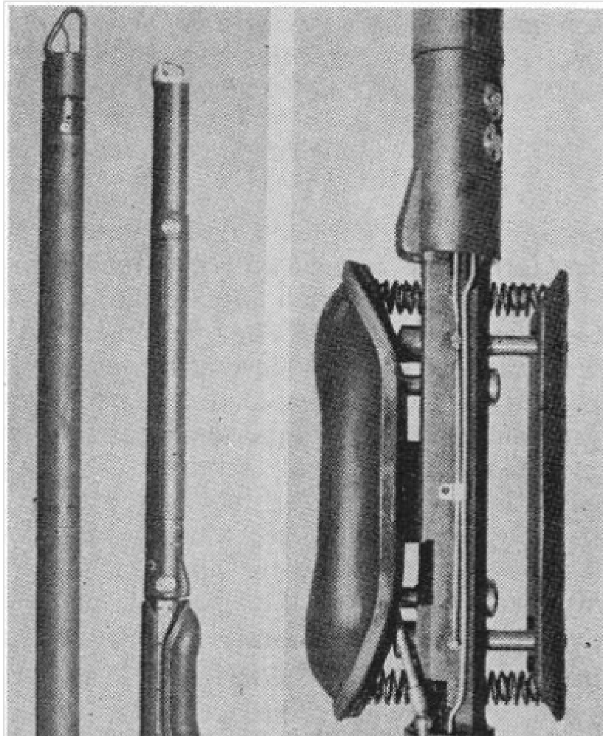

Figure 2.1: The Wireline Formation Tester (1955) was the first commercial formation tester in the oil industry. Courtesy of Schlumberger.

explosive charges to communicate the tool with the formation. Instead, the tip of the flowline is in direct contact with the seal pad or packer (Figure 2.3). Once the tool is set against the borehole, and the seal pad pressed against the formation, the piston that covers the flowline tip is retracted (by the hydraulic system in the tool), and the flowline is open to the borehole. Flowline volume is increased by retracting the piston in the pretest chamber at a controlled speed. This creates the pressure differential that allows the flow of formation fluid into the tool. The pressure gauge is at the other end of the flowline. Modern formation testers, also functioning as fluid sampling tools, isolate the portion of the flowline that is used for pressure measurement from the rest of the tool.

The RFT tool is the archetype of present-day formation testers. Its flowline (Figure 2.2) includes all the elements present in a modern tool: a probe assembly (consisting of packer, probe piston and a filter in the piston barrel), pressure gage, pretest chamber, equalizing valve, and seal valves. More recent advances include improvements in pressure measurement technology with the introduction of higher resolution quartz gauges, and refined control of the pretest drawdown rate either by hydraulic or electromechanical control of the piston movement.

Presently, there are many commercial formation testers used mainly in the oil and gas industry. The latest major development in this area is the introduction in the early 2000's of formation testers that are part of the bottomhole drilling assembly. This service, formation testing while drilling, follows the same operational principles introduced by the RFT.

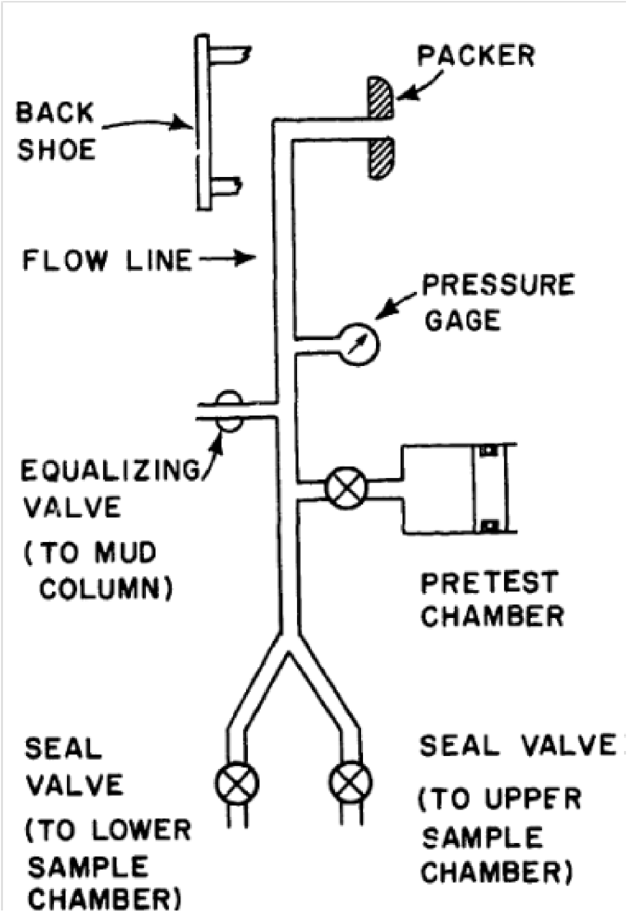

Figure 2.2: Functional schematic of the Repeat Formation Tester (RFT) flowline. Courtesy of Schlumberger.

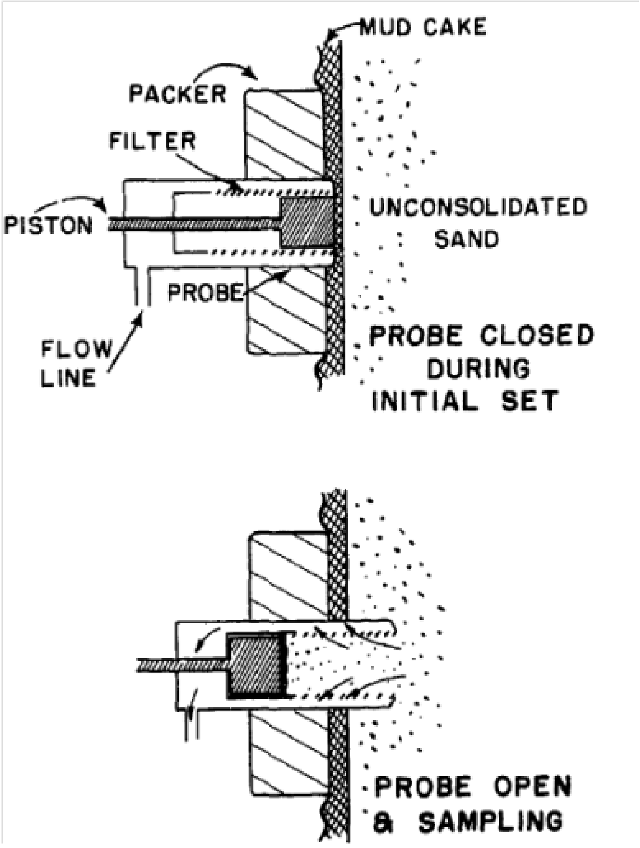

Figure 2.3: Detail of the RFT probe assembly in the closed position (top) and the open position (bottom). Courtesy of Schlumberger.

2.1.1 Single-Probe Formation Tester Components and Basic Operation

A brief description of the basic components of the RFT flowline is given next (Schultz et al., 1975; Smolen and Litsey, 1979; Pelissier et al., 1979). At one end of the flowline is the probe assembly (refer to Figure 2.3), which consists of a packer, the probe barrel (with a filter), and a piston. The tool is lowered in the well in the retracted or closed position. The probe barrel is aligned with the packer and the piston is extended covering the probe orifice (the radius of the probe orifice is referred to as r_{probe}) to prevent the entrance of fluid into the tool. The equalizing valve that communicates the flowline with the wellbore is open; hence, the flowline pressure is the same as the pressure of the mud column in the well. The seal valves that connect to the sample chambers remain closed while the tool is lowered to the well and during the entire pretest.

The operational sequence of a formation tester is as follows. When the tool is set to make a measurement, the back shoe (anchoring system) and the probe assembly are extended from the tool body and pressed against the opposing wall of the borehole. The equalizing valve is closed, and a command is given from surface to push the probe barrel against the formation and retract the probe piston. When the probe piston is retracted, formation fluid enters though the probe orifice, then passes through the filter and is in communication with the rest of the flowline. The probe filter function is to prevent entrance of debris that may obstruct the flowline.

A pretest is initiated when a command is given from the surface to retract the piston in the pretest chamber. The pressure in the flowline is registered by the gauge or gauges during the entire process. Eventually, the measurement ends when a command is given from the surface to open the equalizing valve. The flowline pressure increases to the static pressure in the wellbore and the back shoe and probe assembly are retracted to the closed position.

2.1.2 Pretest Sequence

The pretest consists of two periods: drawdown and buildup. During the drawdown period the pretest piston retracts at a user specified rate, q, to increase the flowline volume, $V_{flowline}$, by a user specified amount, ΔV, known as the pretest volume. Typical values of these parameters are given in Table 2.1. The initial pressure in the flowline is the wellbore pressure, that is, the static pressure of the mud column, and it is typically larger than the formation pressure. The positive value of the difference between the wellbore pressure and the formation pressure, required to maintain the wellbore under control, is referred to as 'overbalance'. During the pretest, the flowline must be decompressed below the formation pressure to allow flow from the formation into the flowline.

$V_{flowline}$	from 50 to 200 cm^3
q	from 0.02 to 2.0 cm^3/s
ΔV	up to 40 cm^3
r_{probe}	0.5 to 2.5 cm

Table 2.1: Typical range of operational parameters of single-probe formation testers.

The buildup period begins when the pretest piston stops. The tool operator waits for the flowline pressure to increase and equilibrate to the pore pressure at the formation face (sandface pressure). It is common practice in field operations to consider that pressure has reached equilibrium from observing the time derivative plot of the pressure signal. Once the operator makes a decision to terminate the pretest, then a choice is made to repeat the pretest sequence to confirm the result, or to terminate the test by opening the equalizing valve. Figure 2.4 shows the flowline pressure, P_{fl}, and the flowline volume change for two consecutive pretests.

2.1.3 Environmental Conditions during the Pretest

Formation testers are mostly used in uncased (openhole) wellbores. Therefore, the fluid in the wellbore around the tool is the drilling fluid, typically water-based mud (WBM) or oil-based mud (OBM). The difference between the pressure in the wellbore, exerted by the static mud column or the circulating mud, and the sandface pressure, is referred to as *overbalance* and could be several thousand psi in some formations.

Another aspect of openhole operations is the presence of a mudcake around the wellbore. An ideal mudcake isolates the formation from the wellbore and minimize the invasion of mud filtrate and mud solids into the formation. In addition, an ideal mudcake should offer minimum resistance to be lifted off the formation sandface during the pretest. Laboratory experiments and analysis of field logs indicate that the pressure differential in the flowline required to lift off or breach the mudcake could be of several hundred psi ($<$ 500psi). The formation flow properties could be affected by solid particles entering the pore space during invasion. This process, known as formation

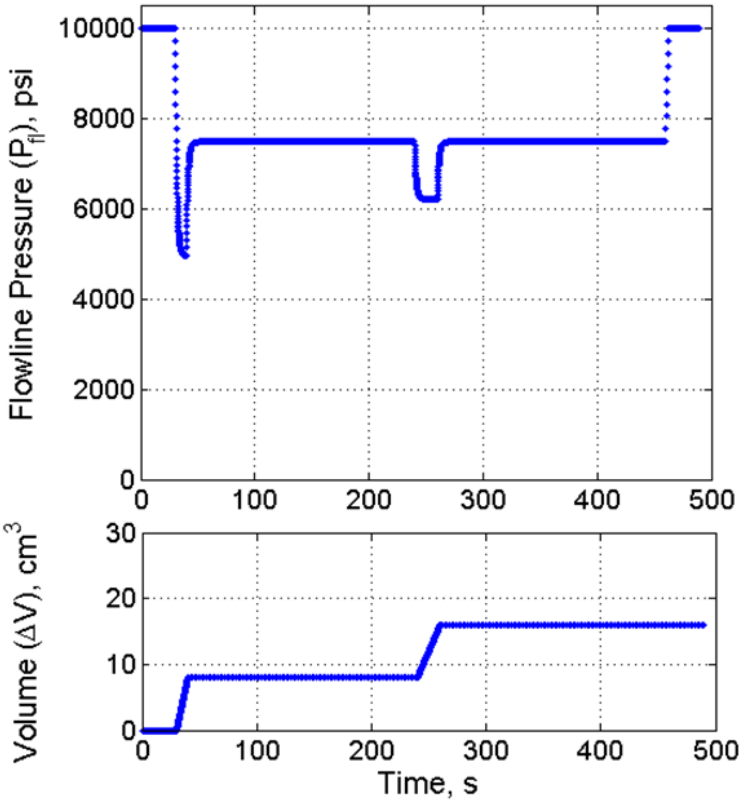

Figure 2.4: Example of flowline pressure and volume measurements made with a formation tester. In this case the initial pressure, that is, the wellbore pressure, is 10,000 psi. Two pretests were performed at this station, the first one starting at 20 seconds and the second one, performed with the pretest piston retracting at one half of the speed of the first one, starting at 240 seconds. For both pretests the volume was 8 cm^3. At the end of the second pretest the equilibration valve is opened and the flowline pressure returns to the wellbore pressure.

damage, may affect the permeability near the wellbore, that is, in the region investigated by the formation tester drawdown mobility.

Invasion is a common situation for all formation evaluation techniques in open holes. An aspect that is particular to formation testers is the increase of formation pore pressure around the well when invaded by drilling fluid filtrate (Pelissier et al., 1979). The rate of invasion decreases significantly when the mudcake forms. In a high permeability formation, the excess pressure diffuses once the filtration slows down, and the formation pressure at the sandface is very close or equal to the initial formation pressure when the measurements with the formation tester are performed. In low permeability formations the excess pressure takes a long time to decline, and when the formation tester measurement is conducted sandface pressure could be several hundred psi above the initial formation pressure. It is said then that the zone is supercharged. Supercharging depends strongly on the capability of the mud to create an effective mudcake, ability of the formation to dissipate pressure disturbance caused by mud filtration (leak-off), time since the mudcake formation, and on mudcake damage caused by drilling operations.

2.2 Literature Review

Moran and Finklea provided the theoretical basis for the analysis of formation tester pressure data in their seminal 1962 paper. Their main contribution was to identify the relevant flow geometries pertinent to formation testers, namely spherical flow for formation layers of sufficient thickness, and radial flow for thin layers. Furthermore, these authors recognized that the pressure data conveyed two values of formation mobility. The first mobility value, a function of the total pressure difference during the test (sandface formation pressure minus steady-state drawdown pressure), which they referred to as drawdown mobility, reflects only the properties of the formation in direct contact with the probe. The second mobility value is obtained from the interpretation of the rate of pressure equilibration during the late part of buildup.

A very significant discovery made by Moran and Finklea was that during the late part of the buildup the presence of the wellbore and the perforation is not relevant for the interpretation of the pressure data. In the case of spherical flow there are no geometric dimensions in the late-time solution; in the case of radial flow only the formation thickness appears in the late-time solution. This implies that the pressure behavior during these flow periods is controlled by formation properties away from the wellbore (at least several borehole radii away from the well).

The potential to characterize the formation properties in a reservoir region away from the wellbore, possibly past the zone damaged by filtrate invasion, is a very promising feature of formation testers. Moran and Finklea also analyzed the effects of permeability anisotropy. Their results extend to anisotropic formations by defining the effective permeability during the spherical flow regime as $k_{eff}^3 = k_H^2 k_V$.

The effects of wellbore storage or afterflow effects on early-time transient pressure behavior have long been recognized in the well testing community. Brigham et al. (1980) extended the work of Moran and Finklea to couple the spherical flow behavior in the far field (late-time pressure measurement at the tool) with conservation of mass in the wellbore, or tester flowline, to account for storage. Conservation of mass within the tool flowline requires that the rate of change of volume in the flowline, caused by the compressibility of the flowline fluid and the compliance of the flowline components, plus the sandface formation flowrate must equal the pretest drawdown flowrate. In their modeling of the conservation of mass within the tool flowline, they assume that the wellbore storage coefficient is constant, which implies a constant compressibility factor of the fluid in the wellbore or the flowline, and do not consider mechanical compliance of the tool. Their model takes into account the effects on the pressure response caused by the presence of the wellbore, but does not consider the effects of the wellbore curvature, which affect the 'intermediate-time' pressure response. This is the basic approach followed by many investigators. Joseph and Koderitz (1985) incorporated the skin effects to the model of spherical flow coupled with storage.

The first reference to the effect of borehole curvature on the pressure signal was found in the paper by Pelissier et al. (1979). Stewart and Wittmann (1979) performed numerical simulations to compute a correction factor (shape factor) for the computation of steady-state mobility for a ratio of the probe radius and wellbore radius, r_{probe}/r_{well}, of 0.0525 ($r_{probe} = 0.21$ in and $r_{well} = 4$ in). Hoggin et al. (1988) presented an analysis of the flow geometries under steady-state conditions for a mini-permeameter and computed the geometric factors, as a function of the probe and sample dimensions, to be used in a form of Darcy's equation pertinent to their problem. Dussan and Sharma (1987, 1992) presented an analysis of the flow within the formation in the area surrounding the probe and derived a procedure to account for permeability anisotropy in the steady-state drawdown equation. Wilkinson and Hammond (1990) performed an analysis of the borehole curvature effect for probe-type formation tester using a perturbation method. They found that the borehole effect is most significant for the computation of mobility as the value of r_{probe}/r_{well} increases, and as the permeability anisotropy increases. Proett and Chin (1996, 1998a, 1998b) succeeded at obtaining an analytic, closed-form solution that contains both the early-time storage and the late-time pressure response corresponding to spherical flow, as well as the presence of skin. Although their derivation neglects the effects of borehole curvature, they mention a correction factor obtained from finite element simulations.

An approximate solution of the problem described by Brigham et al., commonly used within the formation testing community, is obtained by recognizing that for the geometry of formation testers, the time required to diffuse a pressure pulse is much smaller within the formation than within the tool flowline. Therefore, it is valid to assume that with respect to the tool flowline, the formation response can be considered instantaneous. This solution is often referred to as the quasisteady-state or quasistatic approximation. The model then reduces to solving the inner boundary condition, that is, the conservation of mass in the tool flowline, describing the flow through the probe orifice using the steady-state form of Darcy's equation with the appropriate geometry.

Methods to estimate formation pressure and the mobility based on the quasisteady-state solution have been proposed as an alternative to circumvent the long time required for the flowline pressure to equilibrate in low mobility formations. The method by Proett et al. (1994) uses the early portion of drawdown pressure data before the mudcake is breached to estimate the flowline fluid compressibility. Then, a two parameter model containing as input data the flowline pressure and its derivative is fit to the early portion of the buildup data to obtain the formation pressure and the mobility. The method presented by Kasap et al. (1996) substitutes the measured flowline pressure and its derivative into the quasisteady-state approximation and does a multiparameter regression to obtain effective flowline compressibility, drawdown mobility and formation pressure. Kasap's model uses the entire pressure data, that is, drawdown and buildup. Kuchuk (1999) presented a technique to obtain the formation pressure based on the pressure solution to an instantaneous source. Kuchuk's method, which includes afterflow (storage) effects, could be used when the drawdown has not reached steady state, and does not require full development of the flow regimes. Dussan (2011) presented the theoretical foundation of the method used by Schlumberger since the 1980's to calculate formation mobility when the drawdown has not reached steady state.

The first reference to the effects of invasion on formation testers is made by Pelissier et al. (1979) in their discussion of the supercharging phenomenon. Stewart and Wittmann (1979) observed that the analysis of the sink-probe pressure buildup is highly affected by the presence of invasion. Depending on the depth of invasion and the mobility ratio of the invaded and uninvaded zones, the portion of the data corresponding to spherical flow may reflect the properties of the invaded or the uninvaded zone.

Later work by Phelps et al. (1984) used the Buckley-Leverett theory to model invasion in low-mobility formations. Their analysis focused on the effects of invasion on the measurement of the undisturbed formation pressure rather than the estimation of formation parameters, and suggested a method to correct for the effects of supercharging on the pressure data. They proposed accounting for the effects of invasion using a skin factor.

Goode and Thambynayagam (1996) analyzed the effects of an invaded zone on a multiprobe formation tester. They observed that the sink probe would always be highly affected by the invaded zone properties, regardless of the depth of invasion, mobility and compressibility ratios. For the set of test parameters that were considered in their study, it was not possible to derive the properties of the uninvaded formation from the analysis of drawdown or buildup. This result was attributed to the fact that pressure transients originating in the uninvaded zone would occur at a very late time, and without sufficient amplitude to be measurable.

Proett and Chin (1998) analyzed the presence of a concentrated region of reduced permeability in the vicinity of the wellbore by introducing a skin factor in their spherical flow solution with tool storage. They compared the results of their model to finite element simulations of an invaded zone near the wellbore and noted that for typical single probe tool parameters, the use of a skin factor provides good results for invasion depths less than 10 effective probe radii.

Gok et al. (2006) considered the effects of varying the depth of invasion, the ratio of the horizontal and vertical mobilities, and the ratio of the storativity of the invaded an uninvaded zone on the pressure data recorded at the sink probe. Their results showed that for depths of invasion between 6 and 40 in, the pressure at the sink probe was unaffected by the presence of invasion, which they attributed to the fact that the response due to the invaded zone occurs early and is masked by the tool storage. They observed that the larger the values of mobility ratio there would be further delay to observe the properties of the uninvaded zone in the derivative plots. These authors also considered the use of a skin factor to model the effects of invasion, and found a good agreement with their invasion model. Similarly, if the storativity ratio increases, meaning, for instance, that the native fluid is less compressible, there is a delay in detecting the signal originating from the uninvaded zone. However, Gok et al. results correspond to drawdown rate ($q \gg 100$ cc/s) that is considerably larger than for a pretest ($q \leq 2$ cc/s), and also their drawdown time is quite large (about 1 hour), therefore the signal that exhibits spherical flow behavior could be reasonably expected to correspond to a region of the reservoir beyond the invasion front, and has a very large amplitude. For these large drawdown rate and time, the invasion front is unlikely to remain stationary as was one of the assumptions of this model.

The approach of Angeles et al. (2006) consisted of solving simultaneously the process of drilling fluid filtrate invasion into the formation and the pressure transient with a formation tester, with a focus on the straddled packer tool configuration (the sink is a wellbore interval between two packers instead of a probe). In contrast to the work of Gok et al., their model includes the physics of two-phase immiscible flow, including capillary and gravity effects, and accounts for the fact that the invasion front might move during the drawdown. Angeles et al. observed that the viscosity of the native fluid (oil) is the parameter that has the largest impact on the estimation of mobility, and noticed that the viscosity of the invading fluid (water) had only a minor effect during drawdown. This behavior was attributed to the rapid decrease in saturation in the invaded zone as drawdown started, however, as in the case of Gok et al., the drawdown rates ($q \gg 30$ cm^3/s) are larger than for a pretest. Their results indicate also that accounting for the invasion process provides more accurate mobility estimation, and that assuming single-phase flow when two fluid phases are present could lead to an underestimation of the formation mobility.

Regarding the behavior of the formation invasion process, several authors (Goode and Thambynayagam, 1996; Phelps et al., 1984; Dias and Wilkinson, 1987; Ayan et al., 2007) concur that for mobility ratio, M, less than unity in low permeability reservoirs, the displacement of native fluid by the drilling fluid filtrate is piston-like. If this is the case, filtration can be modeled using the Buckley-Leverett theory, and it is reasonable to assume that within the invaded zone, there is only one mobile phase present for the purpose of pressure transient analysis. In the opposite situation, that is if the drawdown rate or drawdown time is large enough to distort the invasion front, then the displacement of the filtrate when the native fluid has much higher mobility is an unfavorable displacement process.

The literature does not address certain pressure responses that are often observed during pretests. For instance, when the formation tester fails to establish hydraulic communication with the formation, because of large overbalance or impermeable formation, the flowline pressure builds up at the end of the drawdown, even though no formation fluid is entering the flowline. In this case, the drawdown is said to be *dry* and the subsequent tool response is referred to as a *false buildup*. This could lead to large errors in the identification of the formation pressure and the estimation of mobility. Even in pretests that achieve hydraulic communication between the tool and the formation, it is often reported that the mobility obtained from the late-time buildup pressure signal has a lower value than the mobility determined using the entire pressure signal (drawdown and buildup), the latter evaluation of mobility being representative of the properties of the formation in the vicinity of the probe. This is counterintuitive as it is reasonable to expect that filtrate invasion during drilling causes damage around the borehole. Even large values of formation anisotropy do not give a satisfactory explanation for this commonly observed tool response (Dussan and Sharma, 1992). Another curious example is that in some pretests the flowline pressure rises above the sandface pressure in the early part of the buildup and then has to decrease (*buildown*) to equilibrate (Brown, 2003). Since the aforementioned pressure responses are undesirable, and their causes are poorly understood, they have not been extensively treated in the literature. It could be concluded that the existing theory is insufficient to take into account all observed phenomena associated with the pretest.

Transient effects in the wellbore pertinent to well testing have been considered both in the petroleum industry and in ground water hydrology (Pickens et al., 1987; Wang and Papamichos, 1994; Hasan et al., 1997; Johns and Ma, 1998). Pickens et al. identified that there are significant thermally induced pressure changes when testing wellbore intervals, particularly in low permeability formations, and that these thermal effects may induce "serious errors" in formation pressure and hydraulic conductivity estimates. Pickens et al. also discuss the effects of the compliance of the testing equipment during the test, something that is difficult to account for in well tests and may be more pronounced in low permeability reservoirs. Johns and Ma presented a method to account for the measured temperature in the transient pressure interpretation also for low permeability water reservoirs. These studies have shown that temperature variations in the wellbore may play an important role in the interpretation of transient test pressure data, especially as the wellbore temperature increases. Though there are certain similarities between well testing and formation testing, the geometries (wellbore interval vs. tool flowline) and the duration of the tests are vastly different.

2.3 Problem Description

The focus of this research is to investigate the disparity between two mobility values that may be obtained from a formation tester pretest, namely drawdown mobility and mobility from buildup data.

As explained in the literature review, drawdown mobility is always computed from pretest data. If the pressure signal reached steady state during drawdown, mobility is computed using the method presented by Moran and Finklea. For unsteady drawdown, mobility could be computed using the entire pressure signal as suggested by Proett et al. (1984), Kasap et al. (1996), and Dussan (2011).

Determining mobility from pretest buildup data, on the other hand, depends on the identification of flow regimes from the rate of change of buildup pressure and fitting the data to the radial or spherical model described by

Moran and Finklea (1962). In practice, identification of these flow regimes is also used for quality control of the measurement, an indicator that the pretest has succeeded at detecting a deep formation response. However, it has been found that there is uncertainty in the interpretation of the latter part of buildup to determine formation mobility, and the method is not considered robust. One possible explanation is that the portion of data used for identification and interpretation of flow regimes (spherical or radial) is near the end of buildup, when the pressure signal is close to equilibrium and the difference between sandface pressure and flowline pressure is likely to be close to the resolution of the tool. The term ‘tool resolution’ is used here to differentiate from the resolution of the pressure sensor. In fact, the nominal resolution of the pressure sensor only represents the lower bound of the resolution of the tool. A formation tester is a complex mechanical system, and some components of the flowline, or other parts of the tool, contribute to the noise in the pressure signal. This is an aspect of the measured signal that is seldom emphasized in conventional analyses of formation tester pressure data.

The first part of the solution approach to this problem is to evaluate the magnitude of the pressure signal during the spherical flow regime for three formation-tester designs and all possible pretest parameters within the operational constraints of the system. This is done for a range of values of formation mobility assuming isothermal conditions and isotropic permeability during the pretest. The purpose of this analysis is to assess theoretically the quality of the pressure signal with respect to the resolution of the tool.

The next aspect of the research is to investigate whether the tool itself may interfere with the pressure signal measured during the late part of buildup; more specifically, the effect of temperature variations during the pretest on the pressure signal. To date, the analysis of pressure transients associated with formation tester pretests assumes that the temperature remains constant during the measurement. Most fluids experience a decrease in temperature when undergoing an expansion, as in the case of the drawdown; therefore, it is to be expected that the temperature of the fluid within the flowline of the formation tester will change for typical pretest conditions. The second objective of this study is to assess the impact of these temperature transients on the pressure signal measured with single-probe formation testers.

A separate problem, not considered here, is the accuracy of the pressure gauge when its temperature changes. It is known that pressure sensors are affected by both pressure and temperature within the gauge (Veneruso et al., 1991; Hailstone and Ovens, 1995; Matsumoto et al., 2000); however, there is a difference between the thermal behavior of the fluid within the entire flowline, which may affect the pressure, and the dynamic performance of the gauge to pressure and temperature changes in its immediate vicinity. The latter is beyond the scope of this dissertation.

In this problem the focus is to understand some of the effects the tool may have on the pressure signal, specifically the response of the system to thermal variations. Other environmental conditions, such as supercharging, damage (skin) and mobility contrasts in the formation caused by filtrate invasion are considered negligible. This would be the case if a good quality drilling fluid were used. It is also assumed here that the formation properties are isotropic.

2.4 Solution Approach

To first address the question of whether it is possible to measure a spherical flow signal with a formation tester, the approach followed here is to define a tool (flowline size and probe radius), define the range of all possible pretests parameters (rate and volume) that meet the operational constraints of that tool (drawdown pressure limit, maximum rate and maximum volume), and calculate the magnitude of the pressure signal at the onset of spherical flow for a given formation (mobility and storativity). This will provide a comparison of the magnitude of the spherical flow signal with respect to tool noise.

The next step is to investigate further the storage period of the pretest. More specifically, analyze the effect that temperature variations during the pretest may have on the pressure signal. The first approach to this problem is to perform a thermodynamic analysis of the limiting case of the pretest, namely the case when the probe is set against an impermeable medium and the pretest piston is retracted to increase the flowline volume. This is referred to as a dry pretest.

The maximum temperature and pressure variation to be expected during drawdown are obtained assuming that the pretest occurs under adiabatic conditions (thermodynamic analysis). This approach also provides the size of pressure buildup that would occur if the temperature is allowed to equilibrate with the external temperature at the end of drawdown.

The next step is to identify the governing equations for the dynamic problem. Density dependence on temperature is accounted for in the equation of conservation of mass, and the equation of conservation of non-mechanical energy is used to model accumulation and transport of heat in the system. Principal scales of the problem and the dimensionless groups are identified. The effect of these groups is analyzed in dimensionless form to gain physical insight into the problem. Generic tool designs are analyzed in dimensional form.

Finally, pretests that would give the maximum size of the spherical flow signal for a given formation and a given tool are simulated with the new storage model to address whether or when it is possible to detect a deep formation pressure signal during the pretest.

Chapter 3

Quantifying Pressure Transients Associated with the Formation during Pretests

3.1 Introduction

The focus of this chapter is to quantify the magnitude of the pretest pressure signal that originates from the recompression of fluids in the formation some distance away from the wellbore, what will be called the *formation signal*. It is of interest to identify the portion of the pressure signal that reflects events in the formation away from the wellbore because it could be used to characterize formation mobility, k/μ, in this region, where there could be none or little damage by drilling mud filtrate invasion. The problem addressed here is to investigate whether it is possible to measure a deep formation response with a formation tester. More specifically, it is of interest to investigate the magnitude of this signal with respect to the resolution of a tool.

Flow within the formation induced by a probe-type formation tester during drawdown has a specific characteristic: the flow near the probe approaches steady state quickly. This behavior differs from the drawdown in a transient well test (line source solution). From a practical point of view, the pretest drawdown takes place during a few seconds. Because of its short duration, the drawdown period can be strongly influenced by flowline storage effects and noise produced by the motion of the pretest piston. Therefore, pressure variations from the deep formation can, in theory, be detected only during the buildup period.

Events originating in the deep formation are recognized by the identification of flow regimes from the rate of equilibration of the buildup pressure signal. Flow regimes particular to formation testers are spherical and radial flow (Moran and Finklea, 1962). However, there are two major drawbacks in the acceptance of mobility from the analysis of buildup data as a reliable parameter to characterize the formation: first, it is not always possible to identify the deep formation signal within the buildup data; and second, whenever a deep formation signal is claimed to be observed from a pretest, the inferred value of k/μ is always much smaller than the drawdown mobility, $(k/\mu)_{dd}$, which reflects properties of the formation near the probe. Even accounting for the possible influence of formation anisotropy (Dussan and Sharma, 1992), the cause for this discrepancy has not been properly identified. This behavior is counterintuitive because it is expected that $(k/\mu)_{dd}$ is most affected by formation damage. Because of this, the mobility determined from buildup data is discredited in most instances.

Throughout this chapter the concern will be chiefly on the spherical flow regime, and the term spherical flow will be used to denote that portion of the buildup pressure signal that exhibits this characteristic behavior. The buildup mobility derived from the analysis of the spherical flow signal will be denoted $(k/\mu)_{sph}$. As recognized by the analysis of Moran and Finklea (1962), the pressure signal during spherical flow is independent of the presence of the wellbore and the tool. However, the early part of the buildup signal is dominated by flowline storage effects, which are influenced by tool properties. Spherical flow can only be observed once flowline storage effects abate; hence, it is indirectly influenced by tool characteristics.

An overview of this chapter is as follows: first a summary of the different stages of a pretest, with associated characteristics of the measured pressure signal and pressure distribution within the formation, is presented. Several concepts are introduced to facilitate the description of the solution approach, which basically consists of computing the magnitude of the spherical flow signal for a variety of pretest parameters. Results cover a wide variety of formations and a representative selection of tools.

3.2 Pressure Behavior during Drawdown and Buildup in a Pretest

The primary objective of the pretest is to establish hydraulic communication between the permeable rock and the tool flowline containing the pressure sensor and the pretest chamber (Refer to Figure 2.2). Once the tool is set against the formation, the pretest is initiated with the retraction of the piston in the pretest chamber. The initial flowline volume, $V_{flowline}$, is increased at a rate q by an amount ΔV, also referred to as the pretest volume.

Besides the choice of where to position the tool along the wellbore for a measurement, the principal tool parameters controlled during the pretest are q and ΔV ($\Delta V = qT$, where T is the total drawdown time). As the flowline volume increases, the flowline pressure, P_{fl} decreases until fluid from the formation enters the flowline, thus establishing hydraulic communication with the formation. One method of detection is that the rate of change of the pressure increases, this may be seen in the first pretest in Figure 2.4 and the example shown in Figure 3.1 (point **B**) as the marked decrease in separation between consecutive P_{fl} data points. When the piston stops, P_{fl} immediately increases until it equilibrates to the pressure of the formation at the sandface, $P_{sandface}$. When the formation is supercharged, $P_{sandface}$ is larger than the actual formation pressure (Pelissier et al., 1979); however, this has no effect on the determination of k/μ. A pretest consists of an entire cycle of drawdown (during the piston stroke) followed by the buildup when the pressure signal equilibrates.

When the tool is set against the formation, the initial flowline pressure is the hydrostatic pressure of the drilling fluid, that is, the wellbore pressure, P_{well}. The difference between P_{well} and $P_{sandface}$, or overbalance, could be tens to thousands of psi; therefore, the first pretest must also decompresses the fluid in the tool flowline to allow formation fluid to enter. In Figure 3.1 the time when the pretest piston starts retracting ($t = t_0$) is marked by point **A** (30s). To breach the mudcake and establish hydraulic communication with the formation, P_{fl}, must be sufficiently smaller than $P_{sandface}$; the time when this occurs is denoted by t^*. In this example, fluid starts entering the tool when $P_{fl} = P_{sandface}$ at point **B** in the figure ($t^* = 32.6$ s); this is the case when the mudcake does not adhere to the wellbore wall. In practice, $P_{sandface}$ is often assumed to be approximately equal to the last pressure measured during buildup. The drawdown ends when the pretest piston stops ($t = t_{dd}$), point **D** (70s). The period of the drawdown during which fluid enters the flowline, T, is $t_{dd} - t^* = 70s - 32.6 = 37.4s$. The drawdown in Figure 3.1 could be divided into two parts, the unsteady flow, between **B** and **C**, and the approximately steady flow, between **C** and **D**. This period, between **C** and **D**, is referred to as steady-state flow because the pressure change is of much smaller magnitude than the resolution of any pressure sensor.

When steady state has been achieved during drawdown it is possible to determine the value of $(k/\mu)_{dd}$ with the following expression:

$$(k/\mu)_{dd} = \frac{\Omega q}{4 r_{probe} \Delta P_{dd}}, \tag{3.1}$$

where $\Delta P_{dd} = P_{sandface} - P_{fl}|_{t_{dd}}$, and r_{probe} is the radius of the probe orifice. This is a well known expression valid when $r_{well} \gg r_{probe}$, where r_{well} is the well borehole radius. The term Ω is a correction factor to account for wellbore curvature (Wilkinson and Hammond, 1990). During drawdown, most of the pressure drop within the formation occurs near the probe, within a radial distance of about $3r_{probe}$ (Dussan and Sharma, 1992) into the formation. Thus, the computed value of $(k/\mu)_{dd}$, characterizes formation properties within this region, where damage by mud filtrate and particulate invasion could occur; this is also true for the other methods cited above when steady-state is not achieved. Though it is desirable to establish steady-state flow during drawdown, in practice, the drawdown period is often terminated before reaching steady state, particularly in low mobility formations ($<$ 1 md/cp). Other methods exist to calculate formation mobility when the drawdown does not reach steady state (Proett et al., 1994, 1998; Kasap et al., 1999; and Dussan, 2011).

The instant the pretest piston stops, there is a pressure gradient throughout the formation with the minimum pressure at the probe. Therefore, the

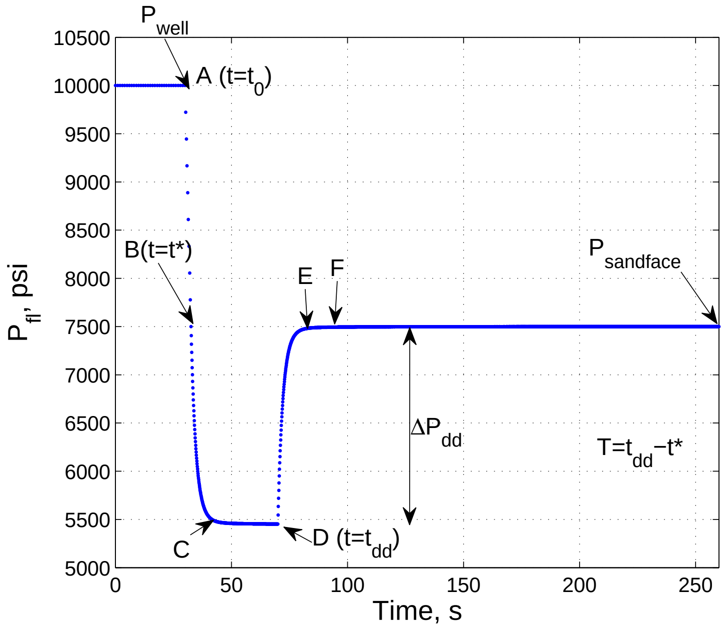

Figure 3.1: Flowline pressure, P_{fl}, versus time. The initial pressure of 10,000 psi corresponds in this case to the wellbore pressure (P_{well}). The drawdown starts at point A ($t = t_0$). From points A to B the flowline is decompressed without formation fluid entering. At point B ($t = t^*$) $P_{fl} = P_{sandface}$ and formation fluid enters the flowline. From B to C the flow is unsteady, and from C to D the flow is approximately steady flow. The drawdown ends when the pretest piston stops ($t = t_{dd}$, point D). Flowline storage effects dominate the first part of the buildup (from D to E), then wellbore curvature effects are manifested in the pressure signal (points E to F). The formation signal can only be detected after point F, and eventually P_{fl} equilibrates to $P_{sandface}$. ΔP_{ddS} denotes the pressure difference between $P_{sandface}$ and the approximate steady-state drawdown pressure.

fluid must continue to flow within the formation to establish equilibrium conditions both within the formation and between the formation and the tool. This flow is responsible for the rise of the pressure signal during buildup.

Three flow periods may be identified during the buildup. The pressure signal, P_{fl}, in the early part of buildup is dominated by the recompression of the fluid contained within the flowline and the mechanical compliance of the tool; this period is known as *storage*. The pressure field in the formation is discussed next. In the storage dominated period the pressure increases mostly in the fluid in the tool and in the formation near the probe (within about $3r_{probe}$). During this time, the fluid entering the orifice is marginally influenced by the presence of the wellbore, that is, the pressure at the probe is practically the same if it is assumed that the wellbore has infinite curvature (a planar wall impermeable everywhere except at the probe). By the end of this period, the pressure both in the tool and in the formation in front of the tool has risen to about 98% of the value of $P_{sandface}$. The pressure outside this region in the reservoir remains about the same as at the end of drawdown. Since the mudcake seals the wellbore wall, the flow must bend around the wellbore in order to reach the probe.

The next period, the intermediate time, accounts for the disappearance of the pressure gradient associated with the presence of the wellbore, that is, within $3r_{well}$ of the wellbore axis. By the end of this time period, the pressure everywhere in the formation within about $3r_{well}$ of the wellbore axis has increased to **F** in Figure 3.2. Now, the only pressure gradient remaining in the formation is further than $3r_{well}$ away from the wellbore. The flow associated

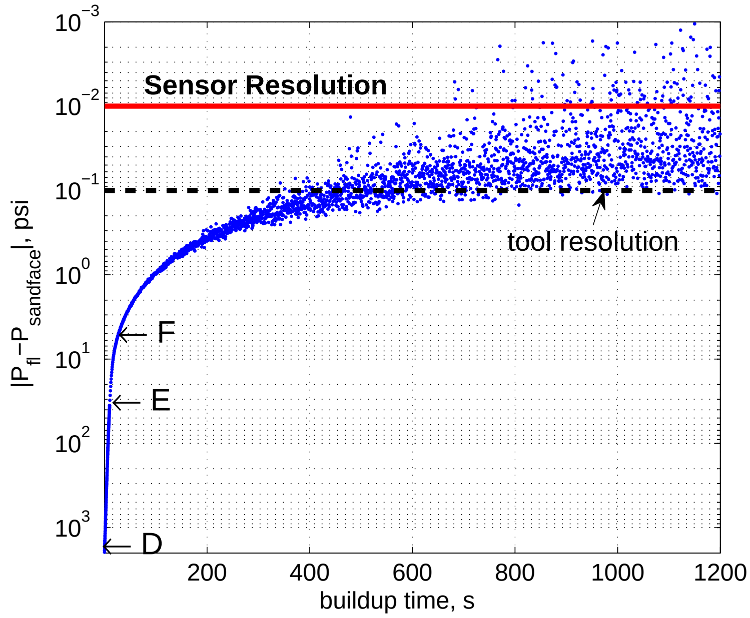

Figure 3.2: Flowline pressure, P_{fl}, during buildup. Flowline storage effects dominate the pressure signal from D to E, over 90% of the pressure change occurs during the storage period. Wellbore curvature effects are manifested in the pressure signal between E and F. Finally, the formation signal, caused by recompression of fluids some distance from the wellbore, begins to be registered at point F. For spherical flow the pressure decay is approximately a function of $t^{-3/2}$.

with the disappearance of this remaining gradient is known as spherical flow. During this time, the pressure in the flowline and in the formation around the wellbore increases at the same rate. At this late time, dP_{fl}/dt (as measured by the tool) is associated with the recompression of fluid in $r > 3r_{well}$ where the flow is geometrically spherical.

A useful way to identify the flow periods is to plot abs $(P_{sandface} - P_{fl})$ vs. time in either a semi-log or log-log plot, as shown in Figures 3.2 and 3.3. The second plot will be referred to as the *buildup equilibration plot*. The storage period occurs between points **D** and **E**, the influence of the wellbore is observed between **E** and **F**, and the spherical flow period starts after point **F**. The nominal resolution of the pressure sensor and the resolution of the tool are also represented in Figure 3.3. The nominal resolution of the pressure sensor only represents the lower bound of the resolution of the tool. A formation tester is a complex mechanical system and some components of the flowline, or other parts of the tool, contribute to the noise in the pressure signal.

Spherical flow may be measured only after tool storage and borehole effects have dissipated, which happens close to the end of buildup; this means that the difference $P_{fl} - P_{sandface}$ during spherical flow tends to have a small value, possibly close to the resolution of the tool. In contrast with a typical analysis of formation tester pressure data, this aspect of the problem, namely the relative size of the spherical flow pressure signal with respect to tool resolution, is emphasized in this dissertation. The last recorded flowline pressure is taken as the sandface pressure. The upper bound of the scattered points at late time is defined as the effective tool resolution (note that the values of the y-axis are reversed). In the example shown in Figure 3.3, based on synthetic data, the resolution of the pressure sensor is 0.01 psi, but the resolution of the tool is 0.1 psi. Without a robust procedure to process the signal, an analysis based on data points with values less than 0.1 psi would be highly uncertain. This plot also provides a useful criterion to establish that the pressure signal has equilibrated. If equilibrium has been achieved, there should be a region of scattered data points with a constant upper boundary for a sustained period of time towards the end of buildup.

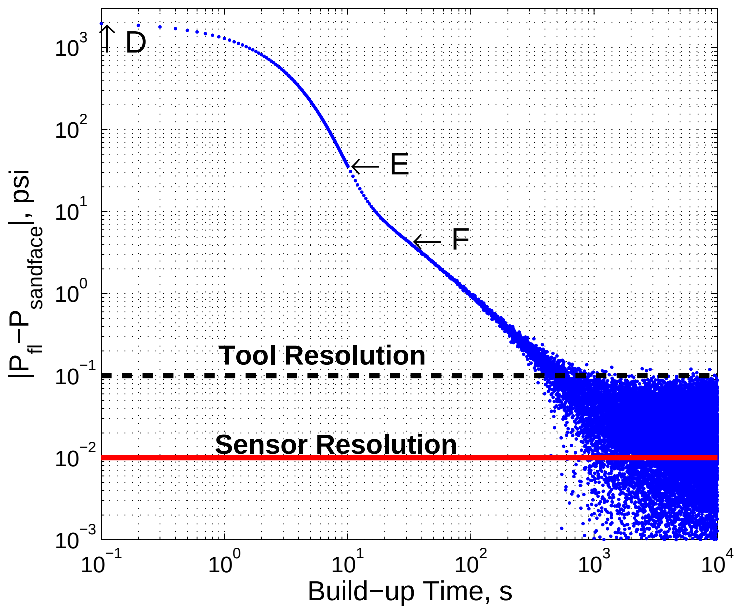

Figure 3.3: Flowline pressure, P_{fl}, during buildup. Flowline storage effects dominate the pressure signal from D to E, over 90% of the pressure change occurs during the storage period. Wellbore curvature effects are manifested in the pressure signal between E and F. Finally, the formation signal, caused by recompression of fluids some distance from the wellbore, begins to be registered at point F. For spherical flow the pressure decay is approximately a function of $t^{-3/2}$. The resolution of the tool (including the pressure sensor) is typically lower than the nominal resolution of the pressure sensor, because of the response of the system to pressure changes, noise introduced by the telemetry, etc.

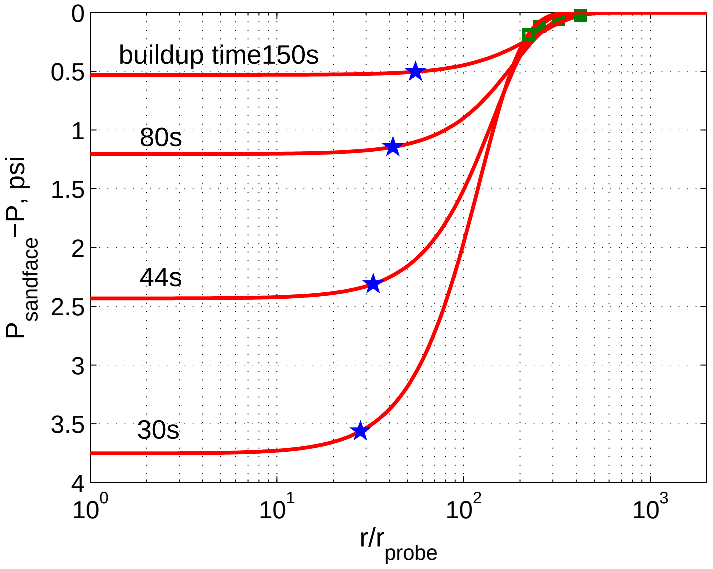

Figure 3.4: Pressure distribution in the reservoir during the spherical flow regime (r_{probe} = 1.1 in) at 30, 44, 80, and 150 seconds since the beginning of buildup. The markers (star and square) on each curve delimit the reservoir region where 90% of the pressure change is registered at a given buildup time.

Figure 3.4 shows pressure within the formation at a specific time during the spherical flow regime, computed using the expressions presented by Moran and Finklea (1962). Markers in each curve delimit the reservoir region where the largest pressure gradient is occurring. According to the spherical flow model, the pressure in the region $r < 3r_{well}$ rises in unison, therefore dP_{fl}/dt (the rate of change of the pressure measured at the probe) is characterizing flow whose spatial pressure gradient is located deep in the formation. This concept of associating dP_{fl}/dt during the late part of buildup with a region in the reservoir, that is, depth of investigation, originated with Moran and Finklea. They further showed that mobility $(k/\mu)_{sph}$ could be determined by the buildup data during the spherical flow period. Since the pressure signal during the spherical flow period is a consequence of events deep in the formation, $(k/\mu)_{sph}$, is less prone to be affected by damage than $(k/\mu)_{dd}$. The expression used to compute spherical mobility is

$$(k/\mu)_{sph} = {\frac{q^2 \phi c_{fm}}{16\pi^3 m^2}}^{1/3}, \tag{3.2}$$

where ϕ and c_{fm} are the formation porosity and total isothermal compressibility, and m represents the pressure rate of change with respect to a pertinent function of time known as spherical time function.

Some Examples of Discrepancy between Drawdown and Buildup Mobility

The following examples are from measurements acquired with formation testers. In the first example the pretest drawdown pressure reached steady state with a flowrate of 0.2 cm^3/s, and $\Delta P_{dd} = 4.85$ atm. The mobility computed with equation 3.1 is 18.5 md/cp ($r_{probe} = 0.55$ cm, $\Omega = 1$). A portion of the data exhibiting spherical flow behavior was identified in the late part of the buildup (Figures 3.5(b) and 3.6), and the spherical mobility value computed with equation 3.2 was 1.3 md/cp (m = 0.51 atm$\times$s$^{-0.5}$, $c_{fm} = 4.6 \times 10^{-5}$ atm^{-1}, $\phi = 0.15$).

In the second example (Figure 3.7), the drawdown mobility was computed to be 15 md/cp (q=1.86 cm^3/s, $\Delta P_{dd} = 57.52$ atm, $r_{probe} = 0.55$ cm, $\Omega = 1$) and the spherical mobility was computed to be 1.5 md/cp (m = 4.35 atm$\times$s$^{-0.5}$, $c_{fm} = 5.0 \times 10^{-5}$ atm^{-1}, $\phi = 0.20$). In these two examples there is one order of magnitude difference between the drawdown and spherical mobility values.

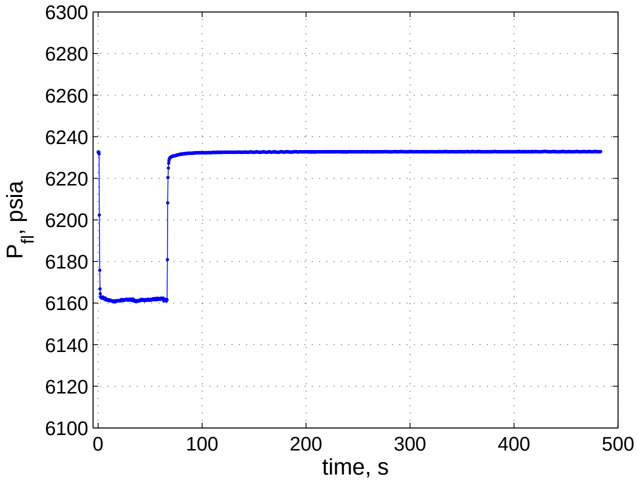

(a) Pressure log

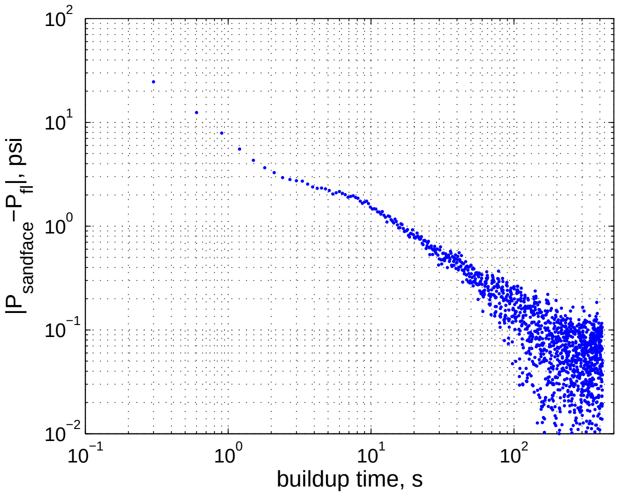

(b) Buildup pressure equilibration

Figure 3.5: First example of different mobility values obtained from drawdown and spherical flow analysis. In this case the drawdown mobility is 18.5 md/cp and the spherical mobility is 1.3 md/cp.

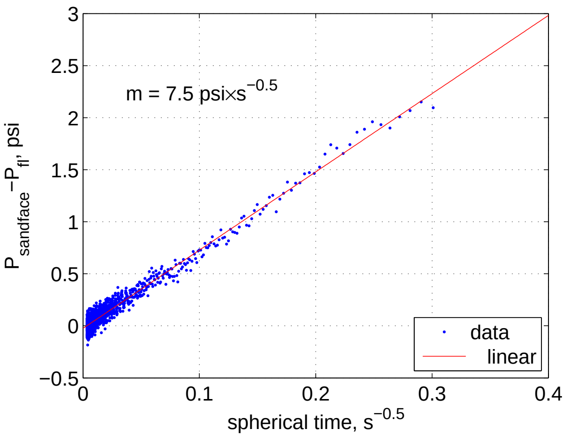

Figure 3.6: Pressure vs. spherical time plot for determining mobility in the example shown in Figure 3.5

A third example is shown in Figure 3.9. In this case the drawdown mobility is 8.5 md/cp (q = 1.0 cm^3/s, ΔP_{dd} = 52.51 atm, r_{probe} = 0.55 cm, Ω = 1) and the spherical mobility was 1.5 md/cp (m = 2.68 atm×s$^{-0.5}$, c_{fm} = 5.0 ×10^{-5} atm^{-1}, ϕ = 0.20).

Finally, consider the following set of 24 pretests acquired in one well at various depths spanning a wellbore interval of 3500 ft. It was possible to identify spherical flow in all the pretests. The spherical and drawdown mobility values are plotted in Figure 3.11. The most striking feature of Figure 3.11 is that the spherical mobility values are very uniform. This is bizarre because the drawdown mobility has an order of magnitude spread, and one would expect that the spherical mobility should exhibit a similar trend.

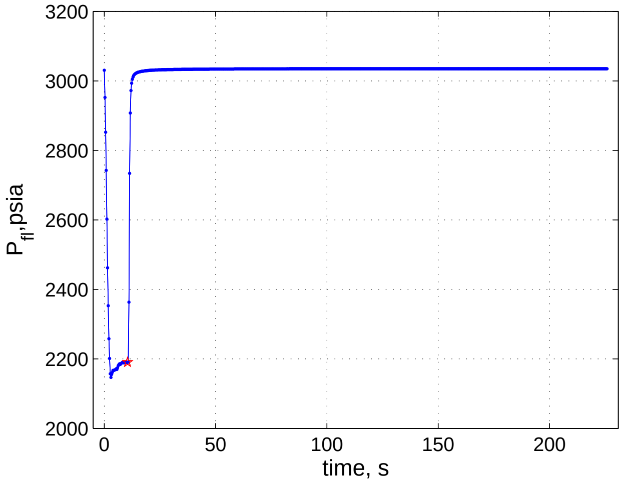

(a) Pressure log

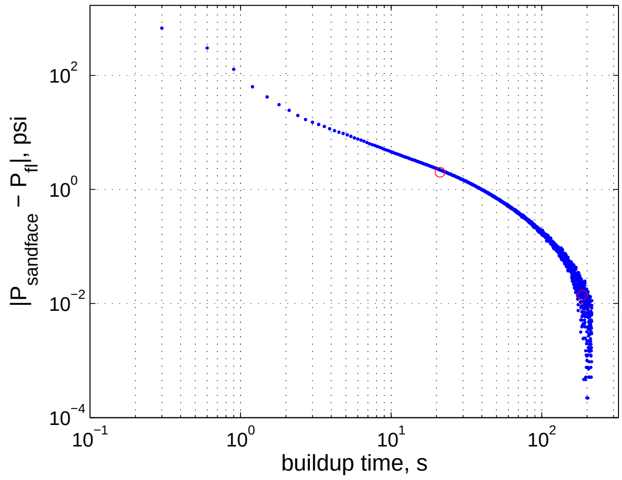

(b) Buildup pressure equilibration

Figure 3.7: Second example of different mobility values obtained from drawdown and spherical flow analysis. In this case the drawdown mobility is 15 md/cp and the spherical mobility is 1.5 md/cp.

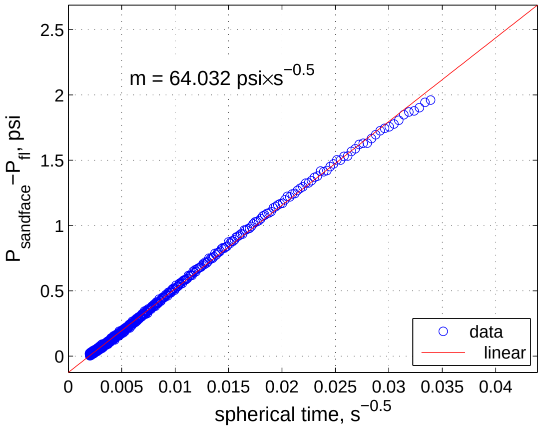

Figure 3.8: Spherical flow analysis for example shown in Figure 3.7. In this case the drawdown mobility is 15 md/cp and the spherical mobility is 1.5 md/cp.

3.3 Approach

The size of the pressure signal at the onset of spherical flow depends mainly on the design of the tool (radius of the probe orifice and flowline volume) and the physical properties of the formation (mostly mobility). The measurement of the spherical flow signal is investigated with three different tools (all with circular probe orifices) for a wide range of mobility (from 0.001 to 100 md/cp) to understand how the selection of pretest parameters could reduce the uncertainty in the determination of $(k/\mu)_{sph}$. More specifically, the purpose of this study is to identify q and ΔV which would result in the maximum pressure signal during spherical flow.

The criterion that will be used to quantify spherical flow is the value of the pressure signal at the beginning of the spherical flow regime, that is, time **F** in Figure 3.3. The exact time when this occurs is not known precisely. However, for practical purposes, it will be regarded as the intersection of the

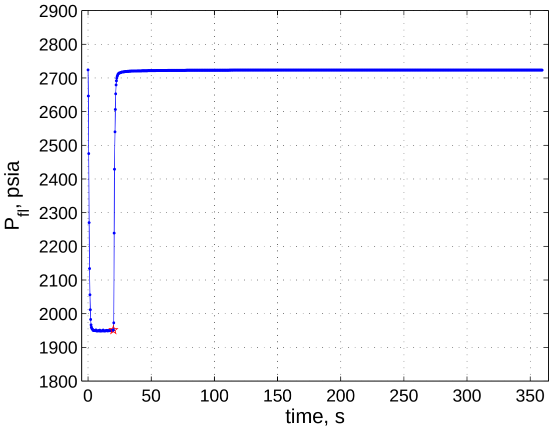

(a) Pressure log

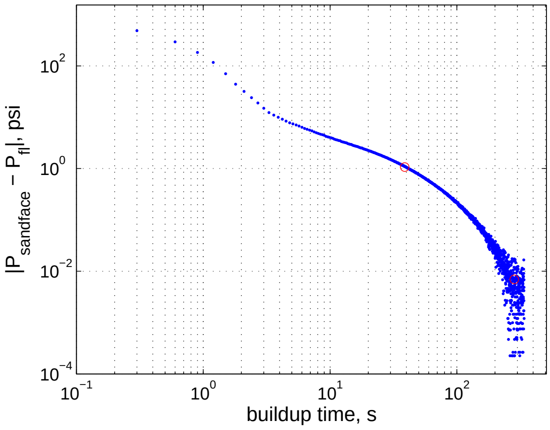

(b) Buildup pressure equilibration

Figure 3.9: Third example of different mobility values obtained from drawdown and spherical flow analysis. In this case the drawdown mobility is 8.5 md/cp and the spherical mobility is 1.5 md/cp.

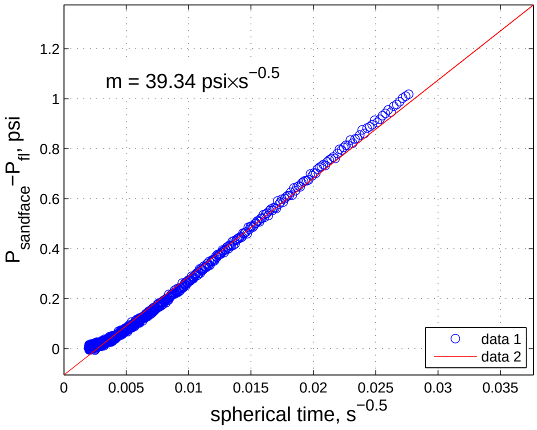

Figure 3.10: Spherical flow analysis for the example shown in Figure 3.9.

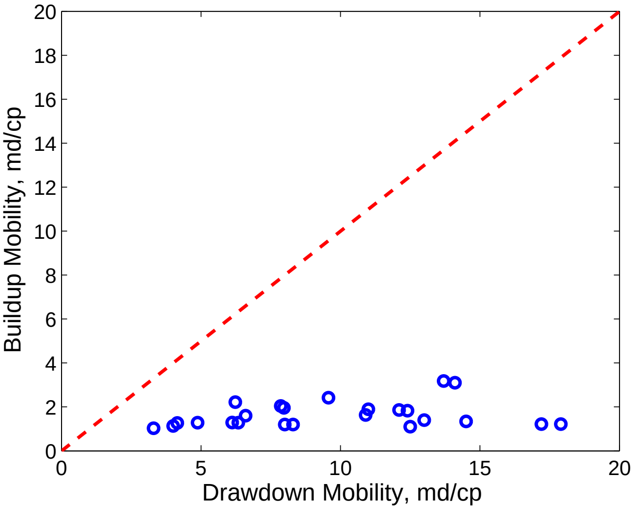

Figure 3.11: Comparison of measured spherical and drawdown mobility values for one well. A total of 24 pretests acquired in one well over a borehole interval spanning 3500 ft. The much lower variation in the spherical mobility values compared to drawdown mobility values is remarkable.

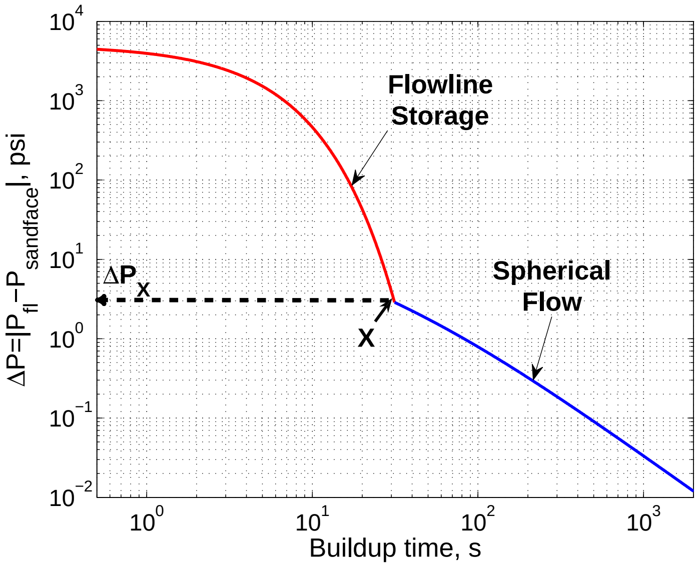

Figure 3.12: The maximum amplitude of spherical flow is defined as the pressure difference, ΔP, at point X, where flowline storage and the spherical flow solutions intersect.

storage solution and the late time spherical flow solution, that is, buildup time X and pressure $\Delta P_X = |P_{flX} - P_{sandface}|$ in Figure 3.12.

Though Proett and Chin (1998) published an analytic solution that encompasses both early time flowline storage and late-time spherical flow behavior, their formulation does not account for the intermediate flow period which is influenced by the presence of the wellbore. Hence, in their solution the transition from the storage to the spherical flow period has no specific physical foundation. With this understanding, the criterion used here is considered justifiable as long as it is kept in mind, when using the results, that the calculated beginning of spherical flow is a guideline.

3.4 Solution Method

The flowline storage solution is obtained from application of the principle of conservation of mass to the tool flowline.

$$\frac{d(\rho_{flowlinefluid}V_{flowline})}{dt} = \rho_{formationfluid}q_{formation} \tag{3.3}$$

Typically, for a pretest $\Delta V \ll V_{flowline}$, this justifies two common assumptions made in practice: $V_{flowline}$ is considered constant, and $\rho_{flowlinefluid}$ is similar to $\rho_{formationfluid}$. The latter is justified because the pretest volumes are typically small and the fluid entering the flowline is basically mud filtrate. It is also assumed that the density is only a function of pressure and pressure gradients in the flowline are neglected, hence it is considered that the pressure in the flowline is uniform and therefore only a function of time (Brigham et al., 1980; Yildiz, et al., 1991; Kasap et al., 1995; Proett and Chin, 1998; Dussan and Sharma, 1992; and Dussan, 2011).

The volumetric flowrate through the probe orifice, $q_{formation}$, is modeled using the quasi-steady state approximation, that is, the formation compressibility, c_{fm} is assumed to have a negligible effect on the pressure during the storage period.

$$q_{formation} = 4r_{probe}\frac{k}{\mu}(P_{sandface} - P_{fl}(t)). \tag{3.4}$$

This expression of $q_{formation}$ is the solution for a circular probe of radius r_{probe} placed against a semi-infinite isotropic formation, with an impermeable boundary at $z = 0$ except for $0 < r < r_{probe}$ (Carslaw and Jaeger, p. 215). This represents the limiting case when $r_{probe} \ll r_{well}$. Correction factors that account for wellbore curvature and anisotropy exist in the literature (Wilkinson and Hammond, 1992).

Changes in flowline volume, $dV_{flowline}/dt$, are a consequence of the compliance to pressure changes (tool and fluid compressibility), $c_{eff} = c_{tool} + c_{fluid}$ and the retraction of the pretest piston, $q_{piston}(t)$.

$$c_{eff} V_{flowline} \frac{dP_{fl}}{dt} = 4 r_{probe} \frac{k}{\mu} (P_{sandface} - P_{fl}) - q_{piston}(t), \tag{3.5}$$

where

$$q_{piston}(t) = \begin{cases} q_{\infty}, & 0 < t \leq T, \\ 0, & t > T, \end{cases} \tag{3.6}$$

where T is the time length of the drawdown period. The solution to Equation 3.5, neglecting overbalance, that is, when $P_{fl}(0) = P_{sandface}$ is:

$$P_{fl}(t) = P_{sandface} - \Delta P_{dd} \left(1 - e^{-t/\tau_{tool}}\right), \quad 0 < t \leq T \tag{3.7}$$

$$P_{fl}(t) = P_{sandface} - \Delta P_{dd} \left(e^{-(t-T)/\tau_{tool}} - e^{-t/\tau_{tool}}\right), \quad t > T \tag{3.8}$$

where

$$\Delta P_{dd} = \frac{q}{4 r_{probe} \frac{k}{\mu}}, \tag{3.9}$$

and

$$\tau_{tool} = \frac{V_{flowline} c_{eff}}{4 r_{probe} \frac{k}{\mu}}. \tag{3.10}$$

The parameter ΔP_{dd} is the pressure difference $(P_{sandface} - P_{fl})$ when the flowline pressure reaches the approximate steady state for a drawdown rate q, and τ_{tool} is the characteristic time (in seconds) due to the effective flowline compressibility.

Some pretests to be considered here have large values of ΔV and it is necessary to account for the fact that the tool volume is a known time-dependent variable during drawdown, $V_{flowline} + qt$. The differential equation in this case is:

$$c_{eff}\left(V_{flowline} + q_{\infty}t\right)\frac{dP_{fl}}{dt} = 4r_{probe}\frac{k}{\mu}(P_{sandface} - P_{fl}) - q_{piston}(t), \tag{3.11}$$

where now $V_{flowline}$ is the flowline volume at the beginning of the pretest. The solution to this equation (for the same initial condition: $P_{fl}(0) = P_{sandface}$) gives the pressure signal during the storage-dominated portion of buildup:

$$P_{fl}(t) = P_{sandface} - \Delta P_{dd}\left(1 - B^{1/(c_{eff}\Delta P_{dd})}\right)e^{-B\Delta t_D}, \tag{3.12}$$

where

$$B = \frac{V_{flowline}}{V_{flowline} + \Delta V} \tag{3.13}$$

$$\Delta t_D = \frac{4r_{probe}\frac{k}{\mu}(t - T - t_0)}{c_{eff}V_{flowline}}, \tag{3.14}$$

For the computation of the pressure signal originating from the recompression of formation fluids, the asymptotic form of the spherical flow solution presented by Moran and Finklea (1962) is used here:

$$P_{fl}(t) = P_{sandface} - mf_s(t), \quad t > T \tag{3.15}$$

$$m = \frac{q}{4}\sqrt{\frac{\phi c_{fm}}{\pi^3\left(\frac{k}{\mu}\right)^3}} \tag{3.16}$$

where m is the derivative of P_{fl} with respect to the spherical time function, f_s, defined as:

$$f_s(t) \equiv \frac{1}{\sqrt{t - T}} - \frac{1}{\sqrt{t}}. \tag{3.17}$$

Time **X** in Figure 3.12 is obtained by finding the time t during buildup when equations 3.12 and 3.15 are equal.

The mathematical problem addressed consists of determining ΔP_X, that is, the pressure difference $(P_{fl} - P_{sandface})$ at time **X** for every combination of q and ΔV satisfying the following constraints:

1. 0.02 cc/s $\leq q \leq 2.0$ cc/s,

2. 0.04 cc $\leq \Delta V \leq 40$ cc,

3. $(P_{sandface} - P_{fl}(t)) \leq 5000$ psi.

These constraints are based on the specifications of the tool. Constraint 3 limits the maximum force acting on different components in the tool to avoid fatigue damage. To take into account overbalance, constraint 3 should be regarded as the maximum pressure drop permitted within the tool minus the overbalance.

The three tools studied are identified by the pair $(r_{probe}, V_{flowline})$ shown in Table 3.1. The tools are labeled *small*, *medium*, and *large*, according to the size of r_{probe}. The reference value of $V_{flowline}$ depends on the size of the probe barrel. In the case of the *small* and *large* tools the probe barrel is the same size; hence, the similar values of $V_{flowline}$ in Table 3.1. For all the tools it is assumed that $c_{eff} = 5.5 \times 10^{-6}$ psi^{-1}. The value of ΔP_X is calculated for formations with $\frac{k}{\mu} = 0.001$, 0.01, 0.1, 1, 10, and 100 md/cp, all with $\phi c_t = 0.45 \times 10^{-6}$ psi^{-1}, for all three tool configurations identified above. This represents 18 separate calculations. The largest value of ΔP_X that satisfies the constraints for a given tool and formation mobility is denoted by ΔP_{max}, that is, $\Delta P_{max} \equiv max\left(\Delta P_X\right)$.

	small probe radius	*medium probe radius*	*large probe radius*
r_p (in)	0.22	0.52	1.12
V_{tool} (cm^3)	75	110	77

Table 3.1: Dimensions of the three tools used to evaluate the size of the formation signal.

3.5 Results

The values of ΔP_X for each tool are presented in Figures 3.14 – 3.17. It is convenient to show the results in terms of pretest parameters q (ordinate) and T (abscissa); correspondingly, $\Delta V = qT$. Overbalance was not considered in the calculations. The level contours in each plot are the values of ΔP_X for particular pretests. For example, 3.13(a) indicates that for $T = 10$ s and $q = 0.1$ cm^3/s in a 0.001 md/cp formation, ΔP_X is 0.2 psi (a value that could be close to the resolution of the tool as indicated in Figure 3.3).

$\frac{k}{\mu}$ md/cp	q cm^3/s	T s	ΔV cm^3	ΔP_{max} psi
0.001	0.02	107	2.14	0.4
0.01	0.02	132	2.64	0.5
0.1	0.08	500	40.00	2.9
1.0	0.76	53	40.00	2.9
10	2.00	19	38.00	1.3
100	2.00	7	14.00	0.2

Table 3.2: Pretest that maximizes the formation signal for the *small probe radius* tool for given values of formation mobility.

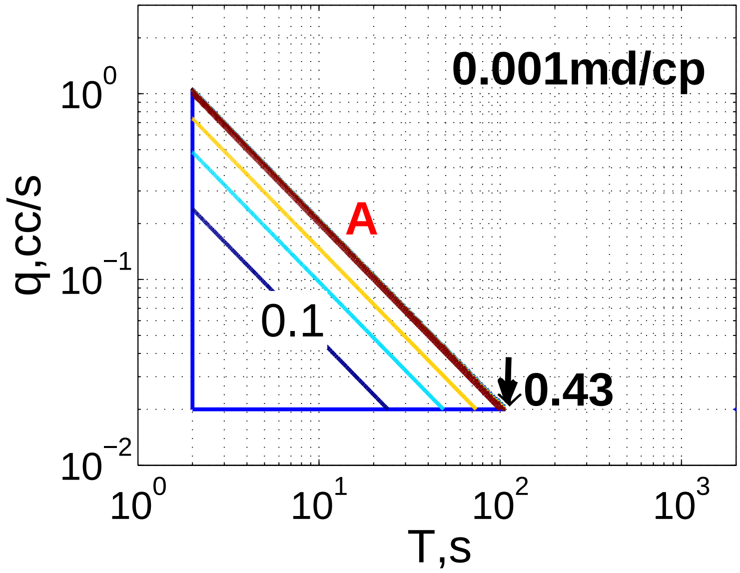

(a)

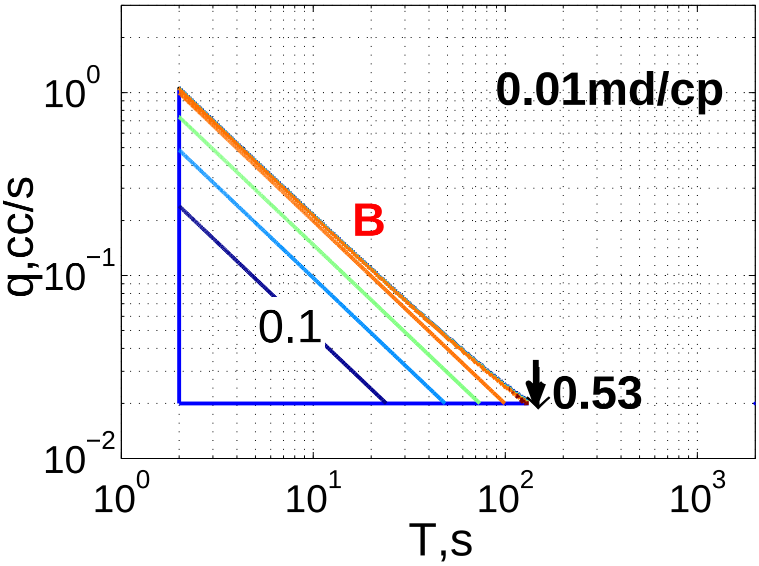

(b)

Figure 3.13: Formation signal, ΔP_X, in psi (refer to Figure 3.12 for definition) for the *small probe radius* tool for different pretests (q, T). The pretest that gives the maximum value is marked by an arrow. The labeled contour indicates the value ΔP_X and the size of the step for successive contours.

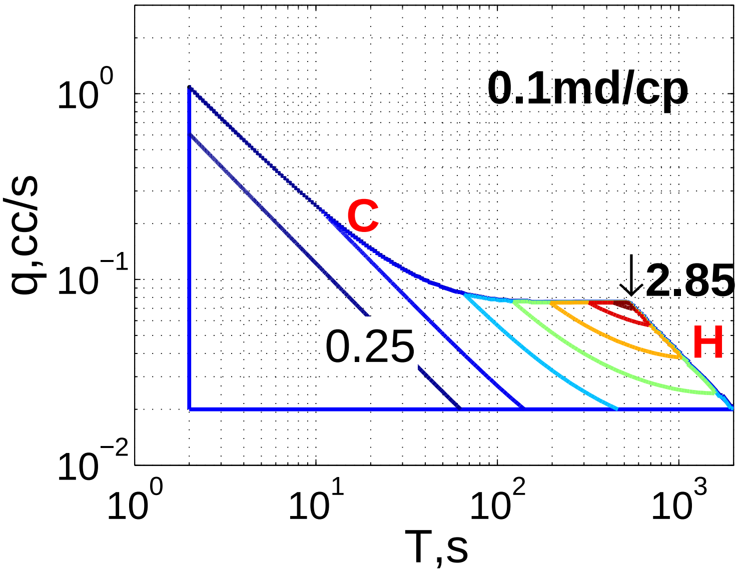

(a)

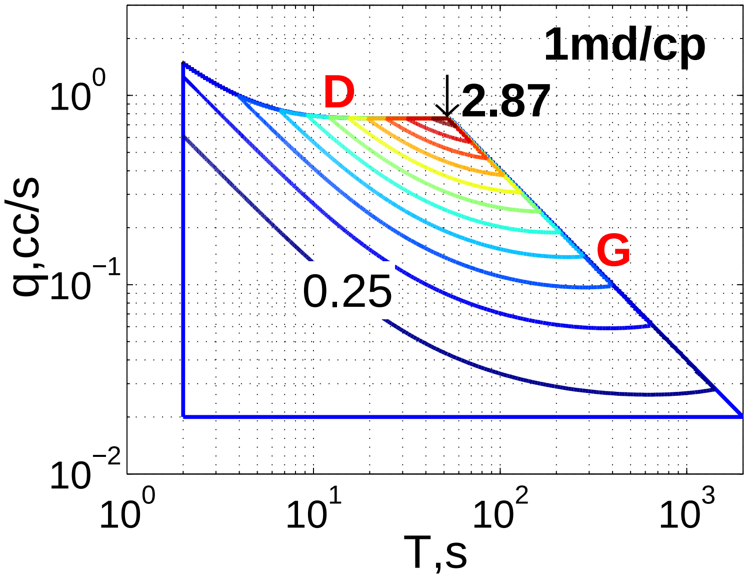

(b)

Figure 3.14: Formation signal, ΔP_X, in psi (refer to Figure 3.12 for definition) for the *small probe radius* tool for different pretests (q, T). The pretest that gives the maximum value is marked by an arrow. The labeled contour indicates the value ΔP_X and the size of the step for successive contours.

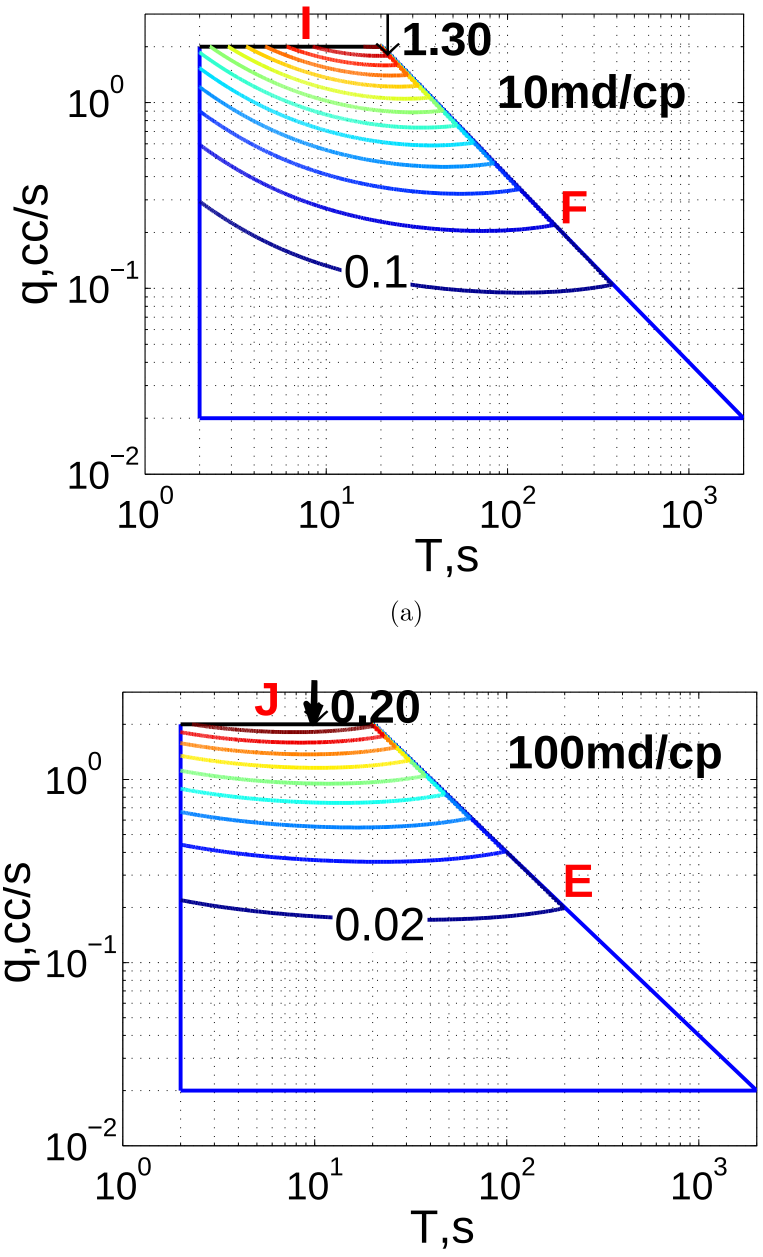

(a)

(b)

Figure 3.15: Formation signal, ΔP_X, in psi for the *small probe radius* tool for different pretests (q, T), $k/\mu \geq 1$ md/cp. The pretest that gives the maximum value is marked by an arrow. The labeled contour indicates the value of ΔP_X and the size of the step for successive contours.

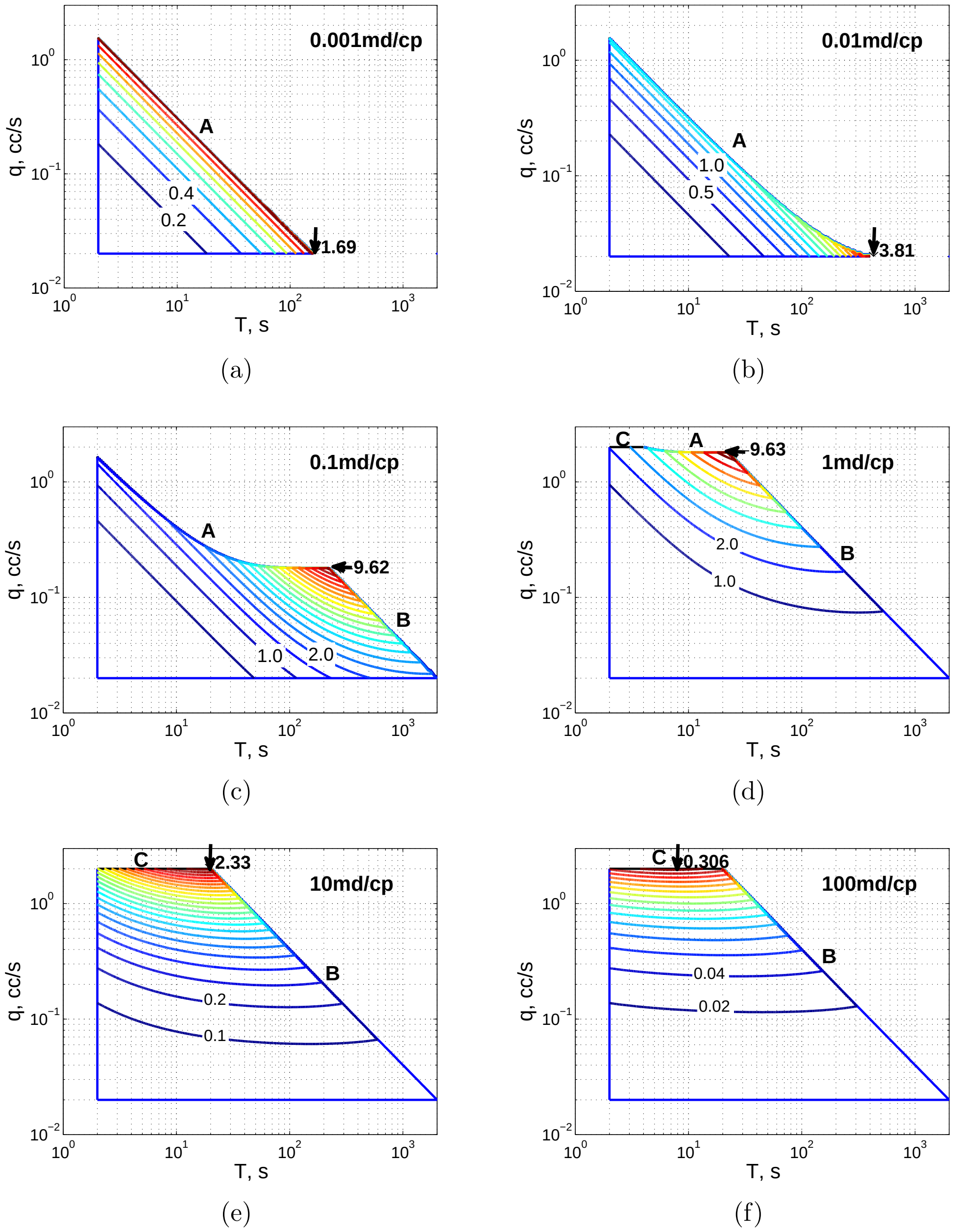

(a) (b) (c) (d) (e) (f)

Figure 3.16: Formation signal, ΔP_X, in psi for the *medium probe radius* tool. The pretest that gives the maximum value is marked by an arrow. Curves labeled A represent the third problem constraint (maximum pressure differential). Curves labeled B represent the constrain that $\Delta V \leq 40cm^3$, and curves C represent $q \leq 2.0cm^3/s$.

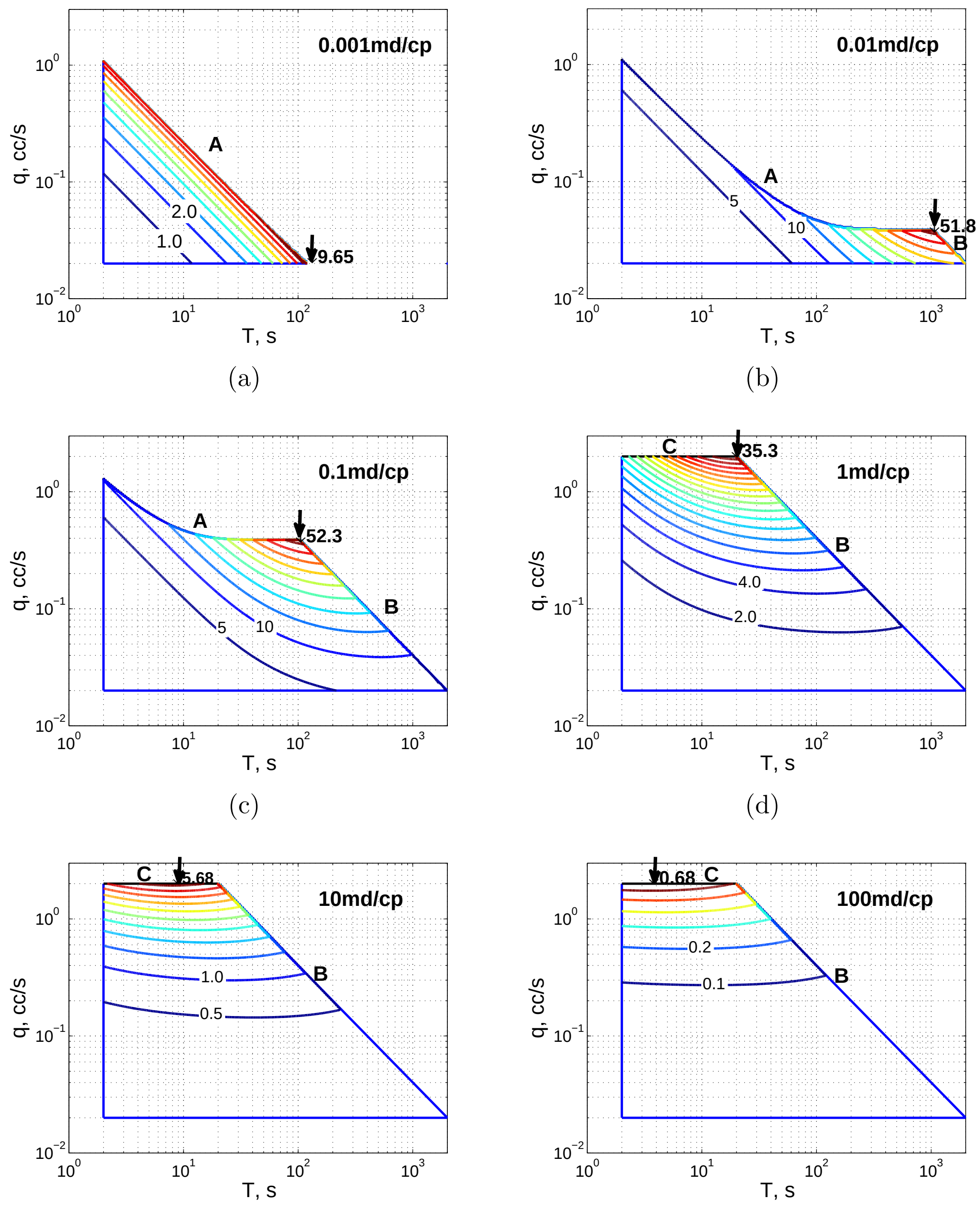

(a) (b)

(c) (d)

(e) (f)

Figure 3.17: Formation signal, ΔP_X, in psi for the *large probe radius* tool. The pretest that gives the maximum value is marked by an arrow. The labels in the bounding curves (A,B,C) have the same meaning as in Figure 3.16.

$\frac{k}{\mu}$ md/cp	q cm^3/s	T s	ΔV cm^3	ΔP_{max} psi
0.001	0.02	160	3.20	1.7
0.01	0.02	400	8.00	3.8
0.1	0.18	220	39.60	9.6
1.0	1.82	22	40.00	9.6
10	2.00	18	36.00	2.3
100	2.00	7	14.00	0.3

Table 3.3: Pretest that maximizes the formation signal for the *medium probe radius* tool for given values of formation mobility.

$\frac{k}{\mu}$ md/cp	q cm^3/s	T s	ΔV cm^3	ΔP_{max} psi
0.001	0.02	117	2.34	9.7
0.01	0.04	1000	40.00	52.0
0.1	0.38	100	38.00	52.0
1.0	2.00	20	40.00	35.0
10	2.00	8	16.00	5.7
100	2.00	3	6.00	0.7

Table 3.4: Pretest that maximizes the formation signal for the *large probe radius* tool for given values of formation mobility.

The region enclosed by the boundaries in Figures 3.14 – 3.17 represents all the possible pretests (each defined by one value of q and ΔV) for the combination of formation mobility and tool, and is defined by the constraints of the problem. For each case, the value of ΔP_{max} is marked with an arrow in Figure 3.14. For example, for a formation with mobility of 1 md/cp (Figure 3.14(b)), ΔP_{max} is 2.87 psi with a pretest of 0.76 cm^3/s for a drawdown time of 53 s ($\Delta V = 40$ cm^3). This is the maximum value of ΔP_X the spherical flow signal that could be obtained in an isotropic 1 md/cp formation. In the case of the small probe radius tool the maximum value of ΔP_{max} occurs when the mobility is between 0.1 md/cp and 1 md/cp.

Individual constraints can be identified by the different boundaries in Figure 3.14. Constraint 3 (maximum pressure differential in the tool) gives curves A, B, C and D in the cases where the formation mobility is less than or equal to 1 md/cp, but does not represent a limiting factor in the higher mobility plots in Figure 3.14. This implies that the size of $(P_{sandface} - P_{fl}(t))$ limits the size of ΔP_{max}. The constraint $\Delta V \leq 40$ cm^3 gives the curves H, G, F and E in formations with $k/\mu > 0.1$ md/cp, and is not a limiting factor when $k/\mu < 0.1$ md/cp for tools in which $q \geq 0.02$ cm^3/s. The constraint $q \leq 2.0$ cm^3/s is represented by curves I and J in the two largest mobility graphs (Figures 3.15(a) and 3.15(b)). That is, in the case of the small probe radius tool ΔP_{max} is limited by q when $k/\mu \geq 10$ md/cp.

The simulated pressure signal during buildup for those pretest conditions that maximize spherical flow are shown in Figures 3.18, – 3.20. The pretest parameters are summarized in Tables 3.2 – 3.4. Some of the values of q and T listed are not typically used in field operations, but it is justifiable to conduct these pretests to support reservoir characterization studies. For the three tools considered, the large probe radius gives the largest pressure signal during spherical flow for any mobility value.

3.6 Discussion

A general observation about the impact of r_{probe} and $V_{flowline}$ on the size of ΔP_{max}, is that, since neither r_{probe} nor $V_{flowline}$ appear in the expression for the pressure signal during spherical flow (Equations 3.15 – 3.17), their impact

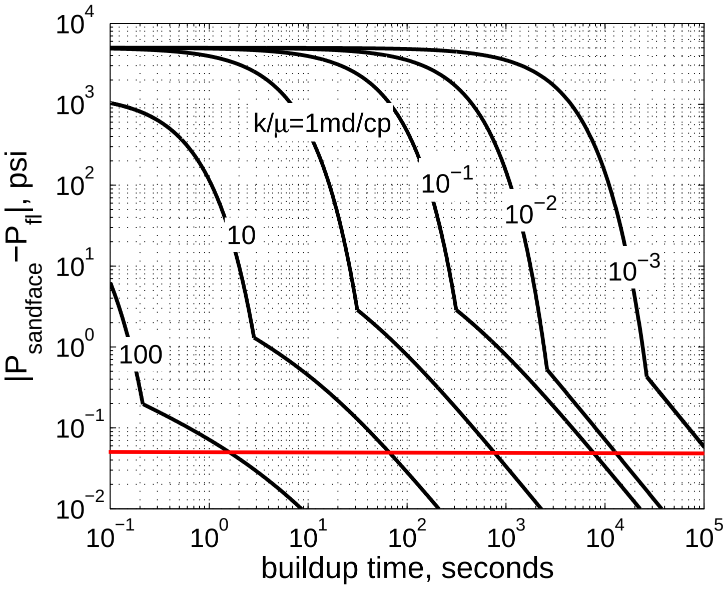

Figure 3.18: Buildup equilibration for the pretests that maximize the spherical flow signal with *small radius probe* tool (q and ΔV defined in Table 3.2).

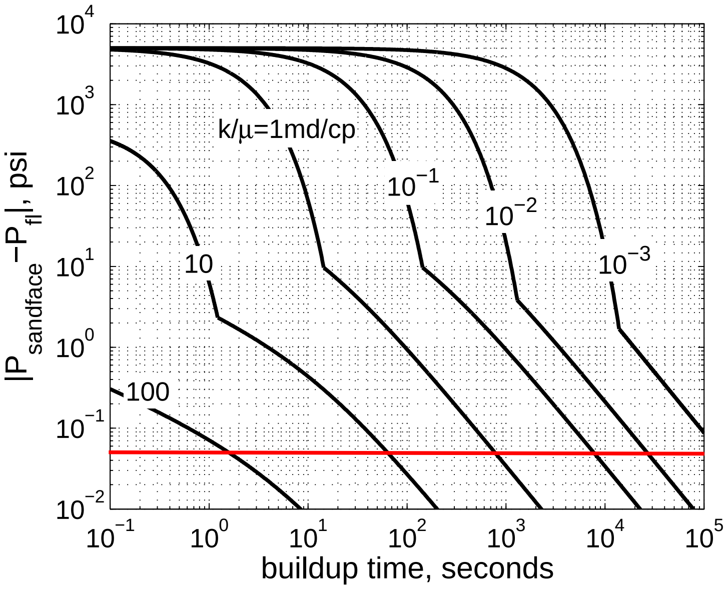

Figure 3.19: Buildup equilibration for the pretests (defined in Table 3.3) that maximize the spherical flow signal, *medium radius probe* tool.

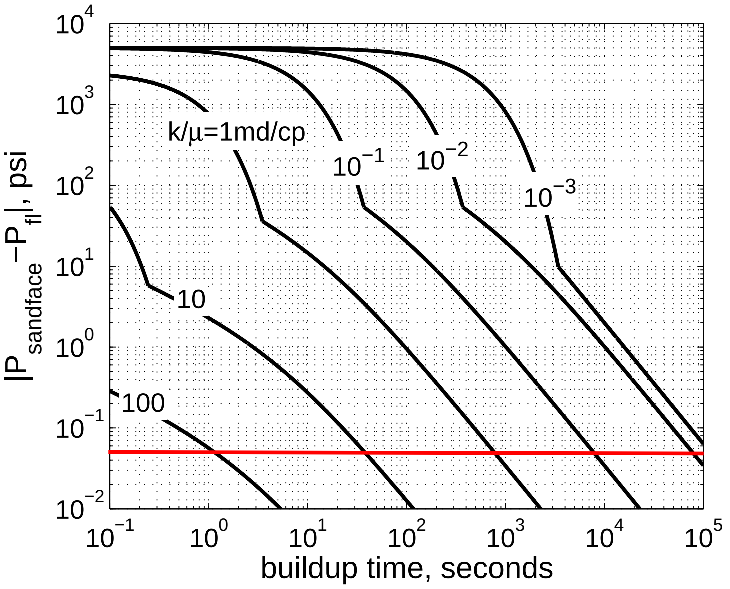

Figure 3.20: Buildup equilibration for the pretests (defined in Table 3.4) that maximize the spherical flow signal, *large radius probe* tool.

on $\mathbf{X}$ and ΔP_{max} comes from their influence on the early part of buildup, the tool storage time period. So, to the extent that these terms could shorten the tool storage period, they would simultaneously contribute to increasing ΔP_{max}.

Table 3.4 shows that the large probe radius tool would measure the largest signal during the spherical flow period for each mobility formation, with the largest signal generated in 0.01 md/cp to 0.1 md/cp formations. The reason for this is that m (Equation 3.16) is large in these cases (and τ_{tool} is not extremely large). To further increase the size of the signal it would be necessary to increase the size of the probe radius, or to increase the size of the drop in pressure during drawdown; however, the latter is not always an option. For example, if the formation pressure is low, e.g., below 5000 psi, or the fluid is close to its saturation pressure, then increasing the drop in pressure could cause gas to come out of solution during the pretest. The results presented here apply only to single-phase flow. Figure 3.17 identifies other options for increasing the signal size, ΔP_{max}; it also identifies the option best suited for formations with a specific range of mobility, as well as options that would not be effective.

For each of the 18 cases investigated, the pretest parameters (q, ΔV) that generate ΔP_{max} lie on the boundary of the region of permissible values (refer to Figures 3.14 – 3.17). This implies that the only way of increasing the size of ΔP_{max} would be to change the limiting value of at least one of the tool's constraints. For instance, let us consider the *large probe radius* tool (Figure 3.17). Here, constraint 3 (maximum permissible pressure drop within the flowline equal to 5000 psi) is limiting the size of ΔP_{max} in the low mobility range, from 0.001 to 0.1 md/cp.

In the mobility range 0.01 to 0.1 md/cp, when the upper boundary curve has a flat, horizontal segment (Figure 3.17, q is constant with a value less than 2.0 cm^3/s) as T approaches its largest value, ΔP_{max} is located at a corner of the boundary, sharing constraints 2 ($\Delta V \leq 40$ cm^3) and 3. Another option to increase ΔP_{max} in these cases is by changing the upper bound in constraint 2. For these cases, ΔP_X is highly sensitive to q as T decreases along the horizontal segment of A (refer to Figure 3.17(c)). For the highest mobility range, from 1 to 100 md/cp, the size of ΔP_{max} could be increased by changing the upper bound for constraint 1 ($q \leq 2.0$ cm^3/s); only in the case of 1 md/cp, does one have the additional option of increasing constraint 2.

In Figures 3.14 – 3.17, there are regions in some of the domains of permissible pretests where the constant ΔP_X contours closely approximate straight lines with slope of -1; this is especially evident for the low mobility cases. These pretests are of a very simple nature. They occur when the duration of the drawdown T is sufficiently short that the amount of fluid entering the tool from the formation is insufficient to affect P_{fl}, that is, during (only) drawdown, P_{fl} has a similar behavior as when the tool is set against an impermeable formation. When this happens over the entire domain, as appears to be the case in Figures 3.13(a), 3.16(a), and 3.17(a), then ΔP_X is almost constant along boundary A, so any point on A could represent ΔP_{max}.

In the high mobility cases shown in Figures 3.15(a), 3.15(b), 3.16(e), 3.16(f), 3.17(e), and 3.17(f), the majority of the constant ΔP_X contours are almost straight horizontal lines. This feature indicates that these pretests achieved steady state by the conclusion of drawdown. The critical issue is the modest size of the steady state drop in pressure ($P_{sandface} - P_{fl}(T)$) at the end of drawdown. For these cases, increasing q has a significant effect on the size of ΔP_X, while increasing T, hence ΔV, hardly affects the size of ΔP_X. Consequently, constraint 1 ($q \leq 2.0$ cm^3/s) must be increased to increase the size of ΔP_{max}.

The cases shown in Figures 3.15(b), 3.16(f), 3.17(e), and 3.17(f), have a unique feature: **X** is not located at a corner of the boundary of permissible pretests. This is a consequence of the slightly more elaborate form of the spherical time function f_s (refer to Equation 3.17) used in this study, implying that at the beginning of the spherical flow period, there is a dependence of

$-m \times f_s$ on both q and ΔV (as opposed to $-m \times T/(2 \times t^{3/2})$) depending only on ΔV). This is also the explanation for the pressure signal during spherical flow in Figures 3.18 to 3.20 deviating from a straight-line of slope -3/2. In any case, there is not a significant variation in ΔP_X, along the upper boundary.

To identify the domain of investigation of $(k/\mu)_{sph}$, the same approach presented by Moran and Finklea is followed here. Since the value of $(k/\mu)_{sph}$ is determined by the time dependent pressure signal during spherical flow, it is assumed that the domain of investigation coincides with the location of the largest pressure gradients within the formation when the spherical flow signature is detected. This is the region across which the pressure experiences a substantial drop. The pressure distribution in the reservoir at the onset of the spherical flow period is presented in Figures 3.21, 3.22, and 3.23 for those pretests that maximize the spherical flow signal. The abscissa denotes the radial spherical distance, r, in the formation with origin at the probe, normalized by the probe radius of that particular tool. The two markers in each curve identify the region across which 90% of the pressure drop occurs.

Figure 3.24 shows the spatial dependence of pressure at time **X** for the three different tools when the formation mobility is 0.1 md/cp. Thus, their initial domains of investigation are: $20 < r < 100$ inches for the large, $30 < r < 200$ inches for the medium size tool, and $50 < r < 300$ inches for the small probe radius tools. Figure 3.25 shows the computed flowline pressure during their entire buildup periods. Here, it is seen that the formation signal for the *large probe radius* tool is largest, because it becomes part of the spherical flow period sooner. At large time, all curves appear to coincide,

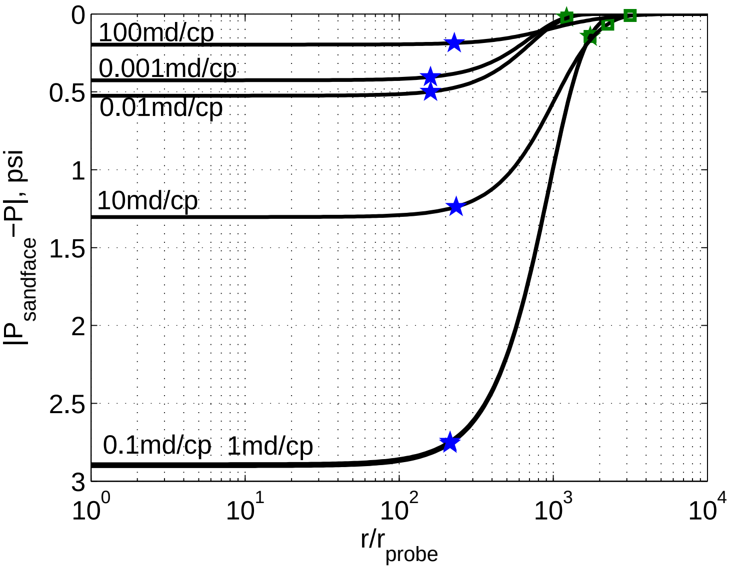

Figure 3.21: Pressure distribution in the reservoir at the onset of spherical flow for pretests that maximize the spherical flow signal (*small radius probe* tool). The markers ($\star$ and $\square$) delimit the reservoir region where 90% of the pressure change occurs.

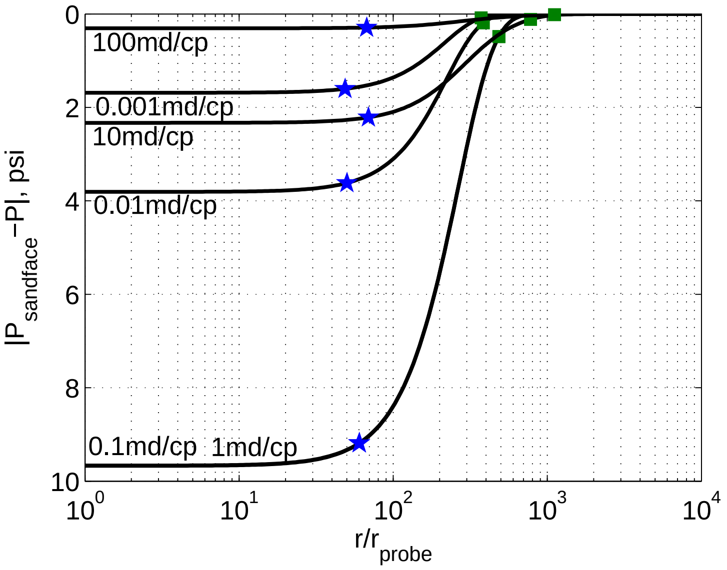

Figure 3.22: Pressure distribution in the reservoir at the onset of spherical flow for pretests that maximize the spherical flow signal (*medium radius probe* tool). The markers ($\star$ and $\Box$) delimit the reservoir region where 90% of the pressure change occurs.

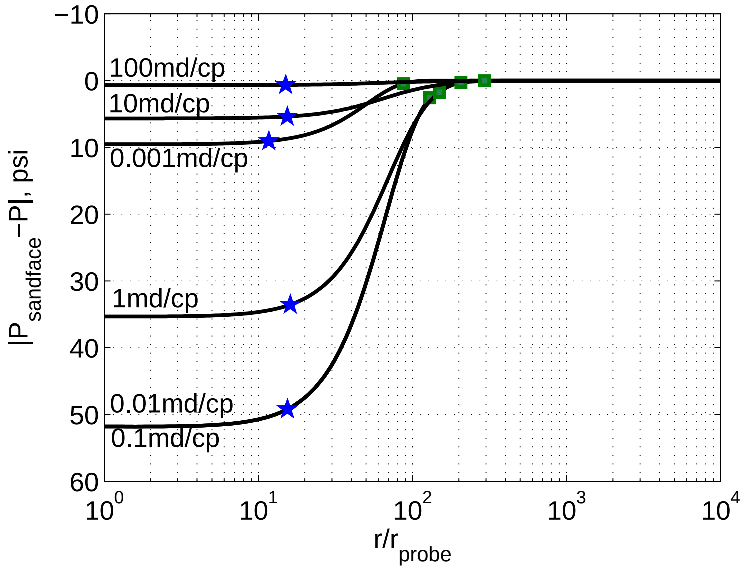

Figure 3.23: Pressure distribution in the reservoir at the onset of spherical flow for pretests that maximize the spherical flow signal (*large radius probe* tool). The markers ($\star$ and $\square$) delimit the reservoir region where 90% of the pressure change occurs.

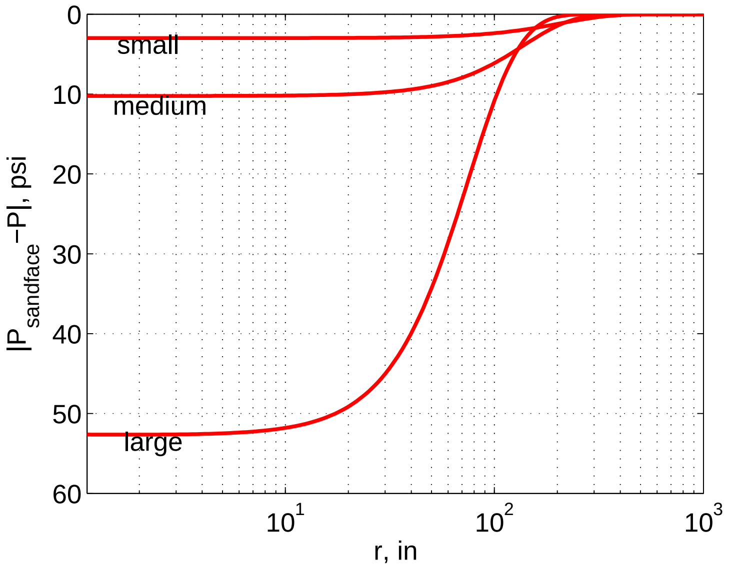

Figure 3.24: Pressure distribution in the reservoir at the onset of spherical flow in a 0.1 md/cp formation for (q,ΔV) that maximize the spherical flow signal for the three tools considered.

because ΔV ≈40 cm^3 (implying that the values of $q \times T$ are the same) for all three cases.

Plots of $\log(|P_{sandface} - P_{fl}(t)|)$ vs. log(buildup time) have been found helpful in assessing the quality of the pressure signal during buildup. An example is given in Figure 3.26 where simulated tool noise has been added to the results from Figure 3.25. This type of plot facilitates assessing the limitation of the data because of tool resolution, and the advantage of using a tool with specifications that optimize the signal during the spherical flow period (advantage of using the large probe radius tool).

It is common practice to use specialized plots for the identification of flow regimes during the buildup. For the interpretation of formation tester data, the spherical and radial derivative plots are often used as quality control

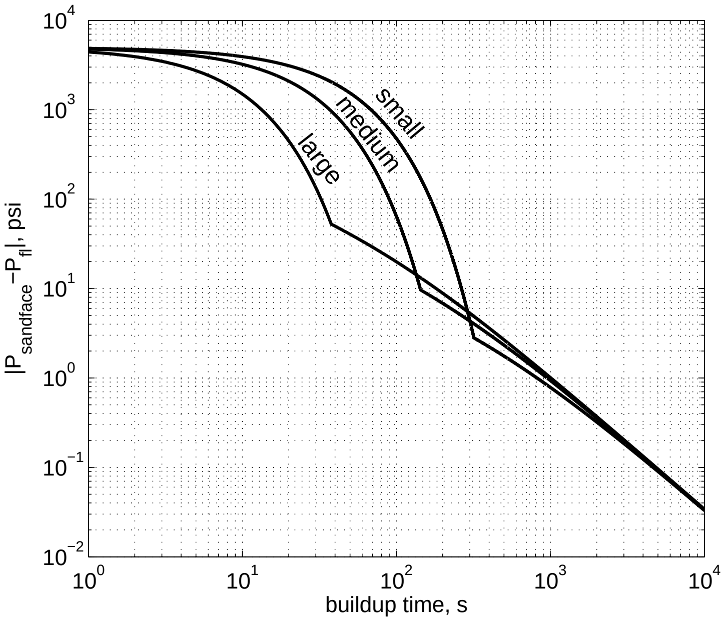

Figure 3.25: Buildup pressure equilibration for 0.1 md/cp formation for $(q,\Delta V)$ that maximize the spherical flow signal for the three tools considered.

indicators when analyzing tests. The results obtained from the analysis of the temperature variations indicate that, under certain situations, it is possible for the pressure signal originated by the tool during the buildup to exhibit a behavior similar to that expected from the formation during the spherical flow period. This will be the topic of the next chapter.

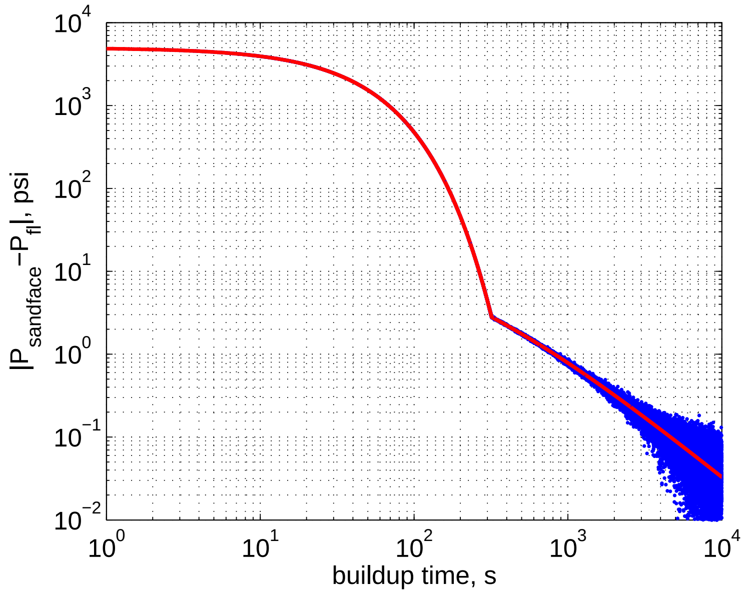

(a) *small* probe radius

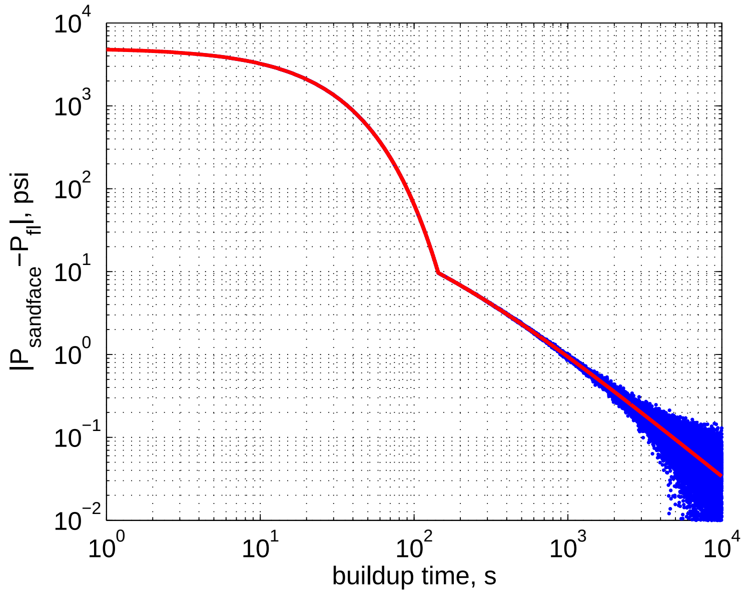

(b) *medium* probe radius

Figure 3.26: Buildup equilibration plots for $(q, \Delta V)$ that maximize the spherical flow signal in 0.1 md/cp with tool noise (normal distribution based on sensor resolution of 0.05 psi).

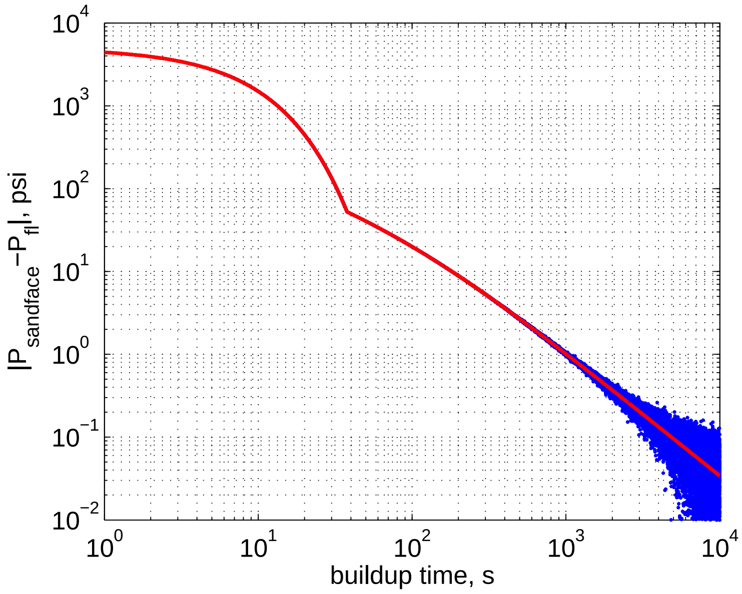

Figure 3.27: Buildup equilibration plots for $(q, \Delta V)$ that maximize the spherical flow signal in 0.1 md/cp with tool noise (normal distribution based on sensor resolution of 0.05 psi) for *large* probe radius tool.

Chapter 4

Analysis of Temperature Variations During the Pretest

4.1 Introduction

Effects of temperature variations within the flowline of a formation tester on the pressure transients recorded during the operation of the tool are considered. Temperature variations in the problem are accounted for by recognizing the pressure and temperature dependence of density in the continuity equation and that temperature has both space and time dependence. Including temperature in the analysis requires taking into account the flowline geometry, which was immaterial for the isothermal analysis. Some tool behaviors that have been unexplained by the isothermal theory, such as false buildups, buildup overshoots and long equilibration times, might be, at least partially, explained by the inclusion of temperature variations in the analysis.

The term "false buildup" refers to the pressure increase that is often observed after a dry drawdown, that is, when there is no inflow from the formation to the flowline, either because the mudcake was not breached or because the flowline pressure remains higher than the sandface pressure when the pretest piston stops. An example of this behavior is given in Figure 4.1. Here, the first drawdown, which ended at around 80 seconds (logging time not drawdown time) is followed by a pressure increase. It was assumed that this

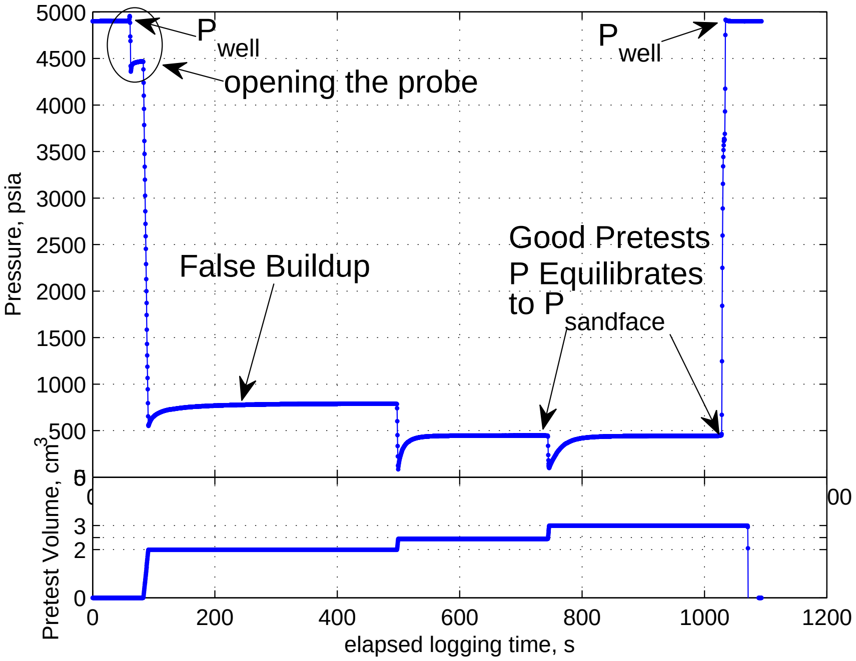

Figure 4.1: Example of false buildup during a pretest followed by two valid pretests (identified in this case by the repeatability of the equilibrium pressure, $P_{sandface}$). The small pressure effect observed at 61 seconds (circled) is the flowline pressure response to opening the probe in preparation for the pretest. It occurs because of the retraction of the filter piston in the probe assembly (refer to Figure 2.3)

was a formation response, and the pressure was allowed to stabilize until 500 seconds logging time. Two subsequent pretests (500 s to 740 s and 740 s to 1020 s) confirmed that the first buildup was not a formation response. The repeatability of the equilibration pressure at about 790 s and about 1020 s is a quality control for the pretest.

A buildup overshoot is when the flowline pressure increases beyond the sandface pressure during buildup and then decreases until equilibrium is reached. This behavior is sometimes referred to as a 'builddown', and an

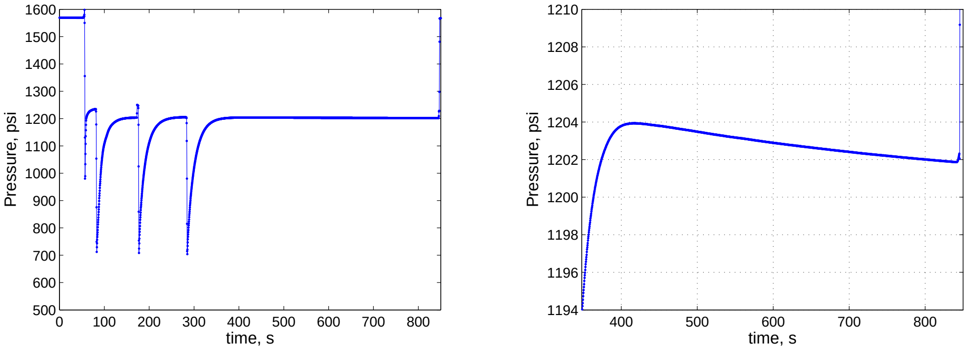

(a) $\Delta t_D = 0$ (b) detail of the last buildup

Figure 4.2: Example of buildup overshoot during a pretest

example is shown in Figure 4.2. The left-side plot shows the flowline pressure during the entire test and the right-side plot focuses on a detail of the last buildup. At 400 seconds, the flowline pressure has reached its maximum value and starts decreasing. The pretest was terminated at around 830 s, without the flowline pressure having reached equilibrium with the sandface pressure. Since this is an aberrant behavior of the pressure signal, it is not possible to perform transient analysis to interpret the late-time pressure data.

4.2 Theoretical Development

The flowline of a formation tester is depicted in a high-level schematic in 4.3 (left side). Based on the absence of constrictions in the flowline, it is reasonable to assume that the pressure of the fluid within the flowline is uniform. Hence, the pressure gauge measures the pressure experienced at the probe, that is, the flowline pressure, P, is only a function of time.[1] On the

---

[1] Since in this chapter the only concern is the pressure within the flowline, the subscript fl on P will be dropped.

other hand, heat transfer between the flowline and the surrounding medium dictates that the temperature, Θ, of the fluid in the flowline is a function of both radial position and time.

The following are the main approximations used in determining the governing equations of the problem:

1. The geometry of the flowline has been simplified (Figure 4.3, right side). Each flowline component –probe, tubes, valves, or pressure gauge– is modeled as a long cylinder of volume, V_i and radius, r_{fli}, axially centered within a tool of radius r_{tool}. End effects are neglected, implying that heat conduction occurs only in the radial direction.

2. The wellbore pressure, P_{well}, is greater than or equal to the formation pressure at the sandface, $P_{sandface}$, the difference, or overbalance, ranges from 100 to 5,000 psi.

3. Heat transfer by natural convection is neglected. The wellbore temperature, Θ_{well}, is constant in the vicinity of the tool.

Other assumptions made here are the same used in the analysis of the isothermal case. 4) the pretest volume, ΔV, is considered small in comparison with the flowline volume, $V_{flowline}$; i.e, $V_{flowline}$ is assumed to be constant. 5) the density of the fluid in the flowline ($\rho_{flowline\ fluid}$) and the density of the fluid flowing into the tool from the formation ($\rho_{formation\ fluid}$) are the same. 6) the formation response is modeled using the quasisteady-state approximation (Equation 3.4), that is, the formation compressibility is neglected when computing the rate of flow through the probe orifice).

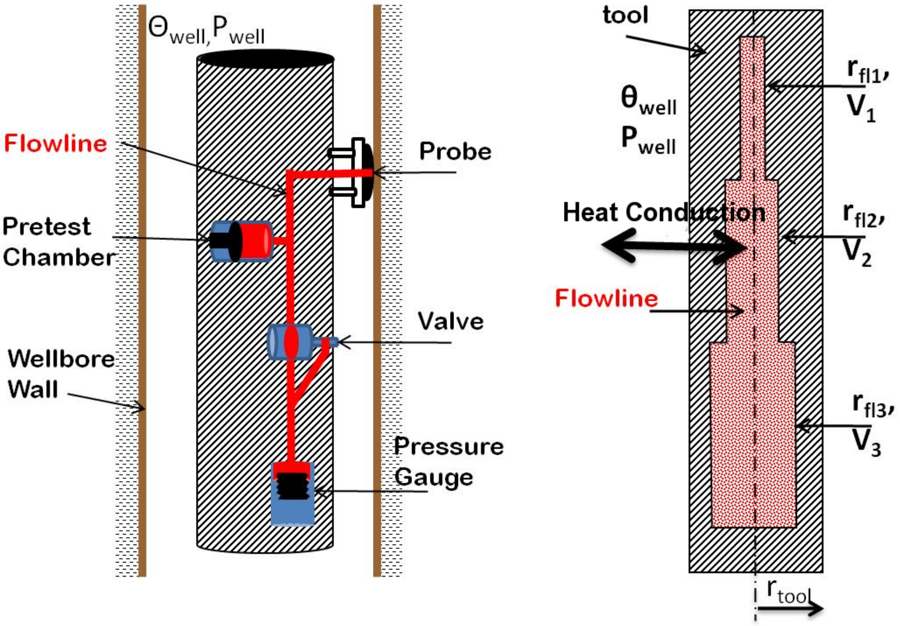

Figure 4.3: Schematic of a generic formation tester flowline (left) showing some of its key components. On the right is the conceptualization of the flowline for the calculation of temperature during the pretest. Larger values of r_{fl} may correspond to the pretest chamber, a valve, or the volume in the pressure gauge. The radius of each flowline segment, r_{fli},$i = 1, 2, 3$,etc. and the tool radius, r_{tool}, are measured from the center of the flowline. The volume of each flowline segment is represented by V_i,$i = 1, 2, 3$, etc.

Insight into the origin of the temperature effects could be gained by examining a limiting case in which no transfer of heat takes place during the pretest, that is, adiabatic conditions, and the tool is set against an impermeable formation (dry drawdown is performed). Adiabatic conditions could be approximated when the piston in the pretest chamber retracts at a relatively fast rate increasing $V_{flowline}$ by ΔV. The pressure change, ΔP_{ddS}, during an adiabatic drawdown on an impermeable formation is:

$$\Delta P_{ddS} \equiv P_{ddS} - P_{well} \approx -\frac{1}{\kappa_S + c_{tool}} \ln\left(\frac{V_{flowline} + \Delta V}{V_{flowline}}\right). \qquad (4.1)$$

The corresponding temperature change, $\Delta\Theta_{ddS}$, is:

$$\Delta\Theta_{ddS} \equiv \Theta_{ddS} - \Theta_{well} \approx -\frac{1}{2\alpha}\left(\frac{\kappa_\Theta}{\kappa_S} - 1\right) \ln\left(\frac{V_{flowline} + \Delta V}{V_{flowline}}\right). \qquad (4.2)$$

where P_{ddS} and Θ_{ddS} are the flowline pressure and temperature at the end of a dry adiabatic drawdown. Since heat transfer has been neglected, P_{ddS} and Θ_{ddS} are uniform throughout the flowline. The initial temperature and pressure, Θ_{well} and P_{well}, are also uniform throughout the flowline. The other variables in Equations 4.1 and 4.2 are α, the coefficient of thermal expansion of the fluid, κ_Θ, the isothermal compressibility of the fluid, κ_S, the adiabatic compressibility of the fluid, and c_{tool}, the compressibility of the tool (Dussan, 2011). Definitions of these coefficients and more detailed derivations are provided in Appendix A. By definition, ΔP_{ddS} and $\Delta\Theta_{ddS}$ are the difference from the final state to the initial state, hence they are negative quantities. Note that $\Delta\Theta_{ddS}$ is the maximum possible temperature change during a pretest of size ΔV, because no heat transfer is allowed (adiabatic case). Likewise, ΔP_{ddS} is

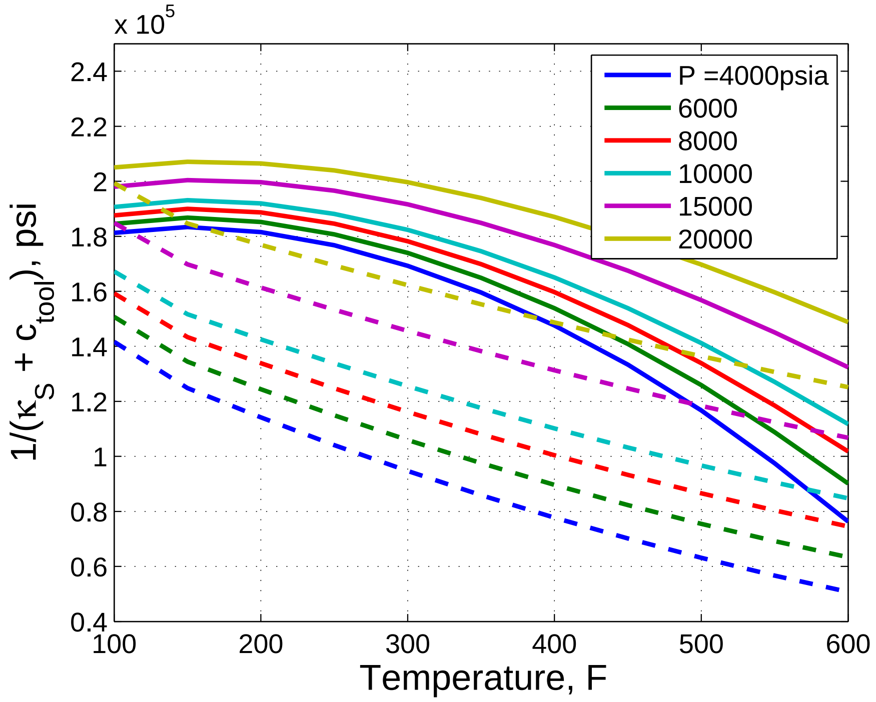

Figure 4.4: Thermodynamic properties of water (solid lines) and n-hexadecane (dashed lines) used for the computation of ΔP_{ddS} with $c_{tool} = 2.7 \times 10^{-6}$psi^{-1} ($4 \times 10^{-5}$atm^{-1})

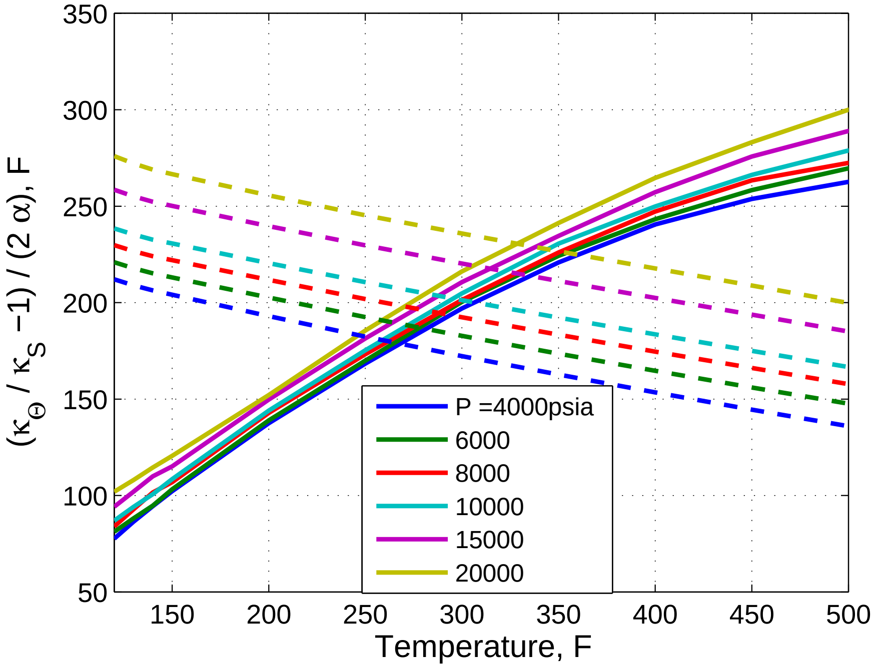

Figure 4.5: Thermodynamic properties of water (solid lines) and n-hexadecane (dashed lines) used for the computation of $\Delta\Theta_{ddS}$

the maximum possible drawdown, because there is no flow through the probe orifice. As heat transfer increases, e.g., as a result of decreasing the piston speed, the pretest approaches the isothermal case.

If the flowline fluid temperature is allowed to equilibrate with the wellbore temperature at the end of the drawdown, the flowline pressure will increase. The total pressure buildup after a dry adiabatic drawdown, ΔP_{bu}, is the difference between the isothermal and the adiabatic drawdown,

$$\Delta P_{bu} = \Delta P_{dd\Theta} - \Delta P_{ddS}, \tag{4.3}$$

that is, the pressure has to buildup to the pressure that would have been reached at the end of an isothermal drawdown, $\Delta P_{dd\Theta}$:

$$\Delta P_{dd\Theta} \equiv P_{dd\Theta} - P_{well} \approx -\frac{1}{\kappa_\Theta + c_{tool}} \ln\left(\frac{V_{flowline} + \Delta V}{V_{flowline}}\right). \tag{4.4}$$

Equation 4.3 is of particular interest because it provides a thermodynamic explanation for the practical problem of ‘false buildups’, that is, the pressure increase that is observed after a dry drawdown. Equation 4.4 can be used to quantify this effect, as it gives the size of the buildup, that is, the maximum pressure increase after a dry drawdown. Expressing the buildup after a dry drawdown in dimensionless form,

$$\frac{\Delta P_{bu}}{\Delta P_{ddS}} = \frac{\kappa_S + c_{tool}}{\kappa_\Theta + c_{tool}} - 1 = \frac{1}{1 + \frac{c_{tool}}{\kappa_\Theta}}\left(\frac{\kappa_S}{\kappa_\Theta} - 1\right). \tag{4.5}$$

Equations 4.2 and 4.5 indicate that the fundamental cause of the temperature effects is the difference between κ_Θ and κ_S. The two values of compressibility are always different for water-based mud (WBM) or oil-based mud (OBM) as may be seen in Figure 4.6; for water, the difference between κ_Θ

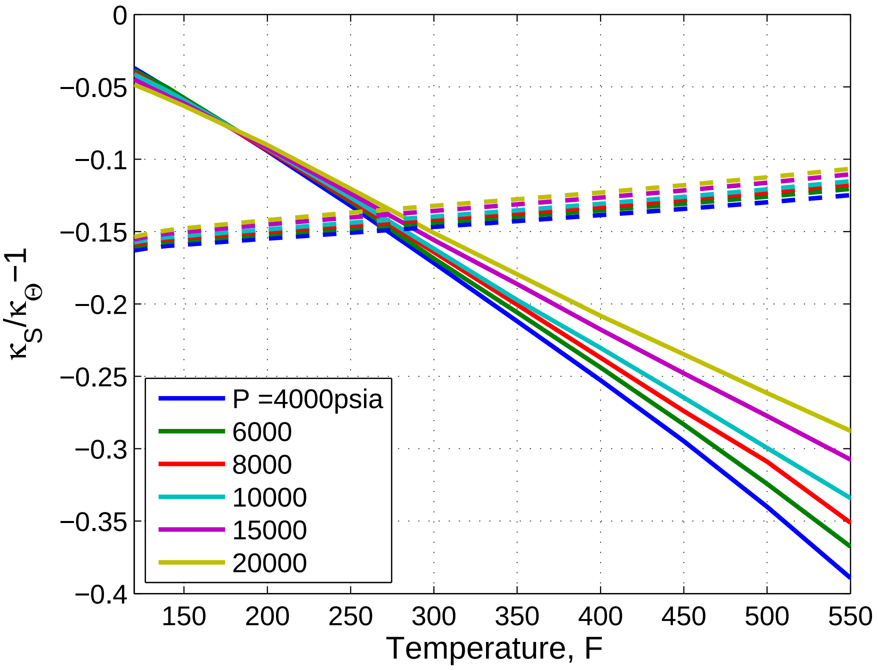

Figure 4.6: Thermodynamic properties of water (solid lines) and n-hexadecane (dashed lines) used for the computation of the pressure increase during a false buildup

and κ_S increases with temperature. Figures 4.4 and 4.5 could be used to estimate ΔP_{ddS} and $\Delta\Theta_{ddS}$ for a given pretest, noting that for $\Delta V/V_{flowline} \ll 1$, $\ln(1 + \Delta V/V_{flowline}) \approx \Delta V/V_{flowline}$.

For example, consider a pretest with $\Delta V = 2$ cm^3 and $V_{flowline} = 100$ cm^3 with $P_{well} = 1360$ atm (20×10^3 psia) and Θ_{well}= 366 K (200 F), and assuming $c_{tool} = 4.00 \times 10^{-5}$ atm $^{-1}$ (2.7×10^{-6} psi $^{-1}$). If the fluid in the flowline is WBM, $\Delta P_{ddS} = 279$ atm (4100 psi) and $\Delta\Theta_{ddS} = 1.7$ K (3 F). If the fluid is OBM, represented hereafter by the properties of hexadecane (nC16), $\Delta P_{ddS} = 238$ atm (3500 psi) and $\Delta\Theta_{ddS} = 2.8$ K (5 F).

The pressure increase at the end of the drawdown could be calculated with Equation 4.5. At 1360 atm (20×10^3 psia) and 366 K (200 F), $\kappa_\Theta = 3.43 \times 10^{-5}$ atm^{-1} for WBM and $\kappa_\Theta = 5.02 \times 10^{-5}$ atm^{-1} for OBM (Figure A.3); hence, $\Delta P_{bu} = 11.6$ atm (170 psi) for WBM and $\Delta P_{bu} = 18.7$ atm (275 psi) for OBM. The analysis so far corresponds to the equilibrium states of the system, the time variation of pressure and temperature in the flowline is discussed next.

4.3 Problem Statement

The governing equation for the flowline pressure is derived from conservation of mass applied to the flowline of the tool, as has been done in all published studies of pressure transients associated with formation tester pretests (Proett and Chin, 1994; Kasap et al., 1995; Dussan, 2011). In contrast with the isothermal analysis, here the fluid density, ρ, is considered a function of pressure and temperature, $\rho = \rho(P, \Theta)$:

$$c_{eff} V_{flowline} \left(\frac{dP}{dt} - \alpha \frac{d\langle\Theta\rangle}{dt} \right) = q_{fm} - q_{piston} \tag{4.6}$$

where $c_{eff} \equiv c_{tool} + \kappa_{\Theta}$ is the effective flowline compressibility, q_{piston} is the speed of the piston in the pretest chamber or pretest rate, and q_{fm} is the rate of flow through the probe orifice, calculated using the quasi-steady state approximation :

$$q_{fm} = 4 r_{probe} \frac{k}{\mu} \left(P_{sandface} - P \right), \tag{4.7}$$

where r_{probe} is the radius of the probe orifice, and $\frac{k}{\mu}$ is the formation mobility. The new term in the conservation of mass equation is the time derivative of $\langle\Theta\rangle$, the mass-average temperature of the fluid in the flowline, defined as:

$$\langle\Theta\rangle \equiv \frac{\sum\limits_{i=1}^{N} \int\limits_{0}^{r_{fli}} \rho(r,t) \Theta_i(r,t) r dr}{\sum\limits_{i=1}^{N} \int\limits_{0}^{r_{fli}} \rho(r,t) r dr} \tag{4.8}$$

where r is the radial coordinate with origin at the center of the flowline, and N is the total number of flowline components. The presence of $\frac{d\langle\Theta\rangle}{dt}$ in Equation 4.6 mandates the inclusion of the equation of conservation of energy, specifically non-mechanical energy, for the fluid in the flowline and the surrounding solid material of the tool:

$$\rho_{fluid} \hat{c}_{Pfluid} \frac{\partial \Theta_i}{\partial t} - \alpha_{fluid} \Theta_i \frac{dP}{dt} = \frac{K_{\Theta fluid}}{r} \frac{\partial}{\partial r} \left(r \frac{\partial \Theta_i}{\partial r} \right), \quad 0 < r < r_{fli} \tag{4.9}$$

$$\rho_{solid} \hat{c}_{Psolid} \frac{\partial \Theta_i^*}{\partial t} = \frac{K_{\Theta solid}}{r} \frac{\partial}{\partial r} \left(r \frac{\partial \Theta_i^*}{\partial r} \right), \quad r_{fli} < r < r_{tool} \tag{4.10}$$

ρ, $\hat{c}_P$, and K_{Θ} are respectively the density, heat capacity, and thermal conductivity of the fluid or the tool material (solid). The temperature of the fluid within the flowline is denoted by Θ and the temperature in the region between the flowline wall and the tool wall is denoted by Θ^*. Equations 4.9 and 4.10 are applied to each flowline component.

The initial conditions for the drawdown are:

$$P(0) = \begin{cases} P_{well}, & \text{for the first pretest after setting the tool,} \\ P_{sandface}, & \text{for subsequent pretests.} \end{cases} \tag{4.11}$$

$$\Theta_i(r,0) = \Theta_{well}, \quad 0 < r \leq r_{fli}, \tag{4.12}$$

and

$$\Theta_i^*(r,0) = \Theta_{well}, \quad r_{fli} < r \leq r_{tool}, \tag{4.13}$$

and the boundary conditions are:

$$\Theta_i^*(r_{tool},t) = \Theta_{well}, \quad r = r_{tool}, \tag{4.14}$$

$$\Theta_i^*(r_{fl_i},t) = \Theta_i(r_{fl_i},t), \quad r = r_{fli}, \tag{4.15}$$

and

$$\left.\frac{\partial \Theta_i^*}{\partial r}\right|_{r=r_{fl_i}} = \frac{K_{\Theta fluid}}{K_{\Theta solid}} \left.\frac{\partial \Theta_i}{\partial r}\right|_{r=r_{fl_i}}. \tag{4.16}$$

4.3.1 Scaling

The convenient scales for this problem are ΔP_{ddS} (Equation 4.1), $\Delta\Theta_{ddS}$ (Equation 4.2), the radius of the first flowline component, r_{fl1}, and the characteristic time due to the flowline compressibility, τ_{tool}:

$$\tau_{tool} \equiv \frac{c_{eff} V_{flowline}}{4 r_{probe} \frac{k}{\mu}} \tag{4.17}$$

The dimensionless dependent variables are defined as

$$P_D \equiv \frac{P - P_{sandface}}{\Delta P_{ddS}}, \tag{4.18}$$

$$\Theta_{Di} \equiv \frac{\Theta_i - \Theta_{well}}{\Delta\Theta_{ddS}}, \tag{4.19}$$

and

$$\Theta^*_{Di} \equiv \frac{\Theta^*_i - \Theta_{well}}{\Delta\Theta_{ddS}}, \tag{4.20}$$

and the independent variables by,

$$t_D = \frac{t}{\tau_{tool}} = \frac{4r_{probe}\frac{k}{\mu}t}{c_{eff}V_{flowline}}, \tag{4.21}$$

$$r_D = \frac{r}{r_{fl1}}. \tag{4.22}$$

Equation 4.6 is written in dimensionless form as

$$\frac{dP_D}{dt_D} + P_D = Y\frac{d\langle\Theta_D\rangle}{dt_D} - Xq_D, \quad \text{for } 0 < t_D \leq \frac{\Delta V}{q_\infty \tau_{tool}}, \tag{4.23}$$

$$\frac{dP_D}{dt_D} + P_D = Y\frac{d\langle\Theta_D\rangle}{dt_D}, \quad \text{for } \frac{\Delta V}{q_\infty \tau_{tool}} < t_D < \infty, \tag{4.24}$$

where q_∞ is the average pretest piston rate, and

$$q_D \equiv \frac{q_{piston}(t)}{q_\infty}.$$

The total duration of the drawdown period is $\frac{\Delta V}{q_\infty}$, and $\frac{\Delta V}{q_\infty \tau_{tool}}$ is the dimensionless drawdown time. Equations 4.9 and 4.10 written in dimensionless form are

$$\frac{\partial\Theta_{Di}}{\partial t_D} = \frac{1}{\gamma_i r_D}\frac{\partial}{\partial r_D}\left(r_D\frac{\partial\Theta_{Di}}{\partial r_D}\right) + \frac{dP_D}{dt_D}, \quad 0 \leq r_{Di} \leq \frac{r_{fl_i}}{r_{fl_1}}, \tag{4.25}$$

and

$$\frac{\partial\Theta^*_{Di}}{\partial t_D} = \frac{1}{\beta_i r_D}\frac{\partial}{\partial r_D}\left(r_D\frac{\partial\Theta^*_{Di}}{\partial r_D}\right), \quad \frac{r_{fl_i}}{r_{fl_1}} \leq r_{Di} \leq r_{eD}, \tag{4.26}$$

where $r_{eD} = \frac{r_{tool}}{r_{fl1}}$ is the dimensionless distance to the tool wall. For the drawdown, the initial conditions are:

$$P_D(0) = \begin{cases} \dfrac{P_{well} - P_{sandface}}{\Delta P_{ddS}}, & \text{first pretest after setting the tool,} \\ 0, & \text{subsequent pretests.} \end{cases} \tag{4.27}$$

$$\Theta_{Di}(r_D, 0) = 0, \quad 0 < r_D \leq \frac{r_{fli}}{r_{fl1}}, \tag{4.28}$$

and

$$\Theta_i^*(r, 0) = \Theta_{well}, \quad \frac{r_{fli}}{r_{fl1}} < r \leq r_{eD}, \tag{4.29}$$

and the boundary conditions are

$$\Theta_{Di}^*(r_{eD}, t_D) = 0, \tag{4.30}$$

$$\Theta_{Di}^*\left(\frac{r_{fli}}{r_{fl1}}, t_D\right) = \Theta_{Di}\left(\frac{r_{fli}}{r_{fl1}}, t_D\right), \tag{4.31}$$

and

$$\left.\frac{\partial \Theta_{Di}^*}{\partial r_D}\right|_{r_D = \frac{r_{fli}}{r_{fl1}}} = \sigma \left.\frac{\partial \Theta_{Di}}{\partial r_D}\right|_{r_D = \frac{r_{fli}}{r_{fl1}}}, \tag{4.32}$$

where $\sigma \equiv \frac{K_{\Theta fluid}}{K_{\Theta solid}}$, is the ratio of thermal conductivities of the liquid and the solid.

4.3.2 Dimensionless Groups

Several dimensionless parameters have been introduced in the preceding equations. The most prominent parameter, Y, is a measure of the impact of temperature effects on the pressure behavior. When written in terms of physical variables of the problem, Y reduces to the difference between the isothermal and the adiabatic compressibility of the fluid. Figure 4.7 shows values of Y for water as a function of pressure and temperature ($c_{tool} = 4 \times 10^{-5}$

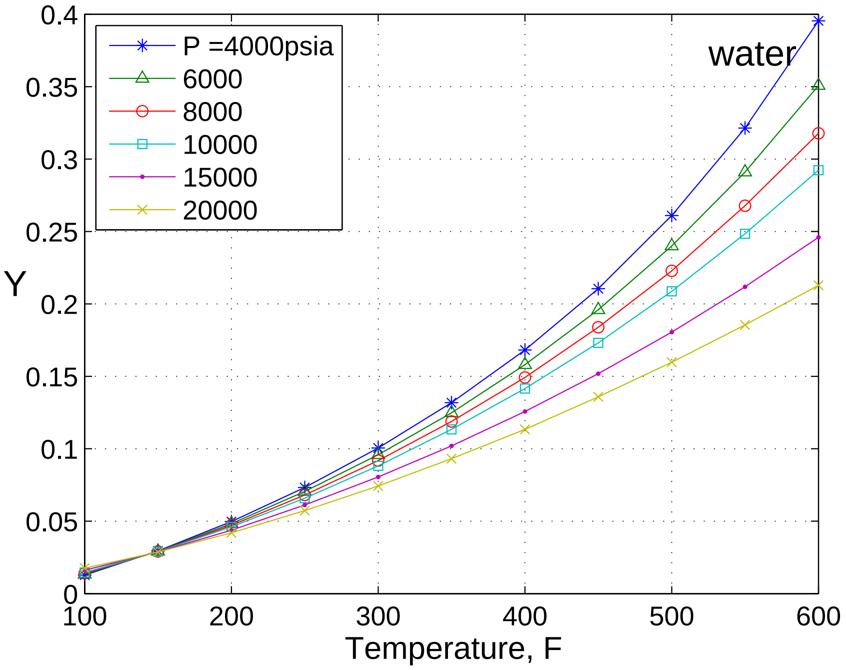

Figure 4.7: Variation of the dimensionless group Y as a function of pressure and temperature for water. Y is a measure of the size of the temperature effects on the pressure signal ($c_{tool} = 4 \times 10^{-5}$ atm^{-1})

atm^{-1}). Hence, $Y = 0$ implies that there are no temperature effects on the pretest.

$$Y \equiv \frac{\alpha \Delta \Theta_{ddS}}{c_{eff} \Delta P_{ddS}} = \frac{\kappa_\Theta - \kappa_S}{\kappa_\Theta + c_{tool}}. \tag{4.33}$$

The dimensionless group, X, is the ratio of the pressure drop,

$$\Delta P_{dd} = \frac{q_\infty}{4 r_{probe} \frac{k}{\mu}},$$

that would occur if a pretest at a given constant rate q_∞ reaches steady state, and the pressure change, ΔP_{ddS}, because of a volume increase in the flowline under adiabatic conditions when the tool is set against an impermeable material. Hence, X is a measure of the size of the pretest, and is a term that appears only in the drawdown equations.

$$\begin{aligned} X &\equiv \frac{\Delta P_{dd}}{\Delta P_{ddS}} = -\frac{\left(\kappa_S + c_{tool}\right) q_\infty}{4 r_{probe} \frac{k}{\mu} \ln\left(\frac{V_{flowline}+\Delta V}{V_{flowline}}\right)}, \\ &\approx -\frac{V_{flowline}\left(\kappa_S + c_{tool}\right) q_\infty}{4 r_{probe} \frac{k}{\mu} \Delta V}. \end{aligned} \tag{4.34}$$

The approximation on the right side of (4.34) is only valid when $\Delta V / V_{flowline} \ll 1$.

The diffusivity coefficients in the temperature equations, $1/\gamma_i$ and $1/\beta_i$, are the ratio of two characteristic times in the problem τ_{tool} corresponding to the isothermal flowline compressibility (storage), and

$$\tau_{heat,i} \equiv \frac{\rho \hat{c}_P r_{fl_i}^2}{K_\Theta}, \tag{4.35}$$

corresponding to heat conduction; hence, they are a measure of the relative duration of heat conduction in the fluid and the solid with respect to tool storage. In terms of physical variables,

$$\frac{1}{\gamma_i} \equiv \frac{\tau_{tool}}{\tau_{heat,i}^{fluid}} = \frac{K_\Theta^{fluid}\left(\kappa_\Theta + c_{tool}\right)}{4 \rho^{fluid} \hat{c}_P^{fluid} r_{fl_i}^2 r_{probe} \frac{k}{\mu}}, \tag{4.36}$$

and

$$\frac{1}{\beta_i} \equiv \frac{\tau_{tool}}{\tau_{heat,i}^{solid}} = \frac{K_\Theta^{solid}\left(\kappa_\Theta + c_{tool}\right)}{4 \rho^{solid} \hat{c}_P^{solid} r_{fl_i}^2 r_{probe} \frac{k}{\mu}}. \tag{4.37}$$

The values of $1/\gamma_i$ and $1/\beta_i$ range from 0 to ∞. When $1/\gamma_i = 0$, the pretest occurs under adiabatic conditions, that is, there is no heat conduction in the fluid. When $1/\beta_i = 0$, there is no heat conduction in the solid portion of the tool; this means that the tool behaves as a perfect thermal insulator. As the value of $1/\gamma_i$ or $1/\beta_i$ increases, heat conduction increases in the fluid or

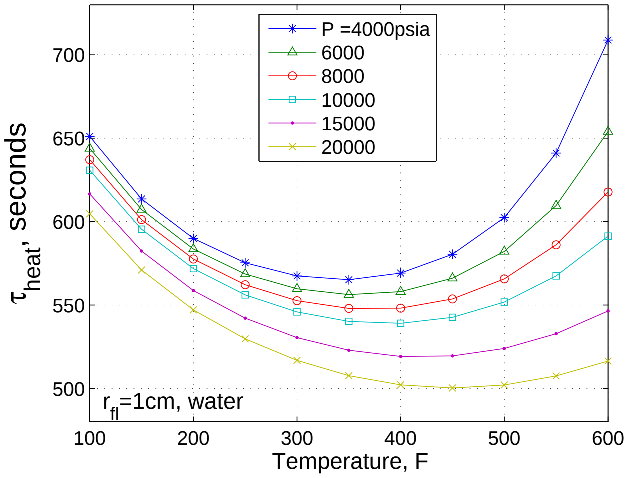

Figure 4.8: Variation of the characteristic heat conduction time, τ_{heat}, for water as a function of pressure and temperature.

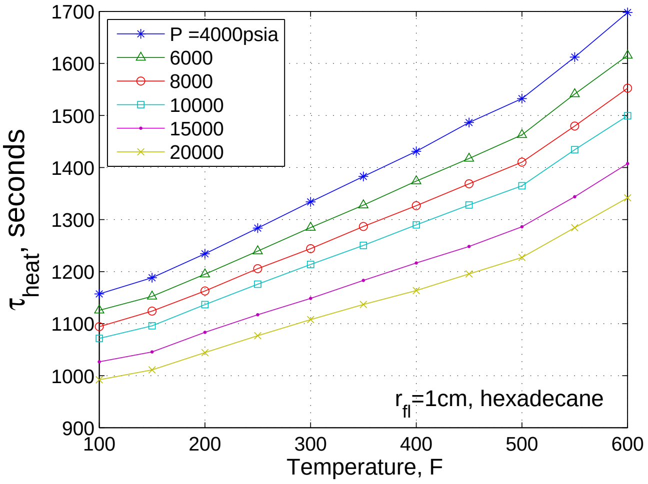

Figure 4.9: Variation of the characteristic heat conduction time, τ_{heat}, for oil (n-hexadecane) as a function of pressure and temperature.

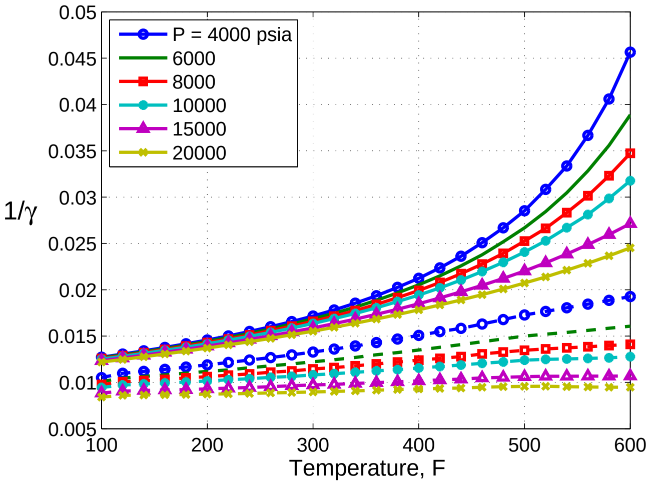

Figure 4.10: Values of the Parameter $1/\gamma$ for water (solid lines) and oil (dashed lines) as a function of pressure and temperature when the tool aspect ratio $\frac{V_{flowline}}{r_{probe}r_{fl}^2} = 100$ and $\frac{k}{\mu} = 1$md/cp.

the surrounding tool. When $1/\gamma_i = \infty$ or $1/\beta_i = \infty$, there is no heat storage or the thermal conductivity is infinite, that is, the temperature in the flowline or the tool is constant with respect to position, r. When both $1/\gamma_i$ and $1/\beta_i$ are equal to infinity ($\forall i$), the pretest occurs under isothermal conditions.

The ratio of parameters $\frac{K_\Theta c_{eff}}{\rho \hat{c}_P}$ has a relatively small variation with pressure and temperature. Typical probe radii and flowline radii values could easily vary by a factor of 5, while mobility values may vary by orders of magnitude. Therefore, $1/\gamma$ and $1/\beta$ are highly sensitive to both tool design and formation mobility.

In summary, the independent variables of the dimensionless problem are t_D and r_D. The dependent variables are P_D, Θ_{Di}, and Θ^*_{Di} and the dimensionless groups are X, Y, $1/\gamma_i$, $1/\beta_i$, σ, r_{eD}, $P_D(0)$, q_D and $\frac{r_{fli}}{r_{fl1}}$, for $i = 1, \ldots, N$.

The definitions of P_D and t_D presented in Equations 4.18 and 4.21 differ from those in the well and formation testing literature. To obtain the usual definitions of P_D and t_D the values given here should be multiplied by $1/X$ and $\frac{\tau_{tool}}{\tau_{fm}}$, respectively, where τ_{fm} is the formation diffusivity,

$$\tau_{fm} \equiv \frac{\phi c_t r_{probe}^2}{\frac{k}{\mu}}.$$

Though ϕc_t is not considered in this study for the computation of the flowline pressure (because the quasisteady-state approximation has been used), it is considered in the presentation of the results by including the curves representing the isothermal storage solution and the expected formation pressure signal according to the isothermal spherical flow solution.

The isothermal tool storage solution written in the new dimensionless variables is:

$$P_D = -X\left(1 - e^{-t_D}\right), \quad 0 < t_D \leq \frac{\Delta V}{q_\infty \tau_{tool}}, \tag{4.38}$$

and

$$P_D = P_D\left(t_D = \frac{\Delta V}{q_\infty \tau_t ool}\right) e^{-\Delta t_D}, \quad \frac{\Delta V}{q_\infty \tau_{tool}} < t_D < \infty, \tag{4.39}$$

where $\Delta t_D = t_D - \frac{\Delta V}{q_\infty \tau_{tool}}$ is the dimensionless time from the start of the buildup period. The pressure signal corresponding to the isothermal spherical flow in these dimensionless variables is:

$$P_D = m \times t_{Dsph}, \tag{4.40}$$

where,

$$m = \frac{X}{\pi^{3/2}}\sqrt{\frac{\tau_{fm}}{\tau_{tool}}} = \frac{X}{\pi^{3/2}}\sqrt{\frac{4\phi c_t r_{probe}^3}{\left(\kappa_\Theta + c_{tool}\right) V_{flowline}}}, \tag{4.41}$$

and

$$t_{Dsph} = \frac{1}{\sqrt{\Delta t_D}} - \frac{1}{\sqrt{t_D}}, \quad t_D > \frac{\Delta V}{q_\infty \tau_{tool}}. \tag{4.42}$$

4.4 Solution Procedure

The solution is obtained by applying the Laplace transform to the initial-boundary-value problem defined by Equations 4.23 to 4.32, then solving for the average temperature, pressure, and temperature distribution in each flowline component. Next, the mean radial temperature is calculated in each component, and the mass-average temperature is calculated over the entire flowline. The temperature distribution in each flowline component, the mass average flowline temperature, and the pressure at the end of drawdown are used as the initial conditions for the buildup calculation. Finally, the solution is numerically inverted to the time domain using the algorithm of Abate and Valko (2004) (Appendix G). Details on the solution for various cases and the numerical evaluation procedure are provided in Appendices D, E and F.

4.5 Results

The effects of the various dimensionless groups on the pressure signal are examined next. Without loss of generality a tool consisting of one flowline component ($N = 1$) is considered first. The parameter Y represents the impact of temperature effects on the pressure signal, $Y = 0$ implies that the flowline temperature remains constant. Physically, different values of Y represent cases with different reference pressure and temperature (P_{well} and Θ_{well}) or a different fluid in the wellbore. In reality, if P_{well} and Θ_{well} change, the parameters that contain thermodynamic properties of the fluid will also change, but they are considered constant in the first example. In all the results shown in Figures 4.11 to 4.15:

1. $P_D(0) = 0$, that is, no overbalance ($P_{well} = P_{sandface}$)

2. $r_{eD} = 1$, that is, infinite conductivity of the tool material ($\sigma = 0$) or zero heat storage in the tool, equivalent to $1/\beta = \infty$. When $r_{fl} = r_{tool}$, $1/\beta$ is irrelevant.

3. γX=-20, constant. This means that the tool, the pretest rate and volume, and other thermodynamic properties are being held constant, hence,

$$X \approx -\frac{V_{flowline} q_\infty (\kappa_S + c_{tool})}{4 r_{probe} \Delta V \frac{k}{\mu}} \approx \frac{-2 \times 10^{-4}}{\frac{k}{\mu}}$$

and

$$\frac{1}{\gamma} = \frac{K_{\Theta fluid} \left(\kappa_\Theta + c_{tool}\right) V_{flowline}}{4 \rho_{fluid} \hat{c}_{P fluid} r_{fl}^2 r_{probe} k/\mu} = \frac{10^{-5}}{k/\mu}$$

These parameters were chosen because they represent typical dimensions of formation testers, and because they are convenient to investigate the effect of Y over the range $10^{-4} \leq k/\mu \leq 10^{-2}$ darcy/cp, while keeping the pretest parameters (q_∞ and ΔV) constant. Typical values of tool dimensions are given in Table 4.1 and fluid properties are given in Appendix A. Figures A.2, A.3, and 4.6 could be used to obtain the value of Y at any pressure and temperature for WBM or OBM –rewriting Equation 4.33 as:

$$Y = -\frac{1}{1 + \frac{c_{tool}}{\kappa_\Theta}} \left(\frac{\kappa_S}{\kappa_\Theta} - 1 \right).$$

The cases presented next are for values of Y ranging from 0 (isothermal case) to 0.15.

	Minimum	Maximum
$V_{flowline}/r_{probe}$ (cm^2)	30	250
r_{fl} (cm)	0.25	2.0
c_{tool} (atm^{-1})	$4{\times}10^{-5}$	$8{\times}10^{-5}$

Table 4.1: Typical tool parameters.

Figures 4.11 and 4.12 show the effect of the parameter Y on $-P_D$ and $-\langle\Theta_D\rangle$. The results are shown in separate plots for different values of k/mu = (10^{-4},10^{-3},10^{-2}) darcy/cp. Except for the case when $k/\mu = 10^{-4}$ darcy/cp (0.1 md/cp), the effect of different values of Y on P_D cannot be appreciated when plotting the entire pretest data (Figure 4.11) because the ordinate scale, when converted to dimensional form, spans several thousand psi. The effects of temperature on the pressure signal are better appreciated on the late-time behavior of the buildup pressure data. Figure 4.12 indicates that for all mobility values the average temperature $-\langle\Theta_D\rangle$ increases beyond Θ_{well} for any value of $Y > 0$ at some time during buildup, although not obvious for $k/\mu = 10$ md/cp.

For the adiabatic case (not shown here), the fluid loses energy during expansion in the drawdown (the fluid does mechanical work on the pretest piston), and gains back the same amount of energy during recompression in the buildup (the formation fluid flowing into the tool does work on the original flowline fluid), provided there is no overbalance. Because there is heat conduction into the flowline during the drawdown, the flowline temperature variation is less than if the same pressure drop had occurred under adiabatic conditions. As the temperature rises during buildup, because of recompres-

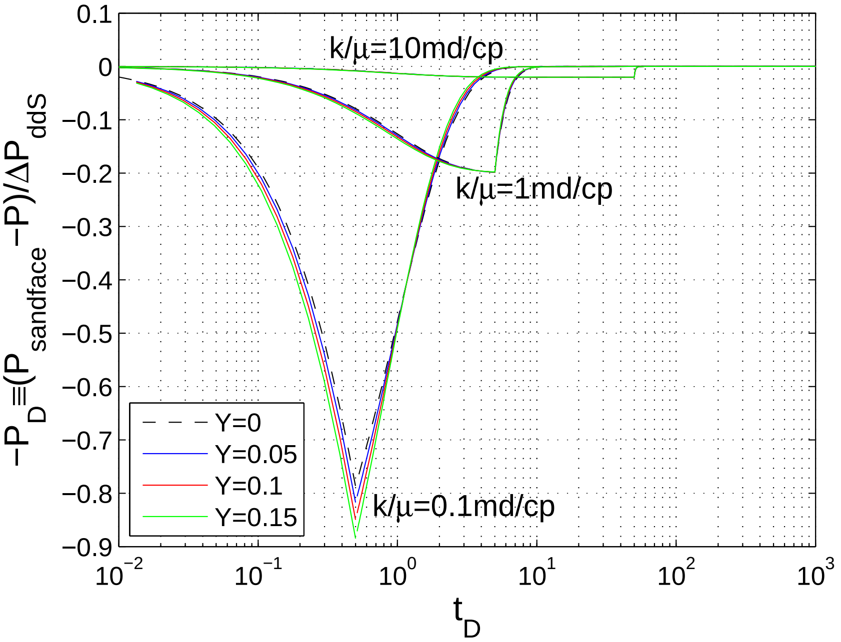

Figure 4.11: Effect of the parameter Y on the dimensionless pressure for different values of formation mobility. By definition, $\Delta P_{ddS} < 0$.

sion of the fluid, heat continues flowing into the flowline, at least during the early stages of buildup when $\Theta < \Theta_{well}$. The irreversible energy gained by the fluid due to conduction in drawdown and the beginning of buildup has to be transferred back to the wellbore; the only way this can be accomplished is if $\langle\Theta\rangle > \Theta_{well}$ during the latter period of buildup. This temperature behavior during buildup extends the duration of the storage effects in the pressure signal, as will be seen next.

The buildup equilibration plot ($\log(|P_D|)$ vs. $log(\Delta t_D)$, where $|P_D|$ is the absolute value of P_D) is more useful to emphasize the behavior of the pressure signal during the latter stages of buildup when P is equilibrating to $P_{sandface}$. These plots are shown for the three values of mobility in Figures

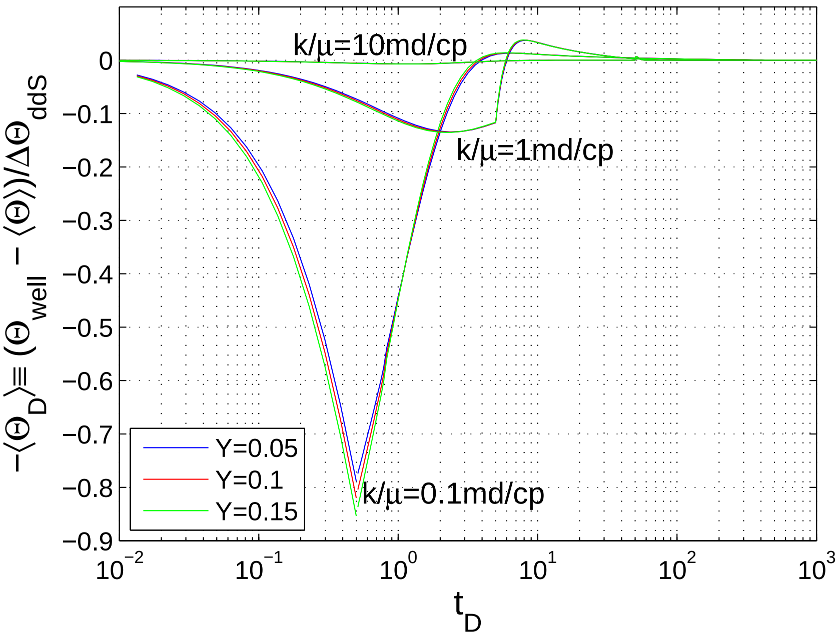

Figure 4.12: Effect of the parameter Y on the dimensionless temperature for different values of formation mobility. By definition, $\Delta\Theta_{ddS} < 0$.

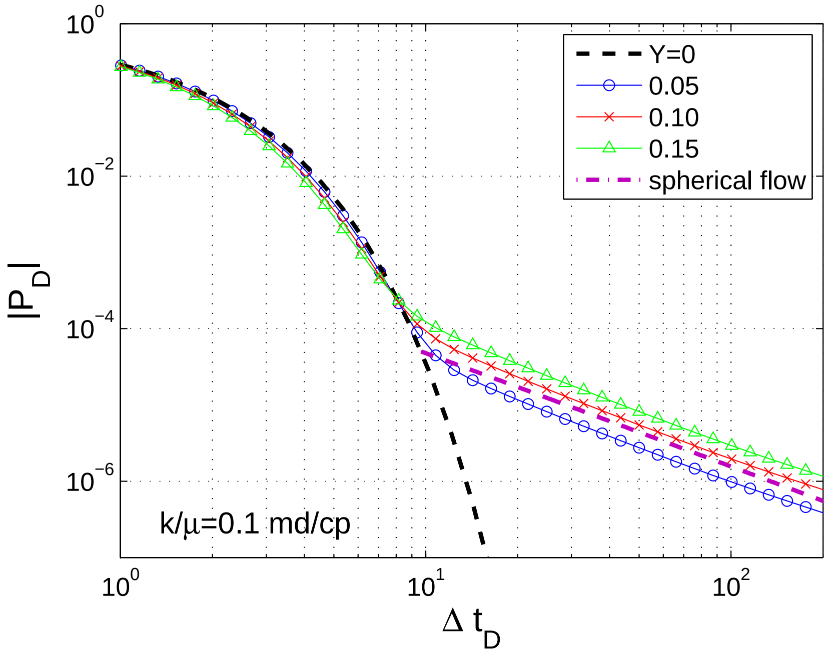

Figure 4.13: Effect of the parameter Y on the pressure behavior during buildup for formation mobility k/μ= 0.1 md/cp. The isothermal storage solution (Y = 0) and the spherical flow solution (dashed line) are plotted as reference.

4.13 to 4.15. The ordinate shows the difference between $P_{sandface}$ and P; this difference goes to zero as Δt_D increases. For example, for the three values of k/μ the early time behavior given by the isothermal storage solution (Y = 0), calculated with Equation 4.39, is shown by the dashed black curve with an exponential decay. The late-time buildup behavior (after the intersection with the isothermal storage solution) is given by the isothermal spherical flow solution calculated with Equation 4.40 ($m = 0.014X$), and is shown here by the dashed red curve.

As may be seen in Figures 4.13 – 4.15, the results indicate that, when temperature is included in the analysis, the storage portion of the pressure

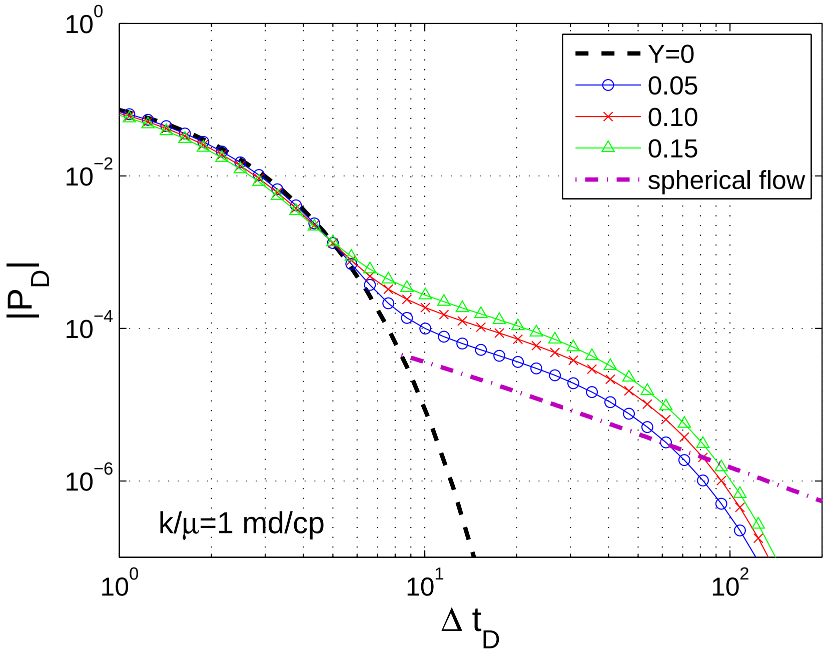

Figure 4.14: Effect of the parameter Y on the pressure behavior during buildup for formation mobility $\frac{k}{\mu} = 1$ md/cp.

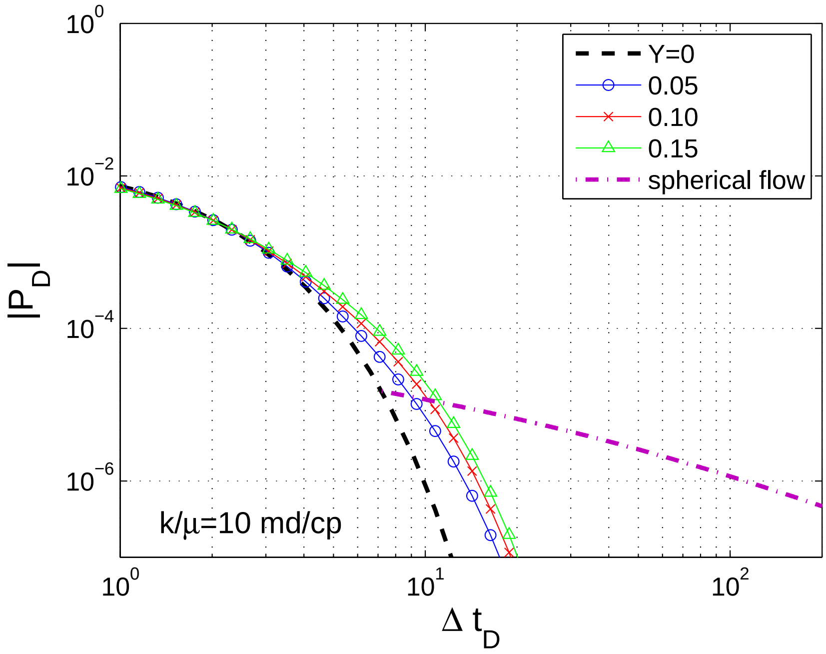

Figure 4.15: Effect of the parameter Y on the pressure behavior during buildup for formation mobility $\frac{k}{\mu} = 10$ md/cp.

buildup deviates from the exponential decay regulated by τ_{tool} and could persist for a much longer time depending on the values of the other parameters. This tendency increases as the value of Y increases. For the cases presented here, the longest duration of the thermal tool storage effects is seen when $k/\mu = 0.1$ md/cp. These results also indicate that the pressure signal may exhibit a similar behavior to the expected isothermal spherical flow, and thus could be mistaken as such.

The effect of the parameter $1/\gamma$, with $1/\beta = \infty$, on the temperature and pressure behavior is examined next. This parameter controls the rate at which the temperature in the flowline equilibrates to the wellbore temperature: when $0 < 1/\gamma < 1$, then $\tau_{heat}^{fluid} > \tau_{tool}$, and when $1 < 1/\gamma < \infty$, then $\tau_{heat}^{fluid} < \tau_{tool}$. It has been found, the results of many simulations, that the largest temperature effect on pressure occurs when $\tau_{heat}^{fluid} > \tau_{tool}$, or $0 < 1/\gamma < 1$. The variation of $1/\gamma$ could be regarded as either a change in k/μ or r_{fl}. In the following example the parameter X is kept constant, and therefore so is the mobility. For a given value of formation mobility, different values of $1/\gamma$ represent the effect of different tool geometries, with larger values of $1/\gamma$ corresponding to smaller values of r_{fl}. The flowline pressure during the entire pretest is shown in Figure 4.16, and the pressure equilibration during the buildup for different values of $1/\gamma$ is shown in Figure 4.17. The other parameters in the problem were kept constant and the values are shown in Table 4.2:

The flowline pressure has a barely noticeable variation when looking at the plot of the entire pretest (Figure 4.16) but the pressure equilibration plot (Figure 4.17)indicates a very different behavior during the latter stages of

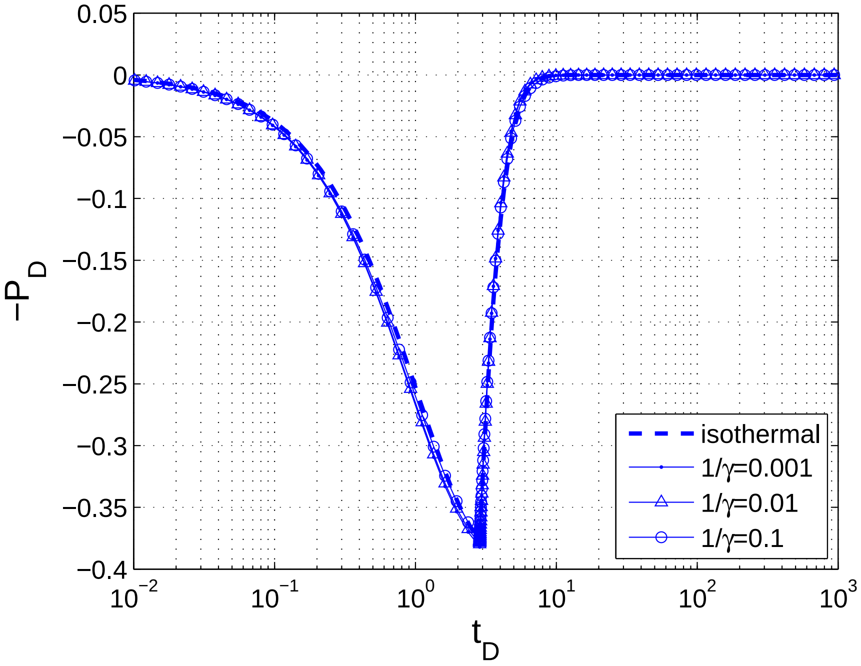

Figure 4.16: Dimensionless pressure vs. time for different values of $1/\gamma$. Other parameters are kept constant ($X = 0.4$; $Y = 0.1$; $P_D(0) = 0$; $r_{eD} = 1$).

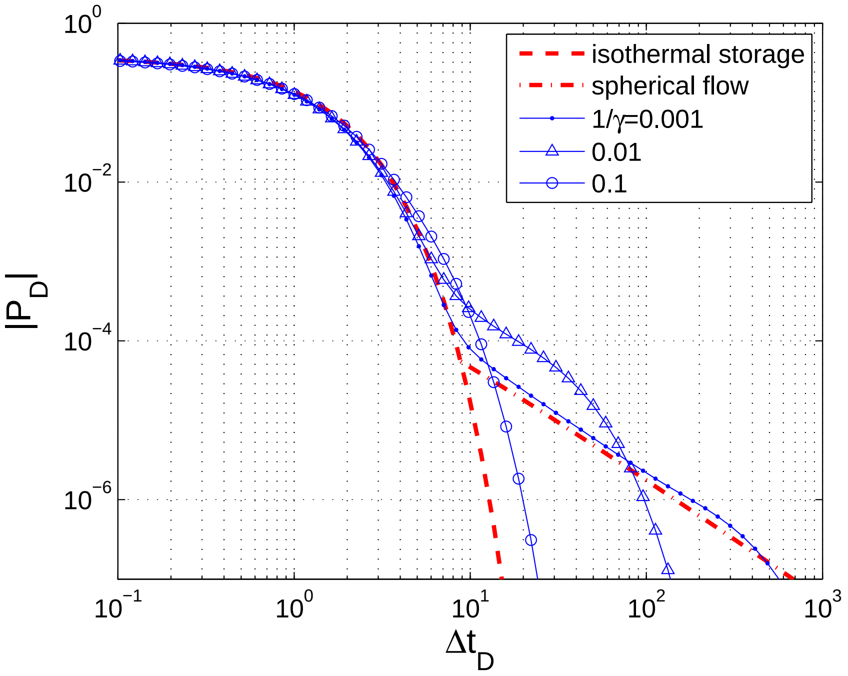

Figure 4.17: Pressure equilibration plot for different values of $1/\gamma$. Other parameters are kept constant ($X = 0.4$; $Y = 0.1$; $P_D(0) = 0$; $r_{eD} = 1$).

Parameter	Value
X	-0.4
Y	0.1
$P_D(0)$	0
r_{eD}	1
σ	0
$1/\beta$	∞

Table 4.2: Parameters for the study of the variation of $1/\gamma$.

buildup for each value of $1/\gamma$ considered here. Other properties kept constant, the pressure signal is less affected by temperature variations in the tool with the smallest flowline radius ($1/\gamma = 0.1$). As before, the expected isothermal spherical flow is plotted as a reference. These results indicate that tool designs with too large r_{fl} may mask the deep formation response (spherical flow) by lingering storage effects.

More insight on the behavior of the pressure signal could be obtained by examining the temperature behavior. The average temperature in the flowline during the entire pretest is shown in Figure 4.18 and the temperature distribution in the flowline at various times since the beginning of buildup ($\Delta t_D = 0$) and at later times (Δt_D=0.5, 2, 5, and 10 are shown in Figure 4.19. The average temperature in the flowline during the buildup (Figure 4.19(f)) is very different for each case. As explained before, in the buildup the temperature always exceeds the wellbore temperature and, after it reaches a maximum, it builds down to equilibrate with Θ_{well}.

For the cases presented here, the largest overshoot and the fastest equilibration of $\langle\Theta_D\rangle$ occur when $1/\gamma = 0$. After $\langle\Theta_D\rangle$ reaches a maximum value

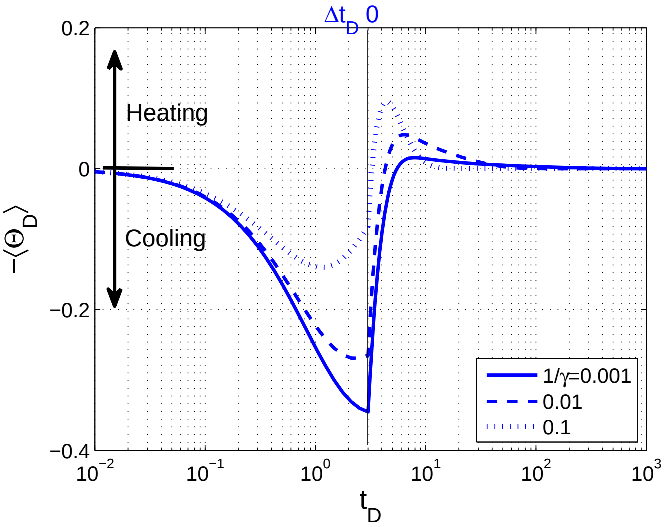

Figure 4.18: Average temperature in the flowline during the entire pretest. Other parameters are kept constant (X = 0.4; Y = 0.1; $P_D(0)$=0; $r_{eD} = 1$)

during buildup, heat must leave the flowline. This is supported by the negative temperature gradient at the flowline wall, $\left.\frac{d\Theta_D}{dr_D}\right|_{r_D=1} < 0$ for all cases at Δt_D=10 and for $1/\gamma \leq$0.1 at Δt_D=2. For Δt_D <10, in the cases when $1/\gamma \leq$ 0.01, the temperature in the center of the flowline is below Θ_{well} while the temperature near the wall is higher than Θ_{well}. The temperature continues increasing because the fluid is still being compressed to $P_{sandface}$, but at the same time there is heat conduction from the fluid near the wall towards the center of the flowline, and also to the wellbore. If $\frac{d\langle\Theta_D\rangle}{dt_D} > 0$, then there is a net increase of energy in the fluid. Eventually, heat will only flow towards the wellbore. The rate at which $\langle\Theta_D\rangle$ builds down to zero regulates the equilibration of P_D in the latter part of buildup (Figure 4.17).

The variations in the parameter X represent the nature of the drawdown; low values of X indicate that the drawdown will tend to reach steady

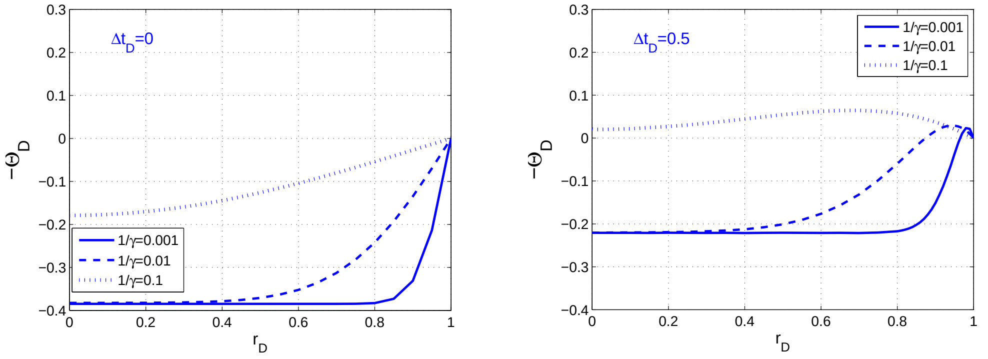

(a) $\Delta t_D = 0$ (b) $\Delta t_D = 0.5$

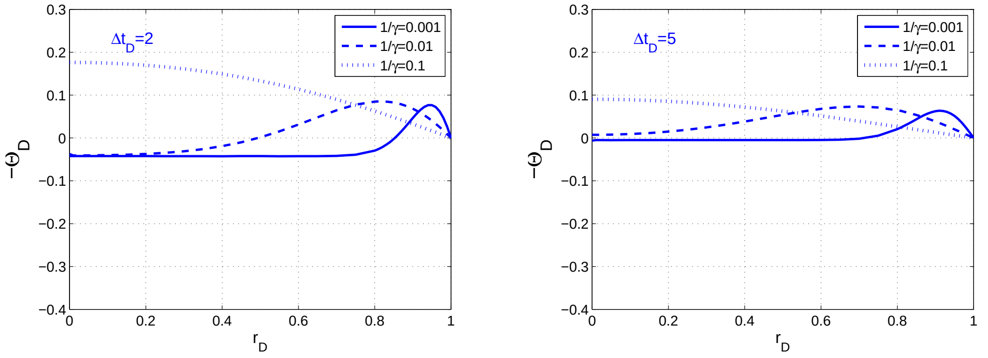

(c) $\Delta t_D = 2$ (d) $\Delta t_D = 5$

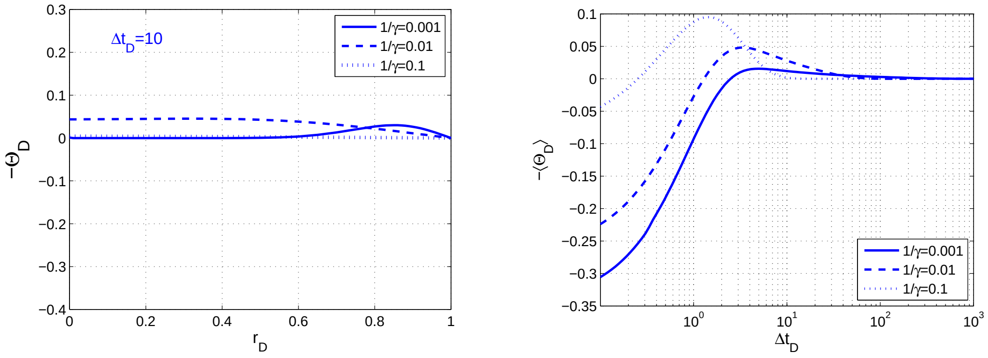

(e) $\Delta t_D = 10$ (f) $\langle \Theta_D \rangle$ during buildup

Figure 4.19: Effect of $1/\gamma$ on the temperature distribution in the flowline at various times during buildup. Other parameters are kept constant according to Table 4.1.

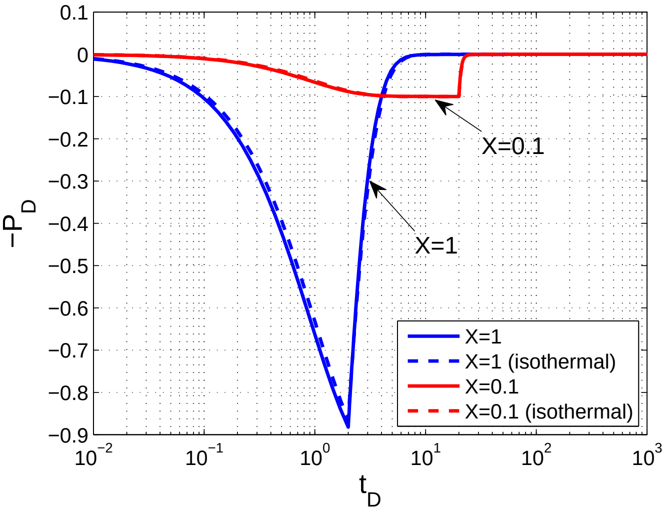

Figure 4.20: Effect of parameter X on the pressure. Other parameters are kept constant ($1/\gamma = 0.01$; $Y = 0.1$; $P_D(0)$=0; $r_{eD} = 1$)

state conditions. Figure 4.20 illustrates the effect of varying X by an order of magnitude. Other things kept constant, this would represent, for instance, the case of varying the pretest rate q. Larger values of X correspond to increasing values of q (refer to Equation 4.34). The pretest with $X = 0.1$ has reached steady state during the drawdown. Figure 4.21 shows the behavior of the flowline pressure during the buildup, and Figure 4.22 shows the average flowline temperature during the entire test. For the pretest that reached steady state ($X = 0.1$), the temperature started increasing during the drawdown and was closer to its initial value by the end of drawdown. The pressure increase during buildup makes the temperature move farther away from its initial value and then it must rely on conduction to equilibrate. The final result is that the time required to reach thermal equilibrium is very similar for the two pretest, in spite that for $X = 1$ the temperature variation was much larger.

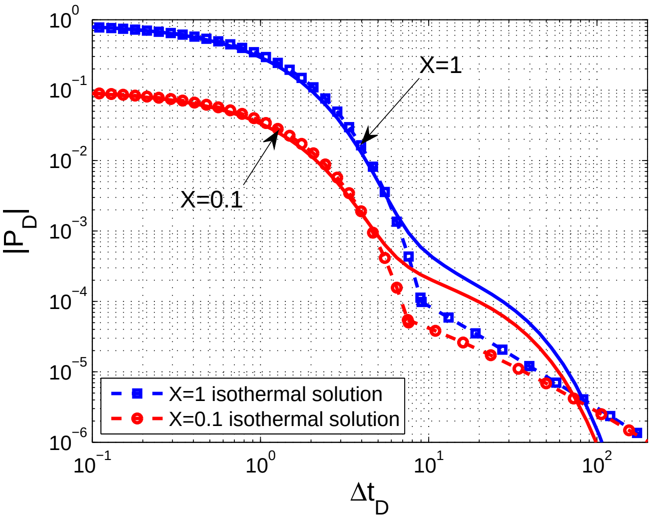

Figure 4.21: Effect of parameter X on the buildup. Other parameters are kept constant ($1/\gamma = 0.01$; $Y = 0.1$; $P_D(0)$=0; $r_{eD} = 1$)

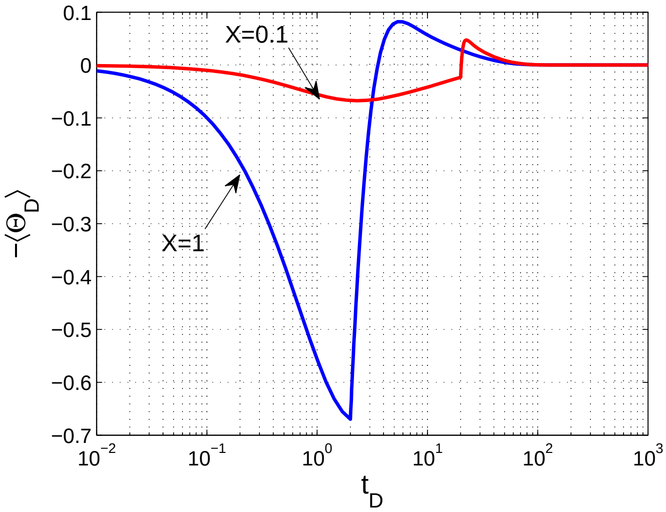

Figure 4.22: Effect of parameter X on the average temperature. Other parameters are kept constant ($1/\gamma = 0.01$; $Y = 0.1$; $P_D(0)$=0; $r_{eD} = 1$)

The consequences of overbalance are explored by varying the initial flowline pressure condition, $-P_D(0)$, which accounts for different sizes of the pressure overbalance, while keeping other parameters constant (X=-0.4; Y=0.1; $1/\gamma$=0.01; r_{eD}=1). The flowline pressure and average temperature for pretests with different size overbalance are shown in Figures 4.23 and 4.24. The initial flowline pressure for the first pretest after the tool is set against the formation is the static pressure of the drilling mud, which is larger than the sandface pressure, $-P_D(0) > 0$. Hence, the first part of the drawdown has to decompress the flowline from the wellbore pressure to the sandface pressure; during this time $P > P_{sandface}$ and there is no flow from the formation into the tool.

When there is overbalance, $-P_D(0) > 0$, the size of the fluid compression during buildup is less than its expansion during drawdown, therefore there is less of an increase in temperature because of compression. This implies that reestablishing thermal equilibrium must be achieved by heat conduction. As the value of $-P_D(0)$ increases, more energy needs to be supplied by conduction from the wellbore into the flowline during buildup. Heat conduction keeps increasing the flowline temperature even after $P \approx P_{sandface}$, causing the pressure in the flowline to also continue increasing. For sufficiently large values of $-P_D(0)$ the flowline pressure may buildup to a value higher than the sandface pressure, that is, the pressure overshoots and then must decrease to equilibrium. This is seen in Figure 4.24 that shows the detail of the buildup pressure (on a linear scale) for the cases without overbalance ($P_D(0) = 0$) and $-P_D(0) = 0.5$. For $-P_D(0) = 0.5$ the pressure reaches a maximum around $t_D = 11$. In the buildup equilibration plot (Figure 4.25) the pressure is in a logarithmic scale and the overshoots are represented by a downward shaped

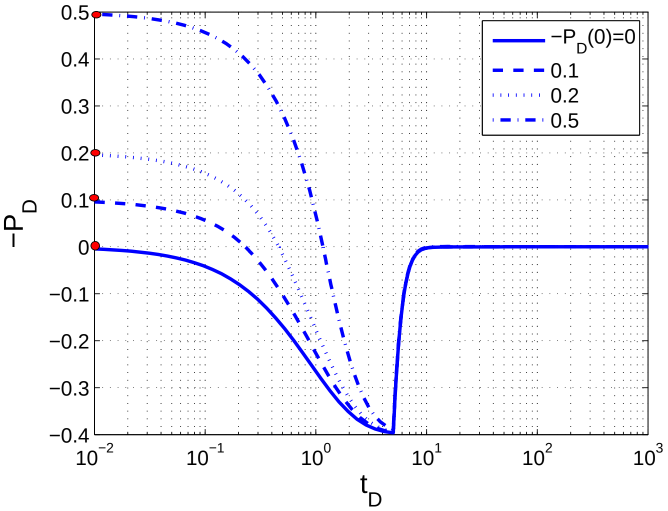

Figure 4.23: Effect of overbalance, $P_D(0)$, on P_D accounting for temperature variations. The case with zero overbalance ($P_{well} = P_{sandface}$) is represented by $P_D(0) = 0$. (For all cases X=-0.4; Y=0.1; $1/\gamma$=0.01; r_{eD}=1).

’spike’ in $\log |P_D|$; this indicates a change of sign in the value of $-P_D$ (seen here for $-P_D(0) = 0.2$ at Δt_D=9.5 and $-P_D(0)$=0.5 at Δt_D=6).

Figure 4.25 indicates that for all the cases, the flowline pressure, $|P_D|$, behaves similarly for $0 < \Delta t_D < 4$; during this period the pressure behavior is dominated by the recompression of the fluid. At Δt_D=4, the maximum value of $-\langle\Theta_D\rangle$ is reached for $-P_D(0)$=0 and $-P_D(0)$=0.1 (Figure 4.26). For the cases when $-P_D(0)$=0.2 and 0.5, $-\langle\Theta_D\rangle$ equilibrates to zero at a slower rate for $\Delta t_D > 4$. When $-P_D(0)$=0.2 the change of $\frac{d\langle\Theta_D\rangle}{dt_D}$ is abrupt and $-\langle\Theta_D\rangle$ appears to remain constant between $4 < \Delta t_D < 10$.

The temperature distribution within the flowline when $-P_D(0)$=0.2 and $\Delta t_D = 4$ is shown in Figure 4.27(d). This plot indicates that $\Theta < \Theta_{well}$ for $0 < r_D < 0.65$, and $\Theta > \Theta_{well}$ for $0.65 < r_D \leq 1$. This means that heat

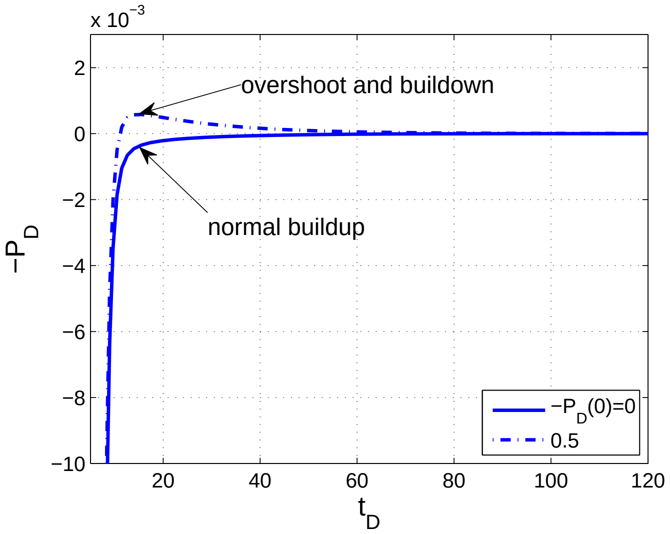

Figure 4.24: Detail of the flowline pressure during buildup for different sizes of pressure overbalance (same data as in Figure 4.23) showing a an overshoot and subsequent build down.

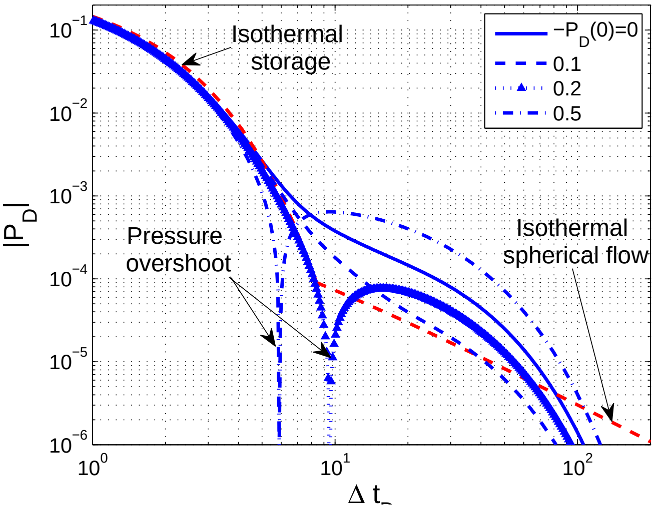

Figure 4.25: Flowline pressure equilibration during buildup for different sizes of pressure overbalance (The spherical flow solution shown in this plot corresponds to the case $P_D(0)$=0. The value of $|P_D|$ during spherical flow is less as overbalance increases. The downward spikes observed when $-P_D = 0.2$ and 0.5 indicate a pressure overshoot (P_D goes to zero and then changes sign).

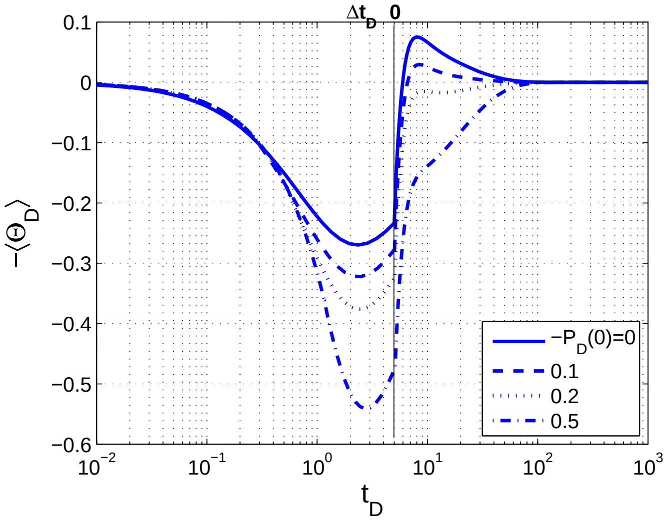

Figure 4.26: Mass-average flowline temperature during the pretest for different sizes of pressure overbalance $-P_D(0)$.

is flowing out of the flowline for a short period of time. However, at Δt_D=10 (Figure 4.27(e), $\Theta < \Theta_{well}$ for $0 < r_D \leq 1$, therefore, heat is flowing in from the wellbore. For $\Delta t_D \geq 10$, as $-\langle\Theta_D\rangle$ increases (Figure 4.26), the pressure overshoots and has to build down (Figure 4.25). The pressure overshoot is larger when $-P_D(0) = 0.5$ because $-\langle\Theta_D\rangle$ is always increasing during the buildup.

Example of Tool Performance

The performance of one particular (generic) formation tester is examined to illustrate the behavior of the pressure signal for a flowline with three components. The volumes and the radii of each component are specified in Table 4.3. There are several commercial formation testers with a wide variety of designs. The dimensions chosen here could represent, for instance, a conduit

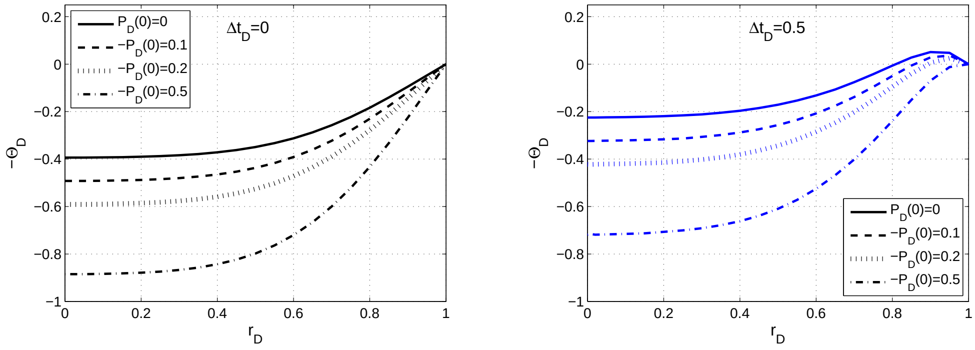

(a) $\Delta t_D = 0$ (b) $\Delta t_D = 0.5$

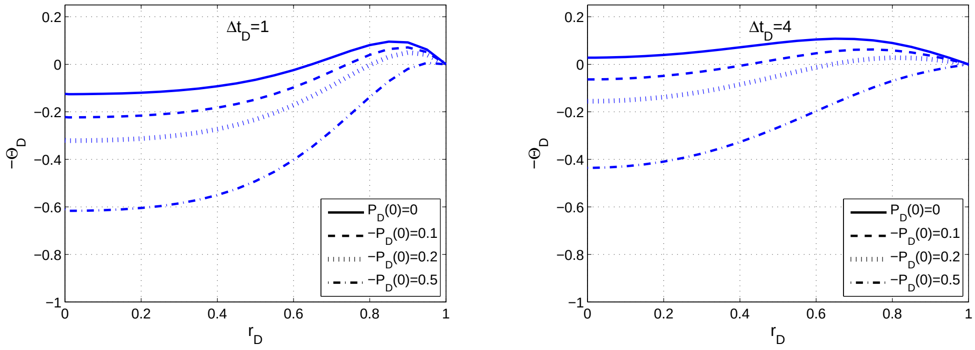

(c) $\Delta t_D = 1$ (d) $\Delta t_D = 4$

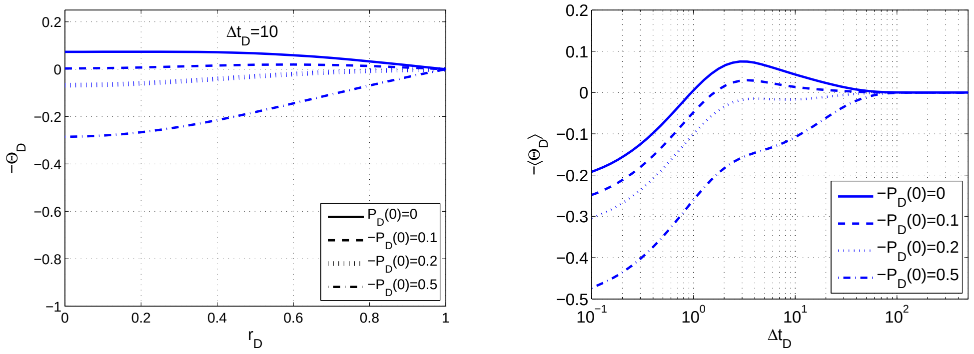

(e) $\Delta t_D = 10$ (f) $\langle \Theta_D \rangle$ during buildup

Figure 4.27: Effect of overbalance $P_D(0)$ on the temperature distribution in the flowline at various times during buildup. Other parameters are kept constant at the values listed in Table 4.2.

with r_{fl} =0.5 cm connecting the flowline components, and the volume contribution from a valve and the pressure gauge where r_{fl} >0.5 cm. For reference purposes, results are presented for a one component flowline with the same total volume, but constant r_{fl} =0.5 cm. In both cases r_{tool} =10 cm, and the tool material is stainless steel $\left(\frac{K_\Theta}{\rho\hat{c}_P}_{steel} = 4.5 \times 10^{-2}\text{cm}^2/s\right)$. The environmental parameters are: P_{well} =15 kpsi, Θ_{well} =300 F, and the fluid in the wellbore is OBM $\left(\frac{K_\Theta}{\rho\hat{c}_P}_{oil} = 8.5 \times 10^{-4}\text{cm}^2/s\right)$. The flowline pressure is computed for two pretests assuming that k/μ=1 md/cp and $P_{sandface}$ =10 kpsi. The dimensionless groups in this case are X =-1.0; Y=0.09; $(1/\gamma_1,\ 1/\gamma_2,\ 1/\gamma_3)$ = (0.01,0.009,0.004); $(1/\beta_1,1/\beta_2,1/\beta_3)$=(0.017,0.004,0.002); σ=0.01; $-P_D(0)$=0.75; Figures 4.28 and 4.29 show the entire pretest and the pressure equilibration during buildup for the two pretests (overbalance and no overbalance).

No. Comps	r_{fl1} cm	V_1 cm^3	r_{fl2} cm	V_2 cm^3	r_{fl3} cm	V_3 cm^3	$V_{flowline}$ cm^3	r_{tool} cm	r_{probe} cm
one	0.5	200					200	10	0.5
three	0.5	100	1.0	25	1.5	50	200	10	0.5

Table 4.3: Flowline dimensions for the tool example.

For the first pretest (Figure 4.28) $q_\infty = 1.0$ cm$^3/s$, $\Delta V = 10$ cm^3, and $P(0) - P_{sandface} = 5000$ psi (overbalance). At the end of drawdown ($t = 10$ s), the flowline pressure $P(t = \Delta V/q_\infty)$=8.6 kpsi (ΔP_{ddS}=-6.6 kpsi), and $\langle\Theta\rangle$ = 291 F for both tools. For the two flowline designs there is a large overshoot ($P - P_{sandface}$) of the flowline pressure during the buildup (about 21 psi for r_{fl} = 0.5 cm, and 17 psi for the three-component flowline), and because the pressure has to decrease to the sandface pressure the time to equilibrate is much longer

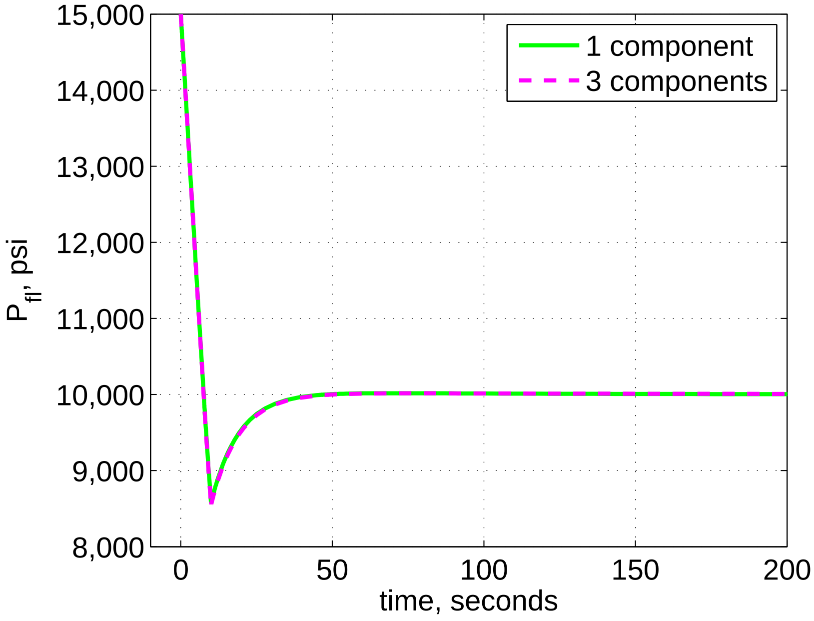

(a) pretest

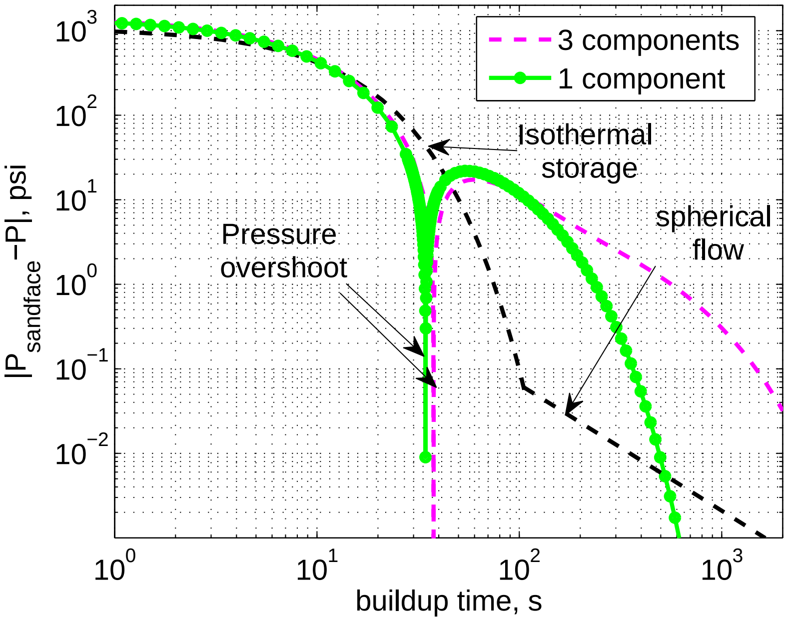

(b) buildup equilibration

Figure 4.28: Example contrasting the performance of a tool with three flowline components and a tool with uniform flowline radius (i.e., one flowline component) for a pretest with 5 kpsi overbalance.

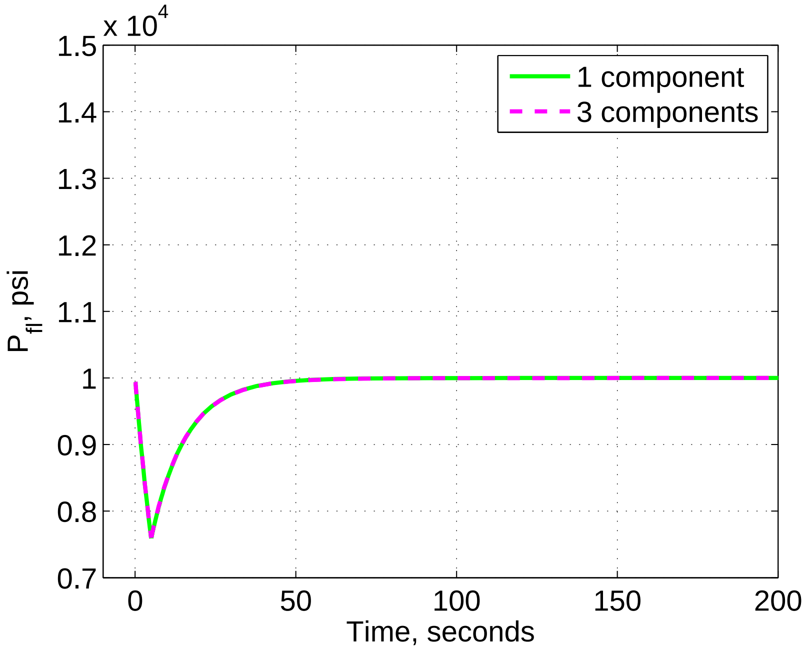

(a) pretest

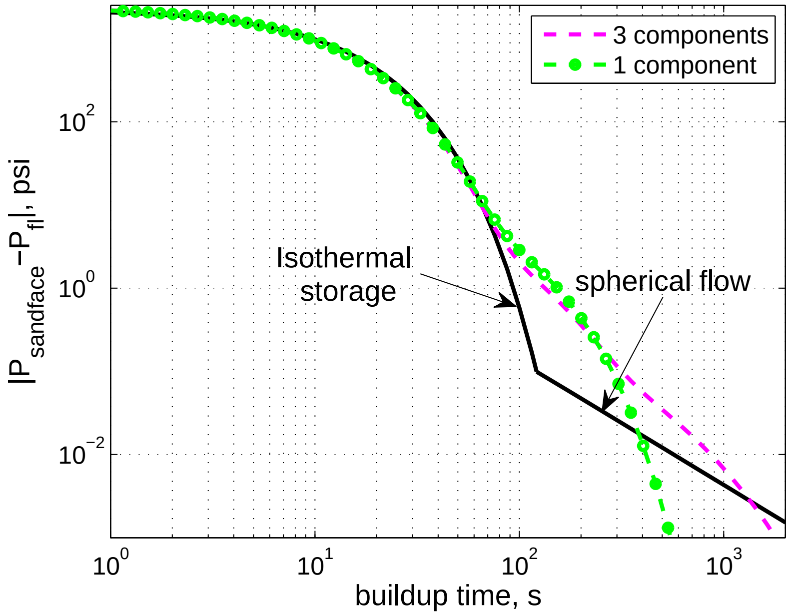

(b) buildup equilibration

Figure 4.29: Example contrasting the performance of a tool with three flowline components and a tool with uniform flowline radius (i.e., one flowline component) for a pretest without overbalance.

than might have been expected according to the isothermal theory (dashed curve). The expected formation response (spherical flow), computed assuming $c_t = 4.7 \times 10^{-7} psi^{-1}$, would be concealed by thermal effects in the tool.

The flowline pressure was computed for a second pretest (Figure 4.29) assuming $\Theta_i(r_D, 0) = \Theta_{well}$ for all components and $P(0) = 0$ (no overbalance). The flow rate in this case is $q_\infty = 1.0 cm^3/s$ and $\Delta V = 5$ cm^3 ($X =$ -2.2; $Y =$ 0.10; ($1/\gamma_1$, $1/\gamma_2$, $1/\gamma_3$)=(0.04, 0.01, 0.004); ($1/\beta_1$,$1/\beta_2$,$1/\beta_3$)=(0.015, 0.004, 0.002)). Even though the volume of the second pretest is one half the volume of the first pretest, the value of X for the second pretest is more than twice; the reason is that the reference pressure is different. At the end of drawdown $P(t = \Delta V/q_\infty)$=7.6 kpsi (ΔP_{ddS} =-3.0 kpsi) and $\langle\Theta\rangle = 295$ F for both tools. The buildup pressure equilibration plot is shown in Figure 4.29.

The results obtained for the two pretests shown here indicate that tool storage effects caused by temperature variations delay the equilibration of the flowline pressure. This delay is more pronounced for the tool with three flowline components because of the long time required for the temperature to equilibrate in the components with r_{fl} >0.5 cm. When a flowline has more than one component, each element affects the pressure signal at different times during the buildup. In this case, the flowline with three components behaves very similar to the tool with r_{fl}=0.5 cm during the time when this component has the strongest effect on the pressure signal (between 30 and 100 seconds for the first pretest and between 70 and 250 seconds for the second pretest).

A third pretest was evaluated for both tools assuming that at the end of drawdown, $t = \Delta V/q_\infty$, the tool did not establish hydraulic communication with the formation. This is equivalent to setting the tool on an impermeable formation or the case when the flowline pressure at $t = \Delta V/q_\infty$ is higher than the sandface pressure. The pretest parameters were $q_\infty = 1.0$ cm$^3/s$ and $\Delta V = 5$ cm^3 with P_{well} =15 kpsi, Θ_{well}=300 F, and OBM. The flowline pressure, P, calculated considering heat conduction is shown in Figure 4.30(a). At the end of drawdown, $P(t = \Delta V/q_\infty) = 11.5$ kpsi; a similar value could be estimated using Equation 4.1 and Figure 4.6, that is, assuming adiabatic conditions. After the drawdown the pressure builds up because the flowline fluid temperature increases to equilibrate with the wellbore; hence, the rate of pressure increase, dP/dt, is governed by the rate of temperature buildup. The pressure difference, $\Delta P = P - P(t = \Delta V/q_\infty)$, and the time derivative of the pressure during buildup is shown in Figure 4.30(b) for the two flowline designs.

The computations with heat conduction indicate that, after 600 seconds, ΔP =246 psi for the one-component tool, and 253 psi for the three-component tool. An estimated value of the pressure increase during the false buildup ΔP_{bu}=300 psi is obtained using Equation 4.5 and Fig. 4.6 with c_{tool}/κ_Θ =0.5. The value of ΔP_{bu} is larger because heat conduction is not considered. The actual pressure increase after a dry drawdown, ΔP, could be less depending on the duration of the drawdown, $\Delta V/q_\infty$, because of flow of heat into the flowline during the drawdown.

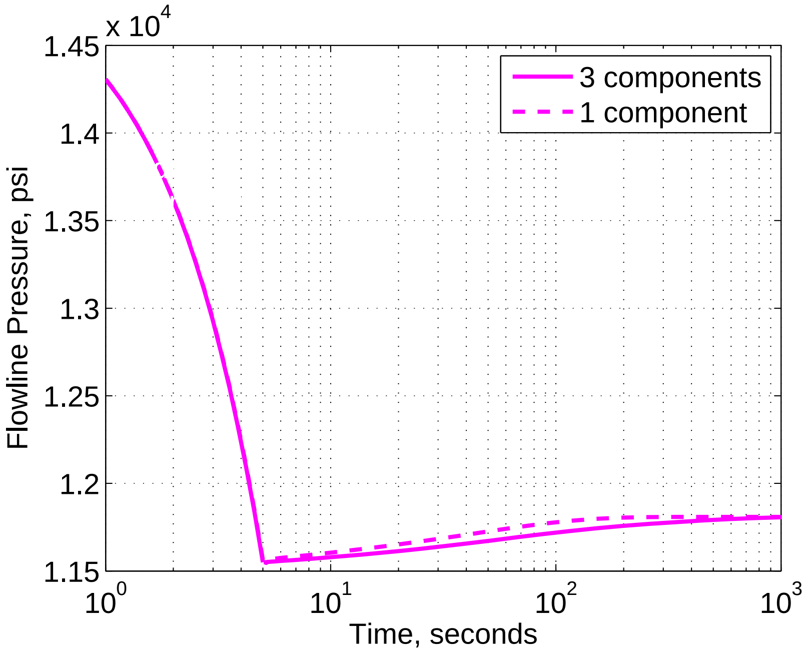

(a) pretest

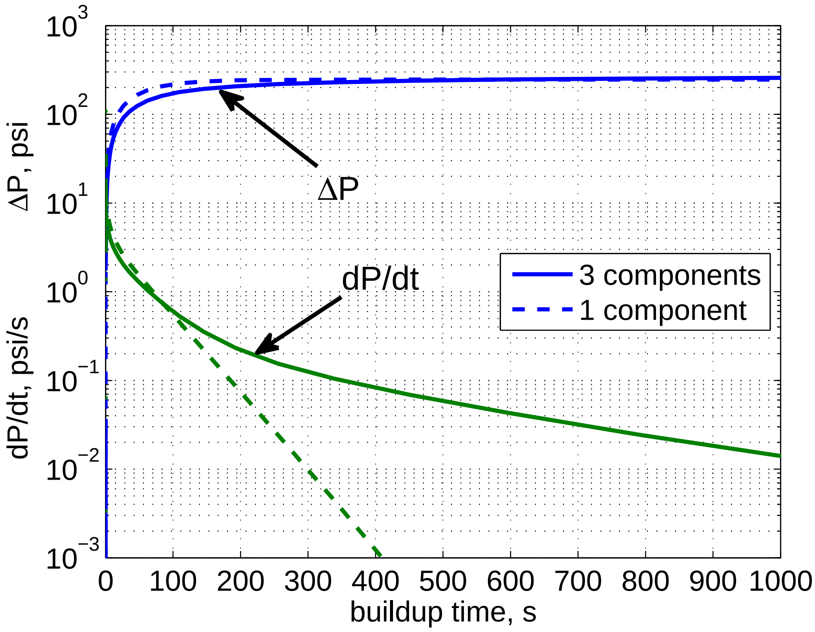

(b) buildup equilibration

Figure 4.30: Flowline pressure difference, $\Delta P = P - P(t = \Delta V/q_\infty)$, and pressure derivative during a "false buildup" following a dry drawdown.

4.6 Discussion

In the analysis of pretest data, it is possible to obtain two values of formation mobility. The mobility obtained using drawdown and buildup data, that is, the entire pressure signal, is well known to reflect the properties of the formation in front of the probe orifice, near the wellbore. The results presented here indicate that temperature variations have a small effect on the pressure, relative to the total pressure change, during drawdown and early part of buildup, where the largest pressure changes occur; therefore, temperature variations have a small impact on the computation of mobility with this method.

A second mobility that could be obtained from a pretest stems from the analysis of the pressure signal during the latter stages of buildup, that is, spherical or radial flow. The results presented here indicate that equilibration of the flowline fluid temperature could extend tool storage effects to the late part of buildup. Furthermore, these storage effects could exhibit a behavior similar to that expected from the formation during the spherical flow period. Thus, flowline thermal storage effects could either completely dominate or interfere with pressure signal regulated by reservoir compressibility (spherical flow). If thermal storage dominates the late buildup pressure signal, mobility computed using the isothermal spherical flow equation does not have a physical meaning. This ‘false’ buildup mobility tends to have a smaller value than drawdown mobility. To increase the pressure signal associated with spherical flow, it would be necessary to increase the pretest volume, and, as the formation mobility increases, it would be necessary to increase the pretest rate

(Betancourt et al., 2010). The effects of temperature variations when ΔV is not small with respect to $V_{flowline}$ will be discussed in the next chapter.

Formation tester performance could vary substantially depending on environmental conditions: type of drilling fluid in the wellbore, wellbore temperature and pressure overbalance. For both oil and water, the temperature change in the flowline fluid during the pretest increases as the wellbore temperature increases. The effects of temperature on the pressure signal tend to be more pronounced when the fluid in the wellbore is an oil-based mud, the fluid most commonly used in high temperature wells, because of the larger compressibility and longer time required to reach thermal equilibrium compared to water-based mud.

Inclusion of temperature variations in the analysis of pretests has provided an explanation of the possible cause of the pressure overshoot during the buildup based on thermodynamic principles. According to the analysis presented here, the cause of the pressure overshoots, and subsequent decrease to the sandface pressure, is the natural cooling of the flowline relative to the wellbore. This cooling is more pronounced in cases of larger pressure overbalance (wellbore pressure minus sandface pressure). This is consistent with the observation that pressure overshoots occur mostly in the first pretest after the tool is set against the formation. Though other factors could contribute to an overshoot in pressure, for instance mechanical effects in the tool, they would tend to exacerbate the situation. On the other hand, the pretest parameters, q and ΔV, could be selected to minimize temperature effects resulting in a faster pressure equilibration.

Analysis of temperature variations has also provided a thermodynamic explanation for the pressure increase after a drawdown that has not established hydraulic communication between the tool and the formation, that is, a dry drawdown. The dynamics of the pressure increase during these false buildups are regulated by the rate of thermal equilibration in the flowline, which is in turn governed by the specifics of the flowline design. This analysis could be helpful to identify false buildups, avoid a misinterpretation of the flowline pressure signal, and optimize the tool operation (reduce the time spent at a station).

The effect of temperature changes on pressure response as a function of mobility was addressed Figures 4.13 4.15. These plots combine the effects of temperature (dimensionless parameter Y) and mobility (dimensionless parameter $1/\gamma$) on the pressure behavior during buildup. There, you could also see a justification for that statement. For instance, in Figure 4.13 the solution with temperature effects has a resemblance to the expected formation response. This happens because the rate of thermal equilibration controls the pressure in the tool. If the tool effect (thermal storage) has a larger magnitude than the formation signal (spherical flow), the buildup is dominated by temperature effects. Furthermore, mistaking the late-time storage effects by a formation response the interpretation of spherical mobility could be entirely wrong.

In Figure 4.17 the temperature is fixed and the effect of the parameter $1/\gamma$ (mobility) on the buildup pressure is analyzed. The results in this figure were obtained by fixing the pretest parameters (rate and volume) and the tool design. However, conclusions extracted from only this plot must be treated carefully. For instance, it could be wrong to conclude that if the formation mobility is 10 md/cp the temperature has no effect, because there could be other tool designs, other pretest parameters, and other wellbore conditions for which temperature could be a factor in the interpretation. For instance, for the same mobility, if a pretest is designed to maximize the formation signal with the small probe radius tool (an actual tool) in an OBM environment at 200 F then, temperature may be a problem as will be seen in the next chapter (Figure 5.7). Ultimately, it all depends on the relative sizes of the two characteristic time scales of the problem (heat conduction and compression). Since actual tool designs are complex, it is not trivial to capture the heat conduction time scale of a given tool. This was the motivation for doing a dimensionless analysis.

Flow and shut in periods affect the thermal behavior of the system, and this has been taken into account in this analysis. For the shut in period, the initial temperature profile is obtained from the conditions at the end of the preceding drawdown. Pretests considered here consist of a sequence of one drawdown and one buildup. Typically, the buildup is sufficiently long and is expected that thermal equilibrium is practically reached at the end of buildup. When modeling more than one pretest in one station.

A question often arises on using the temperature measurement in the flowline to correct the pressure response. In the case of Schlumbergers MDT (Modular Dynamic Formation Tester) the temperature is measured at least at two points in the flowline. The issue with measuring temperature is that, because of heat conduction, local variations of temperature are expected, the consequence of the temperature equilibrating at different rates in different flowline components, and also within a component. So far, the measured temperature has been of more qualitative than quantitative value, but this could be explored further with controlled experiments.

Chapter 5

Examples of Pressure Computations Accounting for Temperature Variations

Thus far two aspects of formation tester pretests have been considered: selection of pretest parameters that maximize the formation signal, that is, spherical flow, for a given tool under isothermal conditions, and effects of temperature variations on the buildup pressure signal. This chapter examines the effect of temperature variations on pretests that are optimized to obtain a high formation signal. The performance of the flowline storage solution, accounting for variable temperature, is compared against actual measurements acquired in the field. Finally, other factors that may affect the interpretation of flowline pressure measurements are discussed.

5.1 Effect of Thermal Transients on Pretests that Maximize the Formation Signal

Depending on the formation mobility, some of the pretests that maximize the formation signal may require large drawdown volumes. The isothermal storage solution was modified in Chapter 3 to account for variable flowline volume. However, in the analysis of temperature transients during the pretest the flowline volume was assumed constant. Accounting for volume and temperature variations will make the equations more complicated. To investigate if this is necessary, the error introduced by assuming constant flowline volume in the isothermal storage solution for several values of mobility is quantified. Tools considered here are the *small probe radius* and the *large probe radius* defined in Chapter 3, with tool and wellbore parameters listed in Table 5.1.

$V_{flowline}$, cm^3	75
r_{fl}, cm	0.25,1.25,0.75
V_i, cm^3	40.0;15.0;30.0
r_{probe}, cm	0.55 (small radius probe); 2.86 (large radius probe)
c_{tool}, atm^{-1}	4.1×10^{-5}
$P_{wellbore}$, atm (psia)	680 (10,000)
$\Theta_{wellbore}$, K (F)	366 (200)

Table 5.1: Tool and wellbore parameters used for all the cases presented in Chapter 5.

5.1.1 Formation Mobility 0.01 md/cp

The first case considered is the pretest that maximizes the pressure signal in a 0.01 md/cp formation. For the *large probe radius* tool, this was achieved with a drawdown flowrate of 0.038 cm^3/s and a pretest volume of 40 cm^3; this represents a 53% flowline volume increase. The effect of variation in the flowline volume is shown in Figure 5.1, where the pretest is computed assuming constant and variable flowline volume. The largest difference between the two solutions is seen at the beginning of buildup (Figure 5.1(b)), and is in the order of $6{\times}10^{-4}$ psi. This error is small compared to the magnitude of the pressure; therefore, it will be assumed that this will also be the case when the temperature varies during the pretest.

Pressure for this pretest is computed next taking into account tempera-

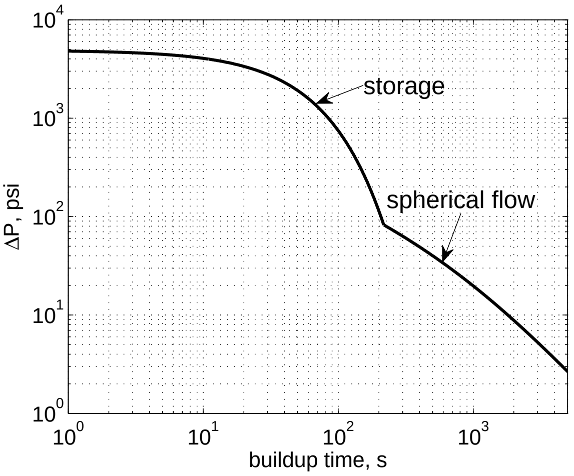

(a) Buildup pressure equilibration under isothermal conditions. Results are shown for two cases: variable and constant flowline volume, no distinction can be made at this scale

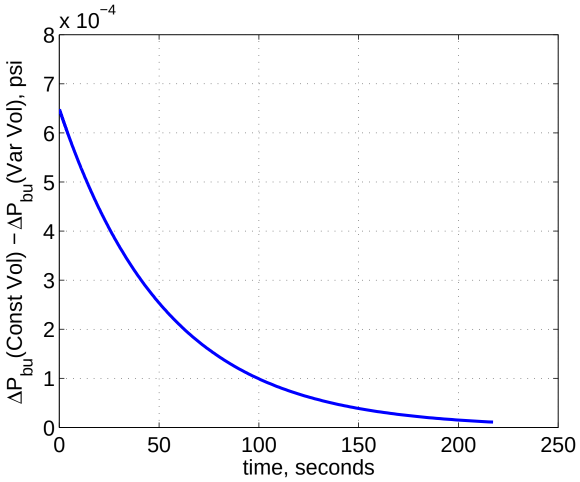

(b) Difference in buildup pressure equilibration during storage dominated period, variable vs. constant flowline volume.

Figure 5.1: Error in the buildup computation introduced by assuming constant flowline volume for the pretest (q = 0.038 cm^3/s, ΔV = 40 cm^3) that maximizes the spherical flow signal for the *large probe radius* tool in a 0.01 md/cp formation. The flowline temperature is kept constant.

ture variations. The pressure equilibration during buildup computed assuming constant flowline volume is shown in Figure 5.2; the pressure was computed for the cases when the fluid in the well is water-based mud (blue curves) and oil-based mud (green curves). The dashed lines represent the constant temperature case. For water-based mud the temperature effects occur at a later time, but by then the formation signal dominates the pressure measurement.

When the fluid is oil-based mud, the storage effects have a longer duration, and larger deviation from the isothermal case. Nevertheless, the results indicate that the formation signal (spherical flow) will also have larger magnitude than storage, and will dominate the late-buildup pressure. For this mobility value, results are shown only for the *large probe radius* tool because it represented the most suitable alternative for this mobility according to the results from Chapter 3. The dimensionless parameters are listed in Table 5.2.

	water-based mud	oil-based mud
X	-0.060	-0.080
Y	0.046	0.095
γ	0.66,16.61,5.98	0.94,23.52,8.47
β	0.013,5.3e-04,0.0015	0.0095,3.8e-04,0.001
ΔP_{ddS}	-5510 atm	-4145 atm
$\Delta \Theta_{ddS}$	-32 K	-63 K

Table 5.2: Parameters for the 0.01 md/cp case with *large probe radius* tool.

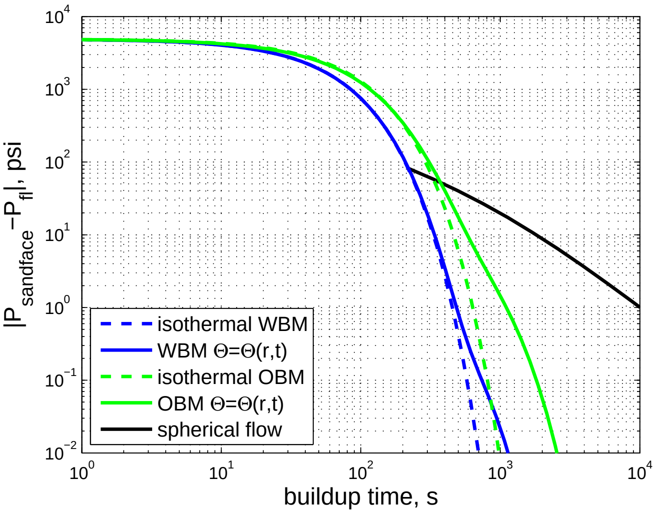

Figure 5.2: Pressure equilibration plot accounting for different fluids in the flowline (water-based mud (WBM) and oil-based mud (OBM)) and temperature variations for the pretest that maximizes the formation signal in a 0.01 md/cp formation (q = 0.038 cm^3/s, ΔV = 40 cm^3) with the *large probe radius* tool. Θ_{well} = 366 K (200 F).

5.1.2 Formation Mobility 0.1 md/cp

The pretest that maximizes the formation signal for this mobility also requires a pretest volume of 40 cm^3, that is, a 53% increase of the flowline volume (q = 0.38 cm^3/s). Pretest computations, under isothermal conditions, are compared in figure 5.3 for both the constant and variable flowline volume cases. The maximum error, observed at the beginning of the buildup (Figure 5.3(a)), is in the order of 10^{-3} psi, much larger than for the previous case (k/μ = 0.01 md/cp). Yet, by 14 seconds from the beginning of buildup the difference decreases by an order of magnitude. Since the main interest is on assessing the effects of temperature on the late-time buildup pressure, the error introduced by a assuming constant flowline volume will be neglected.

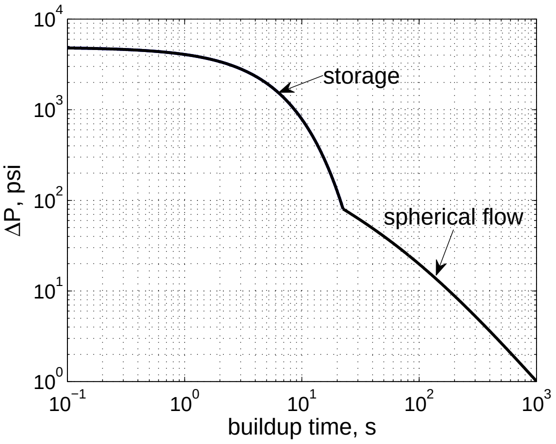

(a) Buildup pressure equilibration - isothermal conditions. Variable vs. constant flowline volume

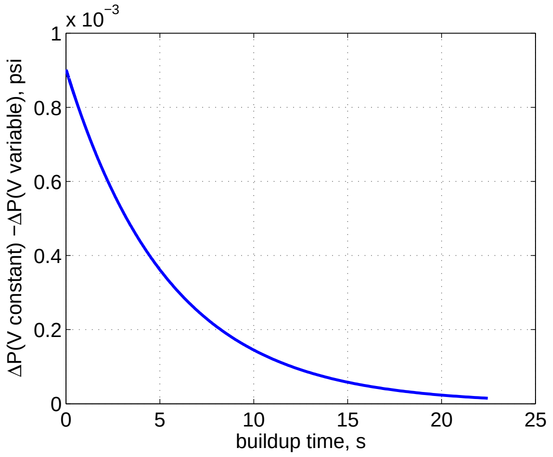

(b) Difference in buildup pressure equilibration during storage dominated period Variable vs. constant flowline volume

Figure 5.3: Error in the buildup computation introduced by assuming constant flowline volume for the pretest (q = 0.38 cm^3/s, ΔV = 40 cm^3) that maximizes the spherical flow signal for the *large probe radius* tool in a 0.1 md/cp formation. The flowline temperature is kept constant.

For this mobility value a larger separation of the isothermal and varying temperature solutions is observed for both water-based mud and oil-based mud (Figure 5.4). In Figure 5.4(a) the same pretest is performed with the *large probe radius* tool when the two types of drilling fluid, and in Figure 5.4(b) the pretest that maximizes the formation response is performed with the *small probe radius* tool (q = 0.08 cm^3/s, ΔV=40 cm^3). Thermal effects have a longer duration for the *small probe radius* tool (more pronounced for oil-based mud) and the formation signal has a lower magnitude; hence, the advantage of using the *large probe radius* tool is that the temperature effects may have less interference with the detection of a formation signal. The dimensionless parameters of the temperature calculations are shown for both tools in Tables 5.3 and 5.4.

	water-based mud	oil-based mud
X	-0.060	-0.080
Y	0.046	0.095
ΔP_{ddS}	-5510 atm	-4145 atm
$\Delta\Theta_{ddS}$	-32 K	-63 K
γ	6.64,166.1,59.8	9.40,235.2,84.7
β	0.13,5.3e-4,0.015	0.095,3.8e-03,0.01

Table 5.3: Parameters for the 0.1 md/cp case - *large probe radius* tool

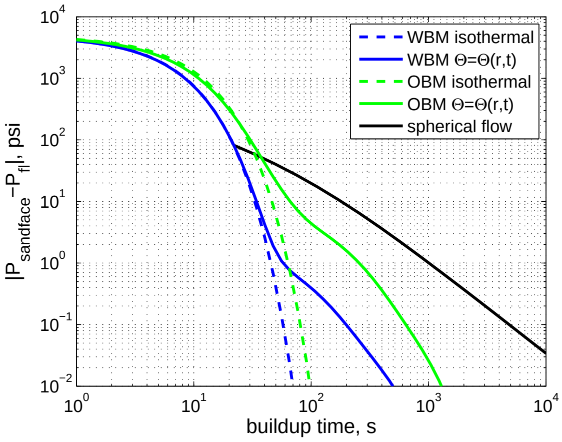

(a) Buildup pressure equilibration with variable temperature (constant flowline volume) water-based mud vs. oil-based mud - *large probe radius* tool

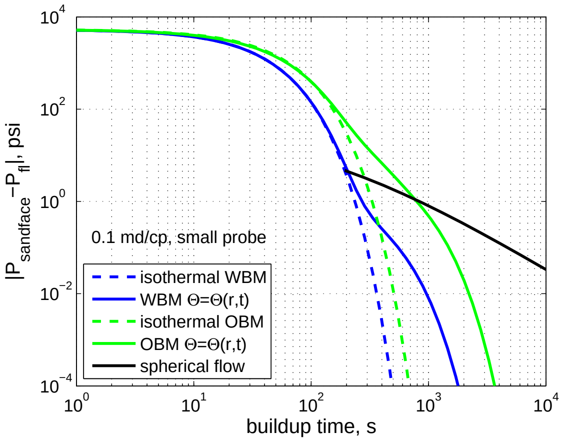

(b) Buildup pressure equilibration with variable temperature (constant flowline volume) water-based mud vs. oil-based mud - *small probe radius* tool

Figure 5.4: Flowline storage effects for the pretests that maximizes the spherical flow signal in a 0.1 md/cp formation. For the *large probe radius* tool (q = 0.38 cm^3/s, ΔV = 40 cm^3) the formation signal (spherical flow) is less affected by the thermal equilibration of the flowline than for the *small probe radius* tool (q = 0.08cm^3/s, ΔV=40 cm^3).

	water-based mud	oil-based mud
X	-0.065	-0.087
Y	0.046	0.095
ΔP_{ddS}	-5520 atm	-4145 atm
$\Delta \Theta_{ddS}$	-32 K	-63 K
γ	1.29,32.3,11.6	1.83,45.7,16.5
β	0.026,1.0e-3,2.9e-3	0.019,7.4e-04,2.1e-3

Table 5.4: Parameters for the 0.1 md/cp case - *small probe radius* tool

5.1.3 Formation Mobility 1 md/cp

Constant and variable flowline volume isothermal solutions are shown in Figure 5.5 for the pretest that maximizes the formation signal with the *large probe radius* tool. It is observed that the difference between the two solutions decreases substantially (10^{-10} psi), with respect to what was observed at 0.1 md/cp, for the same volume increase. The computations including temperature variations are shown in Figure 5.6(a) for the *large probe radius* tool and in Figure 5.6(b) for the *small probe radius* tool. The difference with respect to the isothermal cases has increased in comparison with the results for lower mobility values. For a pretest performed with the *small probe radius* tool in oil-based mud it may be seen that temperature effects would extend significantly the duration of the storage period and mask almost all the formation response (above 0.01 psi).

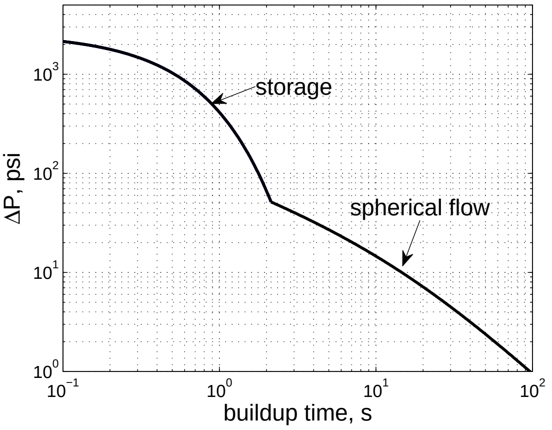

(a) Buildup pressure equilibration - isothermal conditions. Variable vs constant flowline volume

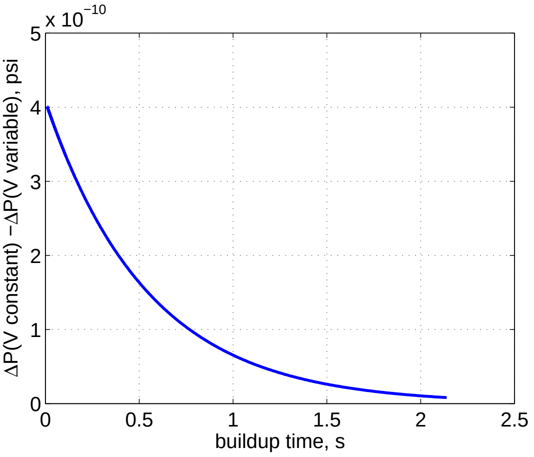

(b) Difference in buildup pressure equilibration during storage dominated period Variable vs constant flowline volume

Figure 5.5: Error in the buildup computation introduced by assuming constant flowline volume for the pretest (q = 2 cm^3/s, ΔV = 40 cm^3) that maximizes the spherical flow signal for the *large probe radius* tool in a 1 md/cp formation. The flowline temperature is kept constant.

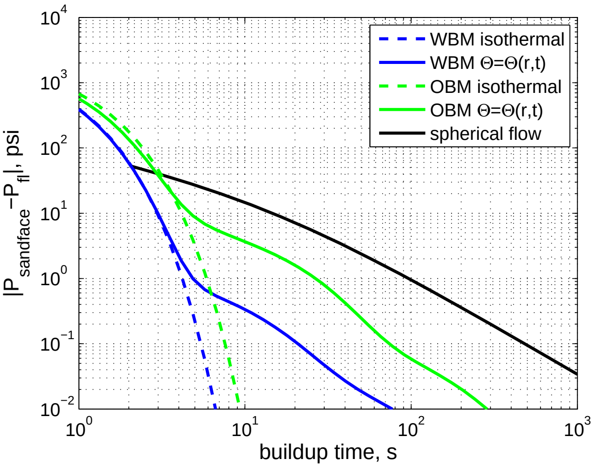

(a) *large probe radius* tool - water-based mud and oil-based mud q = 2.0 cm^3/s ΔV = 40 cm^3

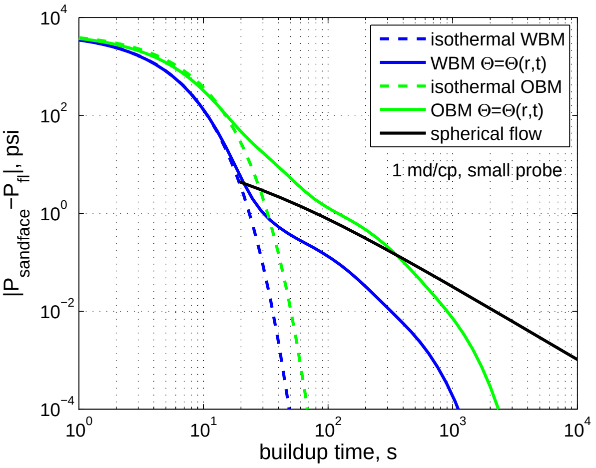

(b) *small probe radius* tool - water-based mud and oil-based mud q = 0.78 cm^3/s ΔV = 40 cm^3

Figure 5.6: Flowline storage effects for the pretests that maximizes the spherical flow signal in a 1 md/cp formation. For the *large probe radius* tool (q = 2.0 cm^3/s, ΔV = 40 cm^3) the formation signal (spherical flow) is less affected by the thermal equilibration of the flowline than for the *small probe radius* tool (q = 0.78 cm^3/s, ΔV = 40 cm^3).

	water-based mud	oil-based mud
X	-0.032	-0.042
Y	0.046	0.094
ΔP_{ddS}	-5520 atm	-4153 atm
$\Delta\Theta_{ddS}$	-32 K	-63 K
γ	66.4,1660,598	94.1,2350,847
β	1.33,0.053,0.15	0.95,0.038,0.11

Table 5.5: Parameters for the 1 md/cp case - *large probe radius* tool

	water-based mud	oil-based mud
X	-0.065	-0.086
Y	0.046	0.094
ΔP_{ddS}	-5290 atm	-3982 atm
$\Delta\Theta_{ddS}$	-31 K	-60 K
γ	12.9,323,116	18.3,457,165
β	0.259,0.010,0.029	0.185,0.007,0.021

Table 5.6: Parameters for the 1 md/cp case - *small probe radius* tool

5.1.4 Formation Mobility 10 md/cp

For this formation mobility, there was no computable difference between the constant volume and the variable flowline volume solutions (error is practically zero) for the pretest conditions that maximize the formation signal for the *large probe radius* tool (q = 2.0 cm^3/s, ΔV = 16 cm^3). The comparison of isothermal and variable temperature solutions for the *large probe radius* and the *small probe radius* are shown in Figure 5.7. The results are similar to the 1 md/cp case, a spherical flow signal may be detected with the *large probe radius* tool, but it could be masked by the thermal tool storage effect in the case of the *small probe radius* if the fluid is oil-based mud.

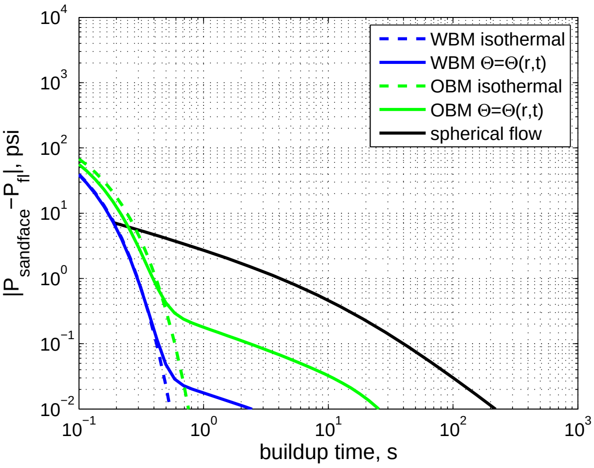

(a) Difference in buildup pressure equilibration during storage dominated period *large probe radius* tool

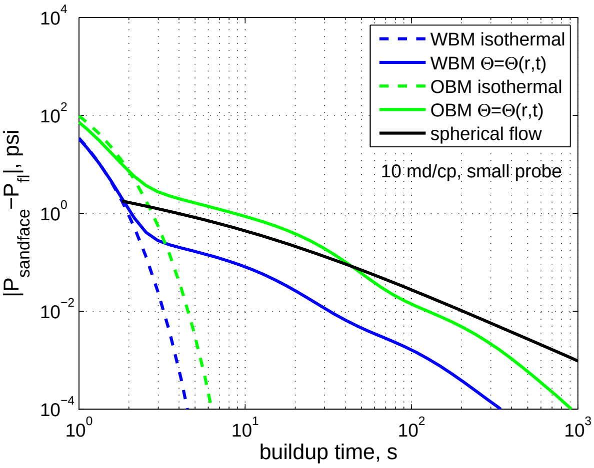

(b) Difference in buildup pressure equilibration during storage dominated period *small probe radius* tool

Figure 5.7: Flowline storage effects for the pretests that maximizes the spherical flow signal in a 10 md/cp formation. For the *large probe radius* tool (q $=$ 2.0 cm^3/s, ΔV $=$ 16 cm^3) the formation signal (spherical flow) is less affected by the thermal equilibration of the flowline than for the *small probe radius* tool (q $=$ 2.0 cm^3/s, ΔV=40 cm^3).

	water-based mud	oil-based mud
X	-0.003	-0.004
Y	0.046	0.095
ΔP_{ddS}	-5520 atm	-4150 atm
$\Delta\Theta_{ddS}$	-32 K	-63 K
γ	664,16610,5980	940,23520,8470
β	13.3,0.533,1.48	9.52,0.38,1.06

Table 5.7: Parameters for the 10 md/cp case - *large probe radius* tool

	water-based mud	oil-based mud
X	-0.018	-0.024
Y	0.046	0.095
ΔP_{ddS}	-5060 atm	-3810 atm
$\Delta\Theta_{ddS}$	-29 K	-58 K
γ	129,3230,1160	183,4570,1650
β	2.59,0.104,0.288	1.85,0.074,0.206

Table 5.8: Parameters for the 10 md/cp case - *small probe radius* tool

5.2 Some Comparisons of Computed and Measured Pressure Data

5.2.1 Example 1

Here, the pressure behavior of two consecutive pretests performed at the same tool station is analyzed. The data was acquired with the *small probe radius* tool in a well drilled with oil-based mud with wellbore temperature of 200 F. Figure 5.8 shows the pressure vs. time behavior for the two tests. There is a pressure overbalance of 700 psi that must be overcome in the first pretest. The second pretest starts right after the first one and the initial pressure is very close to the formation pressure, therefore there is no overbalance. The pressure computed with the solution that accounts for temperature variation

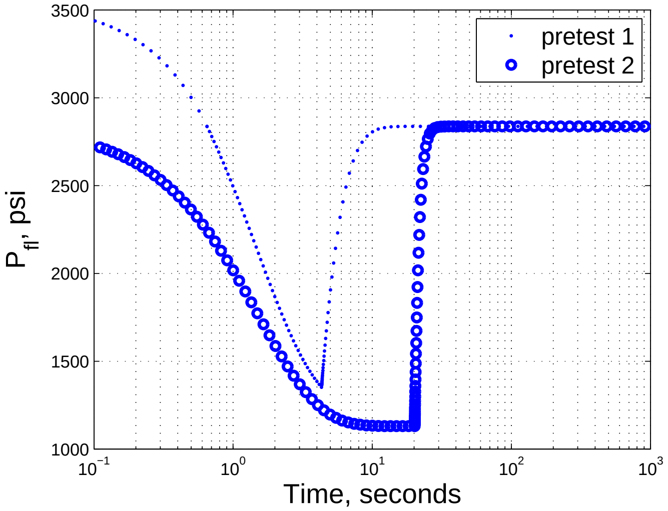

Figure 5.8: Example 1. Pressure log acquired with the *small probe radius* tool in oil-based mud, $\Theta = 366$ K (200 F).

is represented by the dashed pink curve and the pressure measurements are the blue dots.

For the first pretest the drawdown volume was 5 cm^3 at a rate of 1 cm^3/s. An overshoot of the pressure during buildup is observed in the measured data for the first pretest (with overbalance), as shown in Figure 5.9. Then, the pressure builds down to equilibrate. The pressure computed with the new solution also exhibits this behavior. In both cases the pressure overshoots by 0.2 to 0.3 psi. The computed overshoot occurs about 10 seconds earlier, possibly because the solution does not take into account the effects of borehole curvature, which, according to the isothermal model, would be prevalent between the storage and the spherical flow periods. The second pretest had a larger volume (20 cm^3) and reached a steady-state drawdown, from which the drawdown mobility was determined to be 4.1 md/cp. A spherical

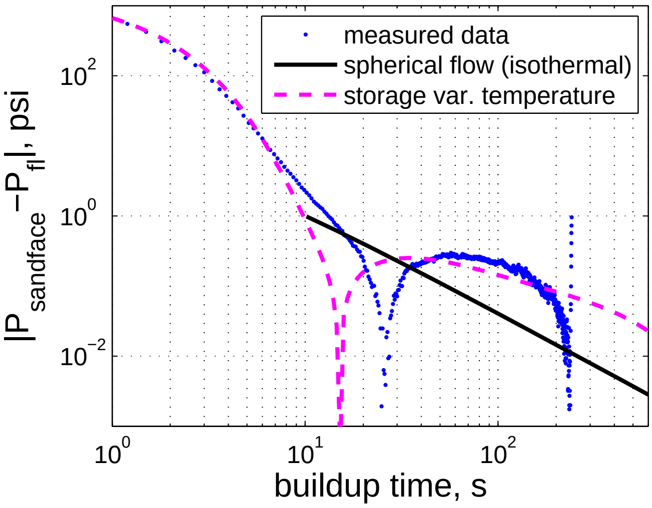

Figure 5.9: Example 1. Buildup equilibration for pretest 1 in Figure 5.8. Both, measured (points) and computed pressure exhibit a 0.02 atm (0.25 psi) pressure overshoot.

flow signal was identified in this pretest and the mobility was computed to be 2.5 md/cp; less than drawdown mobility, although close in value. Flowline pressure computed with the storage solution with temperature variations, again represented by the pink dashed line, is very different from the isothermal storage solution. The late-time storage effects have a resemblance with the expected formation response.

5.2.2 Example 2

This example shows a pretest that forms part of a set of 24 pretests acquired at various depths in a well with the *small probe radius* tool. Drilling fluid is oil-based mud environment and wellbore temperature is 366 K (200 F). This example was chosen because it was possible to identify spherical flow in all the pretests. Three pretests were conducted at each station (8 stations

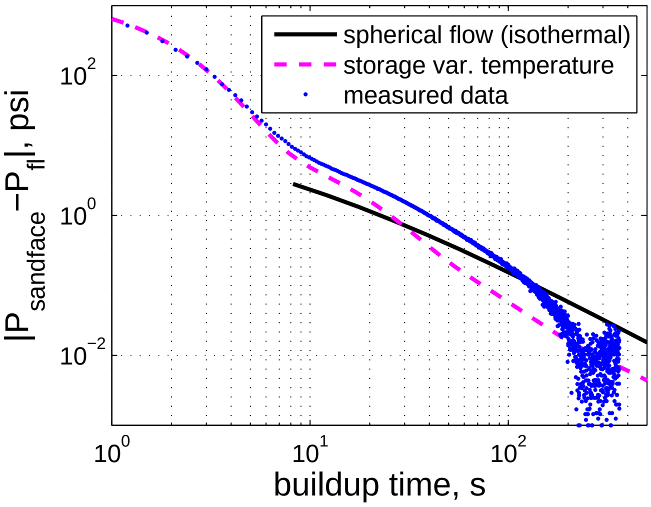

Figure 5.10: Example 1. Buildup equilibration for pretest 2 in Figure 5.8.

total) all with a flowrate of 1 cm^3/s and volumes of 5, 10 and 20 cm^3, and all of them exhibit the typical discrepancy between drawdown and spherical mobility, as may be seen in Figure 5.11. The most striking feature of Figure 5.11 is that spherical mobility values are very uniform. This is bizarre because drawdown mobility values spread over one order of magnitude, and it would be expected that spherical mobility should exhibit a similar trend.

A forward model of the pretests presented in Figure 5.11 was performed to assess whether temperature effects could be a contributing factor on the discrepancy between drawdown and spherical mobility. The pretests were simulated with $r_{probe} = 0.55$ cm, $r_{fl} = 0.2$ cm, base flowline volume of 75 cm^3, and oil-based mud. Simulated data was analyzed with the same procedure used for the measured data to obtain a spherical mobility value, and results are shown also in Figure 5.11.

The ‘forward model’ points in Figure 5.11 were computed as follows:

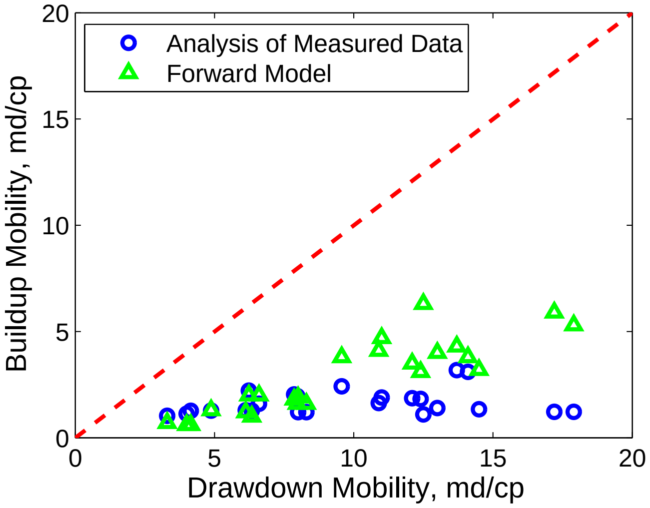

Figure 5.11: Comparison of measured spherical and drawdown mobility values for one well (same as Figure 3.11). A total of 24 pretests acquired in one well over a borehole interval spanning 3500 ft (one of the points in the graph corresponds to Example 2). The much lower variation in the spherical mobility values compared to drawdown mobility values is remarkable. Triangle markers show the buildup mobility for forward model of the same pretest conditions. Pressure data acquired with the *small probe radius* tool in oil-based mud (366 K).

1. Pretests were simulated (forward modeled) using the storage solution that accounts for temperature variations. Input parameters were rate, volume, flowline description, type of fluid in the well, wellbore temperature, and the mobility obtained from measured data during drawdown. Drawdown and early part of buildup are matched as will be shown in Example 2 (Figure 5.13).

2. The model developed in this dissertation only includes recompression of fluids in the flowline (storage) and pressure variation because of temperature changes. It does not consider reservoir compressibility. In this case flowline storage is modulated by the quasisteady-state approximation, simulating formation inflow through the probe orifice. Figure 5.12 shows the spherical derivative plot for one of the pretests simulated with this forward model, that is, derivative of forward modeled pressure with respect to spherical-time function (Equation 3.17). There is a portion of data that exhibits ‘false spherical flow’, where the spherical derivative is constant (circled in Figure 5.12). This constant, m, is used to calculate the ‘false spherical mobility’ (with Equation 3.2). This is labeled ‘false’ spherical flow because the model does not have a reservoir. If the traditional storage model (isothermal solution) had been used, the spherical derivative plot would only have the hump; late-time effects are a consequence of thermal variations.

Figure 5.11 indicates that the discrepancy between drawdown and buildup mobility values is reproduced by the forward model of flowline storage with thermal variations, which does not account for reservoir compressibility (i.e.,

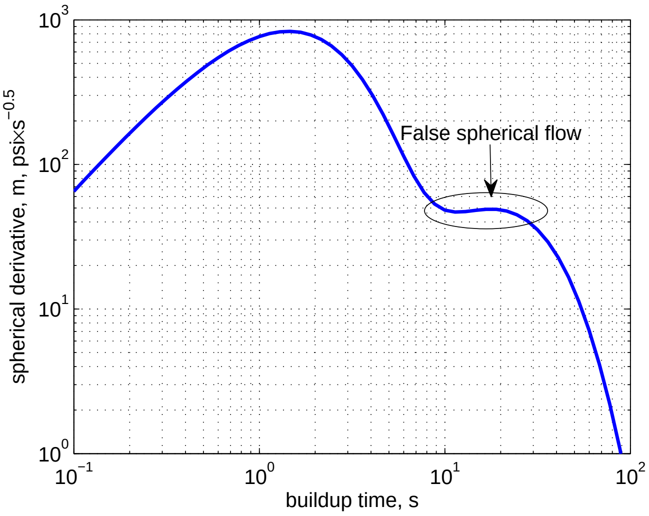

Figure 5.12: Example of 'false spherical flow' in the derivative of a forward modeled pretest from Figure 5.11. The value of m obtained with the forward model (and also in the measured data) is 50 psi/$sqrts$, buildup mobility is a factor of 5 less than drawdown mobility (6 md/cp). In order for buildup mobility to match drawdown mobility, m should be 4 psi/$sqrts$. ($c_{fm} = 4 \times 10^{-5}\text{atm}^{-1}$ $\phi = 0.2$).

spherical flow). The similarity between forward modeled and measured data is stronger in lower mobility cases. Though pressure behavior may be influenced by other factors, as will be discussed in section 5.4, these results indicate that thermal variations could lead to a misinterpretation of pressure transient analyses.

The pretest discussed next belongs to the dataset shown in Figure 5.11. Drawdown reached steady state (Figure 5.13) and $\Delta V = 20$ cm^3. Drawdown mobility, computed with Equation 3.1, is 18 md/cp (q = 1 cm^3/s, ΔP_{dd} =24 atm (350 psi), $r_{probe} = 0.55$ cm, $\Omega = 1$). Other parameters used in the pressure computation were: $c_{tool} = 5{\times}10^{-5}$ atm^{-1}, $\kappa_{\Theta} = 1.12{\times}10^{-4}$ and $V_{tool} = 115$ cm^3 (previous pretests had increased the initial flowline volume from 75 cm^3). The only parameter fitted in the calculation shown in Figure 5.13 was c_{tool}. Buildup mobility, calculated with Equation 3.2 using the value of m that provides the best fit of the pressure data is 1.2 md/cp. In this case, the discrepancy between drawdown and buildup mobility is one order of magnitude; this difference is interesting because buildup mobility is supposedly originating from deep in the formation, beyond the damaged region, and should be larger. Here, the storage solution with temperature variations does not provide a satisfactory explanation to the discrepancy observed between the drawdown and spherical mobility, as may be seen in Figure 5.14.

Figure 5.14 shows the flowline storage solution with variable temperature (dashed curve) and the expected spherical flow signal if the 'deep' formation mobility were equal to the sandface mobility (18 md/cp) (solid curve). Both curves are very similar, but remarkably different to the measured data

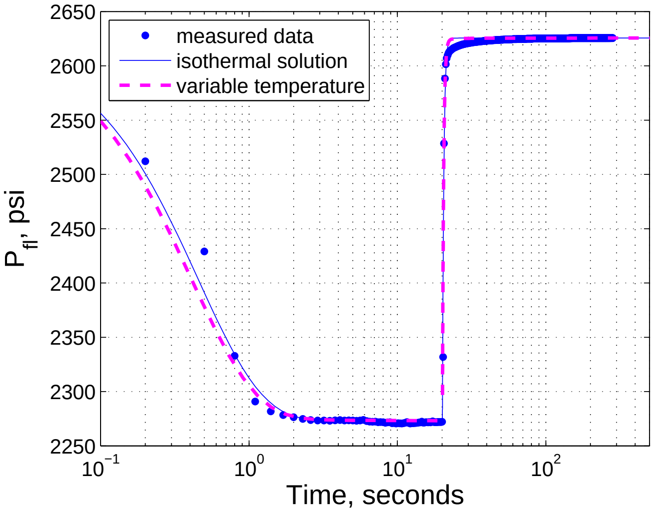

Figure 5.13: Example 2. Pressure log acquired with the *small probe radius* tool in oil-based mud.

(blue markers); the measured data being one order of magnitude larger. The cause of the poor correlation between spherical and drawdown mobility remains an open question. It is a possibility that other tool effects, such as unaccounted compliance of certain tool components, may cause this variation.

5.2.3 Example 3

This example consists of a dry pretest acquired with the small probe tool. The last drawdown pressure was higher than the formation pressure, and hence the tool did not establish hydraulic communication with the formation. However, at the end of drawdown the pressure increases and behaves like a buildup. The measured data (blue dots) and the computed pressure are shown in Figure 5.15 and a magnification of the buildup is shown in Figure 5.16. Though there is good agreement between modeled and measured data, a more refined model of the flowline should give a better match. In this case

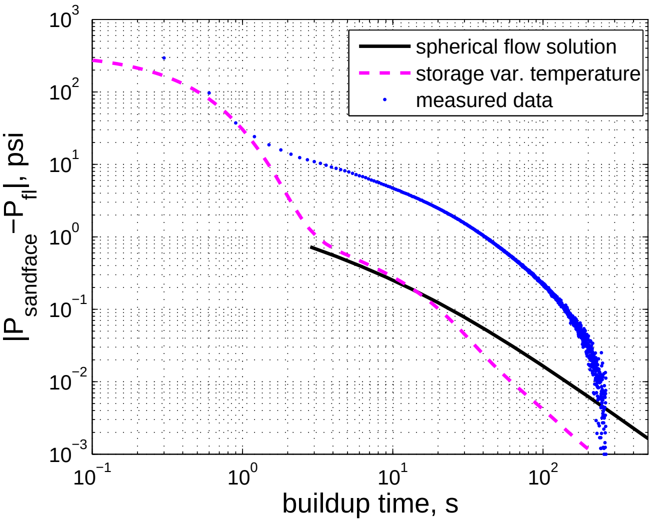

Figure 5.14: Example 2. Buildup equilibration for a pretest acquired with the *small probe radius* tool in oil-based mud. The drawdown mobility is 18 md/cp (q = 1 cm^3/s, ΔV = 20 cm^3 and buildup mobility is 1.2 md/cp. The flowline storage solution with variable temperature (dashed curve) is similar to the expected spherical flow signal if the 'deep' formation mobility were equal to the sandface mobility (18 md/cp) (solid curve). The late-buildup measured data (blue markers) is one order of magnitude larger. In this case the poor correlation between the spherical mobility and the drawdown mobility cannot be explained by temperature effects.

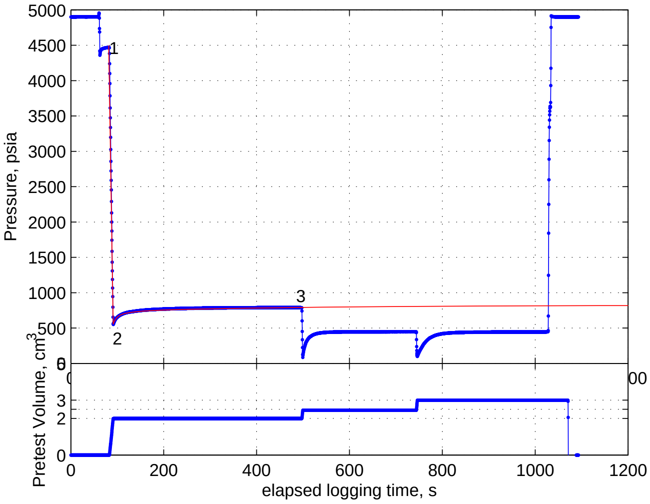

Figure 5.15: Example 3. Pressure log acquired with the *small probe radius* tool in oil-based mud.

the flowline was modeled with the dimensions listed in Table 5.1.

5.3 Discussion

This chapter presented several computations of pretest pressures using a flowline model that is representative of actual tools. For the *large probe radius* tool the error incurred by neglecting flowline volume variations in the storage solution is small for volume increases up 50% with respect to base volume. The maximum difference between constant and variable volume solutions is observed at the end of drawdown (the beginning of the buildup. The difference depended on formation mobility; the largest difference was on the order of 10^{-3} psi for $k/\mu = 0.1$ md/cp, and was at least one order of magnitude lower for other values of formation mobility considered here. The difference between the two solutions decreased quickly as buildup time increased, and within a

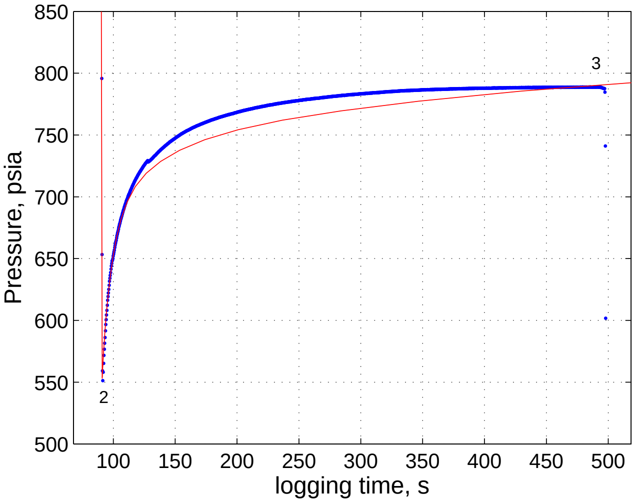

Figure 5.16: Example 3. Pressure log acquired with the *small probe radius* tool in oil-based mud.

few seconds ($\sim$ 15 seconds) it decreased by an order of magnitude. Therefore, it is expected that error introduced by assuming constant volume is negligible during the latter part of buildup, that is, when the deep formation response should dominate the pressure signal.

For the two tools investigated here, probe radius size has a significant influence on the difference in magnitude and behavior between pressure signal originating from the formation beyond the wellbore and late-time storage effects caused by thermal equilibration of the flowline fluid. Results indicate that, for constant flowline volume, a larger probe radius will increase the chances of measuring a larger magnitude formation signal, and therefore less susceptible to be compromised by temperature effects. The difference between formation signal and late-time storage decreases if the fluid in the well is oil-based mud.

Four examples comparing actual pretests acquired in the field with the pressure computed with the flowline storage solution accounting for temperature variations were presented. In some cases, the computed pressure agrees very well with the measurement and the phenomenon of overshoot observed in the field was reproduced in the computation. The pressure behavior after a dry drawdown was also captured reasonably well with the model.

Two examples of pretests that exhibit what might be considered to be spherical flow behavior were presented. In both cases, there is a discrepancy (even of an order of magnitude) between the drawdown and the spherical mobility. For the low mobility case (4 md/cp) the late time storage solution is of the same order of magnitude as the late time pressure data; both have similar behavior, although the computed pressure has a lower value. This result raises questions on whether this pretest is actually capturing a deep formation signal, or if what is attributed to be a formation response is caused by tool effects.

In the second case, drawdown mobility (18 md/cp) is one order of magnitude larger than spherical mobility. In this case, pressure computed during middle-to-late part of buildup is much lower than the measured pressure. This could be interpreted as a deep formation response unaffected by thermal variations. However, this does not clarify why for all the pretests that exhibited a deep formation signal in this well, there is a much lower variation in the spherical mobility values compared to drawdown mobility values at eight different locations spanning 3500 ft of wellbore length (refer to Figure 5.11). This hints to the possibility that other unaccounted tool effects may contribute to this "spherical-flow-like behavior" during the late-time pressure signal.

All the work presented in this dissertation consisted of forward modeling of temperature effects, and there was no inverse fitting of problem parameters. This problem was chosen because single-probe formation testers provide the simplest test that can be done in a well. The flow periods and the rates are known quite well. Once the approximately steady-state flow is reached, it is possible to determine mobility around the probe with very low uncertainty. The only parameter that was fitted (by at most 20%) was the tool compressibility (c_tool); however, this mostly affects the early parts of drawdown and buildup.

5.4 Discussion of Other Factors that Could Influence the Pressure Behavior in the Tool

Several factors could influence the pressure behavior in the tool. All previous studies related to formation testers (e.g. Stewart and Wittmann, 1979; Phelps et al., 1984; Proett and Chin, 1996; etc.) assume that tool performance is perfect and attempt to provide explanations to the pressure signal behavior from the reservoir point of view. The approach followed here is diametrically opposite. It has been considered that the formation is perfect from the point of view of pressure measurement, and the focus is on behaviors within the tool that may affect the pressure signal. The objective is to understand fundamental aspects of tool performance that can be studied analytically while minimizing as much as possible external parameters that add uncertainty. It has been demonstrated that it is possible for pressure transients caused by thermal variations to have similar behavior to flow regimes characteristic of formation testers. For the sake of completeness, some other factors that could compromise pretest interpretation are discussed next.

Supercharching

Supercharging refers to the increase in the formation pore pressure near the well (the sandface pressure) as a result of mud filtrate invasion. A phenomenon observed mainly in low mobility formations, where this excess pressure requires long time to dissipate. Supercharging is a complex problem with many unknowns, some of which are mudcake permeability, mudcake thickness, depth of invasion, history of the invasion process, mudcake erosion, etc. Of the three deliverables of a pretest (sandface pressure, drawdown mobility, and buildup mobility), supercharging affects mostly the sandface pressure, which will have a value larger than in the absence of supercharging.

Assuming that filtration has almost stopped when the pretest is conducted, and there is only a region of increased pressure near the well, the drawdown mobility should not be affected because the difference between supercharged sandface pressure and last drawdown pressure (also larger because of the supercharging) is used for the computation. Even if the pretest did not reach steady state, it is considered that supercharging will have a very small impact on determination of mobility with the corresponding mobility interpretation technique for this situation (e.g. Dussan, 2011).

In low mobility formations, pressure transients induced with the pretest (in the order of minutes) occur much faster than the rate at which the excess pressure is dissipating in the formation (in the order of hours or days). The spherical mobility, assuming that it is not affected by tool effects and can be actually measured, reflects the recompression of formation and fluid far from the well. That is, the analysis looks at relative rates of change. Therefore, a measurable spherical mobility should not be affected by supercharging.

Supercharging is an important problem and of great practical value. It has been studied by various authors and several estimation procedures have been published (e.g. Hammond and Pop, 2005; Chang et al., 2008; Proett and Chin, 1996, Banerjee et al., 2006; Wu et al., 2006; etc.) . In all these studies it is considered that the formation tester is a perfect tool and the effect that is being measured is a formation phenomenon. It is recommended here that these supercharging studies be reassessed in light of more realistic tool responses as analyzed in this dissertation. This could be done by comparing, as it has been done here, the relative sizes of tool effects on the pressure signal and pressure changes expected from supercharging for various formation mobilities and mud properties.

In the author's experience, there are instances of good quality pressure data, as indicated by being able to measure pressure gradients in low mobility formations, when the well is drilled with a good quality mud. Therefore, proper drilling planning and selection of drilling fluid is key for avoiding supercharging and acquiring representative formation data.

Skin

Formation damage, skin, refers to the impairment of transport formation properties in the vicinity of the wellbore, as a result of drilling fluid filtrate and particulate invasion. Skin affects primarily the drawdown mobility, which characterizes this reservoir region. The only effect of skin on the determination of spherical flow mobility is that it extends the duration of the pressure dominated portion of the storage period, and therefore the spherical flow signal has a lower amplitude than in the absence of skin. Lower amplitude of the spherical flow signal may imply low signal to noise ratio and higher propensity to be affected by the temperature dominated portion of the tool storage effects. In fact, it is of great interest to be able to determine spherical mobility in a reliable way in order to assess skin, and this has been one of the motivations of this dissertation.

Storage

Flowline storage has been studied in this dissertation. It has been seen that in addition to the pressure dominated storage, thermal transients may extend the duration of the storage period, a phenomenon that has not been addressed previously. Furthermore, these thermal transients may cause the pressure signal to have a similar behavior and magnitude to that expected from flow regimes characteristic to single probe formation testers.

While isothermal storage depends mainly on flowline volume, probe radius and isothermal effective compressibility (tool and fluid), the non-isothermal storage also takes into account the size of flowline components (radius), and heat conduction and capacity properties of the fluid and the solid surrounding the flowline (the tool). The result is that the storage period may have longer duration that what is normally considered based on isothermal theory.

Flowline Plugging

Certainly, this is a factor that affects the operation of formation testers, since pressure measurement relies on being able to establish hydraulic communication between the flowline and the tool. In the worst case scenario, that is, for a flowline that is completely plugged by solids, the pretest resembles the dry drawdown case discussed in Chapter 4. A partially plugged flowline may require larger drawdown pressure to establish hydraulic communication with the reservoir, this will make the drawdown mobility have a lower magnitude. Similarly to the previous discussion on effects of skin, it is desirable to be able to determine buildup mobility reliably, as it would give an indication of formation properties unaffected by adverse circumstances near the wellbore or in the probe, and possibly quantify skin.

Flowline Contamination

This refers to fluid residing in the flowline that originated from testing at a previous wellbore location. It is a standard practice in formation testing to collect pretest data along the wellbore before acquiring fluid samples. During the pretest small amounts of fluid enter the flowline, consisting primarily of mud filtrate, and are discarded to the well after the pretest. One of the goals of the operation is to avoid contamination of the flowline fluid. In the event that liquid hydrocarbons or water enter the flowline, the thermal properties of the flowline fluid will be affected. Gas entering the flowline is considered in the discussion of multiphase flow effects. If contamination of the flowline is suspected, the tool operator has the option to circulate the fluid in the flowline, replacing the contents with mud from the wellbore.

Non-Homogeneous Formation and Anisotropy

Spatial variation of formation properties could be a possible cause of the difference between drawdown and spherical mobility. If this were the case, there should also be field data examples of buildup mobility having lager value than drawdown mobility. In the author's experience, after analyzing hundreds of field cases, the opposite has always been the case, that is, drawdown mobility larger than buildup mobility.

All the analyses in this dissertation assume homogeneous formation and permeability isotropy. Considering the situation of testing a vertical well with $k_H > k_V$, the average mobility, that is, spherical mobility, will have a lower value and the spherical flow signal will have a higher amplitude. Some have considered that formation anisotropy could explain the discrepancy between spherical and drawdown mobility values (e.g. Dussan and Sharma, 1992, and Noirot et al, 2011). The approach followed here is to understand what could be happening in the tool that could also cause this discrepancy in the determination of mobility values. Once it has been ruled out that tool-caused phenomena are not responsible for the observed pressure behavior, then it will be prudent to interpret pressure transients in light of formation characteristics.

Multiphase Flow Effects

Multi-phase flow effects were not considered in this dissertation. Most formation tester pretests are single-phase flow. Very small amounts of fluid ($<$20 cm^3) are extracted from the formation, consisting mostly of mud filtrate. In addition tool operators control the drawdown pressure if they suspect gas flow from the formation.

Besides formation gas entering the flowline, two phases may be present when testing depleted reservoirs if the flowline pressure decreases below the vapor pressure of the flowline fluid (the drilling mud) during drawdown. This affects the pressure behavior during buildup, primarily by increasing the flowline compressibility. It is possible that having a gas and a liquid phase in the flowline and in the formation near the probe could affect the determination of drawdown mobility. A quantitative assessment of this effect is not yet available.

Difference in Formation Testing Wireline vs. While Drilling

Formation testing while drilling is performed in a very similar way to the wireline operation; however, the former has some specific challenges. While drilling, pressure measurements are acquired very soon after the formation has been drilled and when the mudcake might not have been completely formed. It is believed that supercharging will be a larger problem because there is no sufficient time for the excess pressure to have dissipated. Pressure measurements are sometimes acquired when the mud pumps are active, this adds noise to the signal. A large mud circulation rate increases the equivalent mud density and could erode the mudcake and/or increase filtrate leakoff rate. In addition, the drilling fluid is typically cooler than the formation, this difference could be as high as several tens of degrees Celsius; hence, there are thermal gradients between the formation and the wellbore.

The radius of a wellbore is much larger that of the flowline; therefore, it is expected that the equilibration of the wellbore and formation temperature will be a matter of hours or days. For the analysis presented in this dissertation were are concerned with thermal transients between the tool flowline and the wellbore during the pretest, and we have shown that these transients have a time scale of minutes. Therefore, we consider that the flowline pressure will not be significantly affected by thermal transients between the wellbore and the formation.

In pressure measurement while drilling time is of the essence. Drilling stops for a few moments to make a measurement, and it is desired to resume as soon as possible. Sandface pressure and drawdown mobility are the most important pieces of information extracted from a pretest while drilling, while analysis of spherical flow is of secondary interest. Thermal transients caused by the pretest, as discussed here, are considered relevant to drilling operations because they may affect the rate at which pressure equilibrates, which directly impacts sandface pressure measurement.

Chapter 6

Conclusions

This dissertation described an approach to analyze transient pressure behavior during pretests that accounts for effects of fluid temperature variations on the pressure signal. The focus has been the tool capability to sense pressure transients associated with recompression of formation fluids some distance away from the wellbore. This work was motivated in large part by inconsistencies between drawdown and spherical mobility often observed in measured data.

Two aspects of the problem were treated: first, selection of pretest parameters for a given tool and formation that would increase the signal-to-noise ratio during spherical flow. Secondly, obtaining a solution for flowline storage that accounts for flowline fluid temperature variations during the pretest. The latter implies that additional tool design features, namely flowline dimensions, and thermophysical properties of the fluid, have to be incorporated into the model.

Consequences of temperature variations during formation tester pretests could be twofold: 1) flowline pressure equilibration may take longer than what would be expected assuming isothermal conditions during the pretest, 2) flowline storage effects caused by temperature variations may interfere with the identification of formation flow regimes used to obtain formation properties beyond the wellbore and for quality control of the test. Hence, environmental conditions during the test must be considered in formation tester pressure measurement interpretation.

There are three answers that are sought from a formation tester measurement: the formation pressure, the mobility at the wellbore, and the mobility deep in the formation. Drawdown mobility, which is less affected by the temperature, provides formation properties near the wellbore. Spherical mobility, representative of a reservoir region several inches away from the wellbore, is of interest because it could characterize formation properties beyond the invaded zone. Spherical mobility could be the most affected by temperature variations. It has been shown that it is possible to completely misinterpret the pressure signal and derive a false mobility value using pressure data that is affected by temperature effects. Also, temperature effects may cause the pressure signal to take longer time to equilibrate, which means longer time to make a measurement. This is an issue because in operations a fast measurement is favored.

The range of mobilities considered in this dissertation is 0.001 md/cp to 100 md/cp. Today, formation testers are used in mobilities as low as 0.1 md/cp. Some even go as low as 0.01 md/cp. Supercharging is not an issue if the well is drilled with a good quality drilling fluid. There is also great interest in measuring formation pressure in lower mobility formations; however, current designs of single-probe formation testers require long time to equilibrate (hours) in such conditions. Above 50 md/cp pressure equilibrates very fast, and single probe formation testers have no issues.

The main contribution of this dissertation is the message that those dealing with formation tester data have to be aware that there are tool effects that must be considered in the interpretation. Many practitioners use the identification of flow regimes as an indicator of the quality of the measurement. The most significant discovery arising from this work is the realization that there are tool produced effects that could have the same behavior as the formation response.

It has been found that temperature effects are more far reaching than initially thought. Another contribution of this work, is that a model has been presented that captures the effects of tool design and measurement environment (drilling fluid, temperature and overbalance) on the pressure response of the system.

There are several variables that enter this problem, but among them, the design of the formation tester is of paramount importance. However, this information resides with tool manufactures. In this regard, this dissertation could be of value to improve future formation tester designs, and improve the quality of the measurement. This will ultimately be of benefit to all.

Writing specific guidelines is not a straightforward task because of the large parameter space in this problem. Amidst the conclusions, it is attempted to provide recommendations to practitioners regarding tool selection, and the analysis of single-probe transient pressure data. It is considered that it is reasonable to be critical of the spherical mobility values obtained by most formation testers; and to avoid interpretation of pressure data that exhibits the build-down behavior.

1. The selection of a formation tester and pretest parameters has a large influence on achieving a large pressure signal during the spherical flow period. Uncertainty in mobility calculations using pressure data that exhibit characteristics of spherical flow could be reduced by increasing the signal-to-noise ratio.

2. It has been found that the largest pressure signal during spherical flow is obtained for formations with mobility ranging from 0.01 md/cp to 10 md/cp. Within this range, results may vary significantly depending on tool specifications and operational constraints, namely maximum pretest rate, maximum pretest volume, maximum pressure differential, and pressure overbalance.

3. For low mobility formations ($k/\mu < 0.1$ md/cp), pressure signal amplitude at the onset of spherical flow is mostly a function of pretest volume. For $k/\mu > 1$ md/cp it is mostly a function of pretest rate.

4. Pretests that maximize the amplitude of spherical flow pressure data tend to require longer equilibration times. In the field, when time in the well is important, it may be desirable to conduct different pretests to measure pressure and estimate mobility. For example, one may perform a pretest with a small drawdown volume and fast equilibration time to obtain sandface pressure and drawdown mobility, followed by a pretest designed to investigate mobility deeper in the formation, with the intention of terminating the pretest once sufficient data have been recorded.

5. The origin, behavior and consequences of thermal transients during the

pretest have been analyzed. Governing equations and boundary conditions were identified and solved semi-analytically. The results obtained here indicate that buildup pressure may be highly influenced by the rate of thermal equilibration of the flowline fluid.

6. For some situations (given tool characteristics, pretest parameters, formation mobility, wellbore temperature and fluid type), the storage solution developed here, accounting for temperature variations, exhibits similar behavior to that expected from the spherical flow regime identified by Moran and Finklea (1962). That is, the rate of thermal equilibration controls the measured buildup pressure. This phenomenon has not been considered previously and it is considered to be one of the main contributions of this dissertation.

7. If thermal effects on the buildup pressure signal have larger magnitude than the theoretical formation signal from the spherical flow regime, buildup is dominated by temperature effects. In this case tool effects dominate the flowline pressure and it is not possible to obtain buildup mobility. In fact, this is a possible explanation for the discrepancy between drawdown and buildup mobility often encountered in field operations.

8. Other things kept equal, temperature effects on late-buildup also tend to be more significant for mobility values within 0.1 to 10 md/cp, that is, for those formations more likely, in theory, to exhibit spherical flow regime during buildup, for the tools considered in this dissertation. If the mobility is very low (< 0.01md/cp), then flowline recompression takes

a very long time and temperature comes to equilibrium before pressure does. If mobility is large (>10 md/cp) then pressure equilibrates very fast, and temperature is not an issue.

9. Other things kept equal, temperature effects on the late-buildup are more significant as the size of the flowline radius increases (parameter $1/\gamma$ decreases). Given two tools with the same flowline volume but different flowline radii, the temperature will take longer time to equilibrate in the tool with the largest flowline radius.

10. Complex tool designs, e.g. flowline with various components with large radius variations, require longer time to reach thermal equilibrium than a small, constant radius flowline, and consequently the flowline pressure during buildup requires long time to equilibrate. This delay is a consequence of different elements affecting the pressure signal at different times during buildup. Large radius components require long time to reach thermal equilibrium with the wellbore.

11. Other things kept equal, probe radius size has a significant influence in the difference in magnitude and behavior between the deep formation response and late-time storage effects caused by flowline fluid thermal equilibration. The tool referred as *large probe radius tool* seems to be less affected by temperature effects when performing pretests that were optimized to yield the largest formation signal.

12. Regarding environmental variables, it was found that increase in wellbore temperature and use of oil-based mud as drilling fluid exacerbate

temperature effects on the buildup pressure. In the case of water-based mud, the total temperature variation is larger than for the same pretest using oil-based mud, but the temperature equilibrates faster for water-based mud. The effect of the wellbore temperature is reflected by an increase in the dimensionless parameter Y.

13. Pressure overshoots during buildup, and subsequent decrease to sandface pressure, a behavior observed sometimes in measured data, is, according to this analysis, a consequence of flowline fluid overheating relative to the wellbore and natural cooling afterwards. Two main factors have been found to contribute to this behavior. Chiefly, pressure overbalance, and secondly, the problem time scales, specifically heat conduction time τ_{heat} and flowline storage time τ_{tool}.

14. Pressure overshoots are more pronounced as pressure overbalance (wellbore pressure minus sandface pressure) increases, this is a consequence of the smaller gain in temperature during the early seconds of buildup. That is, the pressure increase at the beginning of buildup, to a value close to sandface pressure, is less than the pressure decrease during drawdown. In this case, fluid recompression during buildup is insufficient to reheat the fluid to the wellbore temperature, and thermal equilibration can only be achieved by heat conduction. This is consistent with the observation that pressure overshoots occur mostly in the first pretest after setting the tool probe against the formation, when overbalance must be overcome.

15. For tools considered here, pressure overshoots during buildup were more prominent in the mobility range of 1 to 20 md/cp. The influence of tool

design, embedded in τ_{heat}, is seen by faster thermal transients registered in small radius components. These transients manifest in the early part of buildup, where these overshoots are more often observed.

16. Mobility determined using the total pressure difference, when approximately steady flow during drawdown is reached, is the most robust measurement, and it is no affected by temperature effects. An alternative approach for determining drawdown mobility (Dussan, 2011), used when the drawdown does not reach this approximate steady state flow (mobility less than 1 md/cp), was found to be slightly affected by temperature. The error was assessed to be in the order of 1%.

17. Spherical mobility could be completely affected by temperature effects, this implies that it might not be possible to measure a pressure signal originating within the deep formation. The *large probe radius* tool discussed here, could, according to this analysis, yield a very large spherical flow signal. Therefore, it is expected to be less affected by temperature effects for the right combination of pretest parameters and formation mobility values.

6.1 Future Directions

The single-probe formation tester is the simplest tool existing today to test a formation and characterize its properties. This tool is used routinely in oil and gas wells; therefore, it behooves us to understand thoroughly the behavior of the tool and identify clearly the circumstances that may interfere with its performance. In order to have a more complete assessment of the effects of tool design and environment on the measurement, it is mandatory to conduct experiments with actual tools at high pressure and temperature. At the same time, there must be numerical simulations of the physical processes occurring in the tool during a pretest to model the response of all the components in the system to pressure and temperature changes.

A question often arises on using the temperature measurement in the flowline to correct the pressure response. In the case of Schlumbergers MDT (Modular Dynamic Formation Tester) the temperature is measured at least at two points in the flowline. The issue with measuring temperature is that, because of heat conduction, it is expected that there are local variations of temperature, the consequence of the temperature equilibrating at different rates in different flowline components, and also within a component. So far, the measured temperature has been of more qualitative than quantitative value, but this could be explored further with controlled experiments.

It is considered prudent to understand thoroughly the system performance before considering refinements in the interpretation schemes. If temperature variations is confirmed to be a significant contributor to the pressure signal during the late part of the buildup, one alternative is to obtain a solution that couples the spherical flow solution representative of the far field with flowline storage effects, with variable temperature, as the inner boundary condition. Eventually, this may lead to the implementation of a real-time inversion process of field data to quantify formation properties and optimize the test design while the tool is positioned in front of the formation.

Because tool design is the one variable that can be controlled, it is important to set clear objectives of what an ideal tool is to achieve: first, to reach a fast pressure equilibration when the primary objective is to measure the sandface pressure; and second, to be certain that the tool is capable of measuring deep formation pressure signal of sufficiently high amplitude to minimize uncertainty in the interpretation, when the objective is to characterize the formation.

It is important to design a tool (flowline dimensions) with the 'reservoir' in mind, and with an understanding of how the tool configuration might interfere with the measurement objectives. One could imagine that, in a similar fashion, more complex systems, such as tools that operate with several probes simultaneously, straddle packer formation testers, and Drill Stem Test equipment, may be susceptible to hardware and environmental effects on the measured signal.

Appendices

Appendix A

Thermodynamic Analysis of the Pretest

This appendix presents a more detailed derivation of the thermodynamic analysis introduced in Chapter 4. The motion of the pretest piston will change the flowline volume V, which in turn will affect the flowline pressure P and temperature Θ. In this analysis, it is assumed that the formation-tester probe is set against an impermeable formation ($k/\mu = 0$), that is, the mass of the system is constant. The objective is to describe the effect of changes in P and Θ as a function of V, more specifically the equilibrium (final) states of the system (the flowline) for the two limiting cases:

- the adiabatic case, when the pretest piston retracts quickly, that is, the drawdown rate, q, is large.
- the isothermal case, when the pretest piston retracts slowly, that is, the drawdown rate, q, is small.

These two processes are depicted in Figure A.1.

The statement of conservation of mass in the flowline is:

$$\frac{d(\rho V)}{dt} = 0, \tag{A.1}$$

where ρ is the density of the flowline fluid and t is the time.

$$V d\rho + \rho dV = 0$$

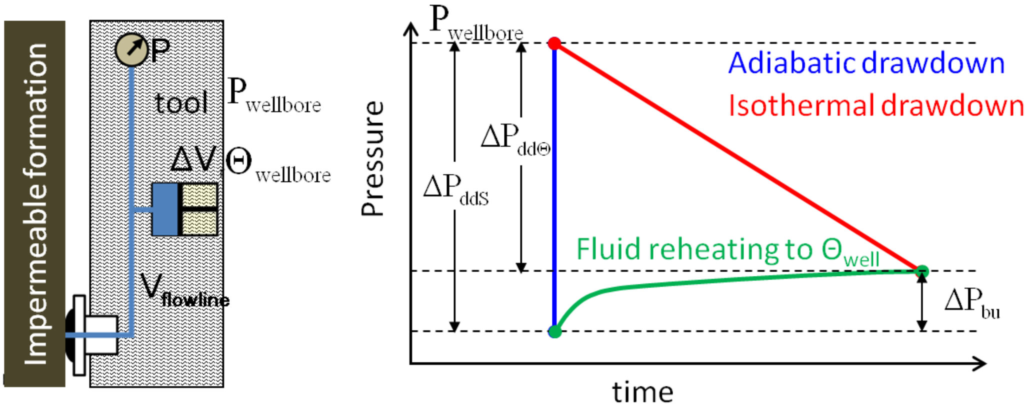

Figure A.1: Explanation of the equilibrium states of the system following a volume increase ΔV when the probe is set against an impermeable formation.

To describe the adiabatic process, density is expressed as a function of entropy S and pressure[1]

$$\rho = \rho(S, P),$$

such that

$$V \left[\left. \frac{d\rho}{dS} \right|_P dS + \left. \frac{d\rho}{dP} \right|_S dP \right] + \rho \left[dV_{piston} + dV_{deform} \right] = 0. \tag{A.2}$$

The flowline volume variation dV occurs in two ways: the movement of the pretest piston, dV_{piston}, which increases the flowline volume during drawdown; and compliance of the tool to changes in pressure, dV_{deform}, which will tend to decrease the flowline volume as pressure decreases; the two processes are included in Equation(A.2).

The definitions of isentropic compressibility, κ_S, and tool compressibility, c_{tool}, are:

$$\kappa_S \equiv -\frac{1}{V} \left. \frac{\partial V}{\partial P} \right|_S, \tag{A.3}$$

---

[1] Throughout this discussion thermodynamic properties are specific.

and

$$c_{tool} \equiv \frac{1}{V}\frac{dV_{deform}}{dP}. \tag{A.4}$$

Assuming that an adiabatic process is equivalent to an isentropic process, $dS = 0$, gives rise to

$$V\kappa_S \rho dP + \rho dV + \rho c_{tool} V dP = 0,$$

and

$$V(\kappa_S + c_{tool})dP + dV = 0.$$

During an adiabatic drawdown the flowline volume increases from the initial value, V_i, to the final value, V_f, and the total pressure change in the flowline is

$$\Delta P_{dd_S} = \int_{P_{well}}^{P_{dd_S}} dP = -\int_{V_i}^{V_f} \frac{1}{\kappa_S + c_{tool}}\frac{dV}{V}. \tag{A.5}$$

Assuming that κ_S and c_{tool} are constant, yields

$$\Delta P_{dd_S} = P_{dd_S} - P_{well} = -\frac{1}{\kappa_S + c_{tool}} \ln\left(\frac{V_f}{V_i}\right), \tag{A.6}$$

where P_{dd_S} is the pressure in the flowline at the end of the adiabatic drawdown and P_{well} is the initial pressure in the flowline.

To calculate the temperature variation in the flowline during an adiabatic drawdown, the entropy is expressed as a function of temperature and pressure (for a system with constant mass), $S = S(\Theta, P)$. The variation in entropy is given by

$$dS = \left.\frac{\partial S}{\partial \Theta}\right|_P d\Theta + \left.\frac{\partial S}{\partial P}\right|_\Theta dP.$$

The following thermodynamic relations are used

$$\hat{c}_P \equiv \Theta \left.\frac{\partial S}{\partial \Theta}\right|_P, \qquad \left.\frac{\partial S}{\partial P}\right|_\Theta = -\left.\frac{\partial V}{\partial \Theta}\right|_P, \qquad \alpha \equiv \frac{1}{V}\left.\frac{\partial V}{\partial \Theta}\right|_P, \tag{A.7}$$

where $\hat{c}_P$ is the specific heat at constant pressure and α is the coefficient of thermal expansion. Thus,

$$dS = \frac{\hat{c}_p}{\Theta} d\Theta - \frac{\alpha}{\rho} dP.$$

For an isentropic process:

$$\hat{c}_P d\Theta = \frac{\alpha\Theta}{\rho} dP.$$

For an adiabatic drawdown dP was derived in Equation (A.5), that is,

$$dP|_S = -\frac{1}{\kappa_S + c_{tool}} \frac{dV}{V}.$$

Using the relation

$$\hat{c}_v = \hat{c}_P - \frac{\Theta\alpha^2}{\rho\kappa_\Theta},$$

where κ_Θ is the coefficient of isothermal expansion, defined as

$$\kappa_\Theta \equiv -\frac{1}{V} \left.\frac{\partial V}{\partial P}\right|_\Theta . \tag{A.8}$$

Noting that

$$\frac{\alpha\Theta}{\rho} = \frac{\kappa_\Theta}{\alpha}(\hat{c}_p - \hat{c}_v), \quad \text{and} \qquad \frac{\kappa_\Theta}{\kappa_S} = \frac{\hat{c}_p}{\hat{c}_v}, \quad \text{yields}$$

$$\Delta\Theta_{dd_S} = \int_{\Theta_{well}}^{\Theta_{dd_S}} d\Theta = -\int_{V_i}^{V_f} \frac{\kappa_S}{\alpha(\kappa_S + c_{tool})} \left(\frac{\hat{c}_p}{\hat{c}_v} - 1\right) \frac{dV}{V} \tag{A.9}$$

$$\Theta_{dd_S} - \Theta_{well} = -\frac{\kappa_S}{\alpha(\kappa_S + c_{tool})} \left(\frac{\hat{c}_P}{\hat{c}_v} - 1\right) \ln\left(\frac{V_f}{V_i}\right) \tag{A.10}$$

The same result is obtained if Θ is expressed as a function of entropy and volume, $\Theta = \Theta(S, V)$, that is,

$$d\Theta = \left.\frac{\partial\Theta}{\partial S}\right|_V dS + \left.\frac{\partial\Theta}{\partial V}\right|_S dV.$$

Using Maxwell's relations, and manipulating the partial derivatives gives

$$\left.\frac{\partial \Theta}{\partial V}\right|_S = -\left.\frac{\partial P}{\partial S}\right|_V = \frac{\left.\frac{\partial V}{\partial S}\right|_P}{\left.\frac{\partial V}{\partial P}\right|_S},$$

and

$$\left.\frac{\partial V}{\partial S}\right|_P = \left.\frac{\partial \Theta}{\partial P}\right|_S = \frac{\left.\frac{\partial V}{\partial \Theta}\right|_P}{\left.\frac{\partial S}{\partial \Theta}\right|_P} = \frac{\Theta\alpha}{\rho\hat{c}_P}.$$

Using these results and the definition of isentropic compressibility (A.3) gives

$$\left.\frac{\partial \Theta}{\partial V}\right|_S = -\frac{\Theta\alpha}{\rho\hat{c}_p\kappa_S V} = -\frac{1}{\alpha}\left(\frac{\hat{c}_P}{\hat{c}_v} - 1\right)\frac{1}{V}.$$

For an isentropic process one has

$$d\Theta = -\frac{1}{\alpha}\left(\frac{\hat{c}_P}{\hat{c}_v} - 1\right)\frac{dV}{V} = -\frac{1}{\alpha}\left(\frac{\hat{c}_P}{\hat{c}_v} - 1\right)\frac{1}{V}(dV_{piston} + dV_{deform}),$$

$$\int_{\Theta_{well}}^{\Theta_{dd_S}} d\Theta = -\int_{V_i}^{V_f} \frac{1}{\alpha}\left(\frac{\hat{c}_P}{\hat{c}_v} - 1\right)\frac{dV_{piston}}{V} - \int_{P_{well}}^{P_{dd_S}} \frac{1}{\alpha}\left(\frac{\hat{c}_P}{\hat{c}_v} - 1\right)c_{tool}dP,$$

and

$$\Theta_{dd_S} - \Theta_{well} = -\frac{1}{\alpha}\left(\frac{\hat{c}_P}{\hat{c}_v} - 1\right)\ln\left(\frac{V_f}{V_i}\right) - \frac{1}{\alpha}\left(\frac{\hat{c}_P}{\hat{c}_v} - 1\right)c_{tool}\left(P_{dd_S} - P_{well}\right).$$

Using Equation (A.14) gives

$$\Delta\Theta_{dd_S} = \Theta_{dd_S} - \Theta_{well} = -\frac{\kappa_S}{\alpha(\kappa_S + c_{tool})}\left(\frac{\hat{c}_P}{\hat{c}_v} - 1\right)\ln\left(\frac{V_f}{V_i}\right). \qquad \text{(A.11)}$$

We are also interested in computing the temperature change for the isothermal process, that is, the limiting case representing a pretest piston moving slowly. To compute the pressure variation during an isothermal drawdown, density is expressed as a function of pressure and temperature in Equation (A.1), namely

$$d\rho = \left.\frac{d\rho}{dP}\right|_\Theta dP + \left.\frac{d\rho}{d\Theta}\right|_P d\Theta,$$

$$V\left[\left.\frac{d\rho}{dP}\right|_{\Theta} dP + \left.\frac{d\rho}{d\Theta}\right|_{p} d\Theta\right] + \rho\left[dV_{piston} + dV_{deform}\right] = 0. \tag{A.12}$$

For an isothermal process $d\Theta = 0$, one has,

$$V\kappa_{\Theta}\rho dP + \rho dV + \rho c_{tool} V dP = 0. \tag{A.13}$$

As done previously for the case of the adiabatic drawdown, it is assumed that κ_{Θ} and c_{tool} are constant, therefore,

$$\Delta P_{dd_{\Theta}} = P_{dd_{\Theta}} - P_{well} = -\frac{1}{\kappa_{\Theta} + c_{tool}} \ln\left(\frac{V_f}{V_i}\right). \tag{A.14}$$

When the system is allowed to re-equilibrate to its initial temperature, then, because the volume of fluid in the flowline at the end of drawdown is constrained to remain constant at V_f, the pressure in the flowline will increase by ΔP_{bu}. To evaluate ΔP_{bu} it is important to recognize that when the temperature re-equilibrates to the initial flowline temperature, the pressure in the flowline will be the same as if the drawdown had been isothermal (see Figure A.1), nammely,

$$\Delta P_{bu} = \Delta P_{dd_{\Theta}} - \Delta P_{dd_S} = \Delta P_{dd_S}\left(\frac{\kappa_S + c_{tool}}{\kappa_{\Theta} + c_{tool}} - 1\right), \tag{A.15}$$

Finally, the three parameters ΔP_{dd_S}, $\Delta\Theta_{dd_S}$, ΔP_{bu} are related by:

$$\Delta\Theta_{dd_S} = \frac{\kappa_{\Theta} - \kappa_S}{\alpha}\Delta P_{dd_S},$$

and

$$\Delta P_{bu} = \frac{\alpha\Delta\Theta_{dd_S}}{\kappa_{\Theta} - \kappa_S}\left(\frac{\kappa_S + c_{tool}}{\kappa_{\Theta} + c_{tool}} - 1\right) = -\frac{\alpha\Delta\Theta_{dd_S}}{\kappa_{\Theta} + c_{tool}}.$$

Values of thermodynamic properties for water and n-hexadecane are given in Figures A.2 - A.7.

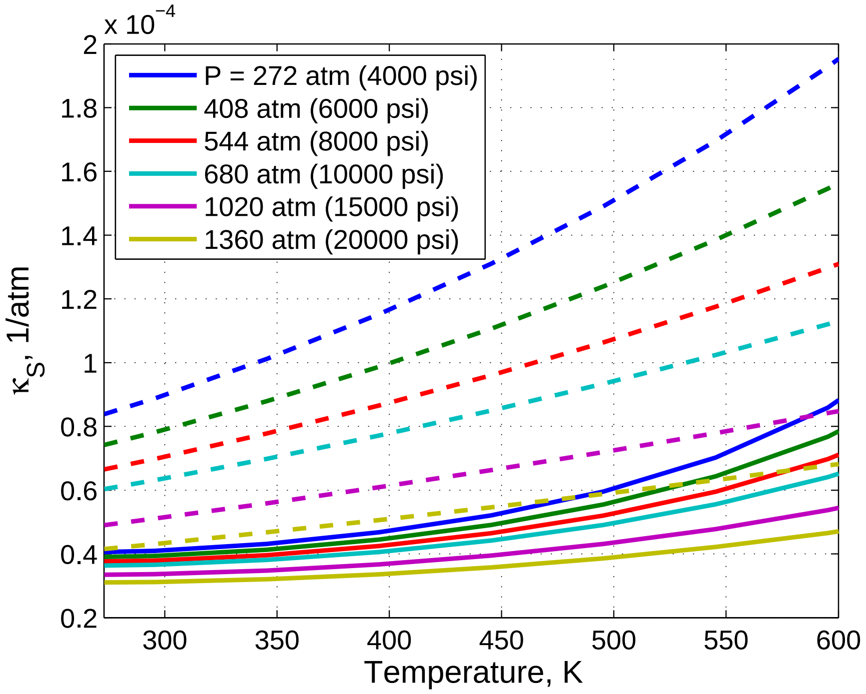

Figure A.2: Adiabatic compressibility of water and hexadecane as a function of pressure and temperature. Values obtained from NIST Supertrapp database (2007).

If a drawdown occurs sufficiently fast, it may be considered adiabatic. The time scale that will determine the validity of this assumption is given by the analysis of the heat transfer process between the wellbore and the flowline. Conduction has been identified as the dominant heat transfer mechanism in this problem; hence, it will determine the time required to equilibrate the flowline temperature to the wellbore temperature at the end of drawdown. The application of the conservation laws of mass and non-mechanical energy to the system (i.e., the flowline and surrounding material) is described in the next section.

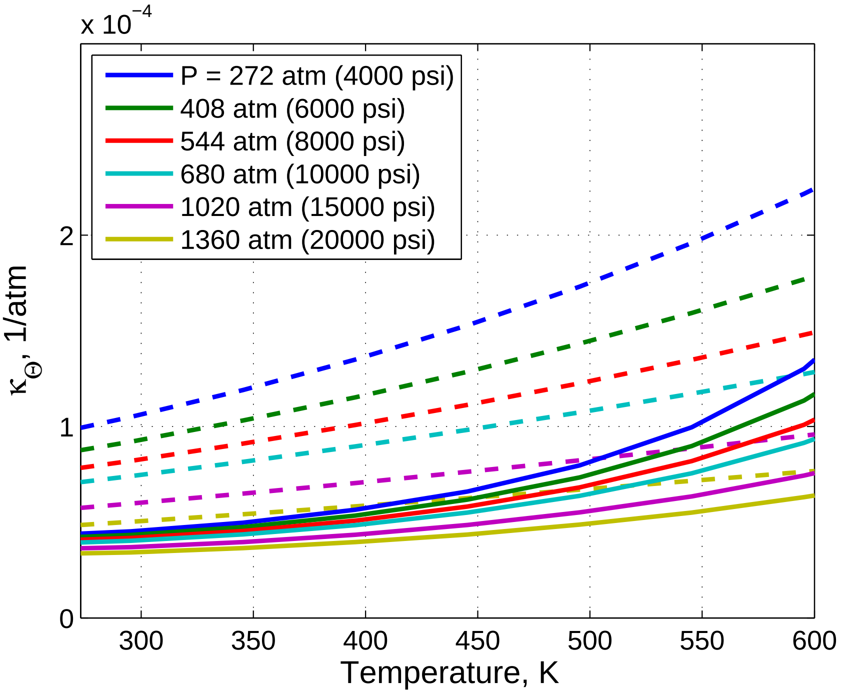

Figure A.3: Isothermal compressibility of water and hexadecane as a function of pressure and temperature. Values obtained from NIST Supertrapp database (2007).

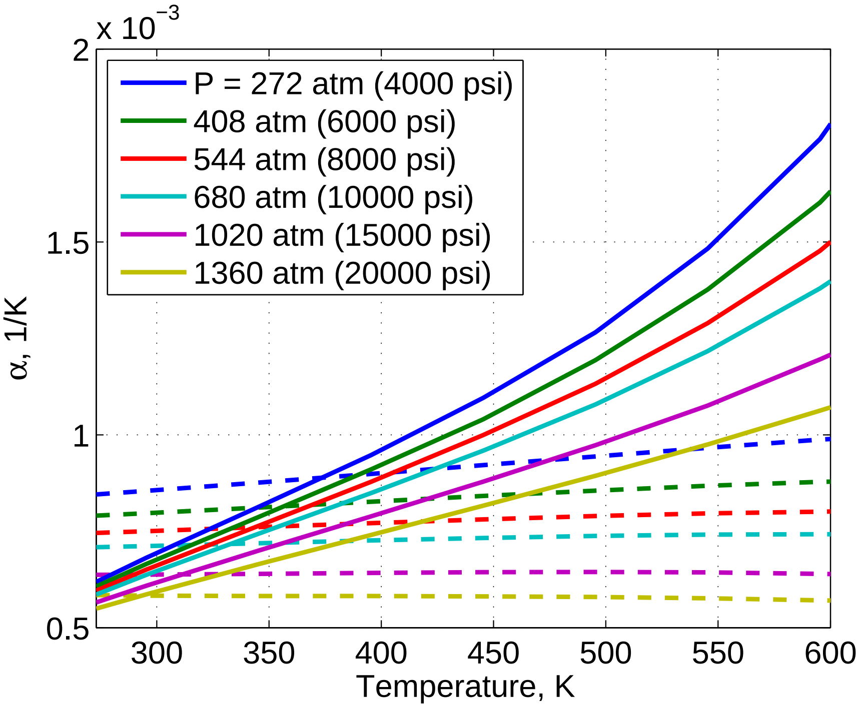

Figure A.4: Coefficient of thermal expansion of water and hexadecane as a function of pressure and temperature. Values obtained from NIST Supertrapp database (2007).

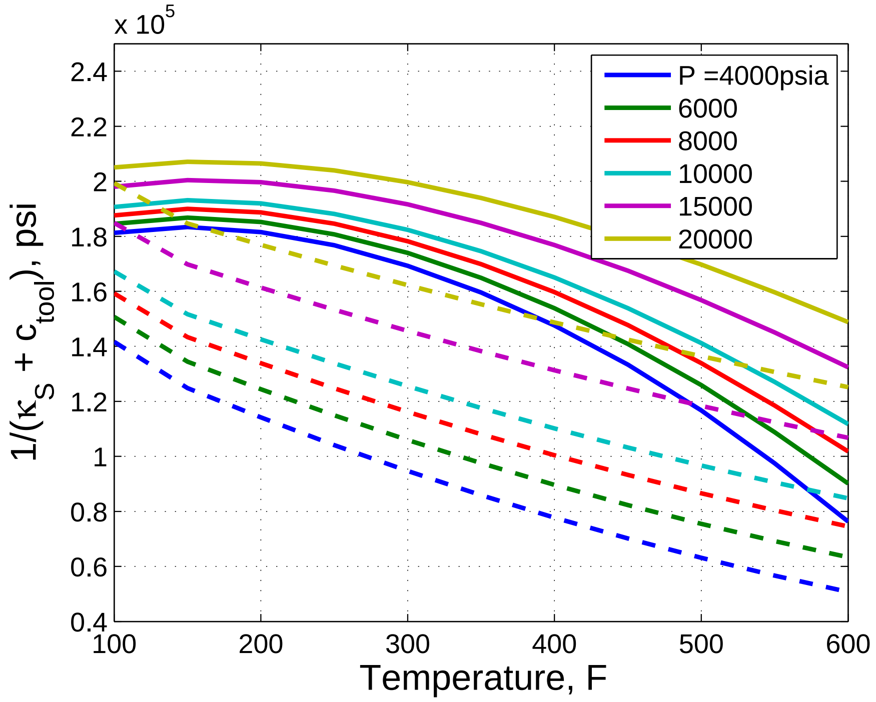

Figure A.5: Thermodynamic properties of water (solid lines) and n-hexadecane (dashed lines) used for the computation of ΔP_{ddS} with $c_{tool} = 2.7 \times 10^{-6}\text{psi}^{-1}$ $(4 \times 10^{-5}\text{atm}^{-1})$.

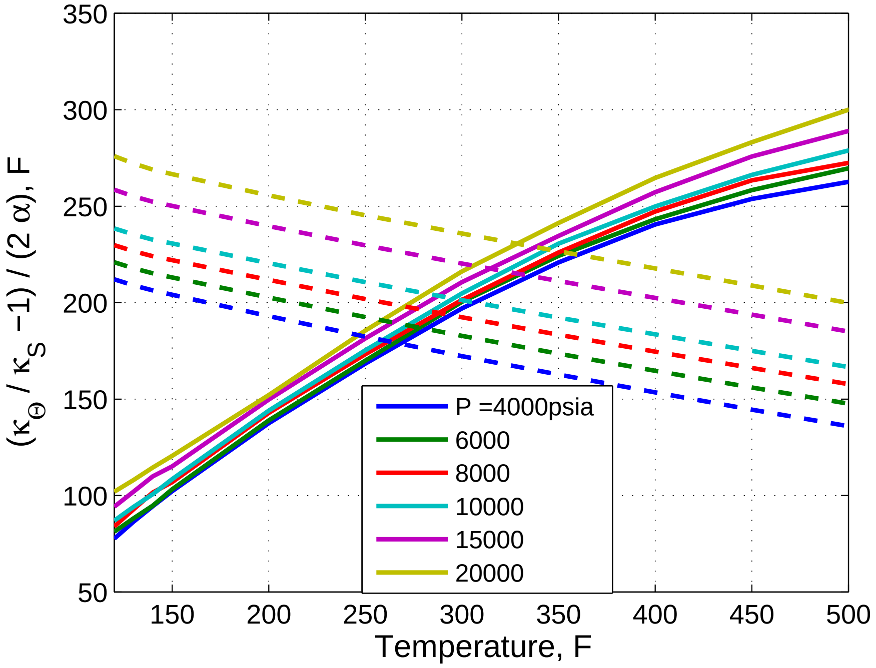

Figure A.6: Thermodynamic properties of water (solid lines) and n-hexadecane (dashed lines) used for the computation of $\Delta\Theta_{ddS}$.

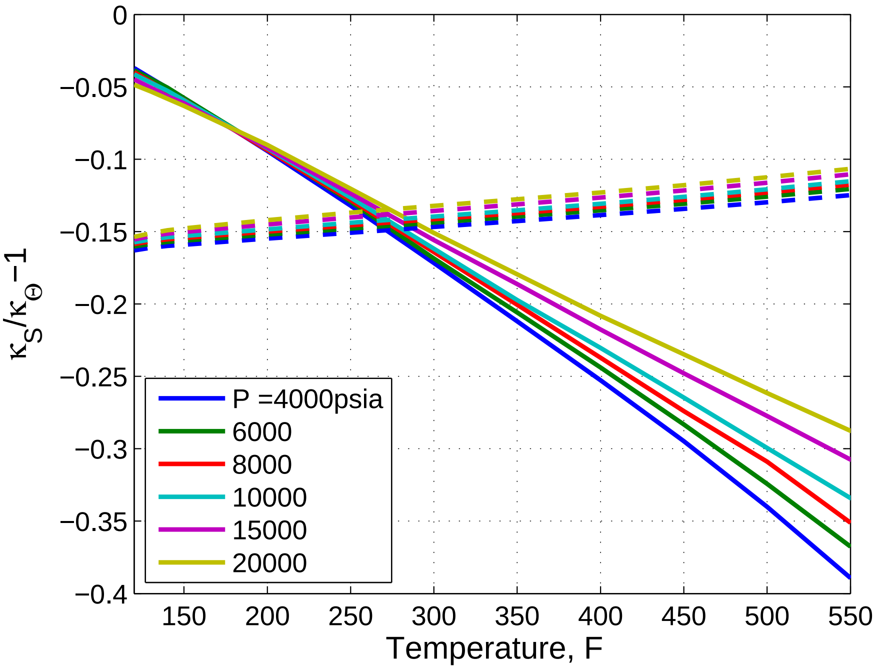

Figure A.7: Thermodynamic properties of water (solid lines) and n-hexadecane (dashed lines) used for the computation of the pressure increase during a false buildup.

Appendix B

Analysis of the Temperature Variation in the Flowline during the Pretest

This appendix provides a more detailed derivation of the equations describing the time variation of the flowline pressure P and temperature Θ as a response to flowline volume changes during the pretest (Chapter 4). In this analysis the control volume is the fluid within the flow line. We begin by applying the principles of conservation of mass and energy to derive the governing equations for this problem. Convenient scales for this problem are identified and the equations are written in dimensionless form. The physical meaning of the relevant dimensionless groups that characterize this problem is discussed.

B.1 Conservation of Mass in the Flowline

Volume changes in the control volume occur because of the retraction of the pretest piston, the volume occupied by fluid entering from the formation, the compressibility of both tool and fluid, and changes in the temperature of the fluid. Conservation of mass in the flowline dictates that:

$$\frac{d(\rho V)}{dt} = \rho \, q_{fm}, \tag{B.1}$$

and

$$V\frac{d\rho}{dt} + \rho\frac{dV}{dt} = \rho q_{fm}. \tag{B.2}$$

Fluid density, ρ is a function of P and Θ, i.e.

$$\frac{d\rho}{dt} = \left.\frac{d\rho}{dP}\right|_{\Theta}\frac{dP}{dt} + \left.\frac{d\rho}{d\Theta}\right|_{P}\frac{d\Theta}{dt}. \tag{B.3}$$

Changes in the flowline volume result from two effects: the volume increase caused by the retraction of the pretest piston at a rate q_{piston}, and the mechanical deformation of the flow line because of pressure changes dV_{deform}:

$$\frac{dV}{dt} = q_{piston} + \frac{dV_{deform}}{dt}. \tag{B.4}$$

Expressing the above equation in terms of α, κ_{Θ}, and c_{tool} gives

$$V\rho_{fl}\left[\kappa_{\Theta}\frac{dP}{dt} - \alpha\frac{d\Theta}{dt}\right] + \rho_{fl}\left[q_{piston} + c_{tool}V\frac{dP}{dt}\right] = \rho_{fm}q_{fm}. \tag{B.5}$$

The following assumptions are made:

1. The density of the fluid entering the flowline (ρ_{fm}) is the same as that of the fluid initially in the flowline (ρ_{fl}),
2. Flowline volume changes are small and volume is assumed constant and equal to the initial flowline volume $V_{flowline}$, and
3. The effective flowline compressibility defined as $c_{eff} = \kappa_{\Theta} + c_{tool}$ is constant.

The equation of conservation of mass in the flowline becomes

$$c_{eff}V_{flowline}\frac{dP}{dt} - \alpha V_{flowline}\frac{d\Theta}{dt} = q_{fm} - q_{piston} \tag{B.6}$$

By assuming instantaneous speed changes in the piston operation, then q_{piston} or pretest rate throughout the pretest is given by:

$$q_{piston} = \begin{cases} q_{\infty}, & 0 < t \leq T \\ 0, & t > T, \end{cases}$$

where q_{∞} is the required pretest rate, and T is the duration of the drawdown period.

The time scale associated with the response of the flowline to pressure changes, i.e. flowline storage is:

$$\tau_{tool} \equiv \frac{c_{eff} V_{flowline}}{4 r_{probe} k/\mu}, \tag{B.7}$$

where $V_{flowline}$ is the initial flowline volume, and r_{probe} is the probe radius.

Quasi-Steady State Approximation of Formation Inflow

Flow from the reservoir into the flowline is modeled using cylindrical coordinates with the center of the well at $r = 0$ and the probe at the wellbore wall, r_{well}.

The outward flux per unit time across the surface of the probe $\mathcal{S}$ is

$$q_{fm} = \int_{\mathcal{S}} \mathbf{u} \cdot \mathbf{n} d\mathcal{S} \tag{B.8}$$

The unit outward normal to the probe surface is $-\widehat{r}$, i.e., the unit vector in the radial direction, the direction of the flow (negative sign means pointing toward the center of wellbore). See Figure B.1

For a homogeneous and isotropic permeable media, the velocity field is given by Darcy's law,

$$\mathbf{u} \cdot (-\widehat{r}) = k/\mu \frac{\partial P}{\partial r} \tag{B.9}$$

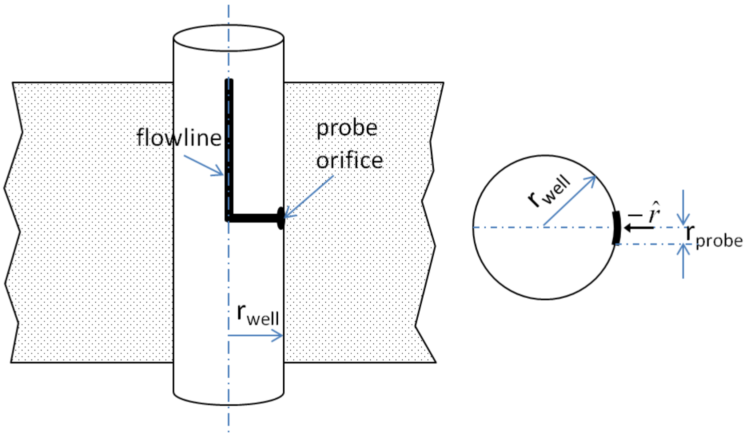

Figure B.1: Definition of the coordinate system to model flow from the reservoir to the flowline.

inserting this expression in B.8:

$$q_{fm} = \int_{\mathbb{S}} k/\mu \frac{\partial P}{\partial r}\bigg|_{r=r_{well}} d\mathbb{S}. \tag{B.10}$$

The time scale associated with the dissipation of pressure transients in the reservoir for this problem is given by

$$\tau_{fm} \equiv \frac{\phi c_{fm} r_{probe}^2}{k/\mu}, \tag{B.11}$$

where ϕ is porosity and c_{fm} is formation compressibility.

In this problem the time scale of the reservoir (τ_{fm}) is 2-4 orders of magnitude shorter than the time scale of the tool (τ_{tool}) (Equation B.28); hence, it is valid to assume that for the storage-dominated period the flow from the formation is steady state. During storage, the flow from the formation entering the probe can be approximated by assuming flow to a disc on the flat surface, impermeable elsewhere, of a semi-infinite medium. This assumption is valid if $r_{probe} \ll r_{well}$. The steady-state rate of flow through the probe for this problem is found in Carslaw and Jaeger (1959) (Chapter VIII, Equation 10, page 215), namely,

$$q_{fm} = \frac{4r_{probe}k}{\mu}(P_{sandface} - P) \tag{B.12}$$

$P_{sandface}$ is the initial sandface pressure, a constant, assumed here to be equal to the far-field formation pressure, and P is the pressure in the flowline, a function of time.

The equation of conservation of mass in the flowline becomes

$$\frac{dP}{dt} - \frac{\alpha}{c_{eff}}\frac{d\Theta}{dt} = \frac{4r_{probe}k/\mu}{c_{eff}V_{flowline}}(P_{sandface} - P) - \frac{q_{piston}}{c_{eff}V_{flowline}}, \tag{B.13}$$

Note that in equation (B.13) it is implied that q_{fm} is zero when the flowline pressure P is larger than $P_{sandface}$. This is to account for the hydrostatic pressure exerted by the fluid in the wellbore. Therefore, when $P(0) > P_{sandface}$ the initial part of the drawdown requires depressurization of the flowline to enable hydraulic communication between the well and the formation. In practice, an additional pressure differential, below formation pressure, may be necessary to breach mudcake and communicate the flow line and the formation. In this analysis, it is assumed that the ΔP required to lift off mudcake is zero.

B.2 Conservation of Energy in the Flowline

Energy balance for the control volume, namely the fluid contained in the flowline (Figure B.2), is imposed to account for the effects of pressure and temperature on the volumetric behavior of the fluid. We use the statement of conservation of non-mechanical energy, also known as thermal energy

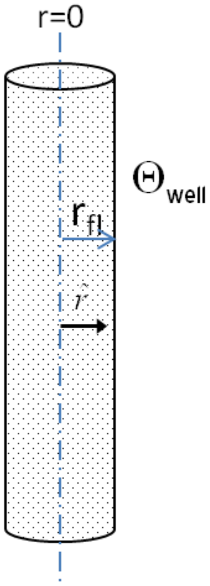

Figure B.2: Definition of the control volume and system of coordinates assumed in the conservation of energy equation for the heat conduction problem.

equation,(Equation 10.1-12 in Bird, et al.,1960), namely,

$$\rho \frac{DU}{Dt} = -(\nabla \cdot \mathbf{q}) - P(\nabla \cdot \mathbf{u}) - (\boldsymbol{\tau} : \nabla \mathbf{u}), \tag{B.14}$$

where U is the specific internal energy and $\frac{D}{Dt}$ is the substantial or material derivative of the internal energy. We wish to express the equation on non-mechanical energy in terms of temperature and heat capacity of the fluid, instead of internal energy. We make use of the fundamental thermodynamic relation $U = U(S, \nu)$, where S is specific entropy and ν is specific volume, namely,

$$dU = \Theta dS - P d\nu. \tag{B.15}$$

We differ from the analysis presented by Bird et al.(1960), who invoked $U = U(T, \nu)$, because this equation is not a fundamental relation and does not convey all the thermodynamic information about the system (Callen, 1960).

Similar to the procedure in Bird et al., we apply the material derivative to Equation B.15 and multiply by density, namely,

$$\rho\frac{DU}{Dt} = \rho\Theta\frac{DS}{Dt} - \rho P\frac{D\nu}{Dt}. \tag{B.16}$$

Writing the volume derivative in terms of density results in the equation of continuity in material form:

$$\rho\frac{D\nu}{Dt} \equiv \rho\frac{D}{Dt}\left(\frac{1}{\rho}\right) = -\frac{1}{\rho}\frac{D\rho}{Dt} = \nabla\cdot\mathbf{u}. \tag{B.17}$$

Substituting (B.17) and (B.16) into Equation (B.14) yields

$$\rho\Theta\frac{DS}{Dt} = -(\nabla\cdot\mathbf{q}) - (\boldsymbol{\tau} : \nabla\mathbf{u}), \tag{B.18}$$

and using the second Gibbs relation in material form (Batchelor, 2009),

$$\Theta\frac{DS}{Dt} = c_p\frac{D\Theta}{Dt} - \frac{\alpha\Theta}{\rho}\frac{DP}{Dt}, \tag{B.19}$$

then the energy equation becomes

$$\rho c_p\frac{D\Theta}{Dt} - \alpha\Theta\frac{DP}{Dt} = -(\nabla\cdot\mathbf{q}) - (\boldsymbol{\tau} : \nabla\mathbf{u}). \tag{B.20}$$

One of the assumptions of the problem is that pressure gradients within the flowline are neglected and therefore heat generation because of viscous forces, i.e. the viscous dissipation term $(\boldsymbol{\tau} : \nabla\mathbf{u})$, is neglected. This is justified because the velocity within the flowline during the pretest is small. In addition, we neglect gravity effects; therefore the flowline pressure P is only a function of time.

The primary mechanism that contributes to the heat flux is conduction, and the constitutive equation is Fourier's law. Our control volume is the fluid in the flowline, which is modeled as a long cylinder with heat conduction occurring only in the radial direction (Figure B.2). Fluid properties are considered isotropic, and the one-dimensional form of Fourier's law becomes

$$q_r = -K_\Theta \frac{\partial \Theta}{\partial r}, \tag{B.21}$$

where K_Θ is the thermal conductivity of the fluid and the negative sign indicates that the fluid loses heat when $\mathbf{q}$ points outward. The energy equation is simplified as:

$$\rho c_P \frac{\partial \Theta}{\partial t} - \alpha \Theta \frac{dP}{dt} = K_\Theta \frac{1}{r} \frac{\partial}{\partial r} \left(r \frac{\partial \Theta}{\partial r} \right). \tag{B.22}$$

B.3 Problem Statement

The main approximations used in determining the governing equations for this problem are:

1. The geometry of the flowline has been simplified (Figure B.2). We model the flowline as a long cylinder with constant radius r_{fl} and volume, V. End effects are neglected, implying that heat conduction occurs only in the radial direction.

2. Wellbore pressure, P_{well}, is greater than or equal to the formation pressure at the sandface, $P_{sandface}$, the difference, or overbalance, ranges from 100 to 5,000 psi.

3. Heat transfer by natural convection is neglected. Wellbore temperature, Θ_{well}, is constant in the vicinity of the tool.

4. Pretest volume, ΔV, is considered small in comparison with the flowline volume, $V_{flowline}$; i.e, $V_{flowline}$ is assumed to be constant.

5. Density of the fluid in the flowline ($\rho_{flowline\ fluid}$) and the density of the fluid flowing into the tool from the formation ($\rho_{formation\ fluid}$) are the same.

6. The formation response is modeled using the quasi-steady-state approximation (Equation B.12), i.e., the formation compressibility is neglected when computing the rate of flow through the probe orifice.

7. Effective flow line compressibility is constant.

8. Changes in the piston speed are immediate.

The initial-boundary-value problem for the pressure and temperature in the flowline is as follows:

$$\frac{dP}{dt} + \frac{\alpha}{c_{eff}} \frac{d\langle\Theta\rangle}{dt} = \frac{q_{fm}}{c_{eff} V_{flowline}} - \frac{q_{piston}}{c_{eff} V_{flowline}}, \tag{B.13}$$

$$q_{piston}(t) = q_{\infty} \left[H(t) - H(t-T) \right], \tag{B.23}$$

and

$$q_{fm}(t) = 4 r_{probe} k / \mu (P_{sandface} - P) H(t - t^*), \tag{B.24}$$

where H is the unit step function (Heavyside function), T is the length of the drawdown, and t^* is defined as

$$P(t^*) = P_{sandface}, \tag{B.25}$$

i.e., t^* is the time during drawdown when hydraulic communication between the tool flowline and the formation is established.

The pretest piston moves while $0 < t < T$. However, the situation may arise that condition (B.25) is not met for $t < T$, in which case the drawdown has failed to probe the formation. This situation is referred to as a ‘dry drawdown’ or a ‘tight test’.

The second term in the equation of conservation of mass is the time variation of *mass-average* temperature, $\langle\Theta\rangle$, in the flow line.[1] This is justified in Appendix C.

The equation of conservation of non-mechanical energy is given by

$$\frac{\partial\Theta}{\partial t} - \frac{\alpha\Theta}{\rho\hat{c}_P}\frac{dP}{dt} = \frac{K_\Theta}{\rho\hat{c}_P}\frac{1}{r}\frac{\partial}{\partial r}\left(r\frac{\partial\Theta}{\partial r}\right), \tag{B.26}$$

with $P = P(t)$ and $\Theta = \Theta(r,t)$.

The initial and boundary conditions of the general problem are:

1.
$$P(0) = P_{well}$$

2.
$$\lim_{t\to\infty} P = \begin{cases} P(T) + \frac{\alpha\Delta\Theta_{dd_S}}{c_{eff}} & \text{if } P(T) \geq P_{sandface}, \\ P_{sandface} & \text{if } P(T) < P_{sandface}, \end{cases}$$

3.
$$\Theta(r,0) = \Theta_{well},$$

4.
$$\lim_{t\to\infty} \Theta = \Theta_{well},$$

and

---

[1] $\langle\Theta\rangle = \frac{\int_V \rho(\mathbf{x},t)T(\mathbf{x},t)dV}{\int_V \rho(\mathbf{x},t)dV}$

5.

$$\Theta(r = r_{fl}, t) = \Theta_{well}.$$

From the problem statement, the following scales are identified:

- *Time scales*
  - Time scale associated with the heat conduction problem is:

$$\tau_{heat} = \frac{\rho \hat{c}_P r_{fl}^2}{K_\Theta} \tag{B.27}$$

  - Time scale associated with the recompression of the flowline, and the fluid in it, i.e. flowline storage is:

$$\tau_{tool} = \frac{c_{eff} V_{flowline}}{4 r_{probe} k/\mu}. \tag{B.28}$$

- *Pressure scales*
  - Pressure scale associated with temperature variation (isentropic) is:

$$\Delta P_{dd_S} = -\frac{1}{\kappa_S + c_{tool}} \ln \left(\frac{V_{flowline} + \Delta V_{pretest}}{V_{flowline}} \right). \tag{B.29}$$

  - Pressure scale associated with volume variation (isothermal) is:

$$\Delta P_{dd} = \frac{q_\infty}{4 r_{probe} k/\mu}. \tag{B.30}$$

- *Temperature scale*

$$\Delta\Theta_{dd_S} = -\frac{\kappa_S}{\alpha(\kappa_S + c_{tool})} \left(\frac{\hat{c}_p}{\hat{c}_V} - 1 \right) \ln \left(\frac{V_{flowline} + \Delta V_{pretest}}{V_{flowline}} \right) \tag{B.31}$$

The following dimensionless variables are defined:

$$t_D = \frac{t}{\tau_{tool}}, \tag{B.32}$$

$$P_D = \frac{P - P_{sandface}}{\Delta P_{dd_S}}, \tag{B.33}$$

$$\Theta_D = \frac{\Theta - \Theta_{well}}{\Delta \Theta_{dd_S}}, \tag{B.34}$$

$$q_D = \frac{q_{piston}}{q_\infty}, \tag{B.35}$$

$$r_D = \frac{r}{r_{fl}}. \tag{B.36}$$

We define $T_D = \frac{T}{\tau_{tool}}$ and note that formation fluid will enter the fluid only when $P_D > 0$.

The following dimensionless groups appear in the statement of the problem in terms of dimensionless variables:

- The diffusivity coefficient in the dimensionless temperature equation, $1/\gamma$, is a measure of the relative duration of heat conduction in the fluid with respect to tool storage, namely,

$$1/\gamma = \frac{\tau_{tool}}{\tau_{heat}}. \tag{B.37}$$

- The dimensionless group, X, is the ratio of the total pressure change when the drawdown reaches steady-state for a given rate q_∞, and the adiabatic drawdown for the same pretest volume. For the adiabatic drawdown there is no inflow from the formation. Hence, X is a measure of the size of the pretest, and is a term that appears only in the drawdown equations.

$$X = \frac{\Delta P_{dd}}{\Delta P_{dd_S}}. \tag{B.38}$$

- The group Y, is a measure of the impact of temperature effects on the pressure behavior. When written in terms of physical variables of the problem, Y reduces to the difference between the isothermal and the adiabatic compressibility of the fluid. Hence, when $Y = 0$ there are no temperature effects on the pretest.

$$Y = \frac{\alpha \Delta \Theta_{dd_S}}{c_{eff} \Delta P_{dd_S}}. \tag{B.39}$$

- The dimensionless group Z that appears in the dimensionless energy equation happens to be a thermodynamic identity.

$$Z = \frac{\alpha \Theta_{well} \Delta P_{dd_S}}{\rho \hat{c}_p \Delta \Theta_{dd_S}} = 1. \tag{B.40}$$

  Z is a thermodynamic identity.

The problem in dimensionless form is:

1. for $0 < t_D \leq t_{dd_D}$ and $P_D \leq 0$ (drawdown with no influx from the formation)

$$\frac{dP_D}{dt_D} = Y \frac{d\langle \Theta_D \rangle}{dt_D} - X q_D \tag{B.41}$$

$$\frac{\partial \Theta_D}{\partial t_D} = \frac{1}{\gamma} \bar{\nabla}^2 \Theta_D + \frac{dP_D}{dt_D}. \tag{B.42}$$

   The Laplacian in (B.42) is dimensionless [2].

$$P_D(0) = \frac{P_{well} - P_{sandface}}{\Delta P_{dd_S}} = P_{D0}$$

---

[2]

$$\bar{\nabla}^2 \Theta_D = \frac{1}{r_D} \frac{\partial}{\partial r} \left(r_D \frac{\partial \Theta_D}{\partial r_D} \right)$$

$$\langle\Theta_D\rangle(0) = 1$$

$$P_D(t_D^*) = 0$$

2. for $t_D^* < t_D \leq t_{dd_D}$ and $P_D > 0$ (drawdown with influx from the formation)

$$\frac{dP_D}{dt_D} + P_D = Y\frac{d\langle\Theta_D\rangle}{dt_D} - Xq_D \tag{B.43}$$

$$\frac{\partial\Theta_D}{\partial t_D} = \frac{1}{\gamma}\bar{\nabla}^2\Theta_D + \frac{dP_D}{dt_D} \tag{B.44}$$

$$P_D(t_D^*) = 0$$

$$\langle\Theta_D\rangle(t_D^*) = \langle\Theta_D\rangle^*$$

$$\Theta_D(r_D, t_D^*) = \Theta_D^*(r_D)$$

$$P_D(t_{dd_D}) = P_{D_{dd}}$$

$$\langle\Theta_D\rangle(t_{dd_D}) = \langle\Theta_D\rangle_{dd}$$

3. for $t_D > t_{dd_D}$ and $P_D > 0$ (buildup with influx from the formation)

$$\frac{dP_D}{dt_D} + P_D = Y\frac{d\langle\Theta_D\rangle}{dt_D} \tag{B.45}$$

$$\frac{\partial\Theta_D}{\partial t_D} = \frac{1}{\gamma}\bar{\nabla}^2\Theta_D + \frac{dP_D}{dt_D} \tag{B.46}$$

$$P_D(t_{dd_D}) = P_{D_{dd}}$$

$$\langle\Theta_D\rangle(t_{dd_D}) = \langle\Theta_D\rangle_{dd}$$

$$\Theta_D(r_D, t_{dd_D}) = \Theta_{dd_D}(r_D)$$

$$P_D(t_D \to \infty) = 0$$

$$\langle\Theta_D\rangle(t_D \to \infty) = 0$$

4. for $t_D > t_{dd_D}$ and $P_D \leq 0$ (buildup without influx from the formation)

$$\frac{dP_D}{dt_D} = Y \frac{d\langle\Theta_D\rangle}{dt_D} \tag{B.47}$$

$$\frac{\partial\Theta_D}{\partial t_D} = \frac{1}{\gamma}\bar{\nabla}^2\Theta_D + \frac{dP_D}{dt_D} \tag{B.48}$$

$$P_D(t_{dd_D}) = P_{D_{dd}}$$

$$\langle\Theta_D\rangle(t_{dd_D}) = \langle\Theta_D\rangle_{dd}$$

$$\Theta_D(r_D, t_{dd_D}) = \Theta_{dd_D}(r_D)$$

$$\langle\Theta_D\rangle(t_D \to \infty) = 0$$

$$P_D(t_D \to \infty) = Y$$

If it is assumed that the change in pressure during drawdown occurs under adiabatic conditions, then the 'initial' conditions in cases 3 and 4, become:

$$P_D(t_{dd_D}) = \frac{P_{sandface} - P_{well} - \Delta P_{dd_S}}{\Delta P_{dd_S}}$$

$$\langle\Theta_D\rangle(t_{dd_D}) = 0$$

The boundary conditions for the temperature have not been specified as they will depend on the geometrical model of the flow line.

Appendix C

Justification for Using the Mass Average Temperature in the Conservation of Mass Equation

Consider an ideal system divided by a frictionless piston as depicted in figure C.1. The initial pressure (P_0) and Temperature (Θ_0) are the same throughout the system. Supposing that the temperature changes instantaneously, such that $\Theta_1 \neq \Theta_2 \neq \Theta_0$, we are interested in determining $P_1(t)$ and $P_2(t)$, i.e. the pressure variation for this system, if the variation of temperature: $\Theta_1(t)$ and $\Theta_2(t)$, the total volume, V, and the mass of each subsystem: M_1 and M_2 are known. The piston is allowed to move and is frictionless, therefore $P_1(t) = P_2(t) = P(t)$. The density of each subsystem is a function of the

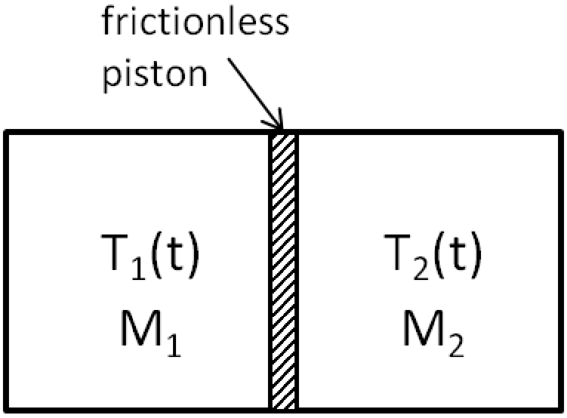

Figure C.1: Ideal system divided by a frictionless piston.

local pressure and temperature: $\rho_1 = \rho(P(t), \Theta_1(t)$ and $\rho_2 = \rho(P(t), \Theta_2(t)$ and since the total system and each subsystem are closed then, from conservation of mass, it follows that:

$$\rho_1(t)V_1(t) = \text{constant} = C_1$$

and

$$\rho_2(t)V_2(t) = \text{constant} = C_2$$

Differentiating each equation with respect to time:

$$V_1 \frac{d\rho_1}{dt} + \rho_1 \frac{dV_1}{dt} = 0$$

$$V_1 \left[\left. \frac{\partial \rho_1}{\partial P} \right|_{\Theta} \frac{dP}{dt} + \left. \frac{\partial \rho_1}{\partial \Theta_1} \right|_{P} \frac{d\Theta_1}{dt} \right] + \rho_1 \frac{dV_1}{dt} = 0$$

Using the definitions of κ_Θ (Equation A.8) and α (Equation A.7), and assuming that κ_Θ and α may be considered constant over small variations of P and Θ (this implies that the product $\frac{1}{\rho}\frac{d\rho}{dP}$ is constant, but density and pressure are allowed to vary), then:

$$V_1 \left[\rho_1 \kappa_{\Theta_1} \frac{dP}{dt} + \rho_1 \alpha_1 \frac{d\Theta_1}{dt} \right] + \rho_1 \frac{dV_1}{dt} = 0 \tag{C.1}$$

$$V_2 \left[\rho_2 \kappa_{\Theta_2} \frac{dP}{dt} + \rho_2 \alpha_2 \frac{d\Theta_2}{dt} \right] + \rho_2 \frac{dV_2}{dt} = 0 \tag{C.2}$$

Equating C.1 and C.2 and noting that $\frac{dV_1}{dt} = -\frac{dV_2}{dt}$, then:

$$\left(V_1 \rho_1 \kappa_{\Theta_1} + V_2 \rho_2 \kappa_{\Theta_2} \right) \frac{dP}{dt} - V_1 \rho_1 \alpha_1 \frac{d\Theta_1}{dt} - V_2 \rho_2 \alpha_2 \frac{d\Theta_2}{dt} + (\rho_1 - \rho_2) \frac{dV_1}{dt} = 0$$

It is assumed that κ_Θ and α are constant over small variations of P and Θ ($\kappa_\Theta = \kappa_{\Theta_0}$, $\alpha = \alpha_0$):

$$\left(V_1 \rho_1 + V_2 \rho_2 \right) \kappa_{\Theta_0} \frac{dP}{dt} - \alpha_0 \left(M_1 \frac{d\Theta_1}{dt} + M_2 \frac{d\Theta_2}{dt} \right) + (\rho_1 - \rho_2) \frac{dV_1}{dt} = 0,$$

where $M_T = V_1\rho_1 + V_2\rho_2 =$ constant is the total mass in the system, and

$$\langle\Theta\rangle = \frac{M_1\Theta_1 + M_2\Theta_2}{M_T}.$$

Solving for the pressure variation:

$$\frac{dP}{dt} = \frac{\alpha_0}{\kappa_{\Theta_0}}\frac{d\langle\Theta\rangle}{dt} - \frac{(\rho_1 - \rho_2)}{M_T\kappa_{\Theta_0}}\frac{dV_1}{dt} \tag{C.3}$$

We need to assess the relative size of the two right-side terms in Equation C.3 to identify any terms that could be dropped to simplify the equation.

$$\begin{aligned}
\frac{(\rho_1 - \rho_2)}{M_T\kappa_{\Theta_0}}\frac{dV_1}{dt} &= -\frac{(\rho_1 - \rho_2)}{M_T\kappa_{\Theta_0}}\frac{M_1}{\rho_1^2}\frac{d\rho_1}{dt} \\
&= -\frac{(\rho_1 - \rho_2)}{M_T\kappa_{\Theta_0}}\frac{M_1}{\rho_1^2}\left[\rho_1\kappa_{\Theta_0}\frac{dP}{dt} - \rho_1\alpha_0\frac{d\Theta_1}{dt}\right] \\
&= -\frac{(\rho_1 - \rho_2)}{\rho_1}\frac{M_1}{M_T}\frac{1}{\kappa_{\Theta_0}}\left[\kappa_{\Theta_0}\frac{dP}{dt} - \alpha_0\frac{d\Theta_1}{dt}\right] \qquad (C.4)
\end{aligned}$$

Doing a Taylor Series expansion of ρ_1 and ρ_2 around ρ_0:

$$\begin{aligned}
\rho_1(P,\Theta_1) &= \rho_0 + \left.\frac{\partial\rho}{\partial P}\right|_{\Theta_0}(P - P_0) + \left.\frac{\partial\rho}{\partial\Theta}\right|_{P_0}(\Theta_1 - \Theta_0) + \cdots \\
\rho_2(P,\Theta_2) &= \rho_0 + \left.\frac{\partial\rho}{\partial P}\right|_{\Theta_0}(P - P_0) + \left.\frac{\partial\rho}{\partial\Theta}\right|_{P_0}(\Theta_2 - \Theta_0) + \cdots \\
\rho_1 - \rho_2 &\approx \left.\frac{\partial\rho}{\partial\Theta}\right|_{P_0}(\Theta_1 - \Theta_2)] \qquad (C.5)
\end{aligned}$$

Substituting this expression of the density difference in the second term of Equation C.3:

$$\begin{aligned}
-\frac{(\rho_1 - \rho_2)}{M_T\kappa_{\Theta_0}}\frac{dV_1}{dt} &= \frac{-\left.\frac{\partial\rho}{\partial\Theta}\right|_{P_0}(\Theta_1 - \Theta_2)}{\rho_1}\frac{M_1}{M_T}\frac{1}{\kappa_{\Theta_0}}\left[\kappa_{\Theta_0}\frac{dP}{dt} - \alpha_0\frac{d\Theta_1}{dt}\right]\frac{\rho_0}{\rho_0} \\
&= \frac{\rho_0}{\rho_1}\frac{\alpha_0}{\kappa_{\Theta_0}}\Delta\Theta\frac{M_1}{M_T}\left[\kappa_{\Theta_0}\frac{dP}{dt} - \alpha_0\frac{d\Theta_1}{dt}\right]
\end{aligned} \tag{C.6}$$

Typical values of the various quantities for this problem are as follows:

- $0 < \frac{M_1}{M_T} < 1$
- $\Delta\Theta \sim 5$ K
- $\frac{\rho_0}{\rho_1} \sim 1$ for water over small changes of P and Θ
- $\frac{\alpha_0}{\kappa_{\Theta_0}} \sim 10^3$ atm/K

When these values are inserted in Equation C.3 it becomes evident that the contribution of the term $\frac{(\rho_1-\rho_2)}{M_T\kappa_{\Theta_0}}\frac{dV_1}{dt}$ is small with respect to $\frac{\alpha_0}{\kappa_{\Theta_0}}\frac{d\langle\Theta\rangle}{dt}$, therefore

$$\frac{dP}{dt} = \frac{\alpha_0}{\kappa_{\Theta_0}}\frac{d\langle\Theta\rangle}{dt} \tag{C.7}$$

An alternate approach to justify the use of the mass average temperature in the calculation of the flowline pressure is to consider a continuum:

$$M_T = \int_{V(t)} \rho(\mathbf{x},t)dV$$

From Leibniz's Rule:

$$\frac{dM_T}{dt} = \int_{V(t)} \left.\frac{\partial\rho}{\partial t}\right|_{\mathbf{x}} dV + \int_{\delta V} \rho\mathbf{u}\cdot\mathbf{n}$$

For a control volume mass is conserved, therefore $\frac{dM_T}{dt} = 0$ and neglecting gravity effects (i.e. there is no free convection) then $\mathbf{u} = 0$ and $P = P(t)$, hence:

$$\frac{dP}{dt}\int_V \kappa_\Theta \rho dV - \int_V \alpha\rho\frac{\partial\Theta}{\partial t}dV = 0$$

$$\frac{dP}{dt} = \frac{\alpha}{\kappa_\Theta}\frac{\int_V \rho\frac{\partial\Theta}{\partial t}dV}{\int_V \rho dV}$$

where the mass average temperature is:

$$\langle\Theta\rangle = \frac{\int_V \rho\Theta dV}{\int_V \rho dV}$$

Appendix D

Model Representation of a Formation Tester with Uniform Flowline Radius

In its simplest form, the flowline is modeled as a cylinder with constant radius, r_{fl}, and with and temperature at the wall constant and equal to wellbore temperature, $\Theta_D(r_D = 1, t_D) = 0$ (see Figure D.1). Cylindrical coordinates with the z-axis coinciding with the center of the flowline is the natural choice for this system. In this model it is assumed that the flowline length is infinite and end effects are ignored, that is, heat is conducted only in the radial direction. Boundary conditions are that $\Theta_D = 0$ for r_D=1, $\forall t_D$ and that Θ_D must have a finite value at $r_D = 0$. The mass average temperature in the flowline is obtained by integration of the density-temperature product over the flowline cross-section divided by the total mass per unit length:

$$\langle\Theta_D\rangle = \frac{\int_0^{2\pi}\int_0^1 \rho(r_D,t_D)\Theta_D(r_D,t_D)r_D dr_D d\theta}{\int_0^{2\pi}\int_0^1 \rho(r_D,t_D) dr_D d\theta} \approx 2\int_0^1 \Theta_D(r_D,t_D)r_D dr_D \quad \text{(D.1)}$$

Our hypothesis is that variations in temperature during a pretest are relatively small (< 10 K) with respect to the downhole temperature (350 - 473 K), and the assumption can be made that spatial variations in fluid density at a given time are also of small order, so that the density of the fluid in the flowline at a given time may be assumed constant. As discussed in the derivation of the equation of conservation of non-mechanical energy, gravity is neglected and hence thermal convection is not considered.

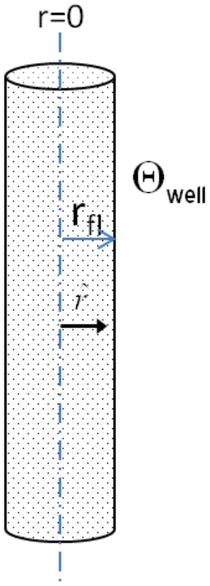

Figure D.1: Definition of the control volume used in the conservation of energy equation and coordinate system for the heat conduction problem.

D.1 Drawdown without Formation Inflow (Dry Drawdown)

In this case, $0 < t_D \leq t_{dd_D}$ and $P_D \leq 0$:

$$\frac{dP_D}{dt_D} = Y\frac{d\langle\Theta_D\rangle}{dt_D} - Xq_D \tag{D.2}$$

$$\frac{\partial\Theta_D}{\partial t_D} = \frac{1}{\gamma}\bar{\nabla}^2\Theta_D + \frac{dP_D}{dt_D} \tag{D.3}$$

$$P_D(0) = \frac{P_{well} - P_{fm}}{\Delta P_{dd_S}} = P_{D0},$$

$$\Theta_D(r_D, t_D) = 0,$$

$$\langle\Theta_D\rangle(0) = 1,$$

$$\Theta_D(1, t_D) = 0,$$

$$P_D(t_D^*) = 0.$$

The temperature in the flowline wall is assumed constant and equal to the wellbore temperature. Combining Equations D.2 and D.3 and expressing the Laplacian in cylindrical coordinates with conduction only in the radial direction [1]. gives:

$$\frac{\partial^2 \Theta_D}{\partial r_D^2} + \frac{1}{r_D}\frac{\partial \Theta_D}{\partial r_D} - \gamma \frac{\partial \Theta_D}{\partial t_D} = \gamma X - \gamma Y \frac{d\langle \Theta_D \rangle}{dt_D}. \tag{D.4}$$

Applying Laplace Transforms:

$$\frac{\partial^2 \hat{\Theta}_D}{\partial r_D^2} + \frac{1}{r_D}\frac{\partial \hat{\Theta}_D}{\partial r_D} - \gamma s \hat{\Theta}_D = \gamma X \frac{1}{s} - \gamma s Y \langle \hat{\Theta}_D \rangle, \tag{D.5}$$

where s is the Laplace Transform parameter. The left side of (D.5) becomes the modified Bessel Equation by doing the substitution $\omega = \sqrt{\gamma s}$. The right side is only a function of s.

$$f(s) \equiv \gamma X \frac{1}{s} - \gamma s Y \langle \hat{\Theta}_D \rangle$$

The solution to the homogenous problem is:

$$\hat{\Theta}_{D_H} = A I_0(\sqrt{\gamma s} r_D) + B K_0(\sqrt{\gamma s} r_D)$$

To have a finite value of $\hat{\Theta}_{D_H}$ at $r = 0$, B must be zero. The particular solution of the problems is

$$\hat{\Theta}_{D_P} = -\frac{f(s)}{s\gamma}.$$

By combining the solution to the homogeneous problem and the particular solution and evaluating the boundary condition at $r_D = 1$, the value of A is

---

[1]

$$\bar{\nabla}^2 \Theta_D = \frac{1}{r_D}\frac{\partial}{\partial r}\left(r_D \frac{\partial \Theta_D}{\partial r_D} \right)$$

obtained and the general solution is:

$$\hat{\Theta}_D = \frac{f(s)}{s\gamma}\frac{I_0(\sqrt{\gamma s} r_D)}{I_0(\sqrt{\gamma s})} - \frac{f(s)}{s\gamma}$$

The average temperature is:

$$\langle\hat{\Theta}_D\rangle = 2\int_0^1 r_D \hat{\Theta}_D dr_D = \frac{2f(s)}{s\gamma\sqrt{\gamma s}}\frac{I_1(\sqrt{\gamma s})}{I_0(\sqrt{\gamma s})} - \frac{f(s)}{s\gamma}.$$

Defining

$$\Xi \equiv \frac{1}{\sqrt{\gamma s}}\frac{I_1(\sqrt{\gamma s})}{I_0(\sqrt{\gamma s})},$$

and solving for $\langle\hat{\Theta}_D\rangle$, the average temperature in Laplace domain is found to be:

$$\langle\hat{\Theta}_D\rangle = \frac{X(2\Xi - 1)}{s^2(1 + Y(2\Xi - 1))} \tag{D.6}$$

When $\gamma \to \infty$, i.e. the fluid conductivity is very small, then $\Xi \to 0$ and this solution gives the same result obtained in the thermodynamic analysis for the adiabatic drawdown. The dimensionless pressure is computed after calculating the inverse laplace transform of (D.6):

$$P_D = P_{D_0} + Y\langle\Theta_D\rangle - Xt_D \tag{D.7}$$

It is desired to compute the temperature profile at t^*, when $P = P_{fm}$ ($P_D = 0$):

$$\hat{\Theta}_D = \left(\frac{-^2YX(2\Xi - 1)}{s^2\left[1 + Y(2\Xi - 1)\right]} + \frac{X}{s^2}\right)\left(\frac{I_0(\sqrt{s\gamma}\ r_D)}{I_0(\sqrt{s\gamma})} - 1\right) \tag{D.8}$$

$\langle\Theta_D\rangle$, P_D and Θ_D are shown in figures (D.2),(D.3) and (D.4).[2].

---

[2] When doing numerical computations with this solution for large values of $s\gamma$, it may be necessary to use the asymptotic approximation in the evaluation of the Bessel functions, i.e. as $s\gamma \to \infty$, then $\frac{1}{\sqrt{\gamma s}}\frac{I_1(\sqrt{\gamma s})}{I_0(\sqrt{\gamma s})} \approx \frac{1}{\sqrt{\gamma s}}$

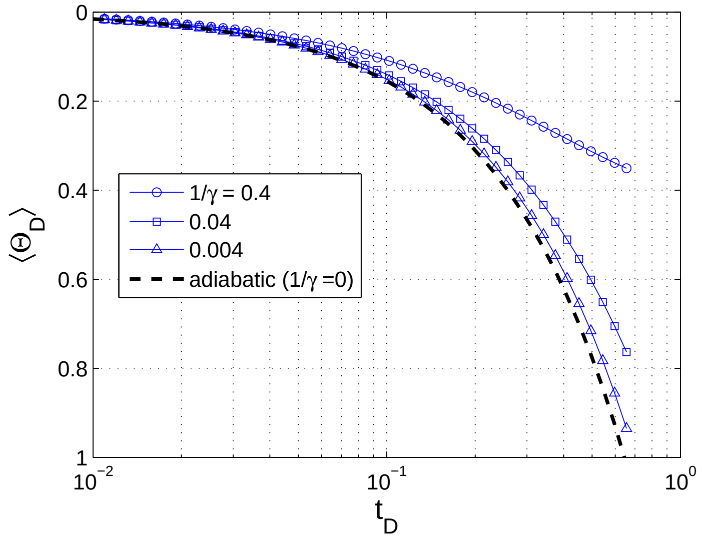

Figure D.2: Dimensionless average temperature during a drawdown without formation influx. As the thermal conductivity value decreases $\tau_{heat} \to \infty$ and $1/\gamma \to 0$ and the solution approaches the adiabatic case. X=-1.4, Y=0.09

D.2 Drawdown with Formation Inflow

In this case $t_D^* < t_D \leq t_{dd_D}$ and $P_D > 0$.

$$\frac{dP_D}{dt_D} + P_D = Y\frac{d\langle\Theta_D\rangle}{dt_D} - Xq_D \tag{D.9}$$

$$\frac{\partial\Theta_D}{\partial t_D} = \frac{1}{\gamma}\left[\frac{\partial^2\Theta_D}{\partial r_D^2} + \frac{1}{r_D}\frac{\partial\Theta_D}{\partial r_D}\right] + \frac{dP_D}{dt_D} \tag{D.10}$$

with the following initial and boundary conditions:

$$P_D(0) = 0,$$

$$\Theta_D(r_D, 0) = \Theta_{D_0}(r_D),$$

$$\Theta_D(1, t_D) = 0,$$

$$\langle\Theta_D\rangle(0) = \langle\Theta_{D_0}\rangle,$$

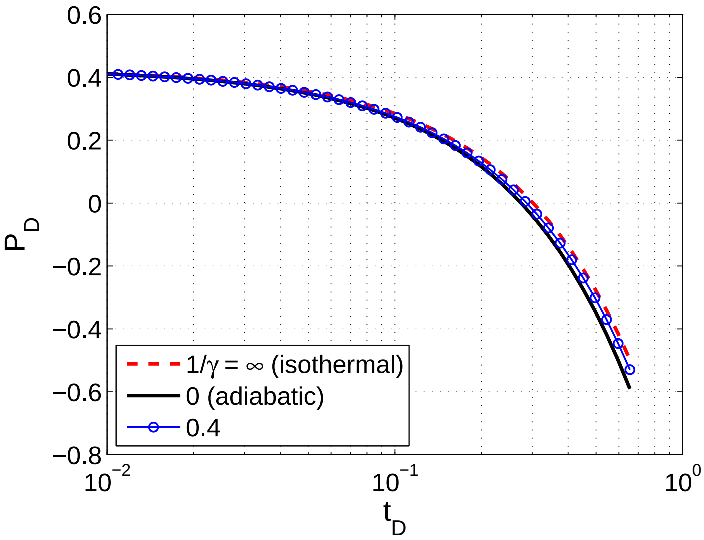

Figure D.3: Dimensionless pressure during a drawdown without formation influx. As the thermal conductivity value decreases $\tau_{heat} \to \infty$ and $1/\gamma \to 0$ and the solution approaches the adiabatic case. X=-1.4, Y=0.09

$$q_D = 1.$$

The Laplace Transforms of Equations D.9 and D.10 are:

$$s\hat{P}_D + \hat{P}_D = sY\langle\hat{\Theta}_D\rangle - Y\langle\Theta_{D_0}\rangle - \frac{X}{s},$$

$$s\hat{\Theta}_D - \Theta_{D_0} = \frac{1}{\gamma}\left[\frac{\partial^2\hat{\Theta}_D}{\partial r_D^2} + \frac{1}{r_D}\frac{\partial\hat{\Theta}_D}{\partial r_D}\right] + s\hat{P}_D.$$

Rearranging terms:

$$\hat{P}_D = \frac{s}{s+1}Y\langle\hat{\Theta}_D\rangle - Y\frac{\langle\Theta_{D_0}\rangle}{s+1} - \frac{X}{s(s+1)} \tag{D.11}$$

$$\frac{\partial^2\hat{\Theta}_D}{\partial r_D^2} + \frac{1}{r_D}\frac{\partial\hat{\Theta}_D}{\partial r_D} - \gamma s\hat{\Theta}_D = -\gamma\Theta_{D_0} - s\gamma\hat{P}_D \tag{D.12}$$

Equation (D.11) is only a function of s. The homogenous solution of equation (D.12) is:

$$\hat{\Theta}_{D_H} = AI_0(\sqrt{\gamma s}r_D) + BK_0(\sqrt{\gamma s}r_D) \tag{D.13}$$

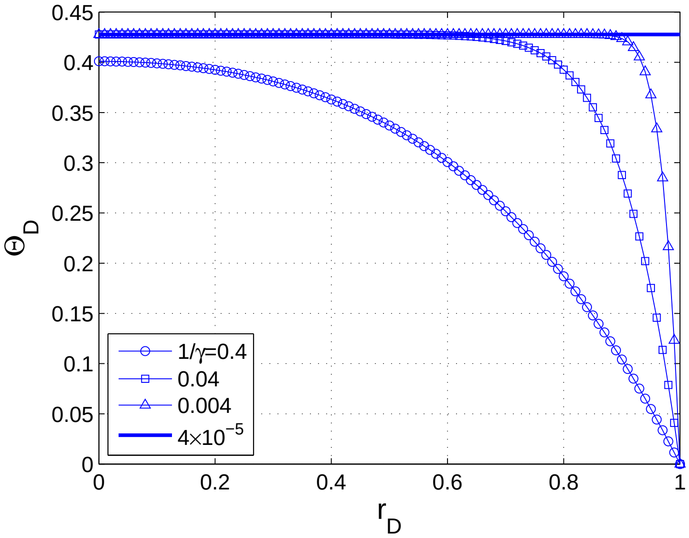

Figure D.4: Dimensionless temperature profile at the end of a drawdown without formation inflow. As the thermal conductivity value decreases $\tau_{heat} \to \infty$ and $1/\gamma \to 0$ and the solution approaches the adiabatic case. X=-1.4, Y=0.09

Given the nature of the right-hand side of (D.12), $g(r_D) = -\gamma\Theta_{D_0}(r_D) - s\gamma\hat{P}_D$, the particular solution is computed using the method of variation of parameters. The basis functions are $f_1 = I_0(\sqrt{\gamma s} r_D)$ and $f_2 = K_0(\sqrt{\gamma s} r_D)$, and the Wronskian is

$$\begin{aligned} W &= \begin{vmatrix} f_1 & f_2 \\ f_1' & f_2' \end{vmatrix} = \begin{vmatrix} I_0(\sqrt{\gamma s} r_D) & K_0(\sqrt{\gamma s} r_D) \\ \sqrt{\gamma s} I_1(\sqrt{\gamma s} r_D) & -\sqrt{\gamma s} K_1(\sqrt{\gamma s} r_D) \end{vmatrix} \\ &= -\sqrt{\gamma s} I_0(\sqrt{\gamma s} r_D) K_1(\sqrt{\gamma s} r_D) - \sqrt{\gamma s} K_0(\sqrt{\gamma s} r_D) I_1(\sqrt{\gamma s} r_D) \\ &= -\frac{1}{r_D} \end{aligned} \tag{D.14}$$

The particular solution is:

$$\begin{aligned} \hat{\Theta}_{D_P} &= -f_1 \int_0^{r_D} \frac{f_2 g}{W} d\tilde{r}_D + f_2 \int_0^{r_D} \frac{f_1 g}{W} d\tilde{r}_D \\ &= -I_0(\sqrt{\gamma s} r_D) \int_0^{r_D} \tilde{r}_D K_0(\sqrt{\gamma s} \tilde{r}_D)(\gamma \Theta_{D_0} + \gamma s \hat{P}_D) d\tilde{r}_D \\ &\quad + K_0(\sqrt{\gamma s} r_D) \int_0^{r_D} \tilde{r}_D I_0(\sqrt{\gamma s} \tilde{r}_D)(\gamma \Theta_{D_0} + \gamma s \hat{P}_D) d\tilde{r}_D \end{aligned} \tag{D.15}$$

$$\begin{aligned}\hat{\Theta}_{D_P} &= -I_0(\sqrt{\gamma s} r_D)\int_0^{r_D} \gamma \tilde{r}_D K_0(\sqrt{\gamma s}\tilde{r}_D)\Theta_{D_0} d\tilde{r}_D \\ &\quad + \sqrt{\gamma s}\hat{P}_D I_0(\sqrt{\gamma s} r_D)\left(r_D K_1(\sqrt{\gamma s} r_D) - \frac{1}{\sqrt{\gamma s}}\right) \\ &\quad + K_0(\sqrt{\gamma s} r_D)\int_0^{r_D} \gamma \tilde{r}_D I_0(\sqrt{\gamma s}\tilde{r}_D)\Theta_{D_0} d\tilde{r}_D \\ &\quad + \sqrt{\gamma s}\hat{P}_D r_D K_0(\sqrt{\gamma s} r_D) I_1(\sqrt{\gamma s} r_D).\end{aligned}$$

Using the relation $K_0(z)I_1(z) + K_1(z)I_0(z) = \frac{1}{z}$, the general solution is simplified as:

$$\begin{aligned}\hat{\Theta}_D &= A I_0(\sqrt{\gamma s} r_D) + B K_0(\sqrt{\gamma s} r_D) - \gamma I_0(\sqrt{\gamma s} r_D)\int_0^{r_D} \tilde{r}_D K_0(\sqrt{\gamma s}\tilde{r}_D)\Theta_{D_0} d\tilde{r}_D \\ &\quad + \gamma K_0(\sqrt{\gamma s} r_D)\int_0^{r_D} \tilde{r}_D I_0(\sqrt{\gamma s}\tilde{r}_D)\Theta_{D_0} d\tilde{r}_D + \hat{P}_D - \hat{P}_D I_0(\sqrt{\gamma s} r_D). \quad \text{(D.16)}\end{aligned}$$

Evaluating the solution as $r_D \to 0$ and using the limiting form of K_0 for small argument ($K_0(z) \sim -\ln z$)

$$\begin{aligned}\hat{\Theta}_D\Big|_{r_D\to 0} &= A + \lim_{r_D\to 0}\left\{-B\ln(\sqrt{\gamma s} r_D) + \gamma\int_0^{r_D} \tilde{r}_D \ln(\sqrt{\gamma s} r_D)\Theta_{D_0}(0) d\tilde{r}_D \right.\\ &\quad \left. - \gamma\Theta_{D_0}(0)\ln(\sqrt{\gamma s} r_D)\int_0^{r_D} \tilde{r}_D d\tilde{r}_D\right\}. \quad \text{(D.17)}\end{aligned}$$

Θ_{D_0} is a continuous function; near $r_D = 0$, Θ_{D_0} may be regarded as a constant. Evaluating the integrals:

$$\begin{aligned}\hat{\Theta}_D\Big|_{r_D\to 0} &= A + \lim_{r_D\to 0}\left\{-B\ln(\sqrt{\gamma s} r_D) + \gamma\Theta_{D_0}(0)\frac{r_D^2}{2}\left[\ln(\sqrt{\gamma s} r_D) - \frac{1}{2}\right]\right.\\ &\quad \left. -\gamma\Theta_{D_0}(0)\frac{r_D^2}{2}\ln(\sqrt{\gamma s} r_D)\right\} \\ &= A + \lim_{r_D\to 0}\left\{-B\ln(\sqrt{\gamma s} r_D) - \gamma\Theta_{D_0}(0)\frac{r_D^2}{4}\right\}\end{aligned}$$

If the solution is to be bounded as $r_D = 0$ (the centerline), then $B = 0$. Evaluating the solution at $r_D = 1$

$$\begin{aligned}\hat{\Theta}_D\Big|_{r_D=1} &= AI_0(\sqrt{\gamma s}) + \hat{P}_D\left(1 - I_0(\sqrt{\gamma s})\right) - \gamma I_0(\sqrt{\gamma s})G_1(1,s) \\ &\quad +\gamma K_0(\sqrt{\gamma s})G_2(1,s) = 0 \qquad \text{(D.18)}\end{aligned}$$

where

$$\begin{aligned}G_1(r_D,s) &= \int_0^{r_D} \tilde{r}_D K_0(\sqrt{\gamma s}\tilde{r}_D)\Theta_{D_0}(\tilde{r}_D)d\tilde{r}_D \\ G_2(r_D,s) &= \int_0^{r_D} \tilde{r}_D I_0(\sqrt{\gamma s}\tilde{r}_D)\Theta_{D_0}(\tilde{r}_D)d\tilde{r}_D \qquad \text{(D.19)}\end{aligned}$$

$$A = -\hat{P}_D\frac{\left(1 - I_0(\sqrt{\gamma s})\right)}{I_0(\sqrt{\gamma s})} + \gamma G_1(1,s) - \gamma\frac{K_0(\sqrt{\gamma s})}{I_0(\sqrt{\gamma s})}G_2(1,s) \qquad \text{(D.20)}$$

$$\begin{aligned}\hat{\Theta}_D &= AI_0(\sqrt{\gamma s}r_D) + \hat{P}_D\left(1 - I_0(\sqrt{\gamma s}r_D)\right) - \gamma I_0(\sqrt{\gamma s}r_D)G_1(r_D,s) \\ &\quad +\gamma K_0(\sqrt{\gamma s}r_D)G_2(r_D,s). \qquad \text{(D.21)}\end{aligned}$$

The mass-average temperature in the flowline is

$$\begin{aligned}\langle\hat{\Theta}_D\rangle &= 2\int_0^1 r_D\hat{\Theta}_D dr_d \qquad \text{(D.22)} \\ &= \frac{2A}{\sqrt{\gamma s}}I_1(\sqrt{\gamma s}) + \hat{P}_D\left(1 - \frac{2}{\sqrt{\gamma s}}I_1(\sqrt{\gamma s})\right) \\ &\quad -2\gamma\int_0^1 r_D I_0(\sqrt{\gamma s}r_D)G_1(r_D,s)dr_D + \\ &\quad +2\gamma\int_0^1 r_D K_0(\sqrt{\gamma s}r_D)G_2(r_D,s)dr_D\end{aligned}$$

The integrals are evaluated by parts:

$$\begin{aligned}
\mathcal{F} &= \int_0^1 r_D I_0(\sqrt{\gamma s} r_D) \int_0^{r_D} \tilde{r}_D K_0(\sqrt{\gamma s}\tilde{r}_D)\Theta_{D_0}(\tilde{r}_D) d\tilde{r}_D dr_D, \\
&= \left[\frac{r_D}{\sqrt{\gamma s}} I_1(\sqrt{\gamma s} r_D) G_1(r_D, s)\right]_0^1 + \\
&\quad - \int_0^1 \frac{r_D^2}{\sqrt{\gamma s}} I_1(\sqrt{\gamma s} r_D) K_0(\sqrt{\gamma s} r_D)\Theta_{D_0}(r_D) dr_D, \\
&= \frac{I_1(\sqrt{\gamma s})}{\sqrt{\gamma s}} G_1(1, s) \\
&\quad - \int_0^1 \frac{r_D^2}{\sqrt{\gamma s}} I_1(\sqrt{\gamma s} r_D) K_0(\sqrt{\gamma s} r_D)\Theta_{D_0}(r_D) dr_D. \qquad \text{(D.23)}
\end{aligned}$$

And,

$$\begin{aligned}
\mathcal{H} &= \int_0^1 r_D K_0(\sqrt{\gamma s} r_D) \int_0^{r_D} \tilde{r}_D I_0(\sqrt{\gamma s}\tilde{r}_D)\Theta_{D_0}(\tilde{r}_D) d\tilde{r}_D dr_D, \\
&= \left[\left(\frac{1}{\gamma s} - \frac{r_D}{\sqrt{\gamma s}} K_1(\sqrt{\gamma s} r_D)\right) G_2(r_D, s)\right]_0^1 + \\
&\quad - \int_0^1 \left(\frac{r_D}{\gamma s} - \frac{r_D^2}{\sqrt{\gamma s}} K_1(\sqrt{\gamma s} r_D)\right) I_0(\sqrt{\gamma s} r_D)\Theta_{D_0}(r_D) dr_D, \\
&= \left(\frac{1}{\gamma s} - \frac{K_1(\sqrt{\gamma s})}{\sqrt{\gamma s}}\right) G_2(1, s) \\
&\quad - \lim_{r_D \to 0} \left[\left(\frac{1}{\gamma s} - \frac{r_D}{\sqrt{\gamma s} r_D \sqrt{\gamma s}}\right) \int_0^{r_D} \tilde{r}_D \Theta_{D_0}(0) d\tilde{r}_D\right] \\
&\quad - \int_0^1 \left(\frac{r_D}{\gamma s} - \frac{r_D^2}{\sqrt{\gamma s}} K_1(\sqrt{\gamma s} r_D)\right) I_0(\sqrt{\gamma s} r_D)\Theta_{D_0}(r_D) dr_D, \\
&= \left(\frac{1}{\gamma s} - \frac{K_1(\sqrt{\gamma s})}{\sqrt{\gamma s}}\right) G_2(1, s) \qquad \text{(D.24)} \\
&\quad - \int_0^1 \left(\frac{r_D}{\gamma s} - \frac{r_D^2}{\sqrt{\gamma s}} K_1(\sqrt{\gamma s} r_D)\right) I_0(\sqrt{\gamma s} r_D)\Theta_{D_0}(r_D) dr_D.
\end{aligned}$$

Substituting these integrals in the expression for $\langle\hat{\Theta}_D\rangle$,

$$\begin{aligned}
\langle\hat{\Theta}_D\rangle &= \frac{2A}{\sqrt{\gamma s}} I_1(\sqrt{\gamma s}) + \hat{P}_D \left(1 - \frac{2}{\sqrt{\gamma s}} I_1(\sqrt{\gamma s})\right) + \\
&\quad -2\gamma \left[\frac{I_1(\sqrt{\gamma s})}{\sqrt{\gamma s}} G_1(1,s) - \left(\frac{1}{\gamma s} - \frac{K_1(\sqrt{\gamma s})}{\sqrt{\gamma s}}\right) G_2(1,s) \right. \\
&\quad \left. - \int_0^1 \frac{r_D^2}{\sqrt{\gamma s}} I_1(\sqrt{\gamma s} r_D) K_0(\sqrt{\gamma s} r_D) \Theta_{D_0}(r_D) dr_D \right] \\
&\quad \left. - \int_0^1 \left(\frac{r_D}{\gamma s} - \frac{r_D^2}{\sqrt{\gamma s}} K_1(\sqrt{\gamma s} r_D)\right) I_0(\sqrt{\gamma s} r_D) \Theta_{D_0}(r_D) dr_D \right), \\
&= \frac{2A}{\sqrt{\gamma s}} I_1(\sqrt{\gamma s}) + \hat{P}_D \left(1 - \frac{2}{\sqrt{\gamma s}} I_1(\sqrt{\gamma s})\right) + \\
&\quad - \frac{2\gamma}{\sqrt{\gamma s}} \left(I_1(\sqrt{\gamma s}) G_1(1,s) + K_1(\sqrt{\gamma s}) G_2(1,s)\right) \\
&\quad + \frac{2}{s} \int_0^1 r_D \Theta_{D_0}(r_D) dr_D. \qquad \text{(D.25)}
\end{aligned}$$

The Wronskian (D.14) was used to simplify the last expression. Inserting the expressions for A (D.20) and $\hat{P}_D$ (D.11):

$$\begin{aligned}
\langle\hat{\Theta}_D\rangle &= -\frac{2}{\sqrt{\gamma s}} \left(\frac{I_1(\sqrt{\gamma s})}{I_0(\sqrt{\gamma s})} - I_1(\sqrt{\gamma s})\right) \left(\frac{s}{s+1} Y \langle\hat{\Theta}_D\rangle - Y \frac{\langle\Theta_{D_0}\rangle}{s+1} - \frac{X}{s(s+1)}\right) \\
&\quad + \frac{2\gamma}{\sqrt{\gamma s}} I_1(\sqrt{\gamma s}) G_1(1,s) - \frac{2\gamma}{\sqrt{\gamma s}} I_1(\sqrt{\gamma s}) \frac{K_0(\sqrt{\gamma s})}{I_0(\sqrt{\gamma s})} G_2(1,s) + \\
&\quad + \left(1 - \frac{2}{\sqrt{\gamma s}} I_1(\sqrt{\gamma s})\right) \left(\frac{s}{s+1} Y \langle\hat{\Theta}_D\rangle - Y \frac{\langle\Theta_{D_0}\rangle}{s+1} - \frac{X}{s(s+1)}\right) + \\
&\quad - \frac{2\gamma}{\sqrt{\gamma s}} \left(I_1(\sqrt{\gamma s}) G_1(1,s) + K_1(\sqrt{\gamma s}) G_2(1,s)\right) + 2\gamma \int_0^1 r_D \Theta_{D_0}(r_D) dr_D \\
&= -(2B-1) \left(\frac{s}{s+1} Y \langle\hat{\Theta}_D\rangle - Y \frac{\langle\Theta_{D_0}\rangle}{s+1} - \frac{X}{s(s+1)}\right) - \frac{2G_2(1,s)}{s I_0(\sqrt{\gamma s})} + \\
&\quad + \frac{2}{s} \int_0^1 r_D \Theta_{D_0}(r_D) dr_D
\end{aligned}$$

$$\langle\hat{\Theta}_D\rangle = \frac{(2\Xi - 1)\left(\frac{Y\langle\Theta_{D_0}\rangle}{s+1} + \frac{X}{s(s+1)}\right) - \frac{2G_2(1,s)}{s I_0(\sqrt{\gamma s})} + \frac{\langle\Theta_{D_0}\rangle}{s}}{1 + \frac{sY(2B-1)}{s+1}}, \qquad \text{(D.26)}$$

where

$$\Xi \equiv \frac{1}{\sqrt{\gamma s}} \frac{I_1(\sqrt{\gamma s})}{I_0(\sqrt{\gamma s})}.$$

The dimensionless pressure is computed by inversion of equation (D.11), which is done using the convolution theorem:

$$\begin{aligned}
P_D &= Y\mathcal{L}^{-1}\left\{e^{-t_D} * \frac{d\langle\Theta_D\rangle}{dt_D}\right\} - X\mathcal{L}^{-1}\left\{1 * e^{-t_D}\right\} \\
&= Y\int_o^{t_D} e^{-(t_D-\tau)}\frac{d\langle\Theta_D\rangle}{d\tau}d\tau - X\int_o^{t_D} 1e^{-(t_D-\tau)}d\tau \\
&= Y\left[e^{-(t_D-\tau)}\langle\Theta_D\rangle(\tau)\Big|_0^{t_D} - \int_o^{t_D}\langle\Theta_D\rangle(\tau)e^{-(t_D-\tau)}d\tau\right] - X\left(1 - e^{-t_D}\right) \\
&= Y\left[\langle\Theta_D\rangle - e^{-t_D}\langle\Theta_{D_0}\rangle - \int_o^{t_D}\langle\Theta_D\rangle(\tau)e^{-(t_D-\tau)}d\tau\right] - X\left(1 - e^{-t_D}\right)
\end{aligned}$$

In the evaluation of the solution the integrals G_1 and G_2 and the integral in the Equation of P_D are computed by quadrature.

D.3 Buildup

In this case $t_D > t_{dd_D}$ and $P_D > 0$.

$$\frac{dP_D}{dt_D} + P_D = Y\frac{d\langle\Theta_D\rangle}{dt_D} \tag{D.27}$$

$$\frac{\partial\Theta_D}{\partial t_D} = \frac{1}{\gamma}\left[\frac{\partial^2\Theta_D}{\partial r_D^2} + \frac{1}{r_D}\frac{\partial\Theta_D}{\partial r_D}\right] + \frac{dP_D}{dt_D} \tag{D.28}$$

with the following initial and boundary conditions:

$$P_D(0) = P_{D_{dd}},$$

$$\Theta_D(r_D, 0) = \Theta_{D_{dd}}(r_D),$$

$$\Theta_D(1, t_D) = 0,$$

$$\langle \Theta_D \rangle (0) = \langle \Theta_{D_{dd}} \rangle,$$

$$q_D = 0$$

The Laplace Transforms of Equations (D.27) and (D.28) are

$$s\hat{P}_D + \hat{P}_D = P_{D_{dd}} + sY\langle \hat{\Theta}_D \rangle - Y\langle \Theta_{D_{dd}} \rangle,$$

$$s\hat{\Theta}_D - \Theta_{D_{dd}} = \frac{1}{\gamma}\left[\frac{\partial^2 \hat{\Theta}_D}{\partial r_D^2} + \frac{1}{r_D}\frac{\partial \hat{\Theta}_D}{\partial r_D}\right] + s\hat{P}_D - P_{D_{dd}}.$$

Rearranging terms in the mass balance equation yields

$$\hat{P}_D = \frac{s}{s+1} Y\langle \hat{\Theta}_D \rangle - Y\frac{\langle \Theta_{D_{dd}} \rangle}{s+1} + \frac{P_{D_{dd}}}{s+1}. \tag{D.29}$$

Rearranging terms in the energy equation and inserting (D.29) gives

$$\begin{aligned} \frac{\partial^2 \hat{\Theta}_D}{\partial r_D^2} + \frac{1}{r_D}\frac{\partial \hat{\Theta}_D}{\partial r_D} - \gamma s \hat{\Theta}_D \quad &= \quad -\gamma \Theta_{D_{dd}} - \gamma \frac{s}{s+1}\left(P_{D_{dd}} - Y\langle \Theta_{D_{dd}} \rangle\right) \\ &\quad -\gamma Y \frac{s^2}{s+1}\langle \hat{\Theta}_D \rangle + \gamma P_{D_{dd}}. \end{aligned} \tag{D.30}$$

The homogenous form solution of this equation is:

$$\hat{\Theta}_{D_H} = AI_0(\sqrt{\gamma s} r_D) + BK_0(\sqrt{\gamma s} r_D). \tag{D.31}$$

The right side of (D.30) is a function of r_D and s, hence it can be simplified as follows,

$$g(s, r_D) = -\gamma \Theta_{D_{dd}} + \gamma h(s)$$

$$h(s) = \frac{1}{s+1} P_{D_{dd}} - Y\frac{s}{s+1}\left(s\langle \hat{\Theta}_D \rangle - \langle \Theta_{D_{dd}} \rangle\right).$$

The particular solution is computed using the method of variation of parameters with same basis functions and Wronskian as in (D.14); therefore,

$$\begin{aligned}
\hat{\Theta}_{D_P} &= -I_0(\sqrt{\gamma s}r_D)\int_0^{r_D}\tilde{r}_D K_0(\sqrt{\gamma s}\tilde{r}_D)(\gamma\Theta_{D_{dd}}(\tilde{r}_D)-\gamma h(s))d\tilde{r}_D\\
&\quad +K_0(\sqrt{\gamma s}r_D)\int_0^{r_D}\tilde{r}_D I_0(\sqrt{\gamma s}\tilde{r}_D)(\gamma\Theta_{D_{dd}}(\tilde{r}_D)-\gamma h(s))d\tilde{r}_D,\\
&= -I_0(\sqrt{\gamma s}r_D)\int_0^{r_D}\gamma\tilde{r}_D K_0(\sqrt{\gamma s}\tilde{r}_D)\Theta_{D_{dd}}d\tilde{r}_D\\
&\quad \frac{\gamma h}{\sqrt{\gamma s}}I_0(\sqrt{\gamma s}r_D)\left(r_D K_1(\sqrt{\gamma s}r_D)-\frac{1}{\sqrt{\gamma s}}\right)\\
&\quad +K_0(\sqrt{\gamma s}r_D)\int_0^{r_D}\gamma\tilde{r}_D I_0(\sqrt{\gamma s}\tilde{r}_D)\Theta_{D_{dd}}d\tilde{r}_D\\
&\quad -\frac{\gamma h}{\sqrt{\gamma s}}r_D K_0(\sqrt{\gamma s}r_D)I_1(\sqrt{\gamma s}r_D). \qquad \text{(D.32)}
\end{aligned}$$

Using the relation $K_0(z)I_1(z)+K_1(z)I_0(z)=\frac{1}{z}$, the general solution is simplified as follows,

$$\begin{aligned}
\hat{\Theta}_D &= AI_0(\sqrt{\gamma s}r_D)+BK_0(\sqrt{\gamma s}r_D)-\gamma I_0(\sqrt{\gamma s}r_D)\int_0^{r_D}\tilde{r}_D K_0(\sqrt{\gamma s}\tilde{r}_D)\Theta_{D_{dd}}d\tilde{r}_D\\
&\quad +\gamma K_0(\sqrt{\gamma s}r_D)\int_0^{r_D}\tilde{r}_D I_0(\sqrt{\gamma s}\tilde{r}_D)\Theta_{D_{dd}}d\tilde{r}_D+\frac{h}{s}\left(I_0(\sqrt{\gamma s}r_D)-1\right). \qquad \text{(D.33)}
\end{aligned}$$

Evaluating the solution as $r_D \to 0$ and using the limiting form of K_0 for small argument ($K_0(z) \sim -\ln z$)

$$\begin{aligned}
\hat{\Theta}_D\Big|_{r_D\to 0} &= A+\lim_{r_D\to 0}\left\{-B\ln(\sqrt{\gamma s}r_D)+\gamma\int_0^{r_D}\tilde{r}_D\ln(\sqrt{\gamma s}r_D)\Theta_{D_{dd}}(0)d\tilde{r}_D+\right.\\
&\quad \left.-\gamma\Theta_{D_{dd}}(0)\ln(\sqrt{\gamma s}r_D)\int_0^{r_D}\tilde{r}_D d\tilde{r}_D\right\}.\\
&= A+\lim_{r_D\to 0}\left\{-B\ln(\sqrt{\gamma s}r_D)+\gamma\Theta_{D_{dd}}(0)\frac{r_D^2}{2}\left[\ln(\sqrt{\gamma s}r_D)-\frac{1}{2}\right]\right.\\
&\quad \left.-\gamma\Theta_{D_{dd}}(0)\frac{r_D^2}{2}\ln(\sqrt{\gamma s}r_D)\right\}\\
&= A+\lim_{r_D\to 0}\left\{-B\ln(\sqrt{\gamma s}r_D)-\gamma\Theta_{D_{dd}}(0)\frac{r_D^2}{4}\right\} \qquad \text{(D.34)}
\end{aligned}$$

If the solution is to be bounded as $r_D \to 0$, then $B = 0$. Evaluating the solution at $r_D = 1$, 1

$$\begin{aligned}\hat{\Theta}_D\Big|_{r_D=1} &= AI_0(\sqrt{\gamma s}) - \gamma I_0(\sqrt{\gamma s})G_1(1,s) \\ &\quad +\gamma K_0(\sqrt{\gamma s})G_2(1,s) + \frac{h}{s}\left(I_0(\sqrt{\gamma s}) - 1\right) = 0, \qquad \text{(D.35)}\end{aligned}$$

where

$$\begin{aligned}G_1(r_D,s) &= \int_0^{r_D} \tilde{r}_D K_0(\sqrt{\gamma s}\tilde{r}_D)\Theta_{D_{dd}}(\tilde{r}_D)d\tilde{r}_D, \\ G_2(r_D,s) &= \int_0^{r_D} \tilde{r}_D I_0(\sqrt{\gamma s}, \tilde{r}_D)\Theta_{D_{dd}}(\tilde{r}_D)d\tilde{r}_D \qquad \text{(D.36)}\end{aligned}$$

and

$$A = \gamma G_1(1,s) - \gamma\frac{K_0(\sqrt{\gamma s})}{I_0(\sqrt{\gamma s})}G_2(1,s) - \frac{h(s)}{s}\left(\frac{I_0(\sqrt{\gamma s}) - 1}{I_0(\sqrt{\gamma s})}\right). \qquad \text{(D.37)}$$

Therefore, the dimensionless temperature distribution in Laplace Domain is

$$\begin{aligned}\hat{\Theta}_D &= AI_0(\sqrt{\gamma s}r_D) - \gamma I_0(\sqrt{\gamma s}r_D)G_1(r_D,s) + \qquad \text{(D.38)} \\ &\quad +\gamma K_0(\sqrt{\gamma s}r_D)G_2(r_D,s) + \frac{h}{s}\left(I_0(\sqrt{\gamma s}r_D) - 1\right),\end{aligned}$$

and the mass-average temperature in the flowline is,

$$\begin{aligned}\langle\hat{\Theta}_D\rangle &= 2\int_0^1 r_D\hat{\Theta}_D dr_d \\ &= \frac{2A}{\sqrt{\gamma s}}I_1(\sqrt{\gamma s}) + \frac{h(s)}{s}\left(\frac{2}{\sqrt{\gamma s}}I_1(\sqrt{\gamma s}) - 1\right) \\ &\quad -2\gamma\int_0^1 r_D I_0(\sqrt{\gamma s}r_D)G_1(r_D,s)dr_D \\ &\quad +2\gamma\int_0^1 r_D K_0(\sqrt{\gamma s}r_D)G_2(r_D,s)dr_D. \qquad \text{(D.39)}\end{aligned}$$

The integrals in D.39 were evaluated in the previous case (Equations D.23 and D.24). Substituting these integrals in the expression for $\langle\hat{\Theta}_D\rangle$ and simplifying yields

$$\begin{aligned}\langle\hat{\Theta}_D\rangle &= \frac{2A}{\sqrt{\gamma s}} I_1(\sqrt{\gamma s}) + \frac{h(s)}{s}\left(\frac{2}{\sqrt{\gamma s}} I_1(\sqrt{\gamma s}) - 1\right) + \\ & \quad -\frac{2\gamma}{\sqrt{\gamma s}} I_1(\sqrt{\gamma s}) G_1(1,s) - \frac{2\gamma}{\sqrt{\gamma s}} K_1(\sqrt{\gamma s}) G_2(1,s) + \frac{\langle\Theta_{D_{dd}}\rangle}{s}.\end{aligned}$$

The Wronskian given in (D.14) was used to simplify the last expression. Inserting the expressions for A (D.20) and $\hat{P}_D$ (D.29) gives

$$\begin{aligned}\langle\hat{\Theta}_D\rangle &= -\frac{2I_1(\sqrt{\gamma s})}{\sqrt{\gamma s}}\left[\gamma G_1(1,s) - \gamma\frac{K_0(\sqrt{\gamma s})}{I_0(\sqrt{\gamma s})} G_2(1,s) - \frac{h(s)}{s}\left(\frac{I_0(\sqrt{\gamma s}) - 1}{I_0(\sqrt{\gamma s})}\right)\right] \\ & \quad + \frac{h(s)}{s}\left(\frac{2I_1(\sqrt{\gamma s})}{\sqrt{\gamma s}} - 1\right)\left(\frac{P_{D_{dd}}}{s+1} - \frac{Y}{s+1}(s\langle\hat{\Theta}_D\rangle - \langle\Theta_{D_{dd}}\rangle)\right) + \\ & \quad -\frac{2\gamma}{\sqrt{\gamma s}}\left(I_1(\sqrt{\gamma s}) G_1(1,s) + K_1(\sqrt{\gamma s}) G_2(1,s)\right) + \frac{\langle\Theta_{D_{dd}}\rangle}{s} \\ &= -\frac{2G_2(1,2)}{sI_0(\sqrt{\gamma s})} - \frac{h(s)}{s}(1 - 2\Xi) + \frac{\langle\Theta_{D_{dd}}\rangle}{s} \\ &= -\frac{2G_2(1,2)}{sI_0(\sqrt{\gamma s})} - (1 - 2\Xi)\left(\frac{1}{s(s+1)} P_{D_{dd}} - Y\frac{1}{s+1}\left(s\langle\hat{\Theta}_D\rangle - \langle\Theta_{D_{dd}}\rangle\right)\right) \\ &= +\frac{\langle\Theta_{D_{dd}}\rangle}{s} \qquad \text{(D.40)}\end{aligned}$$

$$\langle\hat{\Theta}_D\rangle = \frac{(2\Xi - 1)\left(\frac{Y\langle\Theta_{D_{dd}}\rangle}{s+1} + \frac{P_{D_{dd}}}{s(s+1)}\right) - \frac{2G_2(1,s)}{sI_0(\sqrt{\gamma s})} + \frac{\langle\Theta_{D_{dd}}\rangle}{s}}{1 + \frac{sY(2B-1)}{s+1}}, \qquad \text{(D.41)}$$

where

$$\Xi \equiv \frac{1}{\sqrt{\gamma s}}\frac{I_1(\sqrt{\gamma s})}{I_0(\sqrt{\gamma s})}.$$

The dimensionless pressure is computed by inversion of equation (D.29), which is done using the convolution theorem:

$$\begin{aligned}P_D &= Y\mathcal{L}^{-1}\left\{e^{-t_D} * \frac{d\langle\Theta_D\rangle}{dt_D}\right\} + P_{D_{dd}}\mathcal{L}^{-1}\left\{\frac{1}{s+1}\right\} \qquad \text{(D.42)} \\ &= Y\left[\langle\Theta_D\rangle - e^{-t_D}\langle\Theta_{D_{dd}}\rangle - \int_o^{t_D}\langle\Theta_D\rangle(\tau)e^{-(t_D-\tau)}d\tau\right] + P_{D_{dd}}e^{-t_D}\end{aligned}$$

Some of the solutions obtained were quite complex, particularly as the flowline model increases in complexity. The solutions in Laplace Domain were subject to the following checks:

- Evaluate the behavior as $t \to \infty$ to make sure that the temperature equilibrates to the wellbore temperature. In Laplace Transform space (Doetsch, 1961):
$$\lim_{t\to\infty} Y(t) = \lim_{s\to 0} s\hat{Y}(s)$$
- Evaluate the behavior as $t \to 0$ to make sure that the initial condition is reproduced. In Laplace Transform space:
$$\lim_{t\to 0} Y(t) = \lim_{s\to\infty} s\hat{Y}(s)$$
- checking the limiting cases against the known solutions from the isothermal model or the thermodynamic analyis:
  - $1/\gamma \to 0$, i.e. the adiabatic case
  - $1/\gamma \to \infty$, i.e. the isothermal case
  - $Y = 0$: isothermal case

D.4 Alternative Solution of the Radial Temperature Distribution at the End of Drawdown

The radial temperature distribution in the flowline at the end of drawdown ($t_D = t_{dd_D}$), given by equation (D.21), is required for the computation of the average temperature and pressure during buildup. However, the numerical evaluation of this solution using the high precision Laplace transform inversion algorithm of Abate and Valkó (2004) (Appendix G) was not always successful. The solution could be evaluated when the initial temperature distribution (when fluid enters the flowline) was input as constant. This result was compared with the solution of the drawdown problem obtained separately assuming that there is no initial pressure overbalance ($\Theta_D(r_D, 0) = 0$). The results agree.

For low values of the parameter γ (e.g. flowline radius ≤ 0.25 cm) it was also possible to compute a solution, but the value of the precision parameter M in the inversion algorithm had to be decreased, if M is too small then the accuracy of the results suffers. For smaller values of $1/\gamma$ the temperature gradient is expected to be low toward the center of the flowline and very large toward the edges to meet the boundary condition ($\Theta_D(1, t_D) = 0$). Though the problem appears to resemble the adiabatic case, there are differences in the buildup solution when assuming that the drawdown occurred under adiabatic conditions and when heat conduction is accounted for.

To compute the temperature distribution at the end of drawdown the problem was reformulated expressing the flowline temperature and pressure during the entire drawdown as [3]:

$$\begin{aligned} \Theta &= \Theta_1 + \Theta_2 \\ P &= P_1 + P_2 \end{aligned} \tag{D.43}$$

---

[3] in the following discussion all the variables are dimensionless, but the subscript D has been dropped for convenience

for $0 < t < t_{dd}$:

$$\begin{aligned}
\frac{dP_2}{dt} &= Y\frac{d\langle\Theta_2\rangle}{dt} - X \\
\frac{\partial\Theta_2}{\partial t} &= \frac{1}{\gamma}\nabla^2\Theta_2 + \frac{dP_2}{dt} \\
P_2(0) &= P_{D0} \\
\langle\Theta_2\rangle(0) &= 0 \\
\Theta_2(1,t) &= 0 \\
\Theta_2(r,0) &= 0 \qquad \text{(D.44)}
\end{aligned}$$

The time t^* is defined as $P_2(t^*) = 0$. For $0 < t < t^*$:

$$\begin{aligned}
\Theta_1 &\equiv 0 \\
P_1 &\equiv 0 \qquad \text{(D.45)}
\end{aligned}$$

The boundary and initial conditions for Θ_1 over the interval $t^* < t < t_{dd}$ need to be defined. For $t^* < t < t_{dd}$:

$$\begin{aligned}
\frac{dP}{dt} + P &= Y\frac{d\langle\Theta\rangle}{dt} - X \\
\frac{\partial\Theta}{\partial t} &= \frac{1}{\gamma}\nabla^2\Theta + \frac{dP}{dt} \\
P(t^*) &= 0 \\
\Theta(r,t^*) &= \Theta_2(r,t^*) \\
\Theta(1,t) &= 0 \\
\langle T\rangle(t^*) &= \langle\Theta_2\rangle(t^*) \qquad \text{(D.46)}
\end{aligned}$$

substituting (D.43)in (D.46):

$$\begin{aligned}
\frac{dP_1}{dt} + P_1 &= -\frac{dP_2}{dt} - P_2 + Y\left(\frac{d\langle\Theta_1\rangle}{dt} + \frac{d\langle\Theta_2\rangle}{dt}\right) - X \\
\frac{\partial\Theta_1}{\partial t} + \frac{\partial\Theta_2}{\partial t} &= \frac{1}{\gamma}\left(\nabla^2\Theta_1 + \nabla^2\Theta_2\right) + \left(\frac{dP_1}{dt} + \frac{dP_2}{dt}\right)
\end{aligned}$$

inserting the definition of the problem for P_2 and Θ_2 (D.44) from $(t^* < t < t_{dd})$

$$\begin{aligned} \frac{dP_1}{dt} + P_1 &= Y\frac{d\langle\Theta_1\rangle}{dt} - P_2 \\ \frac{\partial\Theta_1}{\partial t} &= \frac{1}{\gamma}\nabla^2\Theta_1 + \frac{dP_1}{dt} \end{aligned} \tag{D.47}$$

the initial conditions for the P_1, Θ_1 problem are determined likewise:

$$\begin{aligned} P(t^*) &= P_1(t^*) + P_2(t^*) = 0 \\ P_1(t^*) &= -P_2(t^*) = 0 \\ \\ \Theta(r, t^*) &= \Theta_1(r, t^*) + \Theta_2(r, t^*) = \Theta_2(r, t^*) \\ \Theta_1(r, t^*) &= 0 \\ \\ \Theta(1, t) &= \Theta_1(1, t) + \Theta_2(1, t) = 0 \\ \Theta_1(1, t) &= 0 \\ \\ \langle\Theta\rangle(t^*) &= \langle\Theta_1\rangle(t^*) + \langle\Theta_2\rangle(t^*) = \langle\Theta_2\rangle(t^*) \\ \langle\Theta_1\rangle(t^*) &= 0 \end{aligned} \tag{D.48}$$

The P_1, Θ_1 problem given by equations (D.47) and (D.48) could be solved by Laplace transforms, however, the solution will require a numerical inversion which would be complicated because P_1 and P_2 have to be evaluated simultaneously over two different times, i.e., $P_1 = P_1(\Delta t)$ and $P_2 = P_2(t^* + \Delta t)$, where $0 < \Delta t < t_{dd} - t^*$. An alternative is to treat the equation of P_1 as a first order ordinary differential equation with variable coefficients:

$$\begin{aligned}
\frac{dP_1}{dt} + P_1 &= Y\frac{d\langle\Theta_1\rangle}{dt} - P_2 = g(t) \\
P_1 &= e^{-t}\int_{t^*}^{t} e^t g(t)dt \\
&= -e^{-t}\left[Y\int_{t^*}^{t} e^t \frac{d\langle\Theta_1\rangle}{dt}dt + \int_{t^*}^{t} e^t P_2(t)dt\right] \\
&= -e^{-t}\left[Y\left(e^t\langle\Theta_1\rangle\big|_{t^*}^{t} - \int_{t^*}^{t} e^t\langle\Theta_1\rangle dt\right) + \int_{t^*}^{t} e^t P_2(t)dt\right] \\
&= -e^{-t}\left[Ye^t\langle\Theta_1\rangle(t) + \int_{t^*}^{t} e^t\left(P_2(t) - Y\langle\Theta_1\rangle(t)\right)dt\right] \qquad \text{(D.49)}
\end{aligned}$$

This requires knowledge of $\langle\Theta_1\rangle$, but according to the definition (D.43) $\langle\Theta_1\rangle = \langle\Theta\rangle - \langle\Theta_2\rangle$. Fortunately, the solution of $\langle\Theta\rangle$ derived previously for the drawdown with formation inflow (D.26) can be inverted numerically and $\langle\Theta_1\rangle$ is available. Hence, $P_1(t)$ and $\frac{dP_1}{dt}(t)$ can be obtained by (D.49) solving the integrals numerically.

An even more convenient approach is to evaluate

$$\frac{dP_1}{dt} = Y\frac{d\langle\Theta_1\rangle}{dt} - P_2 - P_1 = Y\frac{d\langle\Theta_1\rangle}{dt} - P$$

where the derivative of Θ_1 is computed numerically and P is available from the original solution eq.(D.29). Finally, the Laplace transform of the differential equation for $\Theta_1(r,t)$ is:

$$\frac{\partial^2\hat{\Theta}_1}{\partial r^2} + \frac{1}{r}\frac{\partial\hat{\Theta}_1}{\partial r} - \gamma s\hat{\Theta}_1 = -\gamma\frac{dP_1}{dt} \qquad \text{(D.50)}$$

which after solving for Θ_1 and applying the boundary conditions can be written as:

$$\hat{\Theta}_1(r,s) = \frac{1}{\gamma s}\left[\frac{I_0(\sqrt{\gamma s}\; r)}{I_0(\sqrt{\gamma s})} - 1\right]\mathcal{L}\left\{\gamma\frac{dP_1}{dt}\right\} \qquad \text{(D.51)}$$

The inverse Laplace transform of the solution to the homogeneous problem is known [4]:

$$\mathcal{L}^{-1}\left\{\frac{1}{s}\left[\frac{I_0(\sqrt{\gamma s}\ r)}{I_0(\sqrt{\gamma s})}-1\right]\right\}=-2\sum_{n=1}^{\infty}e^{-\alpha_n^2 t/\gamma}\frac{J_0(\alpha_n r)}{\alpha_n J_1(\alpha_n)} \tag{D.52}$$

where J_0 and J_1 are the Bessel functions of the first kind of order zero and one respectively, and α_n are the nth roots of J_0. The solution of (E.22) is obtained by applying the convolution theorem.

$$\Theta_1(r,\Delta t)=2\int_0^{\Delta t}\frac{dP_1}{d\tau}\sum_{n=1}^{\infty}e^{-\alpha_n^2(\Delta t-\tau)/\gamma}\frac{J_0(\alpha_n r)}{\alpha_n J_1(\alpha_n)}d\tau \tag{D.53}$$

The numerical evaluation of this integral at time $\Delta t = t_{dd} - t^*$ has been used successfully to determine the initial conditions for the buildup computations. However, proper caution must be made of the size of the time interval (D.53) and the number of roots, α_n, as the numerical error in the solution could be large for small values of γ (small flowline radius). $n_{\Delta t} = 300$ and $n_\alpha = 300$ has been found satisfactory.

---

[4] Carslaw and Jaeger p. 328

Appendix E

Multi-Radii Flowline with Constant Wall Temperature

The solutions obtained in the previous section correspond to a flowline with constant radius. In reality the flowline of a formation tester consists of several components with different dimensions and geometries. Also, some of the components may be surrounded by air, which would make them behave as thermally insulated. This section presents the procedure for taking into account multiple components in the calculation of the mass-average temperature. It is assumed that all flowline elements are cylindrical, and that the temperature at the wall is constant and equal to the wellbore temperature ($\Theta_i(r = r_{fl_i}, t) = \Theta_{well}$). Thermally insulated components are also taken into account. Refer to Figure E.1.

To take into account the different radii and length of the flowline components, the flowline is modeled as a series of n cylindrical components, each with radius r_i and volume V_i. End effects are ignored. The independent variable r_{Di} is introduced:

$$r_{Di} \equiv \frac{r}{r_i} \tag{E.1}$$

This variable enters in the heat conduction term in the temperature equation

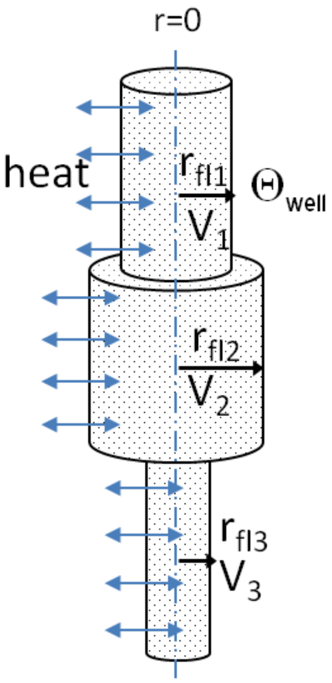

Figure E.1: Flowline model for the computation of Pressure and Temperature accounting for conduction and various flowline components of different radii.

for each flowline component:

$$\nabla\Theta_{D_i} = \frac{\partial^2\Theta_{D_i}}{\partial r_{D_i}^2} \tag{E.2}$$

$\Theta_{D_i}(r_{D_i} = 1, t_D) = 1$, and the temperature is bounded at $r_{D_i} = 0$. The pressure in the flow line is spatially uniform, and depends on the total mass-average temperature:

$$\frac{d\langle\Theta_D\rangle}{dt_D} = \frac{\sum_{i=1}^{n} \frac{d\langle\Theta_{D_i}\rangle}{dt_D}\rho_i V_i}{\sum_{i=1}^{n} \rho_i V_i} \tag{E.3}$$

Where the density of the flowline fluid is assumed constant, as done previously. The average temperature in each flowline segment, $\langle\Theta_{D_i}\rangle$, is computed as in the previous case using equation(D.1).

E.1 Drawdown without Formation Inflow

$$\frac{dP_D}{dt_D} = Y\frac{d\langle\Theta_D\rangle}{dt_D} - X$$

for each flowline component i, $i \in [1, N_c]$

$$\frac{\partial\Theta_{D_i}}{\partial t_D} = \frac{1}{\gamma_i}\nabla^2\Theta_{D_i} + \frac{dP_D}{dt_D} \tag{E.4}$$

$$P_D(0) = P_{D_0},$$

$$\forall i\ , \Theta_{D_i}(r_D, 0) = 0, \ \ \Rightarrow \langle\Theta_D\rangle(0) = 0,$$

and,

$$\forall i\ , \Theta_{D_i}(1, t_D) = 0.$$

Similarly to the solution for a one component system, the temperature in each component (in Laplace Transform Domain) is

$$\hat{\Theta}_{D_i} = \left(\frac{X}{s^2} - Y\langle\hat{\Theta}_D\rangle\right)\left(\frac{I_0(\sqrt{s\gamma}\ r_D)}{I_0(\sqrt{s\gamma})} - 1\right). \tag{E.5}$$

This equation is similar to (D.8), however the difference for a multi-component system is that in equation (E.5) $\langle\hat{\Theta}_D\rangle$ is the total mass-average temperature in the entire flowline. The average temperature for each component $\langle\hat{\Theta}_{D_i}\rangle$ is obtained by integrating (E.5) over the flowline cross-section, and the mass-average temperature of the entire flow line is obtained from the relation:

$$\langle\hat{\Theta}_D\rangle = \frac{\sum_i^{N_c} V_i\langle\hat{\Theta}_{D_i}\rangle}{V_{total}}$$

the mass-average temperature for a flowline with two or more components is:

$$\langle\hat{\Theta}_D\rangle = \frac{\frac{X}{s^2}\sum_1^{N_c} V_i\left(\frac{2}{\sqrt{\gamma_i s}}\frac{I_1(\sqrt{\gamma_i s})}{I_0(\sqrt{\gamma_i s})} - 1\right)}{V_{total} + Y\sum_1^{N_c} V_i\left(\frac{2}{\sqrt{\gamma_i s}}\frac{I_1(\sqrt{\gamma_i s})}{I_0(\sqrt{\gamma_i s})} - 1\right)} \tag{E.6}$$

If some flowline components are thermally insulated, for instance if surrounded by air, then for such components the coefficient $\gamma_i \to \infty$. The total mass-average temperature of the flowline accounting for a certain volume, V_{ins}, that does not conduct heat is

$$\langle \hat{\Theta}_D \rangle = \frac{\frac{X}{s^2} \sum_1^{N_c-1} V_i \left(\frac{2}{\sqrt{\gamma_i s}} \frac{I_1(\sqrt{\gamma_i s})}{I_0(\sqrt{\gamma_i s})} - 1 \right) + V_{ins} \frac{X}{s^2(Y-1)}}{V_{total} + Y \sum_1^{N_c} V_i \left(\frac{2}{\sqrt{\gamma_i s}} \frac{I_1(\sqrt{\gamma_i s})}{I_0(\sqrt{\gamma_i s})} - 1 \right)}, \tag{E.7}$$

with $V_{total} = \sum_1^{N_c-1} V_i + V_{ins}$.

E.2 Drawdown with Formation Inflow

The mass-average flowline temperature is:

$$\begin{aligned} \langle \hat{\Theta}_D \rangle \;\; = \;\; & \frac{\left(\frac{Y \langle \Theta_{D_0} \rangle}{s+1} + \frac{X}{s(s+1)} \right) \left(\sum_1^{N_c-1} V_i M_i - V_{ins} \right) - \frac{2}{s} \sum_1^{N_c-1} \frac{V_i G_{2i}(1,s;\Theta_{D_0})}{I_0(\sqrt{\gamma_i s})}}{\frac{sY}{s+1} \left(\sum_1^{N_c-1} V_i M_i - V_{ins} \right) + V_{total}} \\ & + \frac{V_{total} \frac{\langle \Theta_{D_0} \rangle}{s}}{\frac{sY}{s+1} \left(\sum_1^{N_c-1} V_i M_i - V_{ins} \right) + V_{total}}, \end{aligned} \tag{E.8}$$

where

$$M_i = \frac{2}{\sqrt{\gamma_i s}} \frac{I_1(\sqrt{\gamma_i s})}{I_0(\sqrt{\gamma_i s})} - 1$$

$$G_{2i}(r_D, s, T) = \int_0^{r_D} \tilde{r} I_0(\sqrt{\gamma_i s} \tilde{r}) T(\tilde{r}) d\tilde{r}.$$

The dimensionless pressure is obtained as for the one component case, that is,

$$\hat{P}_D = \frac{s}{s+1} Y \langle \hat{\Theta}_D \rangle - Y \frac{\langle \Theta_{D_0} \rangle}{s+1} - \frac{X}{s(s+1)},$$

and the temperature distribution for each component is

$$\begin{aligned} \hat{\Theta}_{D_i} \;\; = \;\; & A_i(s; \gamma_i, , P_D) I_0(\sqrt{\gamma_i s} r_D) + \hat{P}_D \left(1 - I_0(\sqrt{\gamma_i s} r_D)\right) + \\ & -\gamma_i I_0(\sqrt{\gamma_i s}) G_{1i}(r_D, s; \Theta_{D_0}) + \gamma_i K_0(\sqrt{\gamma_i s} G_{2i}(r_D, s; \Theta_{D_0}), \end{aligned} \tag{E.9}$$

where

$$\begin{aligned} A_i(s;\gamma_i,\Theta_{D_0},\hat{P}_D) &= -\hat{P}_D \frac{1-I_0(\sqrt{\gamma_i s})}{I_0(\sqrt{\gamma_i s})} + \gamma_i G_{1i}(1,s;\Theta_{D_0}) \\ &\quad -\gamma_i \frac{K_0(\sqrt{\gamma_i s})}{I_0(\sqrt{\gamma_i s})} G_{2i}(1,s;\Theta_{D_0}), \end{aligned}$$

and

$$G_{1i}(r_D,s;\Theta_{D_0}) = \int_0^{r_D} \tilde{r} K_0(\sqrt{\gamma_i s}\tilde{r})\Theta_{D_0}(\tilde{r})d\tilde{r}$$

$A_i(s;\gamma_i,\Theta_{D_0},P_D)$ is the value of the temperature at the center of the flowline ($r_D = 0$). However, the numerical inversion of $G_{1i}(r_D,s;\Theta_{D_0})$ is difficult and the alternate approach to solve the problem described in section D.4 is used in the numerical evaluation of $\Theta_{D_{dd}} = \Theta_D(t_{dd})$. Notice that if the initial temperature distribution is zero, then the numerical Laplace transform inversion of (E.9) is successful.

E.3 Buildup with Formation Inflow

The mass-average flowline temperature is:

$$\begin{aligned} \langle\hat{\Theta}_D\rangle &= \frac{\left(\frac{Y\langle\Theta_{D_{dd}}\rangle}{s+1} + \frac{P_{D_{dd}}}{s(s+1)}\right)\left(\sum_1^{N_c-1} V_i M_i - V_{ins}\right) - \frac{2}{s}\sum_1^{N_c-1}\frac{V_i G_{2i}(1,s;\Theta_{D_{dd}})}{I_0(\sqrt{\gamma_i s})}}{\frac{sY}{s+1}\left(\sum_1^{N_c-1} V_i M_i - V_{ins}\right) + V_{total}} \\ &\quad + \frac{V_{total}\frac{\langle\Theta_{D_{dd}}\rangle}{s}}{\frac{sY}{s+1}\left(\sum_1^{N_c-1} V_i M_i - V_{ins}\right) + V_{total}} \qquad \text{(E.10)} \end{aligned}$$

where M_i is defined as before.

Then the dimensionless pressure is obtained as for the one component case:

$$\hat{P}_D = \frac{s}{s+1}Y\langle\hat{\Theta}_D\rangle - Y\frac{\langle\Theta_{D_{dd}}\rangle}{s+1} + \frac{P_{D_{dd}}}{s+1}$$

E.4 Buildup without Formation Inflow

The mass-average flowline temperature is:

$$\langle\hat{\Theta}_D\rangle = \frac{\frac{Y\langle\Theta_{D_{dd}}\rangle}{s}\left(\sum_1^{N_c-1} V_i M_i - V_{ins}\right) - \frac{2}{s}\sum_1^{N_c-1}\frac{V_i G_{2i}(1,s;\Theta_{D_{dd}})}{I_0(\sqrt{\gamma_i s})} + V_{total}\frac{\langle\Theta_{D_{dd}}\rangle}{s}}{Y\left(\sum_1^{N_c-1} V_i M_i - V_{ins}\right) + V_{total}} \tag{E.11}$$

The dimensionless pressure:

$$\hat{P}_D = Y\langle\hat{\Theta}_D\rangle - Y\frac{\langle\Theta_{D_{dd}}\rangle}{s} + \frac{P_{D_{dd}}}{s}$$

E.5 Evaluation Procedure

Note variables with a hat $(\hat{})$ are in Laplace Domain.

1. Computation of the mass-average temperature during drawdown without formation influx. Only for $P_{D0} < 0$. $\Theta_{D2_{avg}}$ is computed here using the function *T_avg_non_adiab_dd_cyl - _winscomp.*

   $$\Theta_{D2_{avg}} = \mathcal{L}^{-1}\left\{\langle\hat{\Theta}_{D2}\rangle = \frac{\frac{X}{s^2}\sum_{i=1}^{Nc-1} V_i M_i + V_{ins}\frac{X}{s^2(Y-1)}}{V_{total} + Y\sum_{i=1}^{Nc-1} V_i M_i}\right\} \tag{E.12}$$

   where

   $$M_i = \frac{2\ \ I_1\left(\sqrt{\gamma_i s}\right)}{\sqrt{\gamma_i s}\ I_0\left(\sqrt{\gamma_i s}\right)} - 1 \tag{E.13}$$

2. Calculation of the flowline pressure during drawdown without formation influx. Only for $P_{D0} < 0$.

   $$P_D = P_{D0} + Y\langle\Theta_{D2}\rangle - Xt_D \tag{E.14}$$

the time t^* when $P_D = 0$ is found by interpolation, and a new time array *t_base_noflow* is created with the corresponding pressure data *PD_dd_noflow*.

3. Calculation of the temperature distribution and mass-average temperature at time t^*.

   The mass-average temperature $Tdavg\_tstar = \mathcal{L}^{-1}\left\{\langle\hat{\Theta}^*_D\rangle\right\}$ is computed using (E.12). The temperature distribution for each flowline component that conducts heat, $\hat{\Theta}^*_{D2_i}(r_D, s^*)$, is computed as follows

   $$\hat{\Theta}^*_{D2_i}(r_D, s^*) = \left(\frac{X}{s^2} - Y\langle\hat{\Theta}_{D2}\rangle\right)\left(\frac{I_0\left(\sqrt{\gamma_i s}\ r_D\right)}{I_0\left(\sqrt{\gamma_i s}\right)} - 1\right) \tag{E.15}$$

   The temperature for the insulated component is computed as

   $$\Theta^*_{D2_{ins}} = \frac{X}{Y-1}t^*_D \tag{E.16}$$

   $\Theta^*_{D2_{ins}}$ is uniform throughout the entire volume of the insulated component.

   This is evaluated in the function *T_dist_non_adiab_dd_cyl_1R_comp*. Temperature distributions for all flowline components are stored in the array *Tdist_tstar*.

4. Mass average temperature during drawdown with formation inflow. Two time arrays are created:

   - Δt_{dd}(*t_base_flow*): $0 < \Delta t_{dd} \le \Theta_{D_{dd}} - t^*_D$, and
   - $t_{dd_{flow}}$(*t_base_flow_noshift*): $t^*_D < t_{dd_{flow}} \le \Theta_{D_{dd}}$

The mass average temperature, assuming flow starts at $t = 0$ is called *Avg_temp_dd_flow*, and is evaluated as

$$Avg\_temp\_dd\_flow = \mathcal{L}^{-1}\left\{\langle\hat{\Theta}_{D_{flow}}\rangle\right\},$$

for the time array Δt_{dd} using

$$\langle\hat{\Theta}_{D_{flow}}\rangle = \frac{\sum_{i=1}^{Nc-1} V_i \left[\frac{\langle\hat{\Theta}_D^*\rangle}{s} - \frac{2G_{i,2}(1,s)}{sI_0\left(\sqrt{\gamma_i s}\right)} + M_i\left(\frac{Y\langle\hat{\Theta}_D^*\rangle}{s+1} + \frac{X}{s(s+1)}\right)\right] + A_{ins}}{V_{total} + \frac{sY}{s+1}\sum_{i=1}^{Nc-1} V_i M_i}, \tag{E.17}$$

where

$$G_{i,2}(r_D, s) = \int_0^{r_D} \tilde{r}_D I_0(\sqrt{\gamma_i s}\tilde{r}_D)\hat{\Theta}^*_{D2_i}(\tilde{r}_D)d\tilde{r}_D, \tag{E.18}$$

and

$$A_{ins} = V_{ins}\left(\frac{\Theta^*_{D2_{ins}}}{s} + \frac{X}{s^2(Y-1) - s}\right). \tag{E.19}$$

This is implemented in the function *T_avg_dd_formation_flow_winscomp*.

5. Computation of $\langle\hat{\Theta}_2\rangle$ and $\langle\hat{\Theta}_1\rangle$ for the new definition of the entire drawdown problem.

   To get the temperature distribution at the end of drawdown, the problem was redefined into $\Theta = \Theta_1 + \Theta_2$. $\langle\Theta_2\rangle$ is computed for $t_{dd_{flow}}$ using the function *T_avg_non_adiab_dd_cyl_winscomp*. This variable is called in the program *T22*. $\langle\Theta_1\rangle$ is computed next:

$$\langle\Theta_1\rangle = \langle\Theta_{D_{flow}}\rangle - \langle\Theta_2\rangle = Avg\_temp\_dd\_flow - T22$$

6. Computation of P_2, P_1 and $\frac{dP_1}{dt}$.

$$P_2 = P_{D_0} + Y\langle\Theta_2\rangle - Xt_{dd_{flow}} \tag{E.20}$$

P_1 is computed for Δt_{dd} as

$$P_1 = -e^{-t}\left[Ye^t\langle\Theta_1\rangle(\Delta t_{dd}) + \int_{t^*}^{t} e^t\left(P_2(t_{dd_{flow}}) - Y\langle\Theta_1\rangle(\Delta t_{dd})\right)dt\right], \tag{E.21}$$

$\langle\Theta_1\rangle(\Delta t_{dd})$ was computed in the previous step, and P_2 is computed in this step. The integral is evaluated numerically by fitting a spline to the integrand and using the Matlab built-in function *quad*. $\frac{dP_1}{dt}$ is computed numerically using a quadratic fit; this is implemented in the function *SandipDeriv*

7. Θ_1 Temperature distribution at the end of drawdown.

   The temperature distribution for each non-insulated component for the Θ_1 problem is computed at time $\Delta t_{dd} = \Theta_{D_{dd}} - t_D^*$ with the following equation:

   $$\Theta_{1_i}(r_D, \Delta t) = 2\int_0^{\Delta t} \frac{dP_1}{d\tau} \sum_{n=1}^{\infty} e^{-\alpha_n^2(\Delta t - \tau)/\gamma_i} \frac{J_0(\alpha_n r_D)}{\alpha_n J_1(\alpha_n)} d\tau. \tag{E.22}$$

   The integrand is fitted with a spline and the integral is evaluated numerically. For the insulated flowline volume the temperature is computed as

   $$\Theta_{1_{ins}}(\Delta t_{dd}) = P_1(\Delta t_{dd}). \tag{E.23}$$

   All the results are stored in the variable $T1dist$

8. Temperature distribution at the end of drawdown.

   The temperature distribution for each of the non-insulated components for the Θ_2 model is computed at time $\Theta_{D_{dd}}$ with the function *T_dist_non_adiab_dd_cyl_1R_comp*. For the insulated volume, temperature is computed with equation (E.16). Results for all components are stored in the variable $T2dist\_atTdd$. The temperature distribution at the end of drawdown is:

$$\Theta_D(r_D, \Theta_{D_{dd}}) = \Theta_1(r_D, \Theta_{D_{dd}} - t_D^*) + \Theta_2(r_D, \Theta_{D_{dd}})$$

in the program: $Tdist\_adimdd = T1dist + T2dist\_atTdd$

9. Flowline pressure during drawdown with formation flow.

   The dimensionless pressure is computed with the following equation:

$$P_D = Y\left[\langle\Theta_D\rangle - e^{-t_D}\langle\Theta_{D_0}\rangle - \int_o^{t_D}\langle\Theta_D\rangle(\tau)e^{-(t_D-\tau)}d\tau\right] - X\left(1 - e^{-t_D}\right) \tag{E.24}$$

10. Flowline pressure during buildup with formation flow.

    Only for $t^* < \Theta_{D_{dd}}$

    The flowline temperature is computed first with the following equation:

$$\langle\hat{\Theta}_{D_{BU}}\rangle = \frac{\sum_{i=1}^{Nc-1} V_i\left[\frac{\langle\hat{\Theta}_{D_{dd}}\rangle}{s} - \frac{2G_{i,2}(1,s)}{sI_0\left(\sqrt{\gamma_i s}\right)} + M_i\left(\frac{Y\langle\hat{\Theta}_{D_{dd}}\rangle}{s+1} + \frac{P_{D_{dd}}}{s(s+1)}\right)\right] + \Theta_{BU_{ins}}}{V_{total} + \frac{sY}{s+1}\sum_{i=1}^{Nc-1} V_i M_i} \tag{E.25}$$

where:

$$G_{i,2}(r_D, s) = \int_0^{r_D} \tilde{r}_D I_0(\sqrt{\gamma_i s}\tilde{r}_D)\hat{\Theta}_{Di_{dd}}(\tilde{r}_D)d\tilde{r}_D \tag{E.26}$$

$$\Theta_{BU_{ins}} = V_{ins}\left(\frac{\Theta_{D_{dd}}}{s} - \frac{P_{D_{dd}}}{s^2(1-Y)+s}\right) \tag{E.27}$$

The flowline pressure during buildup is:

$$\hat{P}_{D_{BU}} = \frac{P_{D_{dd}}}{s+1} + \frac{sY\langle\hat{\Theta}_{D_{BU}}\rangle}{s+1} - \frac{Y\langle\hat{\Theta}_{D_{dd}}\rangle}{s+1} \tag{E.28}$$

11. Build-up after a 'dry' drawdown.

    If $P_{Ddd} < 0$ then the flowline pressure at the end of the drawdown is higher than the formation pressure and the resulting buildup is only because of temperature effects.

Appendix F

Heat Transfer Accounting for the Surrounding Tool

In order to account for heat conduction around the flowline, the tool is modeled as a two concentric cylindrical regions, with the inner region occupied by the flowline (fluid filled) and the outer region representing the body of the tool (solid). The flowline model is depicted in Figure F.1.

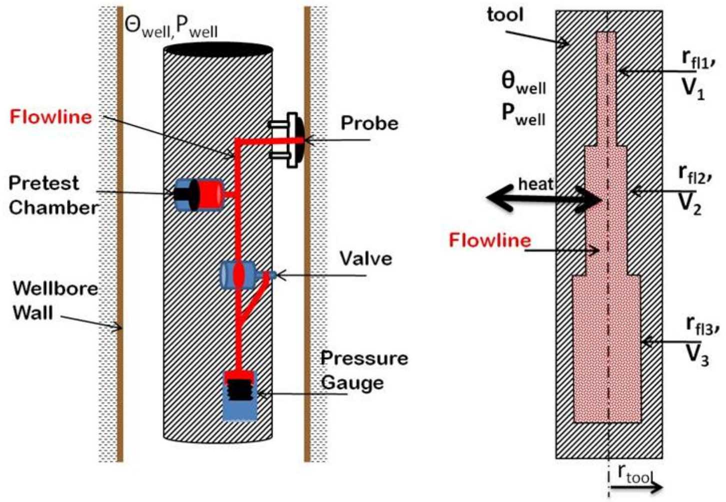

Figure F.1: Flowline model used for the calculation of P and Θ accounting for the presence of the tool

The first approach is to use the quasi-steady- state (qss) approximation to model heat conduction in the outer region and to obtain the solution for a single component system. The solution is then extended for multiple flowline components (different radii) with some of them remaining thermally insulated. Finally the transient temperature behavior of the outer region is incorporated into the model.

Unless otherwise stated, it is assumed here that the thermal conductivity of the material surrounding the flowline (typically stainless steel) is much larger than the thermal conductivity of the fluid in the flowline, and we use the quasi-static approximation to model heat conduction in the outer region. Transient heat conduction is considered only inside the flowline. The problem is stated for a one component cylindrical system with two concentric radial regions:

F.1 Drawdown without Formation Inflow

Conservation of mass in this case is expressed as

$$\frac{dP_D}{dt_D} = Y \frac{d\langle \Theta_D \rangle}{dt_D} - X. \tag{F.1}$$

Conservation of energy within the flowline is given by

$$\frac{\partial \Theta_D}{\partial t_D} = \frac{1}{\gamma} \left[\frac{\partial^2 \Theta_D}{\partial r_D^2} + \frac{1}{r_D} \frac{\partial \Theta_D}{\partial r_D} \right] + \frac{dP_D}{dt_D}, \quad 0 \leq r_D \leq 1, \tag{F.2}$$

and conservation of energy in the outer region is given by

$$\frac{d}{dr_D} \left(r_D \frac{d\Theta_D^*}{dr_D} \right) = 0, \quad 1 \leq r_D \leq r_{eD} \tag{F.3}$$

Initial and boundary conditions:

1.

$$P_D(0) = P_{D0}$$

2.

$$\Theta_D(r, 0) = 0$$

3.

$$\Theta_D^*(r_{eD}, t_D) = 0$$

4.

$$K_\Theta^{solid} \frac{d\Theta_D^*}{dr_D}\bigg|_{r_D=1} = K_\Theta^{fluid} \frac{d\Theta_D}{dr_D}\bigg|_{r_D=1}$$

5.

$$\Theta_D^*\big|_{r_D=1} = \Theta_D\big|_{r_D=1}$$

Applying the Laplace Transform to the three equations:

$$s\hat{P}_D = sY\langle\hat{\Theta}_D\rangle + P_{D0} - \frac{X}{s}$$

$$\frac{d^2\hat{\Theta}_D}{dr_D^2} + \frac{1}{r_D}\frac{d\hat{\Theta}_D}{dr_D} - \gamma s\hat{\Theta}_D = -\gamma Y s\langle\hat{\Theta}_D\rangle + \gamma\frac{X}{s}$$

$$\hat{\Theta}_D = AI_0\left(\sqrt{\gamma s} r_D\right) - Y\langle\hat{\Theta}_D\rangle + \frac{X}{s^2}$$

$$\frac{d\hat{\Theta}_D}{dr_D} = A\sqrt{\gamma s} I_1\left(\sqrt{\gamma s} r_D\right)$$

$$\hat{\Theta}_D^* = \hat{C}_1(s)\ln\left(\frac{r}{r_{eD}}\right)$$

$$\frac{d\hat{\Theta}_D^*}{dr_D} = \frac{\hat{C}_1(s)}{r_D}$$

Applying boundary conditions 4 and 5 ($r_D = 1$):

$$AI_0\left(\sqrt{\gamma s}\right) - Y\langle\hat{\Theta}_D\rangle + \frac{X}{s^2} = -\hat{C}_1(s)\ln(r_{eD})$$

$$\sigma A\sqrt{\gamma s} I_1\left(\sqrt{\gamma s}\right) = \hat{C}_1(s)$$

$$\sigma = \frac{K_\Theta^{fluid}}{K_\Theta^{solid}}$$

$$A = \frac{Y\langle\hat{\Theta}_D\rangle - \frac{X}{s^2}}{\mathrm{M}_I}$$

where

$$\mathrm{M}_I = I_0\left(\sqrt{\gamma s}\right) + \sigma\sqrt{\gamma s}\ln(r_{eD})I_1\left(\sqrt{\gamma s}\right)$$

$$\hat{\Theta}_D = \left(Y\langle\hat{\Theta}_D\rangle - \frac{X}{s^2}\right)\left(1 - \frac{I_0\left(\sqrt{\gamma s}r_D\right)}{\mathrm{M}_I}\right)$$

$$\langle\hat{\Theta}_D\rangle = 2\int_0^1 r_D\hat{\Theta}_D dr_D = \left(Y\langle\hat{\Theta}_D\rangle - \frac{X}{s^2}\right)\left(1 - \frac{2I_1\left(\sqrt{\gamma s}\right)}{\sqrt{\gamma s}\mathrm{M}_I}\right)$$

$$\langle\hat{\Theta}_D\rangle = \frac{X\mathcal{M}}{s^2(1+Y\mathcal{M})}$$

$$\mathcal{M} \equiv \frac{2I_1\left(\sqrt{\gamma s}\right)}{\sqrt{\gamma s}\mathrm{M}_I} - 1 = \frac{2I_1\left(\sqrt{\gamma s}\right)}{\sqrt{\gamma s}\left[I_0\left(\sqrt{\gamma s}\right) + \sigma\sqrt{\gamma s}\ln(r_{eD})I_1\left(\sqrt{\gamma s}\right)\right]} - 1$$

F.2 Extension of the Solution to Multiple Flowline Components

The variable $\mathcal{M}$ is defined for each flowline component:

$$\mathcal{M}_i \equiv \frac{2I_1\left(\sqrt{\gamma_i s}\right)}{\sqrt{\gamma_i s}\left[I_0\left(\sqrt{\gamma_i s}\right) + \sigma\sqrt{\gamma_i s}\ln(r_{eD_i})I_1\left(\sqrt{\gamma_i s}\right)\right]} - 1$$

And the average temperature is:

$$\langle\hat{\Theta}_D\rangle = \frac{X\sum V_i\mathcal{M}_i + V_{ins}\left(\frac{X}{Y-1}\right)}{s^2\left(V_{total} + Y\sum V_i\mathcal{M}_i\right)} \tag{F.4}$$

The sum is done over those elements that are not insulated.

F.3 Drawdown with Formation Inflow

Conservation of mass is

$$\frac{dP_D}{dt_D} + P_D = Y\frac{d\langle\Theta_D\rangle}{dt_D} - X. \tag{F.5}$$

Conservation of energy within the flowline is the same as F.2

$$\frac{\partial\Theta_D}{\partial t_D} = \frac{1}{\gamma}\left[\frac{\partial^2\Theta_D}{\partial r_D^2} + \frac{1}{r_D}\frac{\partial\Theta_D}{\partial r_D}\right] + \frac{dP_D}{dt_D}, \quad 0 \le r_D \le 1,$$

and the equation of conservation of energy in the outer region is the same as F.3

$$\frac{d}{dr_D}\left(r_D\frac{d\Theta_D^*}{dr_D}\right) = 0, \quad 1 \le r_D \le r_{eD}.$$

Initial and boundary conditions are

1. $$P_D(0) = 0,$$

2. $$\Theta_D(r,0) = \Theta_{D0}(r_D),$$

3. $$\Theta_D^*(r_{eD}, t_D) = 0,$$

4. $$K_\Theta^{solid}\frac{d\Theta_D^*}{dr_D}\bigg|_{r_D=1} = K_\Theta^{fluid}\frac{d\Theta_D}{dr_D}\bigg|_{r_D=1},$$

   and

5. $$\Theta_D^*\big|_{r_D=1} = \Theta_D\big|_{r_D=1}.$$

Applying the Laplace Transform:

$$\hat{P}_D = \frac{s}{s+1} Y \langle \hat{\Theta}_D \rangle - \frac{Y \langle \Theta_{D0} \rangle}{s+1} - \frac{X}{s(s+1)}$$

$$\frac{d^2 \hat{\Theta}_D}{dr_D^2} + \frac{1}{r_D} \frac{d\hat{\Theta}_D}{dr_D} - \gamma s \hat{\Theta}_D = -\gamma \Theta_{D0}(r_D) - \gamma s \hat{P}_D$$

$$\begin{aligned} \hat{\Theta}_D &= A I_0 \left(\sqrt{\gamma s} r_D\right) + \hat{P}_D \left(1 - I_0 \left(\sqrt{\gamma s} r_D\right)\right) - \gamma I_0 \left(\sqrt{\gamma s} r_D\right) G_1(r_D, s) \\ &\quad + \gamma K_0 \left(\sqrt{\gamma s} r_D\right) G_2(r_D, s) \end{aligned}$$

$$\begin{aligned} \frac{d\hat{\Theta}_D}{dr_D} &= A\sqrt{\gamma s} I_1 \left(\sqrt{\gamma s} r_D\right) - \hat{P}_D \sqrt{\gamma s} I_1 \left(\sqrt{\gamma s} r_D\right) - \gamma \sqrt{\gamma s} I_1 \left(\sqrt{\gamma s}\right) G_1(1, s) \\ &\quad - \gamma r_D I_0 \left(\sqrt{\gamma s} r_D\right) K_0 \left(\sqrt{\gamma s} r_D\right) \Theta_{D0}(r_D) dr_D - \gamma \sqrt{\gamma s} K_1 \left(\sqrt{\gamma s}\right) G_2(1, s) \\ &\quad + \gamma r_D K_0 \left(\sqrt{\gamma s} r_D\right) I_0 \left(\sqrt{\gamma s} r_D\right) \Theta_{D0}(r_D) dr_D \end{aligned}$$

$$\begin{aligned} \left.\frac{d\hat{\Theta}_D}{dr_D}\right|_{r_D=1} &= A\sqrt{\gamma s} I_1 \left(\sqrt{\gamma s}\right) - \hat{P}_D \sqrt{\gamma s} I_1 \left(\sqrt{\gamma s}\right) \\ &\quad - \gamma \sqrt{\gamma s} I_1 \left(\sqrt{\gamma s} r_D\right) G_1(r_D, s) \\ &\quad - \gamma \sqrt{\gamma s} K_1 \left(\sqrt{\gamma s} r_D\right) G_2(r_D, s) \end{aligned} \tag{F.6}$$

$$\hat{\Theta}_D^* = \hat{C}_1(s) \ln \left(\frac{r}{r_{eD}} \right)$$

$$\frac{d\hat{\Theta}_D^*}{dr_D} = \frac{\hat{C}_1(s)}{r_D}$$

F.4 Buildup

Conservation of mass for the buildup (with formation inflow) is

$$\frac{dP_D}{dt_D} + P_D = Y \frac{d\langle \Theta_D \rangle}{dt_D}. \tag{F.7}$$

Conservation of energy within the flowline is

$$\frac{\partial \Theta_D}{\partial t_D} = \frac{1}{\gamma}\nabla\Theta_D + \frac{dP_D}{dt_D}, \quad 0 \le r_D \le 1, \tag{F.8}$$

and Conservation of energy in the outer region is

$$\nabla\Theta_D^* = 0, \quad 1 \le r_D \le r_{eD}. \tag{F.9}$$

F.5 Extension of the Solution to Multiple Flowline Components

$$\frac{dP_D}{dt_D} + P_D = Y\frac{d\langle\Theta_{D_i}\rangle}{dt_D} \tag{F.10}$$

$$\frac{\partial \Theta_{D_i}}{\partial t_D} = \frac{1}{\gamma_i}\left[\frac{\partial^2\Theta_{D_i}}{\partial r_D^2} + \frac{1}{r_D}\frac{\partial\Theta_{D_i}}{\partial r_D}\right] + \frac{dP_D}{dt_D}, \quad r_D \le 1 \tag{F.11}$$

$$\frac{\partial \Theta^*_{D_i}}{\partial t_D} = \frac{\beta_i}{\gamma_i}\left[\frac{\partial^2\Theta^*_{D_i}}{\partial r_D^2} + \frac{1}{r_D}\frac{\partial\Theta^*_{D_i}}{\partial r_D}\right], \quad 1 \le r_D \le r_{eD} \tag{F.12}$$

where the coefficient β_i is the ratio of the thermal diffusivity of the fluid in the flow line and the surrounding solid:

$$\beta_i = \frac{\tau_{heat}^{fluid}}{\tau_{heat}^{solid}} \tag{F.13}$$

$$\tau_{heat}^{solid} = \frac{\rho_{solid}\hat{c}_P^{solid} r_{fl_i}^2}{K_\Theta^{solid}} \tag{F.14}$$

$$\gamma_i = \frac{\tau_{heat}^{fluid}}{\tau_{tool}} \tag{F.15}$$

As before, the characteristic length scale of the problem is the flowline radius of each component:

$$r_D = \frac{r}{r_{fl_i}}. \tag{F.16}$$

The external radius of the tool marks the outer boundary of the problem

$$r_{eD} = \frac{r_{tool}}{r_{fl_i}}. \tag{F.17}$$

F.6 Validity of the QSS Formation Inflow Approximation

In some of the results obtained so far the flowline pressure tends to overshoot, i.e. it increases beyond the initial sandface pressure and builds down to equilibrium. The size of the overshoot increases with wellbore temperature and overbalance, and is more pronounced in high permeability formations, where the characteristic time τ_{tool} is shorter. Average Temperature always tends to overshoot, however the flowline pressure in low permeability formations increases sufficiently slow that $\tau_{tool} > \tau_{heat}$, hence the heating of the flowline, helps boost the flowline pressure and helps the signal equilibrate faster (though the help is modest). The qss assumption is valid when $|P_{fl} - P_{\infty}| \sim P_{fl} - P_{sph}$. There will be situations when the late time storage effects caused by the thermal equilibration of the flowline fluid will be of similar order of magnitude to the deep formation response (spherical flow). This means that the qss assumption used to model the formation inflow will not be valid. An alternative to this is to solve for the pressure field in the formation (assuming, for instance, spherical flow), and impose the flowline storage problem with variable temperature as the inner boundary condition. This is a significantly more involved mathematical problem.

F.7 Spherical Flow with Flowline Storage (Variable Temperature)

We pose the problem that must be solved to include formation compressibility in the flowline model. The solution presented by Proett and Chin must be extended to account for temperature variations in the flowline during the pretest. For simplicity, the flowline is modeled as one cylindrical region with one component (the surrounding tool is neglected). The equation describing the pressure field in the reservoir during drawdown is:

$$\frac{\partial^2 P}{\partial r^2} + \frac{2}{r}\frac{\partial P}{\partial r} = \frac{\phi \mu c_{fm}}{k}\frac{\partial P}{\partial t}, \tag{F.18}$$

where

$$P = P_{fm}, \text{ for } r \to \infty \ \forall \ t.$$

The equation of conservation of mass in the flow line is the inner boundary condition,

$$\left.\frac{\partial P}{\partial t}\right|_{r=r_e} + \frac{\alpha}{c_e}\frac{d\langle\Theta\rangle}{dt} = \frac{4\pi r_e^2 \frac{k}{\mu}}{c_e V_{tool}} \left.\frac{\partial P}{\partial r}\right|_{r=r_e} - \frac{q_{piston}}{C_e V_{tool}}, \tag{F.19}$$

with the initial condition

$$P(t=0) = P_{fm}.$$

Conservation of energy in the flowline gives

$$\frac{\partial \Theta}{\partial t} - \frac{\alpha \Theta}{\rho \hat{c}_P} \left.\frac{dP}{dt}\right|_{r=r_e} = \frac{K_\Theta}{\rho \hat{c}_P}\nabla^2\Theta, \tag{F.20}$$

with the following conditions:

$$\Theta(r, t=0) = \Theta_0(r),$$

and

$$\Theta(r = r_{fl}, t) = \Theta_{well}.$$

The following dimensionless variables are defined:

$$t_D = \frac{t}{\tau_{tool}}, \qquad P_D = \frac{P - P_{fm}}{\Delta P_{dd_S}}, \qquad \Theta_D = \frac{\Theta - \Theta_{well}}{\Delta \Theta_{dd_S}}$$

$$q_D = \frac{q_{piston}}{q_\infty}, \qquad r_D = \frac{r}{r_{fl}}, \qquad r_{eD} = \frac{r_e}{r_{fl}}$$

where the equivalent probe radius defined as the value of r where the formation pressure and the flowline pressure are equal), i.e.

$$r_e = \frac{r_{probe}}{\pi}$$

The equations in dimensionless form are:

$$\frac{\partial^2 (r_D P_D)}{\partial r_D^2} = \frac{\beta}{r_{eD}^2} \frac{\partial (r_D P_D)}{\partial t_D} \tag{F.21}$$

$$\left.\frac{\partial P_D}{\partial t_D}\right|_{r_{eD}} - Y \frac{d\langle \Theta_D \rangle}{dt_D} = r_{eD} \left.\frac{\partial P_D}{\partial r_D}\right|_{r_{eD}} - X \tag{F.22}$$

$$\frac{\partial \Theta_D}{\partial t_D} = \frac{1}{\gamma} \overline{\nabla} \Theta_D + \left.\frac{dP_D}{dt_D}\right|_{r_{eD}} \tag{F.23}$$

where

$$Y = \frac{\alpha \Delta T_{dd_S}}{c_e \Delta P_{dd_S}}, \qquad X = \frac{\Delta P_{dd}}{\Delta P_{dd_S}}, \qquad \gamma = \frac{\tau_{heat}}{\tau_{tool}}, \qquad \beta = \frac{\tau_{fm}}{\tau_{tool}}$$

The initial and boundary conditions are

1. $P_D = 0, \text{ as } r_D \to \infty, \ \forall t_D$
2. $P_D(r_D, 0) = 0$
3. $P_D\big|_{r_{eD}}$ and $\left.\frac{\partial P_D}{\partial r_D}\right|_{r_{eD}}$ are continuous
4. $\Theta_D(r_D, 0) = \Theta_{D0}(r_D)$
5. $\Theta_D(1, t_D) = 0$

Application of the Laplace Transform yields the following equations:

$$\hat{P}_D = \frac{B}{r_D} e^{-\sqrt{\beta s} r_D / r_{eD}}$$

$$\left.\frac{\partial \hat{P}_D}{\partial r_D}\right|_{r_{eD}} = \frac{-Be^{-\sqrt{\beta s}}}{r_{eD}^2}\left(1+\sqrt{\beta s}\right)$$

$$s\left.\hat{P}_D\right|_{r_{eD}} = sY\langle\hat{\Theta}_D\rangle - Y\langle\Theta_{D0}\rangle - \frac{X}{s} - \frac{Be^{-\sqrt{\beta s}}}{r_{eD}^2}\left(1+\sqrt{\beta s}\right)$$

$$\frac{\partial^2\hat{\Theta}_D}{\partial r_D^2} + \frac{1}{r_D}\frac{\partial\hat{\Theta}_D}{\partial r_D} - \gamma s\hat{\Theta}_D = -\gamma\Theta_{D0}(r_D) - \gamma s\left.\hat{P}_D\right|_{r_{eD}}$$

$$B = \frac{r_{eD}\left(sY\langle\hat{\Theta}_D\rangle - Y\langle\Theta_{D0}\rangle - \frac{X}{s}\right)}{e^{-\sqrt{\beta s}}\left(1+s+\sqrt{\beta s}\right)}$$

The solution in Laplace Domain for the temperature distribution, average temperature and the pressure are:

$$\langle\hat{\Theta}_D\rangle = \frac{\left(1-\frac{2I_1(\sqrt{\gamma s})}{\sqrt{\gamma s}I_0(\sqrt{\gamma s})}\right)\left(\frac{Y\langle\Theta_{D0}\rangle-\frac{X}{s}}{1+s+\sqrt{\beta s}}\right) - \frac{2G_2(1,s)}{sI_0(\sqrt{\gamma s})} + \frac{\langle\Theta_{D0}\rangle}{s}}{1-\left(1-\frac{2I_1(\sqrt{\gamma s})}{\sqrt{\gamma s}I_0(\sqrt{\gamma s})}\right)\frac{sY}{1+s+\sqrt{\beta s}}} \tag{F.24}$$

$$\begin{aligned}\hat{\Theta}_D \;=\; & \left(1-\frac{I_0(\sqrt{\gamma s}r_D)}{I_0(\sqrt{\gamma s})}\right)\left(\frac{sY\langle\hat{\Theta}_D\rangle - Y\langle\Theta_{D0}\rangle - \frac{X}{s}}{1+s+\sqrt{\beta s}}\right) \\ & +\gamma I_0(\sqrt{\gamma s}r_D)\left(G_1(1,s)-G_1(r_D,s)\right) \\ & +\gamma\left(K_0(\sqrt{\gamma s}r_D)G_2(r_D,s) - \frac{K_0(\sqrt{\gamma s})}{I_0(\sqrt{\gamma s})}I_0(\sqrt{\gamma s}r_D)G_2(1,s)\right)\end{aligned} \tag{F.25}$$

$$\hat{P}_D = \frac{e^{-\sqrt{\beta s}(r_D/r_{eD}-1)}}{r_D/r_{eD}}\left(\frac{sY\langle\hat{\Theta}_D\rangle - Y\langle\Theta_{D0}\rangle - \frac{X}{s}}{1+s+\sqrt{\beta s}}\right) \tag{F.26}$$

Appendix G

Laplace Transform Inversion Algorithm

The algorithm presented by Abate and Valkó (2004) was used to invert all the Laplace transforms in this study. This algorithm is of the fixed Talbot category, and therefore it is based on the deformation of the contour of the Bromwich inversion integral and requires complex arithmetic. A summary of the algorithm is as follows:

Given $F(x, s) = \mathcal{L}\left\{f(x, t)\right\}$ for $t = t_1, \ldots, t_n$.

1. Set the value of M, the precision constant[1]

2. $$r_i = \frac{2M}{5t_i}$$

3. $$\theta = \left[\frac{\pi}{M}, \frac{2\pi}{M}, \frac{2\pi}{M}, \ldots \pi - \frac{\pi}{M}\right]$$

   $\theta = \theta_1, \ldots, \theta_m$, $m = M - 1$

   $$\sigma(\theta) = \theta + (\theta \cot\theta - 1)\cot\theta$$

4. for j=1:n

   for k=1:m

   $$\bar{s}(j, k) = r_j \theta_k \cot\left(\theta_k + \sqrt{-1}\right)$$

---

[1] $M = 16$ was found satisfactory for most computations

$$\Delta P_s(j,k) = F\left(x, \bar{s}(j,k)\right)$$

$$\Delta P_f(j,k) = \exp\left[t_j \bar{s}(j,k) + \Delta P_s(j,k)\left(1 + \sqrt{-1}\sigma_k\right)\right]$$

end(k)

$$\Delta P_r(j) = F\left(x, r_j\right)$$

$$f(x,t_j) = \frac{r_j}{M}\exp\left(\frac{2M}{5}\right)\Delta P_r(j) + \sum_{k=1}^{M-1}\mathbb{R}\left[\Delta P_f(j,k)\right]$$

end(j)

Nomenclature

$1/\beta$	dimensionless group reflecting the relative duration of heat conduction in the tool (chassis) with respect to tool storage
$1/\gamma$	dimensionless group reflecting the relative duration of heat conduction in the flowline fluid with respect to tool storage
α	coefficient of thermal expansion
$\Delta\Theta_{ddS}$	temperature change after an adiabatic drawdown on an impermeable formation
ΔP_X	pressure difference ($P_{fl} - P_{sandface}$) at time **X**
ΔP_{ddS}	pressure change after an adiabatic drawdown on an impermeable formation
ΔP_{dd}	pressure change for a formation tester drawdown that reaches steady state.
ΔP_{max}	maximum spherical flow signal for a given tool and formation mobility
Δt_D	dimensionless buildup time
ΔV	pretest volume
$\hat{c}_P$	specific heat capacity
κ_S	adiabatic compressibility
κ_Θ	isothermal compressibility
$\langle\Theta\rangle$	mass-average temperature

Ω	wellbore curvature correction factor for the computation of the drawdown mobility
ϕ	porosity
ρ_{fluid}	fluid density
τ_{heat}	characteristic time associated with heat conduction in the flowline
τ_{tool}	characteristic time associated with the effective flowline compressibility (storage)
Θ	temperature
Θ^*	temperature in the tool chassis
Θ_D	dimensionless temperature
Θ_{well}	wellbore temperature
c_t	total formation compressibility
c_{eff}	effective flowline compressibility, $c_{tool} + c_{fluid}$
c_{fluid}	fluid compressibility
c_{tool}	tool compressibility
f_s	spherical time function
k/μ	mobility (permeability/viscosity)
K_Θ	thermal conductivity
m	derivative of the pressure with respect to the spherical time function
P	pressure
P_D	dimensionless pressure

P_{fl}	flowline pressure
$P_{sandface}$	formation pressure at the sandface, assumed here to be same as the far-field formation pressure
q	pretest rate, speed of retraction of the pretest piston
q_∞	specified pretest piston speed
q_{fm}	rate of flow through the probe orifice
r_D	dimensionless radius, r/r_{fl}
r_{eD}	dimensionless distance to the tool wall
r_{fl}	flowline radius
r_{probe}	radius of the probe orifice
r_{well}	wellbore radius
S	entropy
s	Laplace transform parameter
T	total drawdown time
t_D	dimensionless time, t/τ_{tool}
$V_{flowline}$	flowline volume
X	dimensionless group formed by the ratio of two pressure changes, isothermal steady state and adiabatic drawdown
Y	dimensionless group, a measure of the impact of temperature effects on the pressure behavior

References

Abate, J. & Valko, P. P. 2004 Multi-Precision Laplace Transform Inversion. *International Journal for Numerical Methods in Engineering* **60**, 979–993.

Angeles, R., Lee, H., Alpak, F., Torres-Verdin, C. & Sheng, J. 2007 Estimation of Permeability and Permeability Anisotropy from Straddle-Packer Formation Tester Measurements Based on the Physics of Two-Phase Immiscible Flow and Invasion. *Soc. of Pet. Eng. Journal* pp. 339–354.

API 1952 Standard for Determining Permeability of Porous Media, code 27.

Ayan, C., Petricola, M., Knight, P. & Lalanne, B. 2007 An Investigation of Near-Wellbore Flow Properties Using Sonic Scanner Measurements and Interval Pressure Transient Testing. In *Soc. Pet. Eng. Annual Technical Conference and Exhibition, Anaheim, California. SPE 110304*.

Banerjee, R., Thambynayagam, R. & Spath, J. 2006 A Method for Analysis of Pressure Response with a Formation Tester Influenced by Supercharging. In *SPE Russian Oil and Gas Technical Conference and Exhibition, Moscow, Russia, SPE 102413*.

Batchelor, G. 1967 *An Introduction to Fluid Dynamics*. Oxford, England: Cambridge University Press.

BEAR, J. 1988 *Dynamics of Fluids in Porous Media.* New York: Dover.

BETANCOURT, S., DUSSAN, E. & LAKE, L. 2010 Inducing Spherical Flow Conditions with Formation Testers. In *Soc. Pet. Eng. Annual Technical Conference and Exhibition, Florence, Italy. SPE 133523*.

BETANCOURT, S., DUSSAN, E. & LAKE, L. 2011 Effects of Temperature Variations on Formation Tester Pretests. In *Soc. Pet. Eng. Annual Technical Conference and Exhibition, Denver, Colorado. SPE 146647*.

BIRD, R., STEWART, W. & LIGHTFOOT, E. 1960 *Transport Phenomena.* New York: John Wiley & Sons.

BOURDET, D. 2002 *Well Test Analysis: the Use of Advanced Interpretation Models*. Elsevier Science.

BRIGHAM, W., PEDEN, J., NG, K. & O'NEILL, N. 1980 The Analysis of Spherical Flow with Wellbore Storage. In *Soc. Pet. Eng. Annual Technical Conference and Exhibition, Dallas, Texas. SPE 9294*.

CALLEN, H. 1960 *Thermodynamics*, 1st edn. New York: John Wiley & Sons.

CARSLAW, H. S. & JAEGER, J. C. 1959 *Conduction of Heat in Solids*, 2nd edn. Oxford: Clarendon Press.

CHANG, Y., HAMMOND, P. & POP, J. 2008 When Should We Worry About Supercharging in Formation-Pressure-While-Drilling Measurements. *SPE Reservoir Evaluation and Engineering* pp. 165–174.

Chu, W. & Welch, P. 2008 Identification of Bypassed Pays in Low-Resistivity, Thinly-Bedded, Sand-Shale Sequences in the Ghdames Basin of North Africa through Use of the Wireline Formation Tester. In *Soc. Pet. Eng. Annual Technical Conference and Exhibition, Denver CO. SPE 114478*. Society of Petroleum Engineers.

Dake, L. 1978 *Fundamentals of Reservoir Engineering*. New York: Elsevier.

Dias, M. & Wilkinson, D. 1987 Horizontal Invasion Profiles. Research note. Schlumberger.

Doetsch, G. 1961 *Guide to the Applications of Laplace Transforms*, 2nd edn. New York: Van Nostrand.

Doll, H. 1956 Methods and Apparatus for Determining Hydraulic Characteristics of Formations Traversed by a Borehole, us pat. 2,747,401.

Dussan V., E. April 2011 A Robust Method for Calculating Formation Mobility with a Formation Tester. *SPE Reservoir Evaluation and Engineering* pp. 239–247.

Dussan V., E. & Sharma, Y. 1992 Analysis of the Pressure Response of a Single Probe Formation Tester. *SPE Formation Evaluation* pp. 151–156.

Earlougher, R. 1977 *Advances in Well Test Analysis, SPE Monograph*. Soc. of Petroleum Engineers.

Eijpe, R. & Weber, K. 1971 Mini-Permeameters for Consolidated Rock and Unconsolidated Sand. *Am. Assoc. Petroleum Geologists Bull.* **55**, 307.

GOGGIN, D., CHANDLER, M., KOCUREK, G. & LAKE, L. June 1988b Patterns of Permeability in Eolian Deposits: Page Sandstone (Jurassic), Northeastern Arizona. *SPE Formation Evaluation* pp. 297–306.

GOGGIN, D., THRASHER, R. & LAKE, L. 1988 A Theoretical and Experimental Analysis of Minipermeameter Response Including Gas Slippage and High Velocity Flow Effects. *In Situ* **12**, 79–116.

GOK, I., ONUR, M., HEGEMAN, P. & KUCHUK, F. 2006 Effect of an Invaded Zone on Pressure-Transient Data from Multiprobe and Packer-Probe Wireline Formation Testers. *SPE Reservoir Evaluation and Engineering* pp. 39–49, sPE84093.

GOODE, P. & THAMBYNAYAGAM, R. 1996 Influence of an Invaded Zone on a Multiprobe Formation Tester. *SPE Formation Evaluation* **11** (1), 31–40.

HAILSTONE, J. & OVENS, J. 1995 Do Electronic Pressure Gauges have 20/20 Vision? In *Soc. of Pet. Eng. Annual Technical Conference and Exhibition, Dallas, USA. SPE 30614*.

HAMMOND, P. & POP, J. 2005 A Method for Analysis of Pressure Response with a Formation Tester Influenced by Supercharging. In *Soc. of Pet. Eng. Annual Technical Conference and Exhibition, Dallas, TX, USA. SPE 95710*.

HASAN, A., KABIR, C. & WANG, X. 1997 Development and Application of a Wellbore/Reservoir Simulator for Testing Oil Wells. *SPE Formation Evaluation* .

Johns, R. & Ma, L. 1998 Effect of Pretest Pressure and Temperature on DST Interpretation. *SPE Reservoir Evaluation and Engineering,* pp. 303–310.

Jones, S. C. 1972 A Rapid Unsteady-State Klinkenberg Permeameter. *Soc. of Pet. Eng. Journal* p. 383.

Jones, S. C. 1994 A new, Fast, Accurate Pressure-Decay Probe Permeameter. *SPE Formation Evaluation Journal* .

Kasap, E., Georgi, D., Michaels, J. & Shwe, T. 1996*a* A New, Simplified, Unified Technique for the Analysis of Wireline Formation Test Data. *Presented at the SPWLA 37th Annual Logging Symposium* (SPWLA-96-AA).

Kasap, E., Huang, H., Shwe, T. & Georgi, D. 1996*b* Robust and Simple graphical Solution for Wireline Formation Tests: Combined Drawdown and Buildup Analyses. In *Soc. of Pet. Eng. Annual Technical Conference and Exhibition, Denver, USA. SPE 36525*.

Kasap, E., Huang, K., Shwe, T. & Georgi, D. 1999 Formation Rate Analysis Technique: Combined Drawdown and Buildup Analysis for Wireline Formation Test Data. *SPERE* **2** (3).

Kuchuk, F. 1999 A New Method for Determination of Reservoir Pressure. In *Soc. of Pet. Eng. Annuat Technical Conference and Exhibition, Houston, USA. SPE 56418*.

KUCHUK, F., ONUR, M. & HOLLAENDER, F. 2010 *Pressure Transient Formation and Well Testing*, 1st edn. New York: Elsevier Science.

LEBOURG, M., FIELD, R. & DOH, C. 1957 A Method of Formation Testing on Logging Cable. *Trans. Am. Inst. Mininig Met. Engrs. (Petroleum Development and Technology)* **210**, 260.

LEE, J. 1982 *Well Testing*, *SPE Textbook Series*, vol. 1. SPE.

MATSUMOTO, N., SUDO, Y., SINHA, B. & NIWA, M. 2000 Long-Term Stability and Performance Characteristics of Crystal Quartz Gauge at High Pressures and Temperatures. *IEEE Transactions on Ultrasonics, Ferroelectrics, and Frequency Control* **47** (2).

MATTHEWS, C. & RUSSELL, D. 1967 *Pressure Buildup and Flow Tests in Wells*, *Monograph Series*, vol. 1. Society of Petroleum Engineers.

MORAN, J. & FINKLEA, E. 1962 Theoretical Analysis of the Pressure Phenomena Associated with the Wireline Formation Tester. *Journal of Petroleum Technology* (SPE 177), pp.899–908.

NOIROT, M., MASSONNAT, G. & JOURDE, H. 2011 Simulation of WFT Responses in Heterogeneous Reservoirs. Consequences on Permeability Evaluation at Different Scales. In *73rd EAGE Conference & Exhibition incorporating SPE EUROPEC 2011 Vienna, Austria.*

PELLISIER-COMBESCURE, J., POLLOCK, D. & WITTMANN, M. 1979 Applications of the Repeat Formation Tester Pressure Measurements in the

Middle East. In *Soc. of Pet. Eng. Middle East Oil Technical Conference, Bahrain. SPE 7775*.

Phelps, G., Stewart, G. & Peden, J. 1984*a* The Analysis of the Invaded Zone Characteristics and Their Influence on Wireline Log and Well-Test Interpretation. In *Soc. of Pet. Eng. Annual Technical Conference and Exhibition, Houston, TX. SPE 13287*.

Phelps, G., Stewart, G. & Peden, J. 1984*b* The Effect of Filtrate Invasion and Formation Wettability on Repeat Formation Tester Measurements. In *European Petroleum Conference, London, England. SPE 12962*. Society of Petroleum Engineers.

Proett, M. & Chin, W. 1996 Supercharge Pressure Compensation Using a New Wireline Testing Method and Newly Developed Early Time Spherical Flow Model. In *Soc. of Pet. Eng. Annual Technical Conference and Exhibition, Denver, CO. SPE 36524*.

Proett, M. & Chin, W. 1998 New Exact Spherical Flow Solution With Storage and Skin for Early-Time Interpretation With Applications to Wireline Formation and Early-Evaluation Drillstem Testing. In *Soc. of Pet. Eng. Annual Technical Conference and Exhibition, New Orleans, LA. SPE 49140*.

Proett, M., Chin, W. & Mandal, B. 2000 Advanced Dual Probe Formation Tester with Transient, Harmonic, and Pulsed Time-Delay Testing Methods Determines Permeability, Skin, and Anisotropy. In *SPE International Oil and Gas Conference and Exhibition, Beijing, China*. Society of Petroleum Engineers.

PROETT, M., WAID, M., HEINZE, J. & FRANKI, M. 1994*a* Low Permeability Interpretation Using a New Wireline Formation Tester "Tight Zone" Pressure Transient Analysis. In *SPWLA 35th Annual Logging Symposium*.

PROETT, M., WAID, M. & KESSLER, C. 1994*b* Real Time Pressure Analysis Methods Applied to Wireline Formation Test Data. In *Soc. of Pet. Eng. Annual Technical Conference and Exhibition, New Orleans, LA. SPE 28449*.

RAGHAVAN, R. 1993 *Well Test Analysis*. Prentice Hall Petroleum Engineering.

SCHLUMBERGER 2006 *Fundamentals of Formation Testing*. Schlumberger.

SCHULTZ, A., BELL, W. & URBANOWSKY, H. 1975 Advancements in Uncased-Hole, Wireline Formation-Tester Techniques. *Journal of Petroleum Technology* pp. 1331–1336.

SHEN, C. & RUTH, D. 1994 Steady-State Solutions to Bentsen's Equation. *Transport in Porous Media* **16** (2), 105–123.

SHENG, J. J. 2010 Discussion of Permeability Anisotropy Effect in Transformation. *Journal of Canadian Petroleum Technology* **49** (7), 42–46.

SMOLEN, J. & LITSEY, L. 1979 Formation Evaluation Using Wireline Formation Tester Pressure Data. *Journal of Petroleum Technology* pp. 25–35.

STEWART, G. & WITTMANN, M. 1979 Interpretation of the Pressure Response of the Repeat Formation Tester. In *Soc. of Petrol. Eng. Annual Technical Conference and Exhibition, Las Vegas, NV. SPE 8362*.

STRELTSOVA, T. 1994 *Well Testing in Heterogenous Formations*. John Wiley & Sons.

VENERUSO, A., EHLIG-ECONOMIDES, C. & PETITJEAN, L. 1991 Pressure Gauge Specification Considerations in Practical Well Testing. In *Soc. of Pet.. Eng. Annual Technical Conference and Exhibition, Dallas, TX. SPE 22752*.

WILKINSON, D. & HAMMOND, P. S. 1990 A Perturbation Method for Mixed Boundary-Value Problems in Pressure Transient Testing. *Transport in Porous Media* **5**, 609–636.

WU, J., LEE, J. & MEISTER, M. 2007 New Invasion Model for Supercharging Estimation. In *SPE Annual Technical Conference and Exhibition, Anaheim, California, USA, SPE 110389*.

YILDIZ, T., DESBRANDES, R. & BASSIOUNI, Z. 1991 Flowline Storage Effect on Wireline Formation Tester. In *Soc. of Pet. Eng. Annual Technical Conference and Exhibition, Dallas, Texas. SPE 22753*.

ZIMMERMAN, T., MACINNIS, J., HOPPE, J. & POP, J. 1990 Application of Emerging Wireline Formation Testing Technologies. In *Eighth Offshore South East Asia Conference. Paper OSEA-90081*.

Vita

Soraya Sofia Betancourt received a Bachelor of Science degree in Petroleum Engineering from Universidad del Zulia in Maracaibo, Venezuela. After graduation in 1995, she joined PDVSA in Western Venezuela Lake Maracaibo Region as drilling engineer in development and exploration wells, and later in the Production Technology group in charge of designing, implementing, and evaluating novel artificial lift projects. In 2000, Soraya completed a Master's Degree Program in Petroleum Engineering at the University of Tulsa, where she worked with Prof. Dean Oliver in the evaluation of different methods to assess uncertainty in reservoir flow predictions. Afterwards, she joined Schlumberger's Reservoir Completions Center in Rosharon, Texas as a reservoir engineer in the Advanced Completions group conducting simulation studies to optimize well completion designs involving in-situ pressure and flowrate sensing and zonal flow control technology. In 2001, she moved to Schlumberger-Doll Research in Ridgefield, Connecticut and later to Cambridge, Massachusetts, where to the present day she works in the area of formation testing and downhole fluid analysis. She started graduate studies towards a PhD degree in 2004 in the Petroleum and Geosystems Engineering Department of The University of Texas at Austin.

Permanent address: 13 James Way
Cambridge, Massachusetts 02141

This dissertation was typeset with LaTeX[†] by the author.

[†] LaTeX is a document preparation system developed by Leslie Lamport as a special version of Donald Knuth's TeX Program.